Indentation and Wear Damage Assessment of TiC-Stainless Steel Cermets

by

Chenxin Jin

Submitted in partial fulfilment of the requirements

for the degree of Doctor of Philosophy

at

Dalhousie University

Halifax, Nova Scotia

July 2016

Dedication

To my wonderful husband, Fuyuan Lin, and my amazing family

Table of Contents

List of Tables

List of Figures

Abstract

Cermets, a composite of a hard ceramic phase and ductile metallic phase, are widely used in oil and gas, chemical, mining, and tooling industries, due to their high hardness, toughness, wear and corrosion resistance. A family of TiC - stainless steel cermets was produced in the current study using a simple melt infiltration method, with binder phase (steel grades 304-L, 316-L and 410-L) contents ranging from 5 to 30 vol.%. The materials were sintered at 1475°C for 15 minutes, 1500°C and 1550°C for 60 minutes, and 1550°C for 240 minutes to get fine-, intermediate- and coarse-grained cermets.

The microstructural evolution arising from the sintering process was then examined. It has shown that irregular shaped grains (concave/hollow) were produced, especially when sintered at 1475°C, and was explained using the 'instability of the solid-liquid interface' theory. It was also demonstrated that a multi-layer, core-rim structure arose for the cermets, with selected steel constituents present in the rim of the TiC grains.

The cermets were tested using both 'sharp' and 'blunt' indenters to study contact damage. Materials indented with a 'sharp' Vickers indenter, ranging from 1 to 30 kgf load, revealed an apparent 'indentation size effect', with hardness increasing with decreasing test load. Two primary indentation-cracking patterns were observed, namely median and Palmqvist cracks. Crack patterns were assessed using focused ion beam microscopy (FIB). Cermets loaded with a 'blunt' Hertzian indenter were tested with various WC-Co spheres, ranging from 1.19 to 3.97 mm, with applied loads from 250 to 2000 N. Indentation stress-strain curves were plotted and compared with the calculated Hertzian elastic response, and the materials were found to have a 'quasi-plastic' behaviour and 'strain-hardening' effect.

The reciprocating wear response of cermets with various TiC grain sizes and binder phase contents/compositions, were evaluated using a ball-on-flat reciprocating wear tests, using a WC-Co counter face sphere and loads from 20 to 80 N. The specific wear rate of the cermets was found to increase with applied load, testing time and/or the steel binder content. The morphology of the worn surfaces was studied using scanning electron microscopy (SEM), energy dispersive x-ray spectroscopy (EDS), and FIB microscopy, in order to fully understand the operative wear mechanisms. A transition from two- to three-body abrasive wear was observed, with a further transition to adhesive wear identified through the formation of an oxygen-rich tribolayer.

List of Abbreviations and Symbols Used

Abbreviations

AISI	American Iron and Steel Institute
ASTM	American Society for Testing and Materials
BCT	Body centred tetragonal
CN	Chevron-notch
COF	Coefficient of friction
CIP	Cold isostatic pressing
DBTT	Ductile-to-brittle transition temperature
DCB	Double cantilever beam
DIC	Differential interference contrast microscopy
DSC	Differential scanning calorimetry
EBSD	Electron back scattered diffraction
EDS	Energy dispersive X-ray spectroscopy
FEM	Finite element method
FIB	Focused ion beam microscopy
HIP	Hot isostatic pressing
HV	Vickers hardness
ICP-OES	Inductively coupled plasma optical emission spectrometry
IFR	Indentation fracture resistance
ISE	Indentation size effect
LPS	Liquid phase sintering
LVDT	Linear variable differential transformer
MFP	Mean free path
PDF	Powder diffraction file
PSR	Proportional specimen resistance
SAE	Society of Automotive Engineers
SEM	Scanning electron microscopy
SENB	Single-edge notched beam

SEVNB	Single-edge V-notched beam
SHS	Self-propagating high-temperature synthesis
UMT	Universal micro tribometer
VIF	Vickers indentation fracture toughness
XRD	X-ray diffraction

Symbols

a	Contact radius; half diagonal length of a Vickers indentation
at.%	Atomic percent
A	Constant; area in contact
c	Total distance from a Vickers indentation centre to crack tip
C	Contiguity; hardness constraint factor
δ	Peak deflection during Hertz indentation
d	Average diagonal length of a Vickers indentation
d_b	Binder mean free path
d_c	Mean grain size
D	Sliding distance; spherical indenter diameter; constant
E	Young's modulus
ε	strain
F	Force
G	Strain energy release rate per unit of crack extension; shear modulus
h	Distance
h_r	Indentation depth of residual impression
H	Hardness
κ	Stress concentration factor
k	Specific wear rate; constant; elastic mismatch parameter
K	Bulk modulus
K_C	Critical stress intensity factor, fracture toughness
K_{IC}	Critical stress intensity factor under mode I (tension), indentation fracture resistance

l	Crack length of a Vickers indents, from the corner to the tip; size of microcracks
N	Total number
$N_{c/c}$	Number of carbide-carbide interfaces
$N_{c/b}$	Number of carbide-binder interfaces
σ	Normal stress
σ_m	Mean stress
σ_{max}	Maximum tensile stress
σ_{yy}	Stress field
ρ	Curvature of the tip of a hole
P	load
p_c	Critical load for brittle cone crack
p_m	Mean contact pressure
p_Y	Critical load for quasi-plastic at yield
P_r	Residual driving force
r	Radial distance
R	Spherical indenter radius
Q	Volume wear per unit sliding distance in brittle materials
t	Time
τ	Shear stress
τ_m	Maximum shear stress
V	volume
ν	Poisson's ratio
wt.%	Weight percent
W	constant
γ	Surface energy per unit area
Y	Yield stress

Acknowledgement

I would first like to thank Dr. Plucknett for his guidance, encouragement, faith and support through the years, and helped me developed my interest in the field of microscopy techniques. I am grateful to have Dr. Plucknett not only as my supervisor, but also as my mentor. I would like to thank Dr. Farhat, for his assistance of the equipment and valuable suggestions throughout the project. I would like to thank Dr. Taheri, his extensive knowledge and non-stop encouragement has helped me build up the engineering backgrounds. I would also like to thank Dr. Bishop, Dr. Warkentin and Dr. Doman for their assistance of the equipment and discussions as well.

I would like to express my great appreciation for Ms. Patricia Scallion, for technical support of the SEM-FIB facilities, and Mr. Dean Grijm for the machining and equipment maintenance. I am also grateful for having a lot of wonderful colleagues: Hung-Wei, Chuks, Tyler, Zhila, Greg, Randy, Mark, Md., Will, Rabin, Rusho, Iris from the Department of Process Engineering and Applied Science; Andrew, Abdullah, Andrea from the Department of Mechanical Engineering; Zohreh, Mbarka, Babak, Mohamad from the Department of Civil and Resource Engineering. I truly appreciate you all for your help.

I would like to thank Dr. Lisa White from the Dalhousie Counselling Centre for helping me get through those hard days.

Finally I would like to thank my husband Mr. Fuyuan Lin, for his love, care, patience, and encouragement. His determination and strong believe in me have helped me to get over all the difficulties, especially in the last two years. Though he is not by my side, I can always feel his support. I would like to thank my whole family, I cannot be who I am today without them.

Chapter 1 Introduction

Cermets are composites consisting of a hard ceramic phase, which provides wear resistance and stiffness, and a ductile metal binder phase, that contributes toughness [1]. Cermets, when compared with conventional 'hardmetal' tungsten carbide (WC-Co) materials, are lighter in weight with high mechanical properties such as strength, toughness and thermal conductivity [1-4]. Titanium carbide (TiC) based cermets are considered a promising material due to a high melting temperature, elastic modulus, and hardness, while TiC can retain its mechanical properties at moderately high temperatures [5-7]. Because of the hard but brittle properties of TiC, a variety of metals have been added as a binder phase, such as Ni, Mo, Co and Fe [8-11]. The properties and application of Ni or Co as binders were studied extensively, however, steel alloy binders has been paid relatively little attention, particularly for stainless steel alloys [12]. Austenitic stainless steels have high strength and can maintain moderately good mechanical properties at elevated temperatures [13]. Specifically, 304-L and 316-L stainless steels have reduced carbon that can help eliminate chromium carbide formation and intergranular corrosion. In addition, the molybdenum in 316-L can increase pitting resistance [14]. Though the wear resistance of stainless steels is relatively poor, the reasonable corrosion resistance in combination with a hard ceramic phase has made it a prominent candidate for use in the tooling industry [15,16]. Martensitic stainless steels can be forged and heat treated to obtain properties that require both corrosion and wear resistance. The 410-L grade, for example, provides high strength and hardness with good corrosion resistance in air, water and some acid environments [14].

In the current research, a family of TiC based cermets, prepared with nominally austenitic (304-L and 316-L) and martensitic (410-L) stainless steel grades, were produced using a simple melt infiltration method. As the cermets are commonly used as coatings in pipelines, tooling and mining industries, understanding the damage of the material is essential in estimating the performance and predicting the life cycle. This research uses a combination of optical and electron microscopy techniques to characterise the microstructure, evaluating the mechanical properties such as hardness and indentation fracture resistance. The damage by static load was conducted by indentation techniques

as different crack patterns generated by ‘sharp’ Vickers indenters are related to the tendency of material removal, for example during a sharp particle erosion scenario. ‘Blunt’ Hertzian indentation is essentially used to evaluate the damage by a sphere in static loading motion. The further damage caused by dynamic load, for a similar spherical contact, was conducted by reciprocating wear; the microstructure evolution during the process was then studied using the various microscopy techniques. These approaches, using sharp and blunt indenters, are linked through the various wear processes that may arise during use.

The microstructure evolution that occurs during liquid phase sintering is worth noting, since study of how the microstructure affects the properties of the material is vital in helping understand the overall processing-microstructure-property relationships. Scanning electron microscopy (SEM), associated with energy dispersive X-ray spectroscopy (EDS) were applied for characterisation of the sintered and polished samples, in particular to study the microstructure evolution and stability of TiC-316L stainless steel cermets.

Indentation tests were employed to evaluate the fundamental mechanical properties of the materials, using both sharp (Vickers) and blunt (Hertzian sphere) indenters; the primary aim here being to assess contact damage mechanisms. This allows investigation of the deformation and failure behaviour of the materials in contact, both statically and dynamically, when used in bearings, semiconductors, microelectromechanical systems, biomaterials contact such as bone, teeth and joints [17]. As noted above, the indentation methods are often divided into ‘sharp’ (i.e. Vickers, Knoop, Berkovich, etc.) and ‘blunt’ (i.e. sphere, cylinder). In the current study, Vickers diamond pyramid and Hertzian sphere indentation were selected to characterise the fracture and material response of TiC-stainless steel cermets. The objective of the indentation using ‘sharp’ Vickers indenters, is to study the effect of microstructure and binder content on the hardness and indentation fracture resistance of the cermets. The materials were found to exhibit an ‘indentation size effect’ (ISE) and apparent ‘*R*-curve’ behaviour. Indentation fracture resistance (IFR) values were evaluated with various analytical models, and the different types of indentation-induced cracks were predicted and analysed using site-specific micro-machining in the focused ion beam microscopy (FIB). The aim of studying ‘blunt’

Hertzian indentation is to evaluate the material response under such contact geometries. To achieve this, a series of WC-Co spheres of different diameters were used to study the indentation response of the material, and the role of 'quasi-plasticity' in deformation of the cermets.

The final objective of the current research is to assess the wear damage evolution of a wider range of TiC-stainless steel cermets, using both the austenitic and martensitic steels described earlier. It was estimated some 30 years ago [18] that wear and friction damage costs the Canadian mining industry roughly $940 million per year. As the one of the largest oil and gas companies in Canada, Syncrude Ltd. has an annual budget of approximately $450 million to repair and maintain their equipment, with a significant portion of this related to damage arising from wear and friction [19]. With increasing TiC based cermets being used in industry, it is important to study the wear behaviour of these kinds of material and to be able to develop new variants with improved properties. Reciprocating wear tests were conducted, with a WC-Co counter face sphere, serving as a 'ball-on-flat' geometry, with various applied loads and test durations. To understand the effects of the cermet microstructure, including the TiC grain size and binder phase content, and the steel composition, the specific wear rate of the materials were determined. A major aspect of this work was to utilise a variety of optical, electron and ion beam microscopy techniques to fully evaluate the effects of wear damage on the microstructure of the materials.

The present thesis is divided into ten chapters, which follows the progress of the work. In Chapter 2 a general literature review is presented relating to the current study, including discussion of cermet materials, their fabrication, associated studies for both 'sharp' and 'blunt' indentation, and wear of these materials, noting the current status of each field. Chapter 3 provides further details regarding the experimental procedures used in the current study and, in particular, to focus on aspects that were not fully presented in the following chapters. Chapter 4 presents an in depth study of the microstructure evolution during the liquid phase sintering of TiC-316L cermets, in particular assessing phase stability and modification. Chapters 5 and 6 relate to the behaviour when using 'sharp' Vickers and 'blunt' Hertzian indentation on the TiC-316L cermets, respectively. These studies have focused on the effects of microstructure on the indentation response, and

provided experimental data for future finite element modelling of the indentation behaviour of the cermets. All of the experimental studies, material characterisation and subsequent analyses, and the manuscript preparation, for each of Chapters 4 to 6, were conducted by the thesis author; this was conducted under the guidance of the PhD supervisor. Chapters 7 to 9, inclusive, relate to the wear behaviour of the current materials for all steel compositions examined (i.e. 304L, 316L and 410L). These chapters are joint work, in which all of the wear tests were conducted by an earlier PhD student, Dr. Chukwuma Onuoha. Subsequent data evaluation, numerical analysis and microscopical characterisation (e.g. optical microscopy, SEM, EDS and FIB) were conducted by the thesis author, who also drafted the manuscripts. Chapter 7 focuses on the effects of TiC grain size and steel binder content on the reciprocating wear response of TiC-316L stainless steel cermets. Chapters 8 and 9 are present the wear characteristics and microstructure evolution following wear testing of TiC-304L, TiC-316L and TiC410L cermets, comparing the effects of the different steel binders. Finally, Chapter 10 provides a summary of the principle research findings and makes recommendations for future studies relating to this work.

Chapter 2 Literature Review

2.1 Introduction to Cermets

The traditional 'hardmetals' or cemented carbides were first developed in Germany during the 1920s, as wear resistant materials [20]. Conventional WC-Co 'hardmetals' are still widely used today. These materials are typically obtained through liquid phase sintering, just above the eutectic composition melting point, and an essentially fully densified composite is usually achieved. Cemented carbides are harder than any tool steels, and have extremely good resistance to low-stress abrasive wear. Because of their excellent hardness, and abrasion and wear resistance properties, cemented carbides especially WC based materials were the first kind of ceramic-metal composite, or 'cermet', which was heavily researched. During World War II, the need for high-temperature, high stress-resistant materials was clear, and the supply shortage of tungsten in Germany encouraged scientists to look for an alternative material for tungsten-based hardmetals. German scientists developed an oxide-based material, which appeared very promising for applications in the high-temperature sections of the new jet engines, and consequently development programs were initiated. With the growth of cermet development, many research laboratories contributed to this technology. Ohio State University, University of Illinois, Rutgers University, and the Union Carbide chemical company all contributed to the development of MgO, BeO, and Al_2O_3 based cermets. Kennametal, Inc., American Electrometals, Inc., Sintercast Corporation, Thompson Products, and the Firth Sterling Company all focused research in this area, which resulted in the development of nickel-bonded TiC cermets [1]. A brief historical development of cemented carbides and cermets is listed in Table 2.1.

Cemented carbides and cermets, such as WC and TiC, are also often termed refractory carbides, meaning a material with a high melting point (usually great than 1800ºC), which possess a high degree of chemical stability. Cermets combined the desirable qualities and suppressed the undesirable properties of their constituent ceramic and metal phases, notably combining the high melting point and chemical stability (i.e. the oxidation and corrosion resistance) of the ceramic and the toughness of the metal. Compared with conventional materials, cermets are lighter in weight, with excellent

mechanical properties such as high strength, toughness and thermal conductivity. Cermet cutting tools provide better control of geometry accuracy during machining, better chip and tolerance control, longer tool life, improved surface finish, increased workpiece feed rates, and can provide consistent retention of critical dimensions [21]. High conductivity produces a low temperature gradient resulting in reduced thermal stresses and cracking.

Table 2.1: History of hardmetal and cermet product development, adapted from 'Story of cermet' [22] .

Year	Composition	Trademark	Manufacturer
1930-1931	WC-Co	G1	Krupp-Widia
1930	TiC-Mo_2-C-(Ni,Mo,Cr)	Titanit S	Mettalwerk Plansee
1930	TaC-Ni	Ramet	Fansteel Corporation
1933	TiC-TaC-Ni		Siemens AG
1938-1945	TiC-VC-(Fe,Ni,Co)		Metallwerk Plansee
1945-1955	TiC-(NbC)-(Ni, Co, Cr, Mo, Al)	WZ	Metallwerk Plansee
	TiC-(Nb, Ta, Ti) C-(Ni, Mo, Co)	Kentanium	Kennametal
1952-1954	TiC-(steel, Mo)	Ferro-TiC	Sintercast (Chromalloy)
1960	TiC-(Ni, Mo)		Ford Motor Company
1970	Ti(C, N)-(Ni, Mo)	Experimental alloys	Technical University Vienna
1974	(Ti,Mo) (C,N)-(Ni,Mo)	Spinodal Alloy	Teledyne Firth Sterling
1975	TiC-TiN-WC-Mo_2C-VC-(Ni, Co)	KC-3	Kyocera
1977-1980	TiC-Mo_2C-(Ni, Mo, Al)		Ford Motor Company, Mitsubishi
1980-1983	(Ti, Mo, W) (C, N)-(Ni, Mo, Al)		Mitsubishi
1988	(Ti, Ta, Nb, V, Mo, W) (C, N)-(Ni, Co)-Ti_2AlN	TTI,TTI 15	Krupp-Widia

2.2 Titanium Carbide

2.2.1 Properties of Titanium Carbide

2.2.1.1 Crystal Structural Properties

TiC has a face-centred cubic (FCC) crystal structure, with its unit cell effectively the same as that of the NaCl-type (Figure 2.1), with the carbon atoms in the interstitial positions. The molecular weight of TiC is 59.91 g/mol [4].

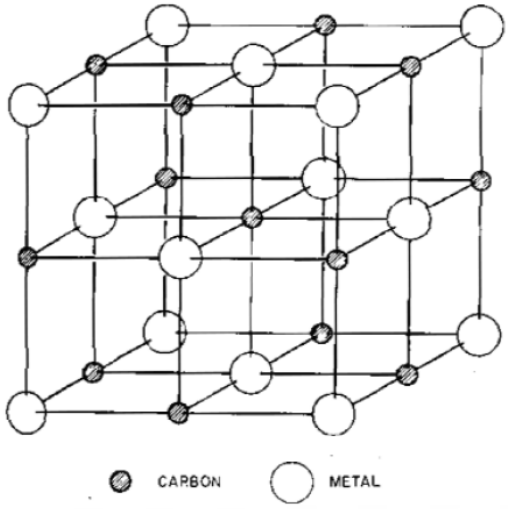

Figure 2.1: NaCl type of structure [2] .

TiC exists as a homogeneous phase, sometimes written as TiC_x, where $0.47<x<1.0$ [23]. The melting temperature of TiC has a range from 1918 to 3067ºC, depending on the composition, which is the value of x, where the high bound conforms to x~1.0. The phase diagram of the C-Ti system is shown in Figure 2.2. The lattice structure has a reported parameter $a_0 = 0.4329 \pm 0.0001$ nm.

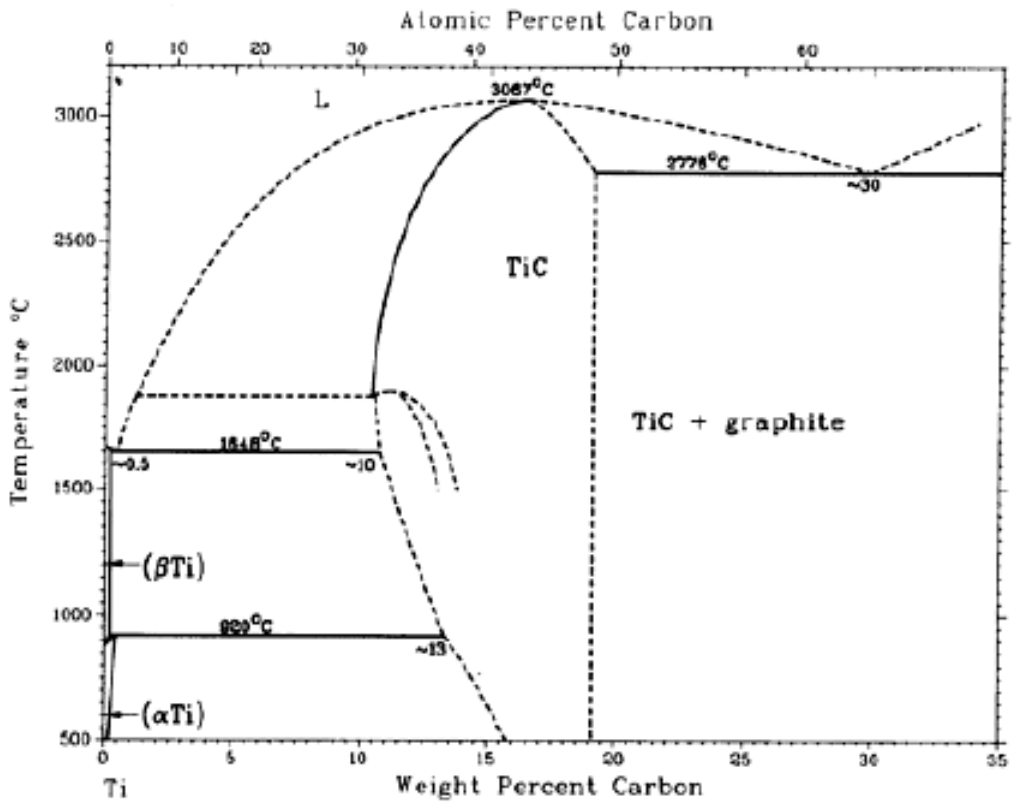

Figure 2.2: C-Ti phase diagram [24] .

Depending on the stoichiometry, the lattice parameter actually changes, which is presented in Figure 2.3 and highlights the variation of lattice parameter as a function of composition. It has been shown that for composition below $TiC_{0.65}$ the measurements agreed well, while the points are mores scattered for the higher carbon content compositions. It has been suggested by Rudy [25] *et al.* that the lattice parameters depends on the quenching temperature, a higher parameter is determined when quenching from higher temperature since it favours production of a purer TiC. There are difficulties in preparing TiC, which requires an O_2 and N_2 free environment [3]. It can effectively be deduced from this figure that the density of TiC decreases from ~4.91g/cm^3 at $TiC_{1.0}$ to ~4.51g/cm^3 at $TiC_{0.5}$.

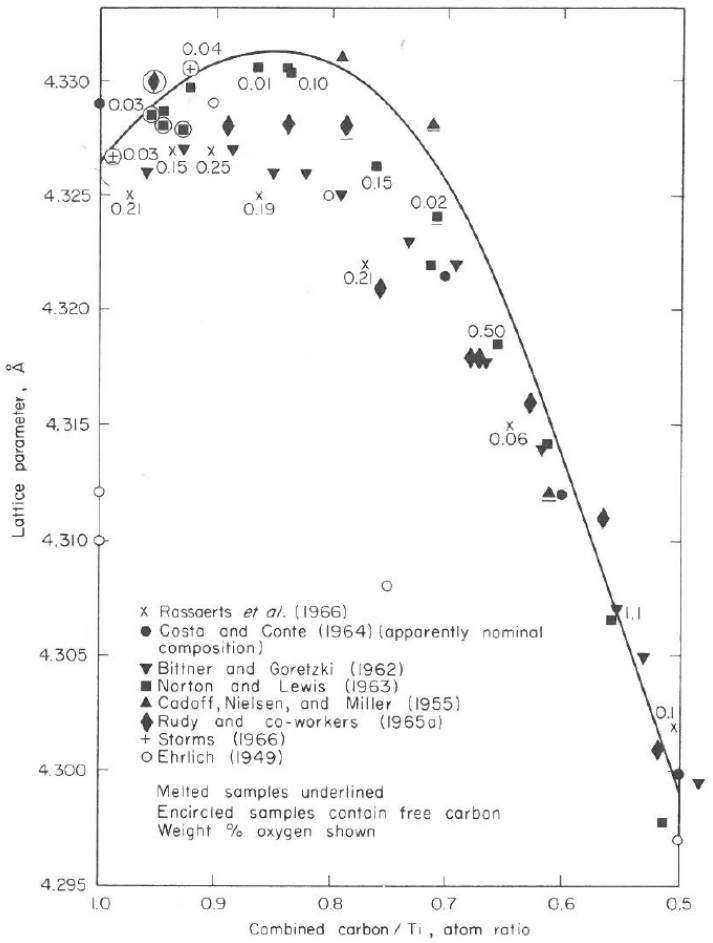

Figure 2.3: Variation of TiC lattice parameter [3] .

2.2.1.2 Mechanical Properties

TiC usually has a given density of 4.91g/cm^3, as an average, neglecting the stoichiometry, with a high melting point of 3067ºC [4]. The mechanical properties have been reported as [4]: Vickers hardness of 28-35 GPa, Young's modulus of 410-510 GPa, transverse shear modulus of 186 GPa, a rupture (i.e. flexure) strength of 240-390 MPa, and a bulk modulus of 240-390 MPa. Poisson's ratio has been determined to be 0.191, with a coefficient of friction of 0.25 (on tool steel, 50% humidity).

A comprehensive study to determine the 'ductile-to-brittle transition temperature' (DBTT) of polycrystalline TiC, by producing four different substoichiometric TiC variants, was conducted by Miracle and Lipsitt [26]. Both the crystal structure and mechanical properties were determined. Powders were blended and vacuum hot-pressed

to fabricate the samples with four C/Ti atoms ratios: 0.65, 0.75, 0.85 and 0.95. It was shown that the mean grain size increased with decreasing stoichiometry, which was most likely due to a diffusion kinetics change. The hardness, using Knoop testing, was also shown to decrease with a decreasing C/Ti ratio. The measured lattice parameters agreed with the literature shown above, in Figure 2.3. The measured data are presented in Table 2.2.

Table 2.2: Properties of sub-stoichiometric TiC, determined by Miracle and Lipsitt [26] .

Material	Density (g/cm^3)	% Theor. Density	a_0 (nm)	Knoop hardness (GPa)	Grain size (μm)
$TiC_{0.93}$	4.8503	≈100	0.43299	17.40±0.74	14
$TiC_{0.83}$	4.6199	97.7	0.43318	15.14±0.74	20
$TiC_{0.75}$	4.6501	99.8	0.43288	14.68±0.64	21
$TiC_{0.66}$	4.5983	99.9	0.43199	12.83±0.42	22

2.2.1.3 Other Properties

Other properties of TiC ceramics have been reported [4]: the specific heat at 298 K is 33.8 J/mole·K, with a thermal conductivity of 21.0 W/m·K at 20 ºC, and a thermal expansion coefficient of 7.4 ($\times 10^{-6}$/ ºC) at 20 ºC. In terms of the electrical properties, the electrical resistivity at 20 ºC is 68 μΩ·cm, the Hall constant at 20 ºC is -15.0×10^{-4} $cm^3/A\cdot s$, and magnetic susceptibility of -7.5×10^{-6} emu/mol. TiC is resistant to most acids, but is attacked by HNO_3 and HF. It can be heated in a hydrogen environment to its melting point without decomposition.

2.2.2 Fabrication of TiC Powders

TiC was first isolated as a compound by Shimer, in 1887 [27], using hydrochloric acid from a titanium-bearing cast iron. Subsequently, a few other methods were developed, including by Moissan [28,29] for the reduction of TiO_2 using carbon. This method has been applied to industrial manufacturing of TiC, and has been extensively studied [4]. The oxide reduction starts at 935ºC [30] by Elyutin in 1958, and proceeds through the sequence reaction between 1000 ºC and 1500 ºC Samsonov in 1956 [31], following:

$$TiO_2 \rightarrow Ti_3O_5 \rightarrow Ti_2O_3 \rightarrow TiO \rightarrow TiC \text{ or } Ti$$

The final product should be present in the form of TiC_xO_y Kutsev and Ormont [32] in 1955. With time, the TiC and/or Ti with a lowered amount of carbon were found when heating at 1200ºC [3]. Subsequently, researchers have found that TiC can be formed more easily in the presence of CO, although a higher temperature required. In 1952, Meerson and Krein [33] demonstrated that a ratio close to 1:1 can be obtained under 1-10 torr CO pressure at 1600-1700ºC. Furthermore, titanium hydride (TiH_2) and C were found to produce stoichiometric carbide, beginning at 900ºC, and completed after 1 hour at 1200ºC (Ogawa and Bando, 1959 [34]). By heating up a tungsten wire in an atmosphere of $TiCl_4$, H_2 and hydrocarbon vapor, Campbell [35] *et al.* also formed the carbide. Preparation of TiC from TiS_2 and C has also been reported by Schuler in 1952 [36].

The commercial manufacture of TiC is primarily conducted using carbothermal synthesis [2]. The starting material is 68.5% of titanium dioxide (TiO_2), mixed and wet or dry milled with 31.5% carbon black or graphite. The carburization is carried out under hydrogen, in carbon-tube furnaces at 1900-2100ºC. The reaction for reduction of TiO_2 by carbon is shown by:

$$TiO_2(s) + 3C(s) = TiC(s) + 2CO(g) \qquad \text{Equation 2.1}$$

This production method is somewhat limited, because the powders may have a wide size range [37], and thus require a subsequent milling process. The reaction time is also long, typically ranging from 10-20 h. The inhomogeneity generated because of diffusion gradients is another issue for the reduction reaction approach [37].

Direction carburization methods are also used to produce TiC powders, following:

$$Ti(s) + C(s) = TiC(s) \qquad \text{Equation 2.2}$$

This method usually requires a reaction time of 5-20h, and the products are agglomerated [37]. It is also relatively expensive since the cost of Ti metal powder is high [37].

The manufacturing of TiC in large scale usually uses carburization with solid carbon and chemical isolation at 1300-1700ºC. By treating titanium-containing cast iron with hydrochloric acid, Shimer [27] has produced fine-grained 71.6% titanium, with impurities, and 16.9% carbon products. The reaction is written as:

$$TiCl_4 + H_2 + C_xH_y^a = TiC + HCl + (CH)^b \qquad \text{Equation 2.3}$$

A similar production route is the reaction between $TiCl_4$, H_2, and C, by decomposition the carbides form from a gaseous phase. The gas reaction is driven by a tungsten or carbon filament, at 1530-1880ºC. Single crystal or polycrystalline TiC is directly grown on the filament, therefore the quantity is quite limited. Also the reaction has to be handled with care since the precursor $TiCl_4$ and HCl are corrosive. The reaction is written as:

$$TiCl_4(g) + 2H_2(g) + C(s) = TiC(g) + 4HCl(l) \qquad \text{Equation 2.4}$$

Self-propagating high temperature synthesis, or SHS, is a self-sustaining combustion reaction that is extensively used at a laboratory scale. The reaction is fast, since the starting particles are fine and highly reactive. The heat released from the reaction is sufficient to continue the reaction after the ignition. The products are also reported to be pure, with better mechanical properties. The powders can be combusted in both loose and pressed form [23]. The powders were mixed in a ratio of 81.0 wt.% of Ti and 19.0 wt.%, to give a nominal C/Ti ratio of 0.936, slightly lower than the maximum value (0.967) of the TiC single-phase region [23], since experimental studies have shown that the final ratio will be higher than initially prepared. After igniting the powder by a heated tungsten coil, the combustion would spontaneously continue, finishing up with the product of C/Ti ratio of 0.953. The pressed powders were ignited in a glove-box under argon atmosphere. Final microstructure studies reveal that porosity exists, while the level of impurities is low [23].

2.3 Steel and Stainless Steel

Steels are one of the most widely used and studied materials in human history; it has been defined as an alloy of iron and small amount of carbon, and potentially further elements [14]. As a consequence, the C-Fe phase diagram one of the most important binary phase diagrams, as shown in Figure 2.4 [24]. The ferrite phase is the stable form at room temperature, which has a BCC structure, is also called α-iron. Transformation to FCC austenite (γ-iron) would happen at 972ºC on heating, followed by a reverse back to a BCC phase, termed δ-ferrite, at 1394ºC [38].

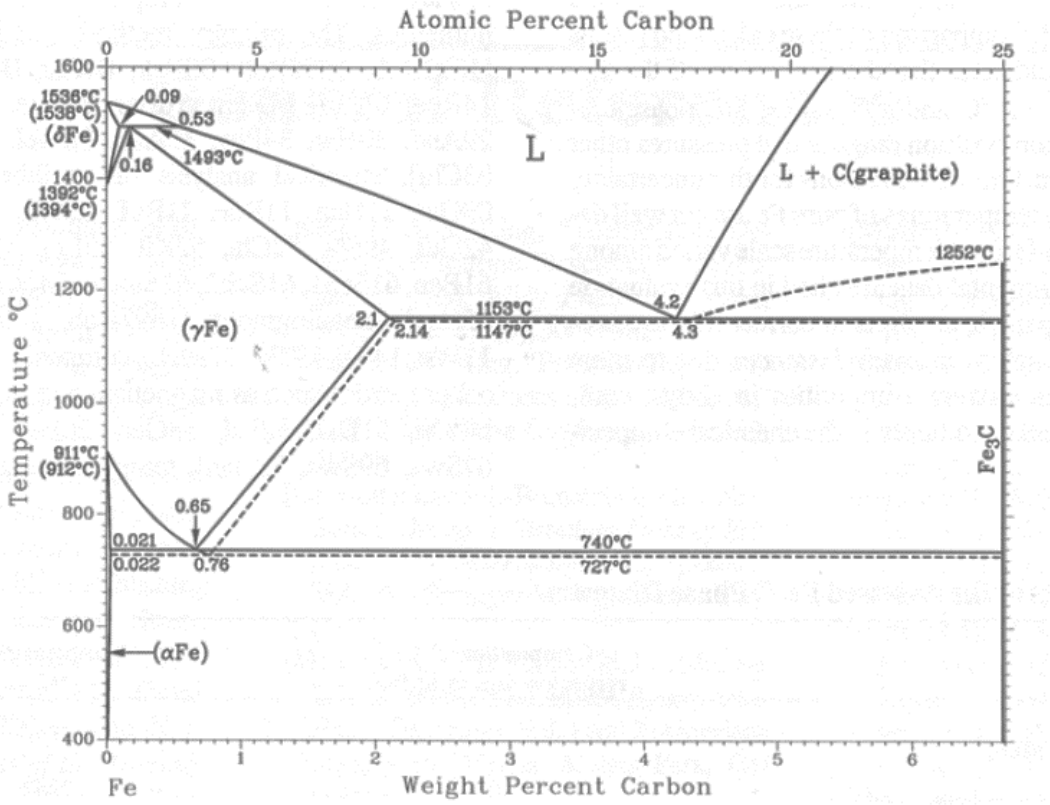

Figure 2.4: The C-Fe phase diagrams [24] .

The American Iron and Steel Institute (AISI) and the Society of Automotive Engineers (SAE) developed a system to designate carbon and alloy steel grades, by using four-digit numbering system. The first two specify the major alloy elements, and if not present, is presented as 10. The last two digits specify nominal carbon contents. For example, 1060 steel is a kind of plain-carbon steel, in the family of 1xxx, with 0.6 wt.% of carbon.

2.3.1 Stainless Steel Classification

Stainless steel comprises the group of iron alloys with the addition of specific elements, especially Cr in excess of 12 wt.%, designed to increase the alloy corrosion resistance. These steels also invariably have reasonable formability, high room temperature and cryogenic toughness, resistance to oxidation and scaling, and good elevated temperature creep resistance [14]. Examples are summarised below:

200 series: austenitic chromium-nickel-manganese alloys

300 series: austenitic chromium-nickel alloys

400 series: ferritic and martensitic chromium alloys

500 series: heat-resisting chromium alloys

600 series: originally created for proprietary alloys, which are no longer given SAE grade numbers

2.3.2 Austenitic Stainless Steels

Table 2.3 listed the compositions of selected AISI 300 austenitic stainless steels. The 300 series steels are used in many fields, especially in corrosion resistance applications. One example contains 18% Cr and 8% Ni, and is also known as 18/8 steel [39]. By increasing the Ni content the properties are improved, and increasing the Cr content can further improve the intergranular corrosion resistance [39]. The grades 301, 302 and 304 have better stability during cold working in comparison to martensitic grades [39]. By eliminating the chromium carbide formation, the reduction in carbon and use of alloying additions can reduce the intergranular corrosion for types 304L, 316L, 321 and 347. Similarly, the molybdenum content in type 316 can increase the pitting resistance, typically in chloride containing solutions [39]. Types 309 and 310 are used for their high-temperature strength performance and scaling resistance [14].

Austenitic stainless steels cannot be hardened through heat treatment, but can be strengthened by cold working. The austenitic stainless steels show typical stress corrosion cracking, which can occur under relatively small stresses, from either applied or residual stresses. In high Ni content austenitic stainless steels the potential for stress corrosion cracking is significantly decreased [39]. However, while the materials are not very strong they show good ductility [39]. Austenitic stainless steels also exhibit good high-temperature oxidation resistance, and high creep properties, aided through precipitation of intermetallic phases [39].

Table 2.3: Compositions of selected AISI type 300 austenitic stainless steels [40] .

	Nominal composition, %				
AISI type No.	**C**	**Mn**	**Cr**	**Ni**	**others**
301	0.15 max	2.0	16-18	6.0-8.0	…
302	0.15 max	2.0	17-19	8.0-10	…
304	0.08 max	2.0	18-20	8.0-12	…
304L	0.03 max	2.0	18-20	8.0-12	…
309	0.20 max	2.0	22-24	12-15	…
310	0.25 max	2.0	24-26	19-22	…
316	0.08 max	2.0	16-18	10-14	2-3 Mo
316L	0.03 max	2.0	16-18	10-14	2-3 Mo
321	0.08 max	2.0	17-19	9-12	(5×%C) Ti min
347	0.08 max	2.0	17-19	9-13	(10×%C)Nb-Ta min

Type 200 austenitic stainless steels are alloyed with manganese and nitrogen, to replace nickel and stabilize the austenitic phase. Table 2.4 lists the compositions of several type 200 austenitic stainless steels.

Table 2.4: Compositions of AISI type 200 austenitic stainless steels [40] .

	Nominal composition, %				
AISI type No.	**C**	**Mn**	**Cr**	**Ni**	**others**
201	0.15 max	7.5	16-18	3.5-5.5	0.25N max
202	0.15 max	10.0	17-19	4.0-6.0	0.25N max

2.3.3 Martensitic Stainless Steels

The original term of ‘martensitic’ stainless steels was named after its first observer, Adolf Martens, in the 1890s. These steels possess a body centred tetragonal (BCT) microstructure. Martensitic stainless steel can be forged and heat treated for a variety of applications which requires high corrosion resistance, wear resistance, together with

strength and hardness [14]. The common AISI 400 grades martensitic stainless steels are listed in Table 2.5.

Table 2.5: Compositions of AISI type 400 martensitic stainless steels [40] .

	Nominal composition, %				
AISI type No.	**C**	**Mn**	**Cr**	**Ni**	**others**
403	0.15 max	1.0	11.5-13	…	…
410	0.15 max	1.0	11.5-13	…	…
416	0.15 max	1.2	12-14	…	0.15S min
420	0.15 min	1.0	12-14	…	…
431	0.20 max	1.0	15-17	1.2-2.5	
440A	0.60-0.75	1.0	16-18	…	0.75Mo max
440B	0.75-0.95	1.0	16-18	…	0.75Mo max
440C	0.95-1.20	1.0	16-18	…	0.75Mo max

2.4 Titanium Carbide Cermets

2.4.1 Introduction

Aside from the traditional cemented carbide based tool materials (WC), carbide-based cermets are still by far the largest category among the cermet family [14]. TiC-based cermets are mainly used as tooling and wear resistant materials. Depending on the binder phase employed, the applications can be broadened to high-stress, high-temperature and wear resistance environments [14]. These kinds of cermets were initially not widely used because of their comparatively low strength and toughness, which were only about 50-60 % of the values for conventional WC-Co cemented carbides, at the beginning of the studies back in around 1930s [5]. Later, the advantages of cost and component availability have gained increasing interest for their continued development [24]. TiC based cermets also have new potential uses, since it has a higher melting temperature and better oxidation resistance when compared to the tungsten based materials [24]. TiC has a combination of good high temperature strength and toughness, but the relatively low impact resistance has limited applications [5]. It was not until 1959 that the Ford Motor

Company were able to significantly improve the properties TiC based cermets [41-43]. Soon after that, the materials have gained greater interest for use as a tooling material.

The brittle characteristic of TiC requires combination with metals to reach the desired mechanical requirements. The major binder metallic alloys that were studied include: Ni-Mo, Ni-Mo-Al, Ni-Cr and Ni-Co-Cr. Nickel is the most commonly used metallic binder in TiC based composites, which is mainly due to the relatively low wetting angle during liquid phase sintering [6]. The addition of Mo further reduces the wetting angle with TiC to essentially zero, and the core-rim structure that is often generated leads to excellent mechanical properties. TiC cemented with Ni-Mo alloys have proved to be applicable as cutting tools and in severe wear environments [44]. Steel bonded carbides are used as tooling materials, but the relatively low wear resistance and modest strength restricts their wide application. Conventionally, nickel-bonded and steel-bonded titanium carbide cermets are used in industry.

2.4.2 TiC-based Cermets as Tool Materials

The nickel bonded TiC-based cermets were studied extensively in the 1960s [24] because of their high strength, and relatively good oxidation resistance at elevated temperatures. These cermets also provided good mechanical and thermal shock resistance. In nickel-bonded cermets, the binder phase usually contains further alloying components, such as Mo, Al, Cr, and Co, etc. Conventional hard metal production (i.e. “press and sinter”) and infiltration are the two main methods to produce nickel-bonded TiC cermets [24]. While Mo improves the wettability of the metal phase, it also has a refinement effect on the TiC grain size in the material. This microstructure change invariably increases the strength and hardness of the material [5]. The hardness for TiC cermets often show somewhat higher values than for conventional hardmetals, as shown by Moskowitz and Humenik [5]. It has been shown that the nickel bonded TiC cermets show a better cratering resistance than that of WC-Co hardmetals, and comparative tool-life data has shown that the life has been increased for an equivalent level of hardness.

Steel-bonded TiC cermets were developed subsequent to the nickel-bonded cermets, due to issues potential issues with jet engine and gas turbine applications because of the

brittle nature of the TiC phase [24]. The steel-bonded cermets, with 25-50 vol.% of TiC, have met the requirements for the newer wear resistance and longer tooling life materials [24]. These kinds of cermets can be machined under annealed conditions by conventional tools and equipment. It also gives an equivalent or better performance than the conventional cemented carbide. Depending on the binder phase chosen, the cermets are applied in oxidation, corrosion and heat resistance applications [24].

The manufacturing process of steel-bonded TiC based cermets are outlined below, with two principal approaches shown [24]:

1. Preparation of the powders by ball milling → static/hydrostatic cold compaction → liquid phase sintering under vacuum at high temperature → hot isostatic re-pressing and annealing
2. Static/hydrostatic cold compaction → encapsulation in a steel can →hot isostatic pressing and annealing → decanning

2.4.3 Alternate TiC-based Cermets: Ni_3Al-containing Materials

Ductile nickel aluminides (Ni_3Al), when used as a binder phase for TiC based cermets, showed exceptional high temperature strength and chemical stability. Becher and Plucknett [45] studied the properties of Ni_3Al bonded titanium carbide ceramics by fabricating the materials using melt-infiltration sintering and conventional 'press-and-sinter' fabrication methods. Experiments showed that full density can be achieved with binder contents of >12 vol.% at temperatures above 1300ºC. Thermal properties of the composites, such as the linear coefficient of thermal expansion can be increased with the binder phase content, as expected. The Young's modulus and hardness values decrease, and the density increases, with increasing aluminide content. The composites showed improving oxidation resistance, and a high fracture strengths (>1 GPa) are retained to >900ºC, with fracture toughness values exceeding 10 $MPa.m^{1/2}$ when the Ni_3Al content is >12 vol%. For the strengths at elevated temperatures the effective 'yield strength' of the composite, which shows some plasticity above 900ºC, also decreases as the stressing rate is reduced. As for the oxidation and corrosion resistances of the composites, increasing the Ni_3Al binder content diminishes the weight loss from the acid immersion tests. It is

apparent that the composites are more resistant to sulfuric acid corrosion than to nitric acid. Plucknett [46] *et al.* further reported on the processing and properties of TiC/Ni_3Al cermets fabricated by melt-infiltration process. TiC and Ni_3Al are the only phases detected in the densified materials. For Ni_3Al contents from 8 to 25 vol.%, densities in excess of 98% of theoretical are readily obtained when processing at 1450ºC. The ductility of Ni_3Al is retained after fabrication which leads to the possibility of ductile phase toughened TiC composites for elevated temperature applications. The four-point flexure strengths of the composites at 22ºC increased as the Ni_3Al content increased. Because of the reduced TiC grain size, the highest strengths were observed for composites processed at 1300ºC. The strengths at elevated temperatures also increased with test temperature. From this research, a maximum in composite strength (~1350 MPa) as a function of temperature was observed at 950ºC, ~300ºC above the nominal yield strength maximum for the alloy. Even at high loading rates, at 1135ºC, extensive plastic strain was achieved with the yield stress dependent on the applied loading rate [47]. In terms of the cermet fabrication, preliminary examination indicated the infiltration kinetics approximate to parabolic at 1300ºC. Compositional analysis showed only minimal titanium dissolution into the Ni_3Al alloy of the densified materials, which had a carbide composition of $TiC_{0.93}$. Cubic grain-growth kinetics are observed for TiC-16% Ni_3Al, with an activation energy of ~400 ± 60 kJ/mol [48]. Figure 2.5 shows a typical SEM image of the TiC-16 vol.% Ni_3Al cermet [46], fully densified by using melt infiltration method.

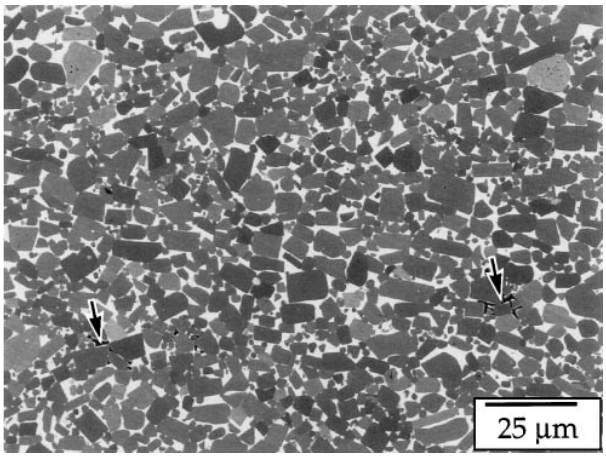

Figure 2.5: SEM image of TiC-16 vol.% Ni_3Al fabricated by melt infiltration [46] .

Collier [49] *et al.* produced TiC-Ni_3Al cermets by melt infiltration using aqueous slip cast TiC preforms and Ni_3Al contents from 10 to 50 vol.%. Spherical indentation tests of the composites were undertaken, with applied loads from 250 to 2000 N, using WC-Co spheres. The indentation stress-strain curves were calculated and the plastic-elastic Hertzian type response was compared. The stress-strains curves demonstrated a decreasing maximum stress with increasing Ni_3Al binder content, with three distinct regions identified as pseudo-elastic, elastic-plastic and fully pseudo-plastic deformation. The slopes also provided a good indication of when the composites began to exhibit quasi-plasticity, with particularly close agreement at the higher binder contents. The curves showed a behaviour analogous to strain hardening, which is believed to be due to the formation of microcracks in the internal structure, the eventual breakdown of this structure and the fracture of the TiC grains under load. SEM and DIC microscopy analysis were used to study the microcracks and subsurface damage, and it appears that the TiC grains were partially rearranged as the ductile binder plastically deformed and the material underwent a period of plastic flow within the Ni_3Al matrix material.

2.4.4 Recent Studies on TiC-iron Alloys Cermets

A variety of stainless steel binders have been used for the TiC-based cermets, including 304-L, 316-L and 410-L. Persson [50] *et al*. studied two manufacturing routes for TiC/Fe

cermets, and liquid phase sintering (LPS) was found to be most effective, due to easier process control, yielding a more homogeneous material than self-propagating high-temperature synthesis (SHS). Both of the methods produced composites with a relatively high degree of porosity, and the compaction has a strong influence on the resulting density after processing. By using SHS, the difficulties were encountered in eliminating the intrinsic porosity during the reaction. Akhtar and Guo [12] examined the processing, microstructure and wear behaviour of TiC/stainless steel matrix composites, which contained 50 to 70 wt.% of TiC. The microstructure of the composites demonstrated the TiC particles were distributed uniformly in the matrix. The hardness of the composites increased with TiC content. Assessment of the fretting wear resistance of the composites, sliding against high speed steel, showed that the material's wear rate was increased at higher loads and lower TiC content. Stewart [51] *et al.* produced TiC based cermets with a stainless steel binder by aqueous slip casting and melt infiltration. Samples with steel contents varied from 5 to 30 vol% were melt-infiltrated at temperatures between 1500 and 1550ºC. The densities of the cermets were in excess of 98% of theoretical, with a TiC grain size around 5 microns. The Vickers hardness of the resulting TiC-stainless steel composites was dependent on the volume fraction of stainless steel, the samples with higher contents exhibited lower values.

2.5 Cermet Fabrication

2.5.1 Powder Compaction

It is usually preferable to obtain a finished product with essentially full density, and therefore optimise the mechanical properties for a component when used in its' respective application. A variety of powder compaction methods are utilised to produce a range of particulate materials, including ceramics. The compaction of the powders must reach the required green strength for handling, while full strength is developed in the subsequent sintering process (i.e. densification), thus attaining higher properties for later applications of the material. Compaction deforms the particles and, with this, comes a decrease in porosity and an increase in particle bond strength [52].

2.5.1.1 Powder Die Compaction

The majority of powder metallurgical components are produced using die compaction for shaping and partially densifying the powder mixture, where the powders are uniaxially compacted using hard, rigid tooling into a desired shape. Typically, this process is performed at room temperature. Die compaction is widely used because of its cost effectiveness, high production rate and its ability to produce compacts with very close dimensional tolerances.

When the pressure is applied on the die punches, the powders are subjected to a sequence of events, noted as (i) rearrangement, (ii) localized deformation, (iii) homogenous deformation and (iv) bulk compression. A sequence showing the representative motion and powder compaction in a die is presented in Figure 2.6 [53]. The initial lower punch is at the fill position, with subsequent pressure, the upper punch is fed into the die and both of the punches are pressed towards the centre. After compaction, the upper punch returned and the lower punch ejects the pressed material.

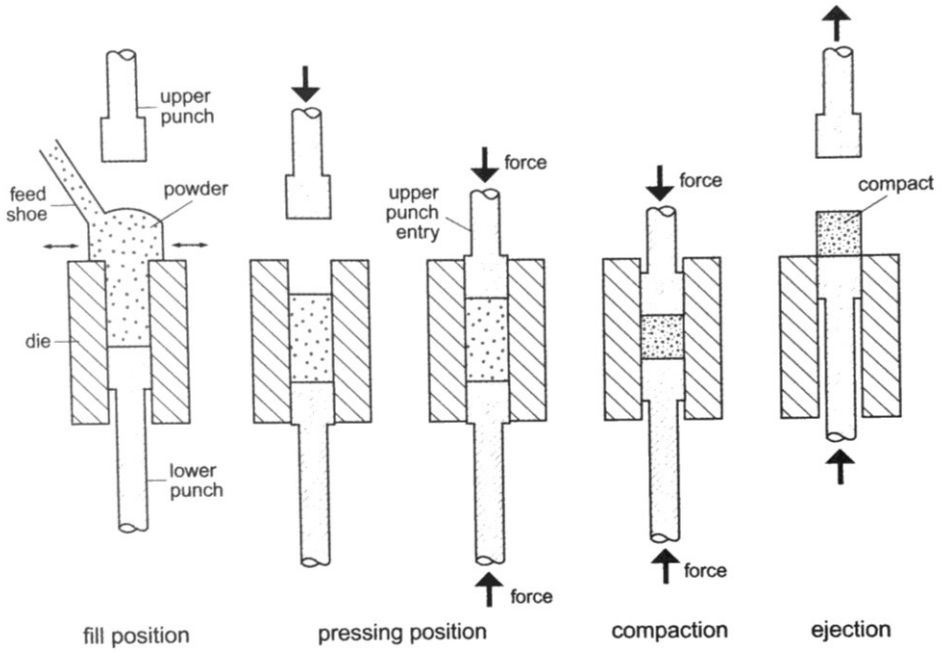

Figure 2.6: Schematic figure showing a cycle of powder compaction [53] .

During single die compaction of the powders, there are few issues that may be encountered. First of these is the die wall friction, which causes the effective applied

pressure to decrease with depth travelled into the powder. As a consequence, the green density is therefore non-uniform in the component. These green density variations will not only happen between the die wall and the powder, but also between the punch and the powder. To minimize this effect, “double-action-compaction” can be used; the gradient of the density is therefore symmetrical. Figure 2.7 [53] shows the variation of density, illustrated as ‘iso-density’ lines, in a compact for copper powder.

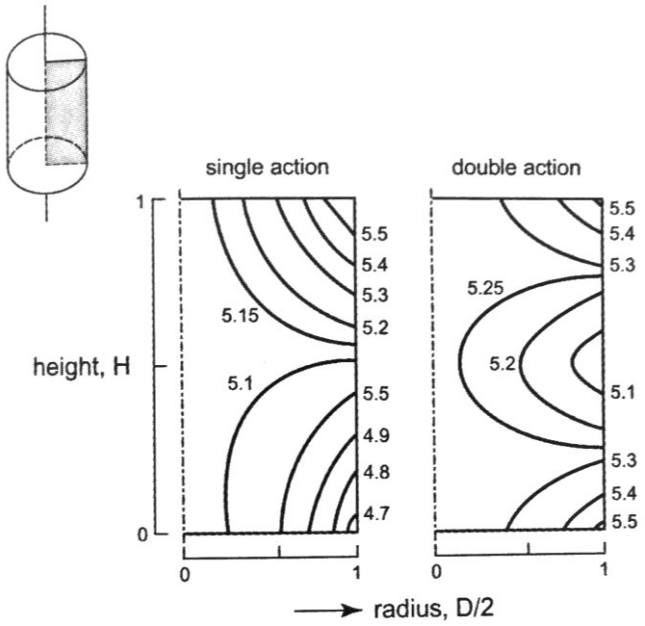

Figure 2.7: Constant density lines in a die for Cu powders [53] .

Lubricants are needed for high volume die compaction, to reduce the die wall friction and consequently improve green density. It can also lower the ejection forces and improve the tooling life of the die. The lubricants are usually blended in with the powders or sprayed directly on the tooling materials [53].

2.5.1.2 Cold Isostatic Pressing

There are a number of alternative compaction methods to uniaxial die compaction, which can also be used as a follow up stage for die pressing. For example, with cold isostatic pressing (CIP) the samples are pressed equally from all directions in a simultaneous manner. CIP is usually applied for complex shape compaction, and the tooling materials

are rubber, latex, etc. instead of hardened steels or carbides. Two types of CIP compaction, wet-bag pressing and dry-bag pressing, are commonly used. Wet-bag pressing usually seals the powders in a mould, which is immersed in a chamber filled with pressurised fluid, where the pressure is applied using a hydraulic pump. A schematic diagram of wet-bag cold isostatic compaction is shown in Figure 2.8 [53]. Dry-bag CIP is favoured for high volume production. CIP provides the complex shape compaction that conventional uniaxial die compaction cannot, and the densities are usually slightly higher since there is effectively no die wall friction. The CIPed samples also exhibit minimal density gradients [53], which leads to reduced distortion when it comes to sintering. As a consequence, CIP is widely used for cemented carbides, ceramics, and many other powders.

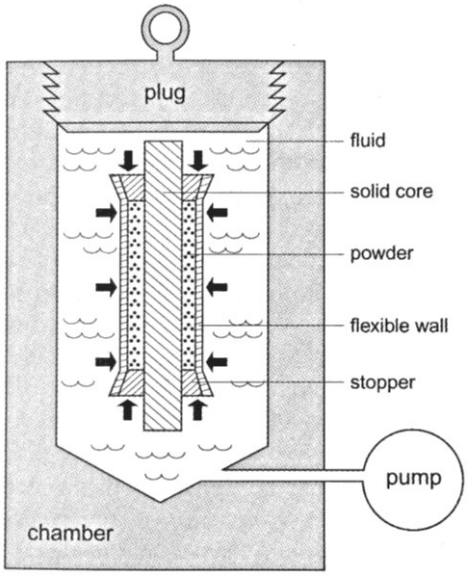

Figure 2.8: Cold isostatic compaction [53] .

2.5.2 Liquid Phase Sintering

To fully densify and achieve the desired mechanical properties of a powdered material, a sintering process is needed. Liquid phase sintering invariably provides faster sintering and essentially complete densification, without external pressure, in comparison to solid state sintering. The enhanced atomic diffusion that occurs in the presence of a liquid

phase drives the faster sintering response. The various liquid phase sintering stages are shown in Figure 2.9 [53]. The mixed powders are firstly heated to a required temperature where a liquid forms. A capillary force results, leading to rapid densification through wetting of liquid on solid particles, rearrangement and some solubility. The elimination of porosity that occurs throughout the system minimizes the total surface energy. This procedure occurs in three overlapping stages: (i) rearrangement, (ii) solution-reprecipitation, and (iii) final-stage sintering.

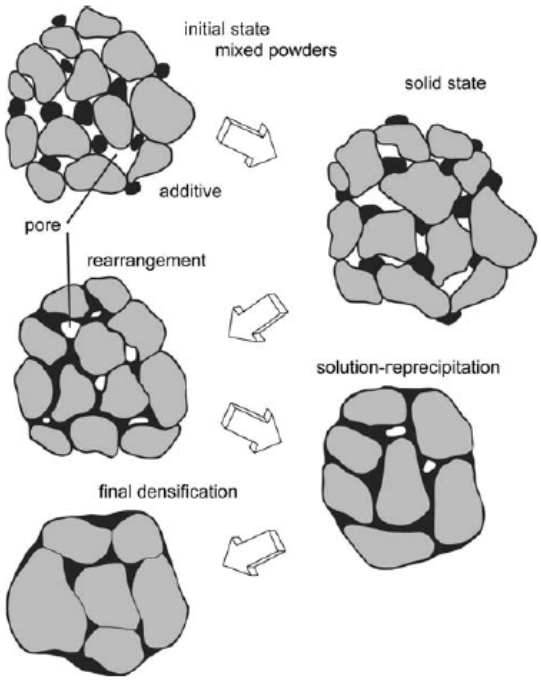

Figure 2.9: Stages of liquid phase sintering [53] .

During the second stage of liquid phase sintering, rearrangement ends, densification by rearrangement consequently slows, with solubility and diffusion effects becoming dominant in the progress, which is also referred to as a 'solution/reprecipitation' process. Solution-reprecipitation not only contributes to grain coarsening, but also to densification. The densification process in this stage is driven by Ostwald ripening and solubility considerations [53]. As large grains grow, they become more rounded which increases packing efficiency and results in an increasing density [53]. In this stage, high solubility and low wetting angle both contribute to better densification. In addition, densification is associated with grain shape accommodation, which takes place by contact

flattening at points of grain-grain contact, dissolution of small grains with reprecipitation on large grains, and coalescence involving grain boundary migration and co-operative solution-reprecipitation [54].

The final stage of liquid phase sintering is effectively an extension of the intermediate stage. Grain size, distribution, shape and binder phase distribution changes take place during this stage. The maximum density is also attained in the final stage. The coarsening process is dominant in the final stage, and the sintering driving force is the reduction of surface energy. This process is relatively slow and rarely achieved, and in many instances causes a loss in density. Microstructural coarsening will occur and the pores will grow if they contain trapped gas. The longer the sintering time, the coarser the particles, so short sintering times are preferred.

2.5.3 Melt Infiltration Method

Melt infiltration is a variation of conventional liquid phase sintering, which started to be examined in the mid-1970s. It can be "pressureless" for wetting systems [55-57] or pressure-assisted for poorly wetting systems [55,58,59]. The capillary force is the driving force for wetting system, and a variety of material systems were examined with this kind of method, such as TiC-Al, TiC-Ni_3Al. Figure 2.10 shows a schematic figure of the melt infiltration process for a TiC-stainless steel system. The "infiltrant" powder, in this instance stainless steel, is applied on the top of the green body (TiC) pellets. With the increasing temperature, the powder starts to melt and wet the preform surface. The capillary force will then draw the molten metal into the porous ceramic preform. After a suitable period of time, a dense, fully infiltrated composite can be obtained. Previous studies have shown that complete infiltration is achieved for 300 series austenitic steels of TiC based cermets [51].

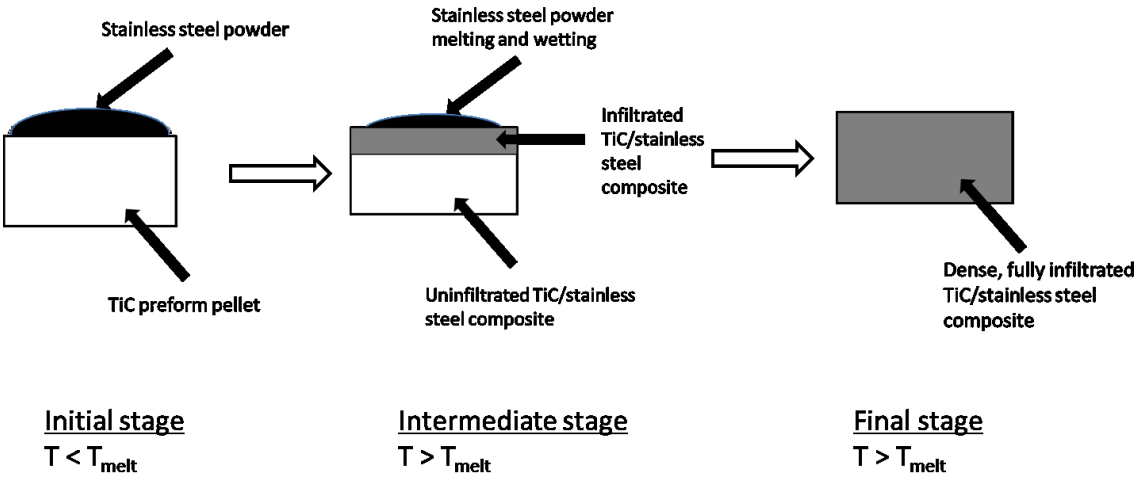

Figure 2.10: Schematic figure of melt-infiltration method of TiC- stainless steel cermet.

2.6 Indentation Hardness and Indentation Fracture Resistance

The sintering process bonds the powders together at high temperatures, leading to significant improvement of the strength of the materials. Following the sintering, mechanical properties of the material are usually determined. Among the common mechanical properties, a combination of desired hardness and fracture toughness is usually the key to material selection. The following section presented the two properties determined by using indentation method.

2.6.1 Hardness and Indentation Hardness Testing

Hardness can be defined in a variety of manners, such as the resistance to permanent deformation, resistance to wear, resistance to scratching, etc. in a wide variety if engineering fields. The hardness test is by far the most widely used approach for evaluating the mechanical properties of metals, as well as other materials. Hardness shows the resistance to localized plastic deformation; the larger the resistance to deformation, the harder the material appears.

In ancient times, people tested the hardness of a material through performance tests of tools and weapons. By 1822, Friedrich Mohs established a 10-step scratch hardness scale, which was based on the principle that “the hardness of a mineral to be tested is

determined by the two reference minerals it scratches or is not able to scratch" [60]. However, Mohs theory is not applicable for materials other than minerals because the differentiation is quite low. Subsequently, Martens referred to hardness, *H*, the resistance to deformation as:

$$H = \frac{F}{A} \qquad \text{Equation 2.5}$$

where *H* is the resistance, *F* is the test force and *A* is the surface area. Hardness gives units of strength, and it is often related to the yield strength of the material, σ_Y. The common relation is given as: $H = C\sigma_Y$, where *C* is the proportionality constant [61].

Many different kinds of hardness testing approaches have been developed. Figure 2.11 shows the standard Vickers hardness indentation procedure. The Vickers indentation is in the form of a square-based pyramid, with an angle of 136°. The indenter tip is polished and sharp. The standard loads are 5, 10, 20, 30, 50, 100, and 120 kg. For most applications of hardness tests, 50 kg is the maximum load employed. This scale is subjected to a known load, *P*; after the load is removed, a microscope is then used to measure the size of the indenter impression.

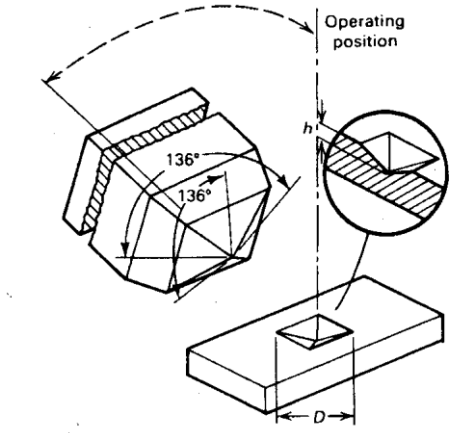

Figure 2.11: Pyramidal Vickers indenter and resulting indentation [60] .

The calculation of the hardness from the indent size is determined as follows [62]:

$$HV = 1.854\frac{P}{d^2}$$ Equation 2.6

where P is the load, in kg, and d is the mean diagonal length of the indent impression, in mm.

The Vickers hardness number also can be reported in GPa, as follows [62]:

$$HV = 0.0018544(\frac{P}{d^2})$$ Equation 2.7

where P is the load, in N, and d is the average length of the two diagonals of the indentation, in mm.

The Vickers hardness number is typically expressed in either of two different units (1 HV=1 MPa). Presentation in MPa, or GPa, is convenient for comparison with tensile or fracture strength values.

2.6.2 Fracture Mechanics and Indentation Fracture Resistance

In 1913, Inglis [63] published his work showing that the presence of corners, holes and notches make the local stress higher than the average applied stress. He concluded that the stress magnification depends on the radius of the curvature of the hole, the smaller the radius, the greater the concentration. Inglis defines "*stress concentration factor*", κ, for an elliptical hole equals:

$$\kappa = 1 + 2\sqrt{\frac{c}{\rho}}$$ Equation 2.8

where c is the major radius of the hole and ρ is the curvature of the tip of the hole, as shown in Figure 2.12.

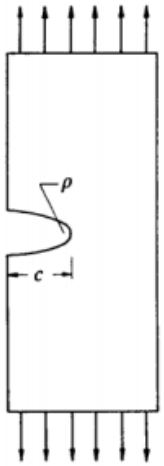

Figure 2.12: Schematic figure of the radius and curvature of the tip of a hole.

The value of κ is usually equal to 3 for a circular hole, where effectively the stress at the edge is 3 times the applied uniform stress, as shown in Figure 2.13. The contours for σ_{yy} was generated using finite element analysis [64].

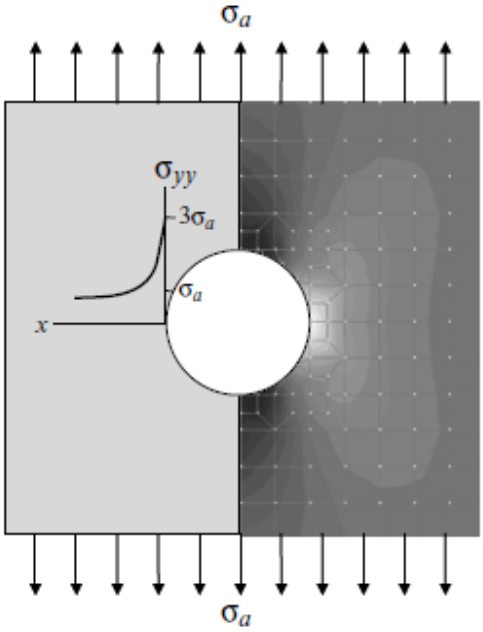

Figure 2.13: Stress concentration around a hole in plate under uniform far-field stress [64].

In 1920, Griffith [65] first proposed the energy balance criterion for fracture, which was focused on the effects of scratches and surface finish (damage) on the strength of materials. Griffith based his treatment of fracture on energy criteria. He has shown that the *strain energy release rate* and the *surface energy creation rate* can be determined and balanced, so the critical condition for crack growth is then:

$$\frac{\pi\sigma_a^2 c}{E} \geq 2\gamma \qquad \text{Equation 2.9}$$

where c is half crack length of a double-ended crack in an infinite plate, σ_a is a uniformly applied stress, E is the Young's modulus, γ is the fracture surface energy of the solid per unit area. On the left side of Equation 2.9 is the strain energy release rate per increment of crack length extension/contraction, which is a linear function of crack length. The required rate of surface energy, per unit of crack length, is a constant for a given material. This equation is called the Griffith energy balance criterion [64].

The application of fracture mechanics has gained engineers attention and developed into an engineering discipline primarily because the fracture of the Liberty ships during World War II. Before that engineers ensured that the maximum stress within a structure was limited to a certain percentage of the "tensile strength", which is usually measured in a laboratory or taken from reference sources. However, the effects of holes, which can cause premature failure, were not encountered [64]. After that, the research led by Dr. Irwin, from the Naval Research Laboratory, was developed which is now known as fracture mechanics. Irwin studied the early work of Griffith, Inglis and others, and one of the subsequent contributions was to extend the Griffith approach to metals, by including the energy dissipated by local plastic flow [66]. In 1957, Irwin [67] showed that the stress field $\sigma(r,\theta)$ of a sharp mode I crack tip can be expressed as:

$$\sigma_{yy} = \frac{K_I}{\sqrt{2\pi r}}\cos\frac{\theta}{2}\left(1 - \sin\frac{\theta}{2}\sin\frac{3\theta}{2}\right) \qquad \text{Equation 2.10}$$

The first term K_I is also called the *stress intensity factor*, and is defined as:

$$K_I = \sigma_a Y\sqrt{\pi c} \qquad \text{Equation 2.11}$$

where σ_a is the applied stress, Y is a geometry factor and c is the half crack length. In this equation, π and Y are constants, so the stress intensity factor is only dependent upon the applied stress and the crack length. The stress intensity factor is usually given with units of $MPa \cdot m^{1/2}$ (or $Ksi \cdot in^{1/2}$).

The stress intensity factor is usually given with a subscript, indicating the mode of loading. Three modes of loading can be applied to a crack, where Mode I is the most commonly used, which is denoted as the I in K_I, and is associated with tensile loading, as shown in Figure 2.14.

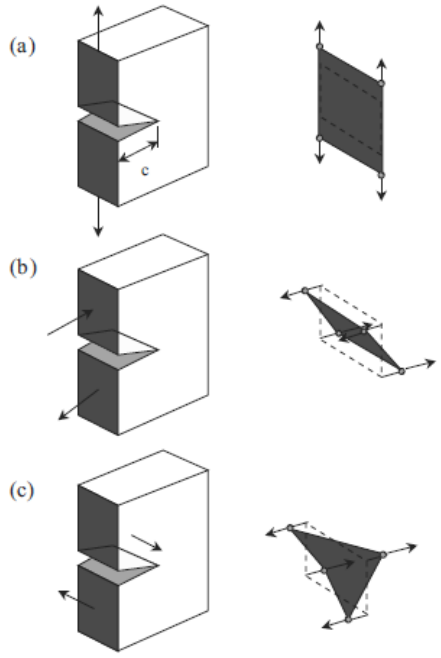

Figure 2.14: Three modes of fracture [64] .

If G is defined as the strain energy release rate:

$$G = \frac{\pi \sigma^2 c}{E} \qquad \text{Equation 2.12}$$

By substituting Equation 2.11 into Equation 2.12, G is then written as:

$$G = \frac{K_I^2}{E} \qquad \text{Equation 2.13}$$

When $K_I = K_{IC}$, then G_c is the critical value of the strain energy release rate, which propagates the extension of the crack and possibly fracture. The relationship between K_I and G means K_{IC} is both a necessary and sufficient criterion for crack growth. The critical value, K_C is the measure of fracture toughness, which is used to describe the ability of the material resist to fracture when containing a crack. It is a material property, which is dependent on the both crack size and geometry.

The fracture toughness of the material can be determined experimentally. In standard tests, loading is applied in a universal mechanical testing machine. Several standard K_{IC} test procedures have been established [68]: by bending (edge-cracked specimen, chevron-notched specimen), or double-cantilever-beam test, double-torsion test, etc. The latest ASTM standard C1421-10 is the standard method for determine fracture toughness of advanced ceramics at ambient temperature.

Fracture toughness values obtained by using indentation tests (Vickers indentation fracture (VIF) toughness, either by direct, indirect, or modified methods) are also used. The VIF method has gained broad use because of its simplicity and applicability to small samples, and is nominally a convenient way to determine K_{IC} [69], although there is still much conjecture over the application of this test. The fracture toughness resistance theory was originated by Palmqvist in the 1950s, but the concept was first advocated as a fracture toughness test by Evans and Charles [70] in the mid-1970s. Evans and Charles [70] gave a brief introduction to the development of Vickers indentation fracture toughness, and presented a generalized equation that appeared to be applicable to many different materials, with either Palmqvist cracks or median cracks. A schematic figure of the two crack patterns are shown in Figure 2.15 Subsequently, other authors used similar curve fitting methods and analyses from Vickers indention to evaluate the fracture toughness for both of the crack geometries [71-76]. To get a fracture toughness value for a material, the lengths of the indentation cracks, along with the indentation load, the impression size, the hardness, and the elastic modulus of the material are needed [69]. In Vickers indentation, the crack pattern develops into two distinct stages during indenter loading, which are crack initiation and propagation. Different types of cracks would be generated as a result of the Vickers indentation test. As alluded to above, two major types of cracks are formed: (i) median-radial cracks perpendicular to the surface and (ii) lateral cracks

that are approximately parallel to the surface [77]. In the following section, various types of cracks will be discussed, along with the empirical equations developed for estimating a material's fracture toughness.

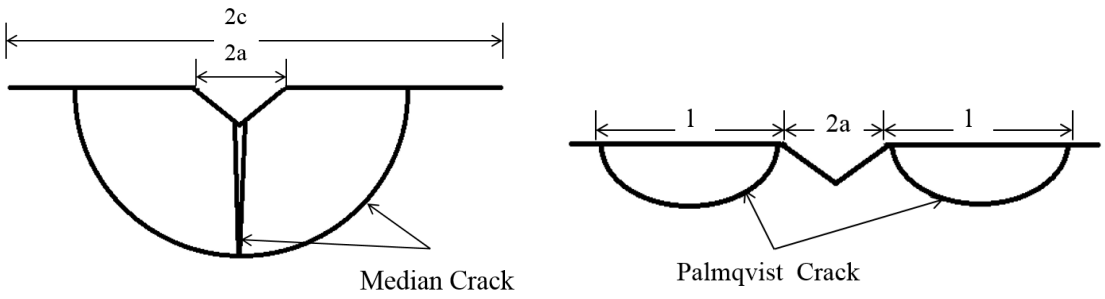

(a) (b)

Figure 2.15: Schematic figure of (a) the 'median' crack and (b) Palqmvist crack.

2.7 Indentation with 'Sharp' and 'Blunt' Indenters

For the use of 'sharp' indentation, the major approach is to study the morphology and growth behaviour of the cracks formed by indenting the surface, usually with a Vickers hardness indenter. As noted above, in this approach, two major types of cracks are formed [77].

Cook and Pharr [78] studied the geometrical deviations that occurred in different materials and summarised the crack patterns generated as follows. Loading by sharp indenters leads to a surrounding plastic impression in the surface which is known as the "elastic-plastic" zone. In these cases, radial cracks are generated from the edge of the plastic contact impression, parallel to the loading axis, and these remain close to the surface, as shown in Figure 2.16(B) [78]. At light loads, the median stages may be suppressed so that only surface radial cracks (known as "Palmqvist" cracks) are formed [79]. Median cracks also propagate parallel to the axis of force and are generated beneath the plastic deformation zone, forming full circles or parts of circles, as shown in Figure 2.16(C). Another common crack morphology is the half-penny crack, presented in Figure 2.16(D), although it is unclear whether they are formed by median growth toward the surface, or

radial propagation downwards, or a combination of both, as suggested by previous studies [78]. According to Lawn and Fuller [72], as presented in Figure 2.17, the median crack system nucleates from a plastic contact zone (shaded region), forms into a contained 'penny' (broken circle), and ultimately develops into a full half-penny. Lateral cracks are also produced under the deformation zone, which is parallel to the surface, and are circular in form, as shown in Figure 2.16(E).

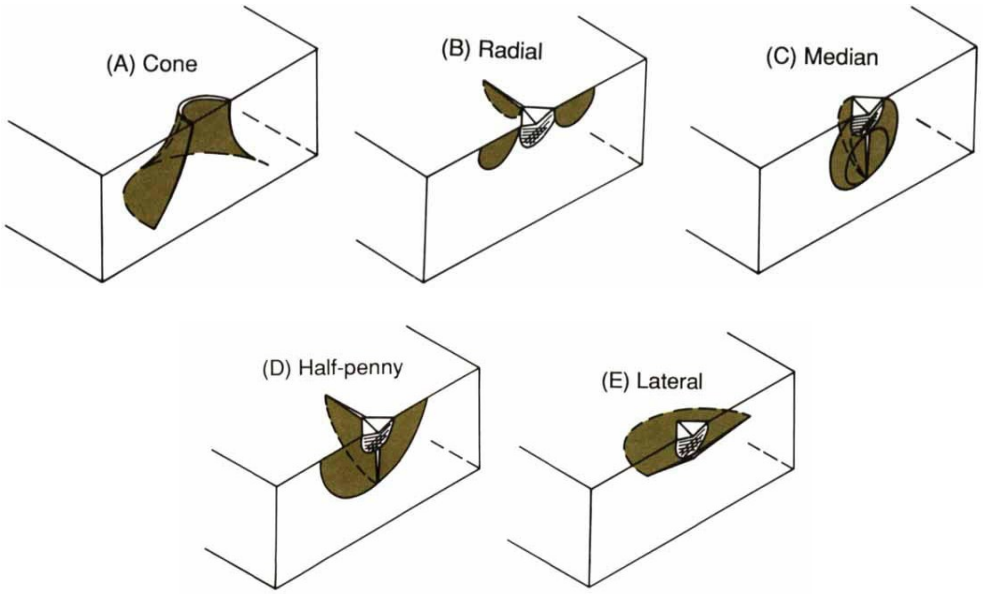

Figure 2.16: Different crack patterns [78] .

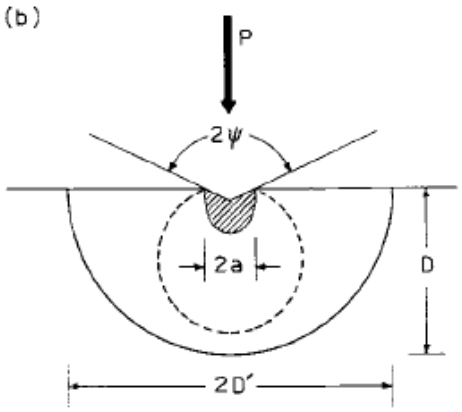

Figure 2.17: Median crack system [72] .

2.7.1 The Median/Half-penny Crack System

Cracks induced by elastic-plastic contact can be verified into two primary systems [79]: the median/half-penny crack, which is symmetric to the median planes, and the lateral cracks parallel to the surface. Early studies focused on crack patterns in soda-lime glass, since it was convenient to observe the crack generation, and indicated that median cracks primarily formed during loading, which was driven by elastic components of the applied stress field. A schematic figure of a common median/half-penny crack system is shown above in Figure 2.15(a). On the other hand, lateral cracks are formed entirely during unloading, which means the driving force is the residual stress in the irreversible deformation zone [72], which will be discussed in the next section.

Lawn and Swain [71] first considered the growth of sub-surface median cracks within an essentially elastic point-contact field. Based on their observations, they predicted a linear dependence for the median crack depth. It can be argues that the research oversimplified the problem, by using two-dimensional fracture mechanics to solve a three-dimensional problem [75]. Subsequent research [72] took the observation of all well-developed cracks into account. The modified analysis retained the assumption that the primary crack driving force is derived from the elastic field, where they noted the residual stresses played some role in the crack evolution. Lawn and Fuller [72] stated that median cracks did not develop as half-penny cracks during loading. They also emphasized the role of residual stress associated with the deformation zone in expanding the median cracks to

the surface during unloading. Evans and Wilshaw [76] performed an analysis dealing with an elastic/plastic field from the outset, and thereby noted that the ratio *H/E* should complement toughness as a controlling parameter in the fracture mechanics. They also extended the range of observations from soda-lime glass to polycrystalline ceramics. Marshall and Lawn [81] studied newly formed plastic impressions and gave recognition to both elastic and residual stress terms in the stress intensity formulation. This analysis provided a quantitative explanation of the evolution of median cracks in glass, and considered the fracture mechanics during unloading as well as loading of the indenter. Lawn [75] *et al.* developed a fracture mechanics model, which presents the framework for a quantitative analysis of the median/radial crack system in elastic/plastic indentation. From Evans and Charles [70], and the work of other researchers [74,76], they found that a simple but powerful means for determining the toughness of ceramics is needed. They measured the K_c values independently [75]. Other researchers also proposed equations to estimate the intensity factor based on median/half-penny system. Anstis [82] *et al.* developed an equation based on evaluating glasses, glass-ceramics, and polycrystalline ceramics, and tested these materials with a double cantilever beam geometry, leading to an equation as follows:

$$K_{\mathrm{IC}} = 0.016\left(\frac{E}{H}\right)^{\frac{1}{2}}\left(\frac{P}{c^{\frac{3}{2}}}\right) \qquad \text{Equation 2.14}$$

where E is the Young's modulus, H is the hardness, P is the applied load and c is the distance from the centre of the indentation to the crack tip. This equation was used in the current study to calculate the fracture toughness value if the 'median/half penny' type of crack was generated.

2.7.2 The Radial (Palmqvist) Crack System

Radial cracks are often named after their original discoverer, Palmqvist, when he studied the impressions on WC-Co surfaces. Many studies showed that they exist for a wide range a contact loads and well above those surmised to generate half-penny cracks [78]. The plastic deformation generates a localised load, and it is the driving force for such a

crack. The crack growth happens during the loading segment of the cycle [78]. A schematic representation of a Palmqvist crack is shown above in Figure 2.15(b).

The studies by Lankford [82] suggested that the crack length, *c*, measured from the centre of the indentation varied with a $P^{2/3}$ dependence for a wide range of contact loads. In 1981, Niihara [83,84] *et al.* indicated that the Evans and Charles [70] description of indentation cracks lengths broke down at small crack lengths, and an empirical equation was developed using the model in Figure 2.18. Later study by Lankford [85] showed that the question raised by Niihara [84] is more a function of the choice of plotting, and not real failing with their analysis [78].

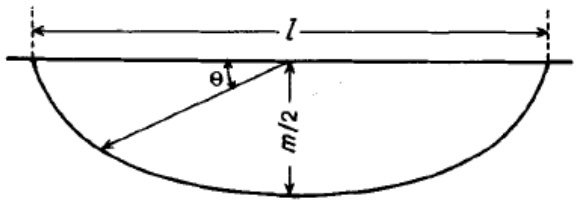

Figure 2.18: Semi-elliptical crack model for the Palmqvist cracks.

In 1985, Shetty [86,87] *et al.* provided data for indentations in WC-Co and fine-grained glass-ceramics, showing only radial cracks up to 200 N load in the latter material. With their further papers [88,89], they generated the conclusions that the measured surface traces of the cracks for both materials were better fitted to Palmqvist cracks than to the circular crack relationship indicated by Lankford. A modified Shetty's equation is used to calculate the 'Palmqvist' type of crack's fracture toughness in the current study, which is given as:

$$K_{\mathrm{IC}} = 0.0319P/(al^{\frac{1}{2}}) \qquad \text{Equation 2.15}$$

where *P* is the applied force, *a* is the half-diagonal length, and *l* is the crack length from the corner of the indents to the tip.

Laugier [90,91] subsequently presented a series of papers examining the indentation cracks, especially in the WC-Co system. In 1987, Laugier [92] provided analysis of surface traces

of cracks for both radial and half-penny geometries. This paper provided experimental support for the analysis and suggested that crack length measurements alone are no guarantee of determining crack morphology.

The geometry of Palmqvist cracking is not ideally elliptical as shown in the schematic figure for cermets, and most of ceramics. A typical crack profile determined by Langier [92], using a sectioning technique, is shown in Figure 2.19; the material is a Al_2O_3-ZrO_2 ceramic composite subjected to 30 kg of loading with a Vickers indenter.

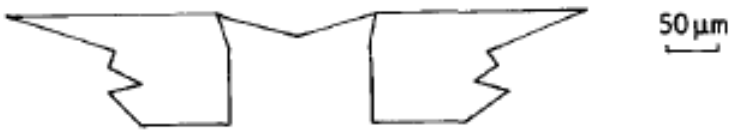

Figure 2.19: Typical Palmqvist crack profile in a cermet [92] .

2.7.3 The Lateral Crack System

Lateral cracks are usually regarded as a secondary indentation crack and are difficult to model, as previously reported [78]. An idealised lateral crack system is shown in Figure 2.20. A crack, with radius, *c*, is produced by the contact load, *P*, at depth, *h*, below the surface. The plastic zone including angle, 2ψ, with characteristic radius, *a*, extends outward to a radius, *b*, supporting the indenter. The residual driving force, P_r, acts on the crack when the indenter is withdrawn, and a residual tensile stress develops at the nucleation centre near the base of the deformation zone. The driving force, P_r, reaches a maximum at full loading and continues until the indenter is removed. Lateral cracks are proposed [93,94] to be important in controlling wear and material removal in brittle materials.

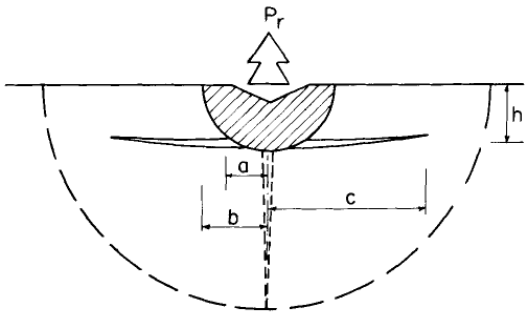

Figure 2.20: Lateral crack system [95] .

2.7.4 Indentation with Spheres

Indentation with spheres, made of hard steel or tungsten carbide, to generate cone cracks has been studied for over 100 years. The first research by Hertz, in the 1880s, was on silicate glass. He was observing optical interference of two lenses, concerning elastic deformation [96]. The visible damaged caused by a particular type of crack, which was generated by spheres, has also related to the other mechanical properties such as strength, toughness and wear [97]. The importance of such damage behaviour was recognised in many engineering applications, especially for bearings and engine components [97]. A typical cone crack, generated by point load in glass, is shown in Figure 2.21. The fracture begins as a surface ring crack and, at some critical load, propagates downwards and outwards, ending with a cone configuration.

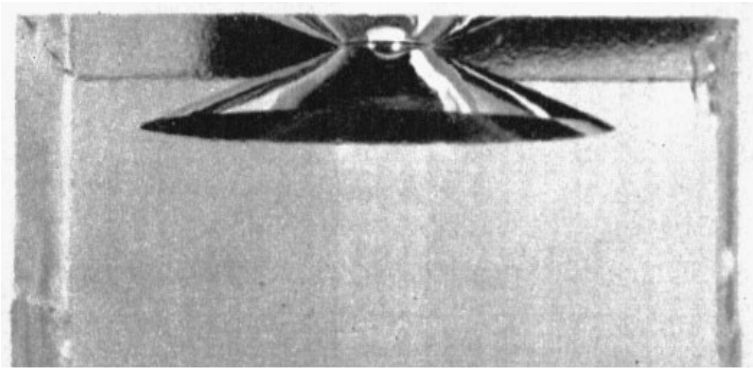

Figure 2.21: Hertzian cone crack in soda-lime glass [98] .

Shortly after Hertz, Auerbach (1896) developed an empirically observed linear relation between the critical load and sphere size, which is now known as "Auerbach's Law". This has also led to the most famous paradox in brittle fracture theory [99]. Auerbach's Law violates the requirement that cone cracks should initiate when the maximum tensile stress in the indented body exceeds the bulk strength of the material. Subsequently, in the 1960s, use of Griffith-Irwin fracture mechanics first accounted for this paradox and many refinements have been made since [100].

Over the past 100 years, indentation with spheres has been extensively studied on both brittle materials and metals, with respect to fracture mechanics and the materials' deformation properties. An understanding of the damage arising from sphere contacts has been extended from brittle homogeneous materials to tough heterogeneous ceramics, characterised by materials with an *R*-curve response. Recent study [101] using Hertzian indenters has related to both the experimental studies and modelling of these quasi-plastic ceramics. The elastic-plastic behaviour has been modelled using the finite element method; a "shear faults/wing cracks" model [101] has been used for modelling of the strength degradation and cyclic fatigue of the tough ceramics.

2.7.5 Hertzian Contact Mechanics

2.7.5.1 Elastic Stress Field and Elastic Contact

Hertz assumed an ellipsoidal distribution of pressure. The principal stresses σ_1, σ_2, and σ_3 in the *rz* plane are then given by the following equations. The principal stresses σ_1, σ_2, and σ_3 are normal stresses acting on the principal planes, σ_1 and σ_3 are the maximum and minimum values, σ_2, has a value in between, and $\sigma_1 > \sigma_2 > \sigma_3$. τ_{max} is the maximum shear stress.

$$\sigma_{1,3} = \frac{\sigma_r + \sigma_z}{2} \pm \sqrt{\frac{(\sigma_r - \sigma_z)^2}{2} + {\tau_{rz}}^2} \qquad \text{Equation 2.16}$$

$$\sigma_2 = \sigma_\theta$$ Equation 2.17

$$\tau_{\max} = \frac{1}{2}(\sigma_1 - \sigma_3)$$ Equation 2.18

where σ_r and σ_z are the radial stress and normal stress respectively, τ_{rz} is the shear stress, σ_θ is the hoop stress, which is always a principal stress, and its magnitude is equal to the radial stress. Hertzian stress field contours are shown in Figure 2.22 [3].

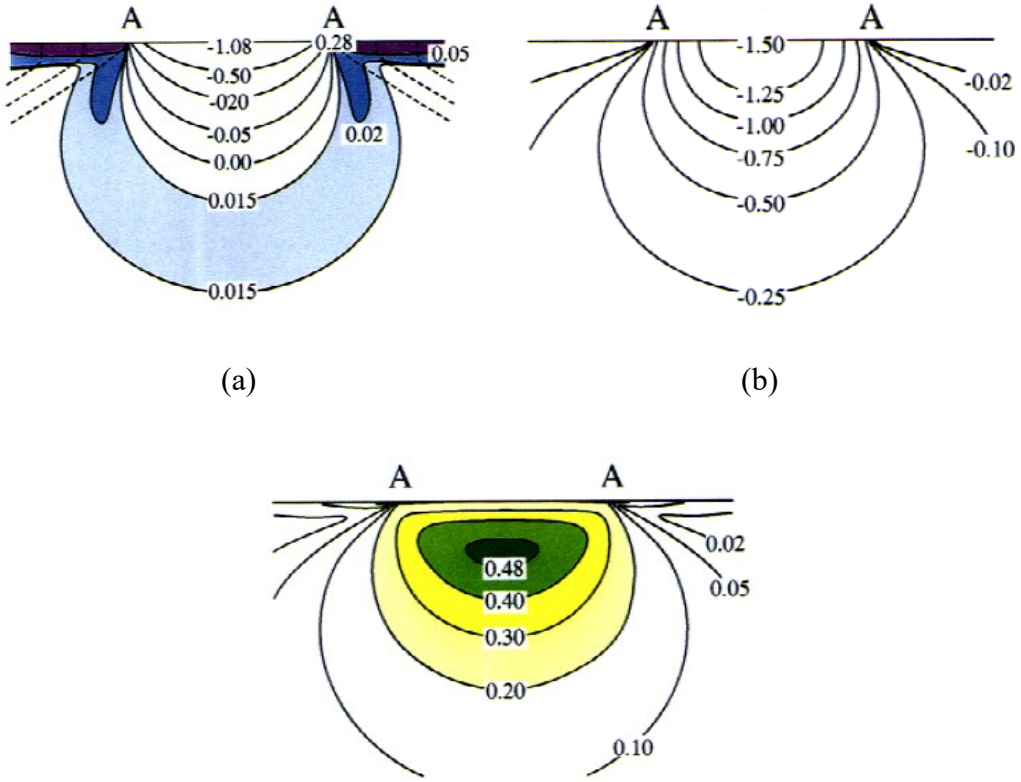

Figure 2.22: Hertzian stress filed as (a) principle normal stress σ_1, (b) principle normal stress σ_3 and (c) principle shear stress τ_{max} [3].

The basic Hertzian elastic contact solutions are well documented; the radius of the circle of contact, *a*, is given by indenter normal load, *P*, and the radius of the sphere, *R*, and the the elastic modulus, *E*, following:

$$a^3 = \frac{4kPR}{3E} \qquad \text{Equation 2.19}$$

where E is the combined Young's modulus of the specimen, and k is given by:

$$k = \frac{9}{16}\left[(1-\nu^2) + (1-\nu'^2)\frac{E}{E'}\right] \qquad \text{Equation 2.20}$$

where E' and ν' and E and ν are the Young's modulus and Poisson's ratio of the indenter and specimen, respectively.

The mean contact pressure, p_m, is a normalizing parameter and defines the intensity of the contact field:

$$p_m = \frac{P}{\pi a^2} \qquad \text{Equation 2.21}$$

The mean contact pressure can be also written as:

$$p_m = (\frac{3E}{4k})^{2/3}(\frac{P}{\pi R^2})^{1/3} \qquad \text{Equation 2.22}$$

It can be seen that the contact area is proportional to $P^{2/3}$, and p_m is proportional to $P^{1/3}$, therefore:

$$p_m = \frac{P}{\pi a^2} = \frac{3E}{4\pi k}\frac{a}{R} \qquad \text{Equation 2.23}$$

The linear relationship between mean contact pressure as the "indentation stress", and a/R, as the "indentation strain" are then used to obtain stress-strain information for the material being tested [102,103].

For a fully elastic response, the maximum principal shear stress, τ_m, is located $\approx 0.5a$ beneath the indenter with a value of:

$$\tau_m \approx 0.48\, p_m \qquad \text{Equation 2.24}$$

Applying either the Tresca or von Mises criteria, where the plastic flow occurs at [102]:

$$\tau_m \approx Y/2 \qquad \text{Equation 2.25}$$

the plastic deformation can then be first expected to occur at $p_m \approx 1.1Y$.

2.7.5.2 Elastic-Plastic Stress Field and Elastic-Plastic Contact

Plastic deformation can be generated by a Vickers indenter in brittle materials, or by a sphere indenter/cylindrical punch in ductile materials. The indentation stress field for the elastic-plastic contact under the specimen are usually assessed using finite element analysis [104-108]. The modelling is highly dependent on the material properties and the geometries. Figure 2.23 shows the contact stress distribution for both elastic and elastic-plastic contact, with a load P =1000 N and sphere radius of R = 3.18 mm. The plotted results are normalized to the elastic case, with a mean contact pressure p_m = 3.0 GPa and a contact radius a = 0.326 mm.

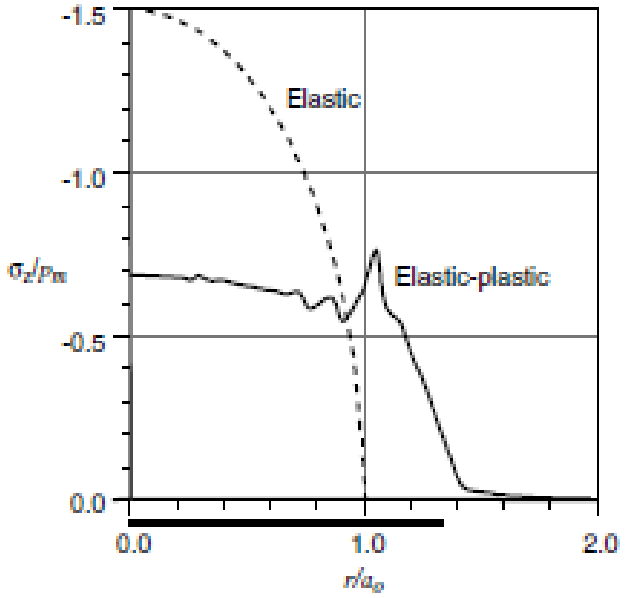

Figure 2.23: Contact pressure distribution for elastic (equation) and elastic-plastic contact (FEM) [109].

2.7.6 Hertzian Fracture

As mentioned above, the relationship between contact radius, indenter radius and elastic properties of both the specimen and indenter is given by Equation 2.19 and Equation 2.20. The maximum tensile stress is at the edge of the contact circle is given as:

$$\sigma_{\max} = (1 - 2\nu)\frac{P}{2\pi a^2} \qquad \text{Equation 2.26}$$

It can be also expressed as below, if we substitute Equation 2.20 in Equation 2.26:

$$\sigma_{\max} = [\frac{(1 - 2\nu)}{2\pi}](\frac{4E}{3})^{2/3} P^{1/3} R^{-2/3} \qquad \text{Equation 2.27}$$

The tensile stress near the edge of the circle of contact is responsible for the Hertzian cone cracks, while the angle which is developed in the cone depends on the Poisson's ratio of the material.

2.7.7 Material Response

2.7.7.1 Brittle Response

The study of the brittle response for traditional ceramics and glasses has been well developed, and has often been associated with the study of transitions of ceramics from 'brittle-ductile' properties. The technique using bonded interface samples, with Normarski differential interference contrast (DIC) illumination, has been commonly used in these cases to study the surface and sub-surface damage [110,111]. In the study by Lee [112] *et al.*, one of the materials being evaluated was a fine grained silicon nitride (termed F-Si_3N_4), with 75 vol.% equiaxed α-Si_3N_4 grains, 10 vol.% glass phase and 15 vol.% elongated β-Si_3N_4 grains, with a mean length of 1.5 μm and diameter of 0.4 μm. For this structure, the surface ring cracks are obvious, with no irreversible deformation, and acoustic signals were strong, indicating deep crack growth. Figure 2.24 shows the half surface and sub-surface damage following the Hertzian contact on the fine grain silicon nitride, after indentation with a WC indenter of radius 1.98 mm and load 4000 N. The sub-surface cone crack is fully developed, and the crack propagates at an angle of 19 ± 2° to the top surface [112]. Also, there is no detectable deformation beneath the circle.

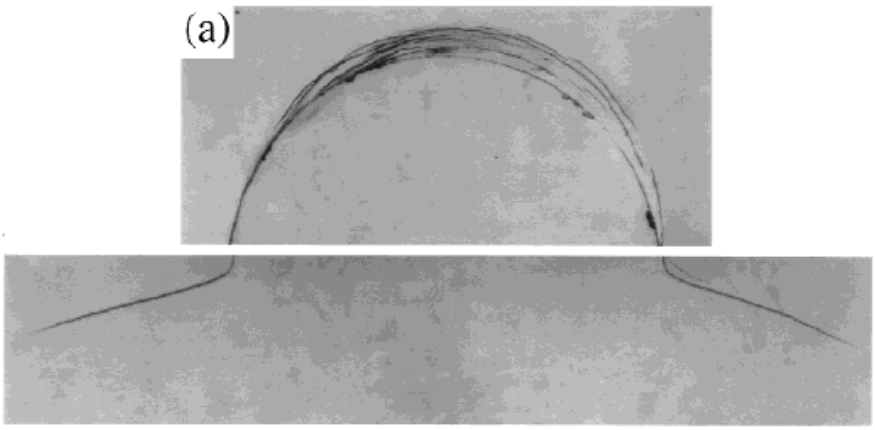

Figure 2.24: Hertzian contact damage of F-Si_3N_4 [112] .

A related study on alumina also shows well-defined cone cracking, initiated outside the contact circle in the fine-grained structures. Guiberteau [115] *et al.* used a critical contact pressure ≈ 5 GPa, for a range of mean grain sizes from 3 to 48 μm, for mono-phase alumina; below a threshold grain size, the classical cone cracks appeared. As Figure 2.25 shows, there is no obvious evidence of plastic deformation occurring; the indentation pressure here is 8.0 GPa. However, using DIC imaging, as the researchers indicated, at the spatial resolution limits of optical microscopy, there are restrictions to the scale of observation.

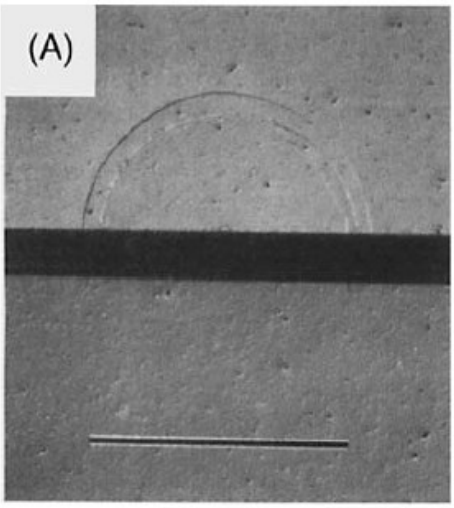

Figure 2.25: Nomarski DIC illumination showing half-surface and section view of alumina with a grain size of 3 μm [115] .

2.7.7.2 Quasi-Plastic Response

R-*curve behavior*

Some heterogeneous ceramic materials have shown a crack size dependent toughness property. In those materials, the crack resistance, R, and fracture toughness, K_C, may increase with increasing crack length [77]. This is the so-called *R-curve* property, which is often associated with transformation toughening mechanisms, which alters the microstructure of the material, for example as in partially stabilized zirconia [113]. The phase transformation leads to energy being absorbed as the crack propagates. As shown in Figure 2.26, when the crack begins to propagate and it is initially short, so only the frontal zone is affected. As the crack grows, a larger crack-wake zone is affected. After a certain amount of growth, a steady state is reached and a process zone has been developed. The crack resistance is thus increased by amount of ΔK_R. The R-curve nominally increases as $\tan^{-1}(\Delta c/h)^5$, where h is the width of the transformations zone [114]. This is a typical response for materials that show crack-wake energy absorbing phenomena. Griffith fracture occurs as the stress and crack length exceeds K_{IC}. For materials with an R-curve, the crack resistance K_R increases as c increases, as shown in Figure 2.26.

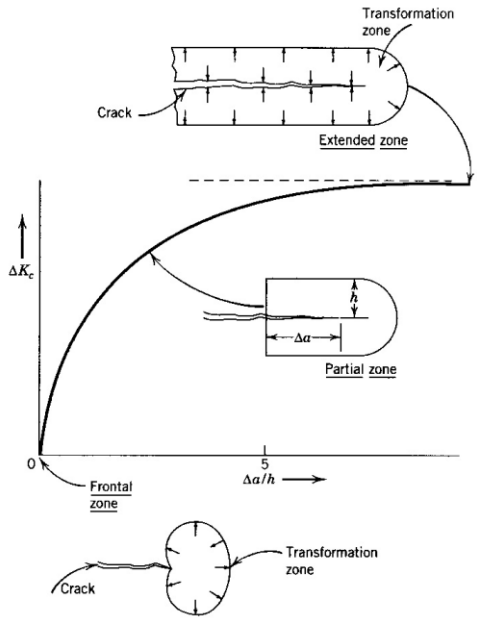

Figure 2.26: Predicted crack resistance *R*-curve [113].

Quasi-Plastic Deformation

The study of quasi-plastic deformation of tough ceramics started in the 1990s [110,111,115-119]. As mentioned in the last section, bonded interface samples are widely used for the study of sub-surface damage of the deformation. Quasi-plasticity occurs at a critical value p_Y; combining Equation 2.22, Equation 2.24 and Equation 2.25, it can be determined that:

$$p_Y/r^2 = (1.1\pi Y)^3(4k/3E)^2 = \text{constant} \qquad \text{Equation 2.28}$$

In the study of Lee [112] *et al.*, the quasi-plastic deformation zones are well developed. Three categories of controlled microstructures were examined: fine scaled β-Si_3N_4 grains with α-Si_3N_4 grains (F-Si_3N_4), medium with mostly β-Si_3N_4 grains (M-Si_3N_4) and coarse grains with elongated β-Si_3N_4 grains (C-Si_3N_4). Figure 2.27 presents the indentation stress-strain curves plotted, from the Hertzian contact experiments, where the solids lines are FEM fits, and the dashed lines on the top right corner are the Vickers hardness values [112]. The deviations from linearity indicate the onset of "yielding". In the microstructure images in Figure 2.28 and Figure 2.29, the damage follows a transition from brittle fracture to quasi-plastic deformation, as the grains get coarser [112]. As shown in Figure

2.28(b), the cone crack has a shorter crack length than that in Figure 2.24, and sub-surface quasi-plastic deformation has arisen [112]. The sub-surface quasi-plastic deformation zone is more obvious with increasing grain size, as shown in Figure 2.28(c) [112].

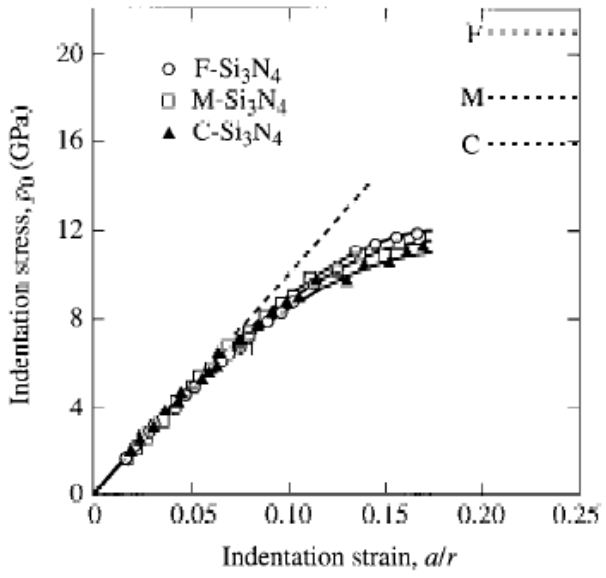

Figure 2.27: Indentation stress-strain curves for silicon nitride [112] .

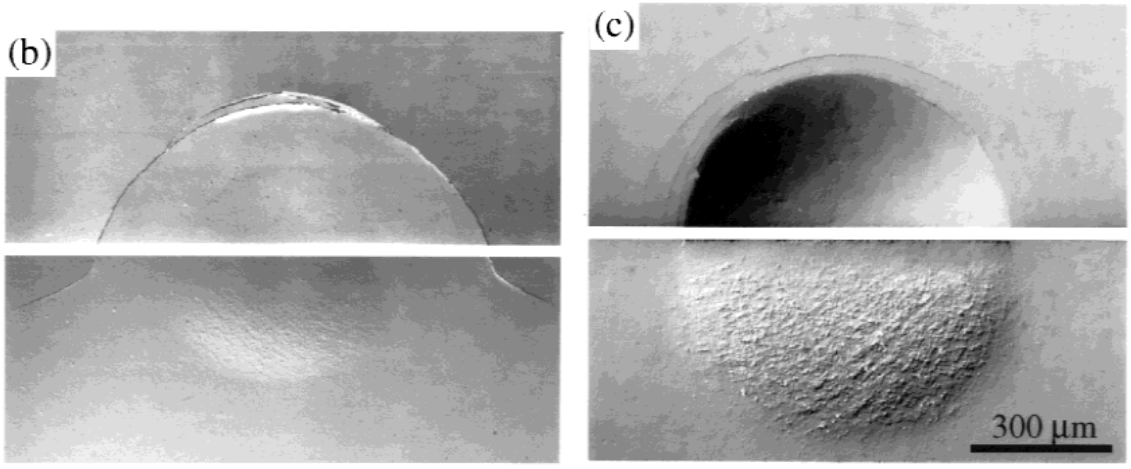

Figure 2.28: Hertzian contact damage for M-Si_3N_4 and C-Si_3N_4, with a sphere radius R = 1.98 mm and load P = 4000 N; half surface and side views are shown [112] .

Figure 2.29 presents the sub-surface damage in coarse grain silicon nitride subjected to increasing applied loads; the radius of the contacting sphere in this instance is 1.98 mm. The damage started where the shear stress is the maximum, and then grew into a fully plastic deformation zone [112].

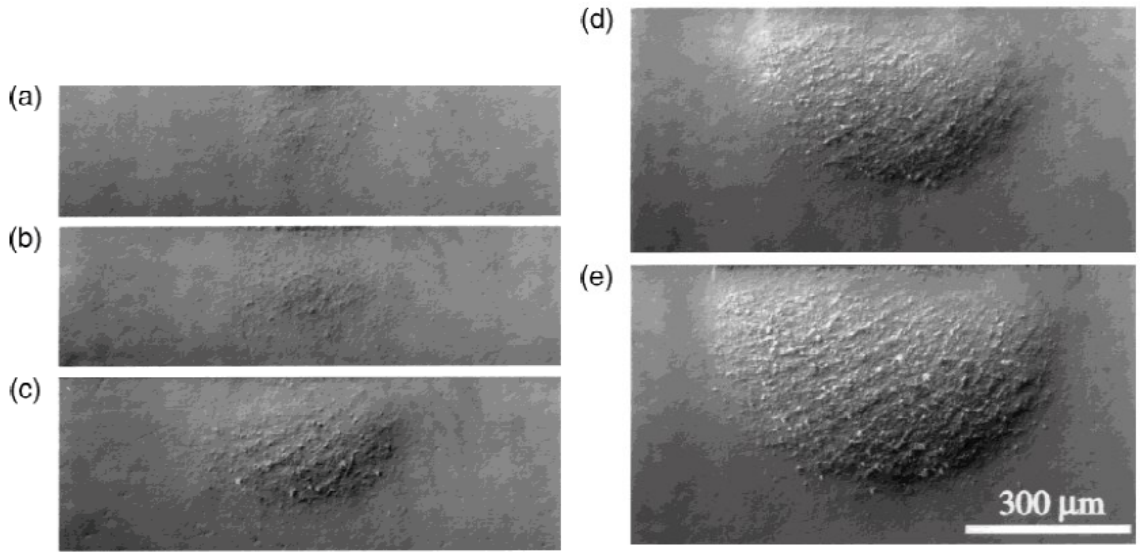

Figure 2.29: Evolving contact damage in C-Si_3N_4, side views shown [112] .

Figure 2.30 shows a plot of Hertzian ring crack geometry as a function of the indentation load *P*. Again the deviation of the plot from linear has confirmed the quasi-plasticity.

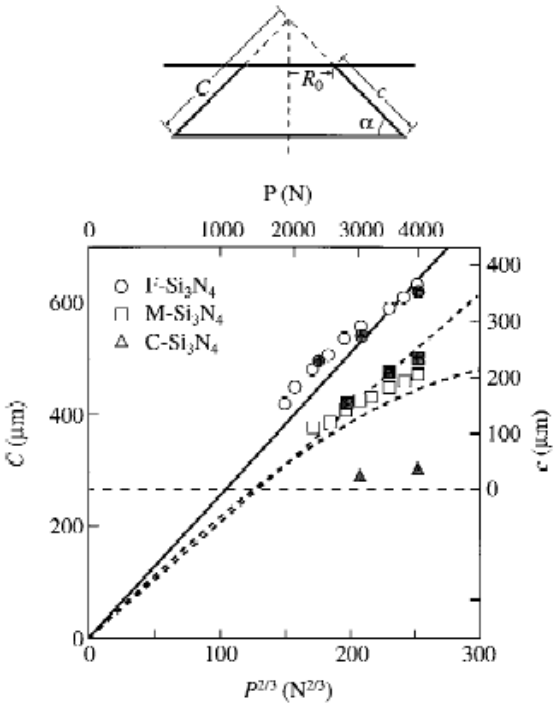

Figure 2.30: Hertzian ring crack dimensions/geometry [112] .

Similar patterns of transition, from cone crack to subsurface damage, are also observed in alumina ceramics. As shown in Figure 2.31, the indentation stress-strain curves for alumina subjected to Hertzian indentation show the response of the specimens with two different grain sizes. The dashed line is the Hertzian elastic response; the solid curve is an empirical data fit from intermediate grain size alumina [115], and the sequence A-B-C-D shows sectional views of the damage beneath the specimen surface, corresponding to the microstructures in Figure 2.31 [115]. The lower inclined dash line is the linear relationship for pure elastic contact, and the deviation indicates the "yield" of the specimen. As shown in Figure 2.32 [111], the formation of sub-surface damage zone initiation and expansion are apparent.

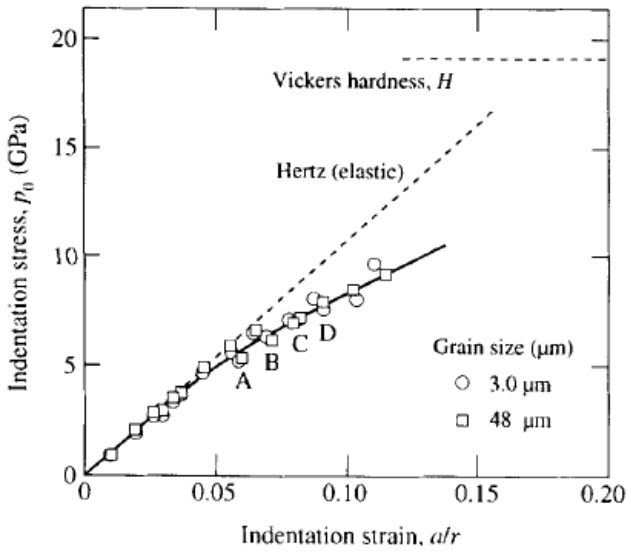

Figure 2.31: Indentation stress-stain curve of alumina [115] .

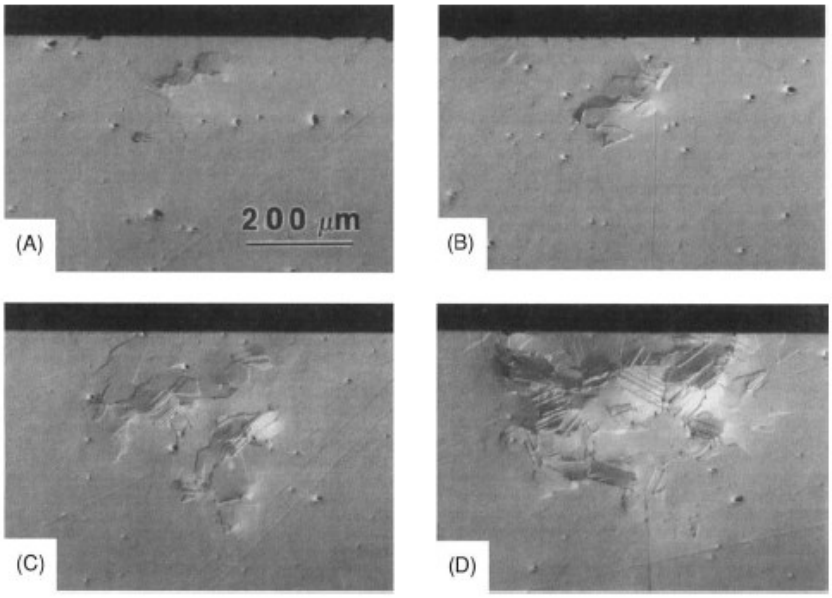

Figure 2.32: Optical microscopy images using Nomarski DIC illumination, showing the sectional view of alumina with a grain size of 48 μm [111] .

Figure 2.33 shows the 'brittle-ductile' transition in pure, dense alumina specimens with a range of grain size from 3-48 μm, subjected to a load of 2000 N with a sphere radius of 3.18 mm. The surface ring cracks still form in all cases, but are restrained by downward damage, 'ultimately to one grain depth of less'. In addition, the quasi-plastic zones are constrained below the contact [111].

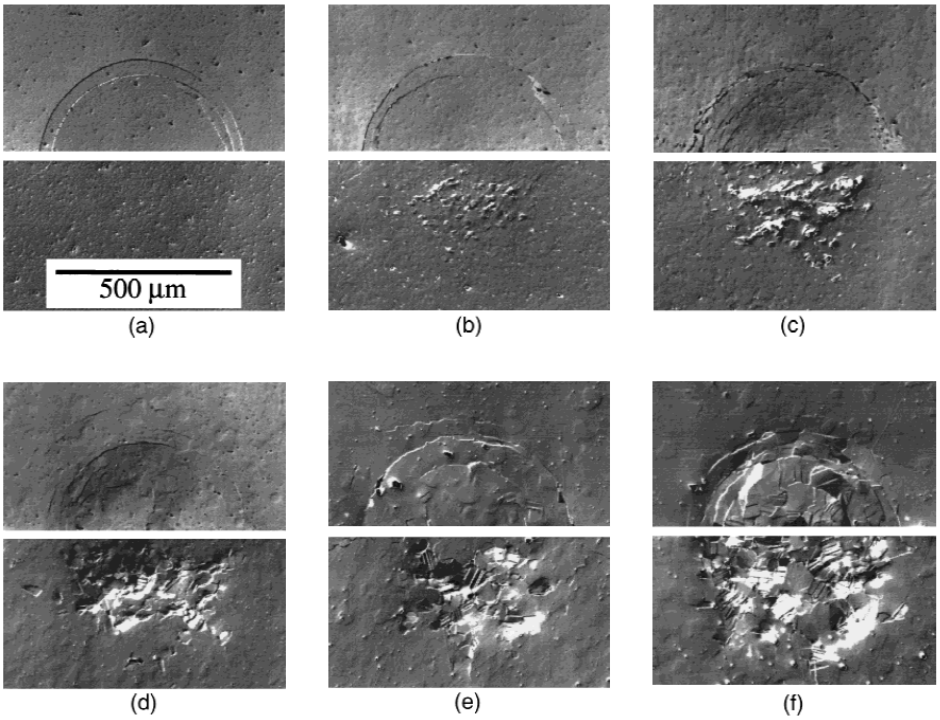

Figure 2.33: Hertzian indentation in alumina [111] .

2.8 Wear

The previous section reviewed the indenter in contact with a surface in a static mode, however many applications include the relative motion of the two surfaces. Due to the relative motion between a surface and a secondary contacting substance or substances, wear is a form of surface damage involving a progressive loss of material [120]. Many methods have been applied to categorize the wear. Kato [121] has suggested, based on the wear mechanism occurring, that it can be 'mechanical', 'chemical or 'thermal' wear, and for the wear mode(s) it can be categorized as 'abrasive', 'adhesive', 'flow' and 'fatigue'. Another way to define wear is through the mechanism of losing material. The mechanism of the loss of material can be shear fracture, extrusion, chip formation, tearing, brittle fracture, fatigue fracture, chemical dissolution, and diffusion [120]. The damage occurring by shear fracture is related to the shear force leading to a plastic shear deformation, and usually is a sign of adhesive wear [120], which will be discussed in the following section. Wear by extrusion occurs in sliding or rolling contact, where the material is squeezed out

[120]. Surface damage by chip formation is usually a sign of abrasion, where the hard particles cut the material out of the surface and accompanied by severe plastic deformation [120]. Tearing generally occurs in polymer materials. Wear by brittle fracture [120] is common in ceramics, cemented carbides, ceramic coatings, and hardened steels, as a result of high tensile stresses which exceed the fracture stress of the surface material, and this would also lead to a very high wear rate. Wear dominated by fatigue fracture is the result of repeated loading, either unidirectional or reciprocating sliding. The so-called 'fretting' wear, which is the low-amplitude oscillatory sliding, may lead to fatigue wear as well. A schematic figure of selected wear modes are shown in Figure 2.34.

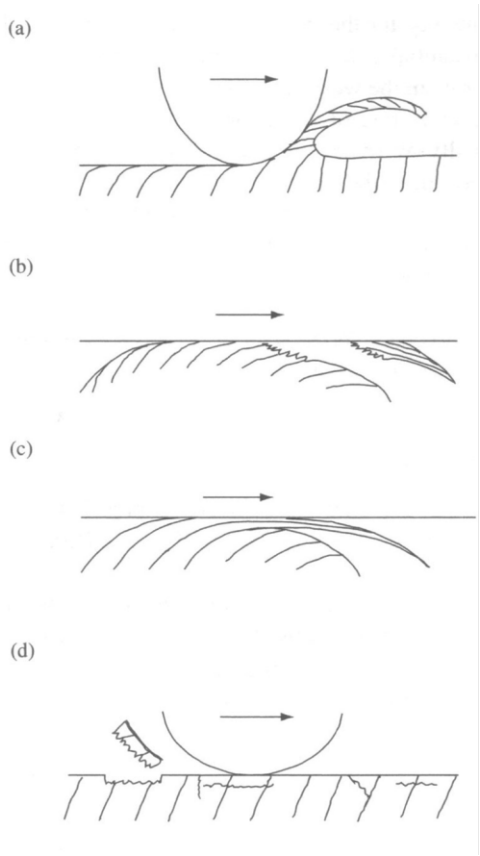

Figure 2.34: Schematic figures of wear modes [122] showing: (a) abrasive wear by microcutting, (b) adhesive wear by adhesive shear and material transfer, (c) flow wear by plastic flow and (d) fatigue wear by crack initiation and propagation.

2.8.1 Abrasive Wear

Abrasive wear happens due to hard particles or protuberances involved in the wearing system, which are forced against and moving along the surface [123]. Through the type of contact, abrasive wear can be categorised as "two-body" or "three-body". Two-body abrasive wear [123] is where the hard particles or protuberances, which produce the wear of one body, are fixed on the surface of the opposing body. The particles are sliding over the surface against each other [93,94]. Three-body abrasive wear [123] occurs when wear is induced by loose particles, either introduced or generated between the contacting surfaces. The particles in this case are free to roll over themselves between the surfaces [93,94]. Since the particles are free to move, studies have suggested that the wear rate of the two-body abrasive wear is significantly higher than that of three-body.

The hardness of the abrasive particles has a strong influence on the wear rate of the material. An index is usually used to describe the abrasive wear, where the hardness of the particles is H_a, and the hardness of the wearing surface is H_s. In this instance, when $H_a/H_s > 1.2$, it is defined as 'hard abrasion', whereas when $H_a/H_s < 1.2$, it is usually called 'soft abrasion' [93].

The mechanism(s) of a two-body abrasive wear usually includes ploughing, wedge formation, cutting, micro-fatigue and micro-cracking, as shown schematically in Figure 2.35 [120]. The ploughing, wedge formation and cutting modes are related to two-body wear by plastic deformation, while the latter two modes, are related to two-body wear by brittle fracture [93].

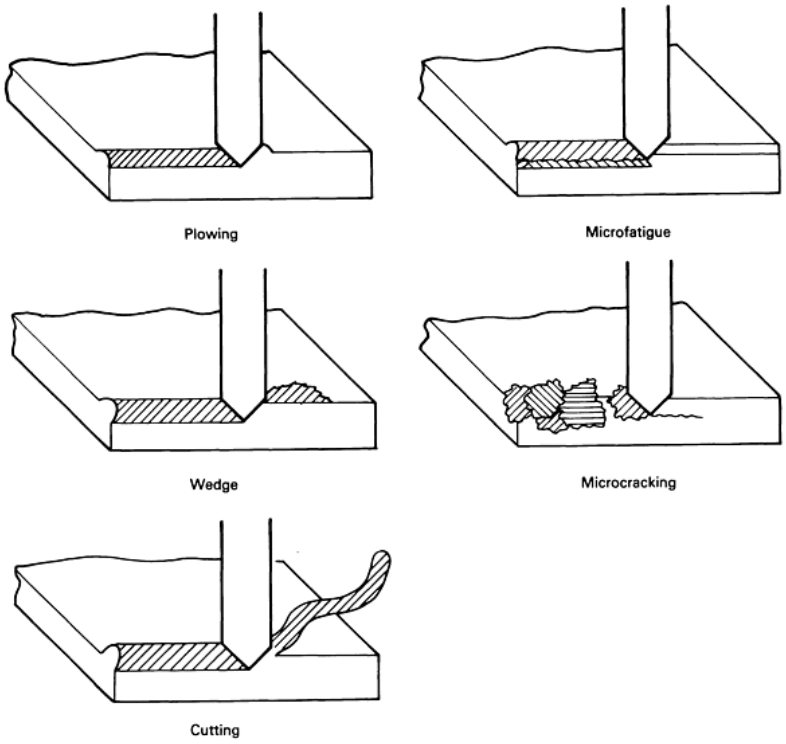

Figure 2.35: Mechanism of abrasive wear [120] .

2.8.1.1 Abrasive Wear by Plastic Deformation

Two-body abrasive wear by plastic deformation includes ploughing, wedge formation and cutting [94]. Ploughing is the material being pushed to the sides of the wear groove, and hence being built up around the outside of the wear track. Ploughing occurs mostly under low loads; this wear mode does not really result in real material loss. The material flows beneath the front face of the particle [93]. In the wedge formation mode, a wedge can be developed at the tip of the abrasion region, and the material displaced from the groove is greater than that to the sides. This mode removes the material from the surface [93]. The cutting mode removes material from the top of the surface [93], forming a chip at the abrasive tip, and usually occurs in ductile materials. The amount of material displaced is less than is displaced to the sides [120]. The transition from ploughing to wedge formation, and further to cutting, depends on the critical penetration depth [124] and critical attack angle [93]. In three-body abrasive wear, the particles are free to move, and

therefore the cutting mode, as in two-body abrasive wear, occurs less often, invariably leading to a lower wear rate [93,94].

Various equations were developed to estimate the extent of abrasive wear, and one of the better known among them was Archard's equation [125]. Though derived from adhesive wear, the equation also described abrasive wear very well, and is usually written as:

$$V = \frac{k_1 PL}{H} \qquad \text{Equation 2.29}$$

where k_1 is the wear coefficient or wear rate, which is to be determined, V is the material volume loss, in mm^3, P is the applied load, in N, L is the sliding distance, in m, and H is the Vickers hardness number of the material.

Another variation on this type of equation is the so-called Lancaster equation [126]:

$$k_2 = \frac{V}{PL} \qquad \text{Equation 2.30}$$

where k_2 is the 'specific wear rate', in mm^3/Nm.

2.8.1.2 Abrasive Wear by Brittle Fracture

Abrasive wear also occurs in brittle materials such as ceramics. Due to the high local plastic deformation, cracks are generated, which leads to material removal. Previous sections have discussed the cracks produced by indentation in some detail. As mentioned before, the median cracks grow down from the surface under loading, while the lateral cracks generated by residual stresses happen during unloading of an indentation. As a consequence, the lateral cracks can lead to wear.

Many models have been developed to analyse and estimate the abrasive wear by brittle fracture. One of them is the 'lateral crack' model; a schematic figure of this model is demonstrated in Figure 2.36 [127]. The length of the cracks, c, is given by:

$$c = \alpha_1 \frac{(\frac{E}{H})^{3/5} w^{5/8}}{K_c^{1/2} H^{1/8}}$$ Equation 2.31

where w is the normal load on the particle, E is the Young's modulus, H is the indentation hardness, K_c is the fracture toughness, and α_1 is a constant that depends on the shape of the particle.

The depth of the crack, b, is described as:

$$b = \alpha_2 (\frac{E}{H})^{2/5} (\frac{w}{H})^{1/2}$$ Equation 2.32

where α_2 is another constant. Therefore, the volume wear per unit sliding distance (i.e. the wear rate) for all particles, Q, is:

$$Q = \alpha_3 N \frac{(\frac{E}{H}) w^{9/8}}{K_c^{1/2} H^{5/8}}$$ Equation 2.33

where α_3 is a material-independent constant, N is the number of particles in contact with the surface.

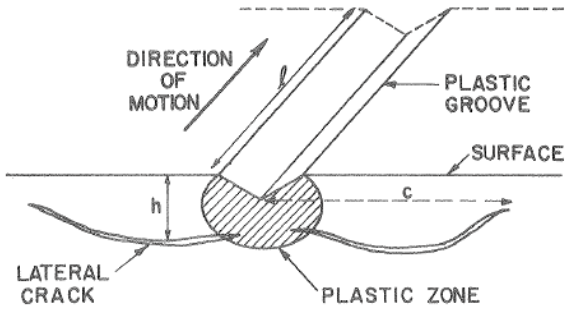

Figure 2.36: Abrasive wear by brittle fracture by the formation of lateral cracks [127] .

The wear rate was also determined as:

$$Q = \alpha_4 N \frac{w^{5/4}}{K_c^{3/4} H^{1/2}}$$ Equation 2.34

Based on this, the wear rate is not dependent on the Young's modulus of the material.

Some other equations can be used to describe the abrasive wear by brittle fracture, and the equations all show some correlation between the wear rate and fracture toughness, suggesting in the brittle materials that the fracture toughness is an important material property related to wear. However, the equations all obtain higher wear rates than those determined by plastic deformation.

It can be seen from above that abrasive wear can be dominated by plastic deformation or brittle fracture, where hardness is the primary controlling factor in the first case, and fracture toughness becomes more important in the second scenario. A correlation of wear resistance and hardness is usually found in the wear of metals, where fracture does not always occur [128].

2.8.2 Adhesive Wear

Adhesive wear is usually related to high wear rates and an unstable coefficient of friction [129]. During the relative motion between two surfaces, the particles or removed material are transformed from one surface to the other, either temporarily or permanently, through a solid-phase 'welding' process [123,130]. This could involve the loss of material from either one surface or both of the surfaces in contact [123,130]. Archard's equation is actually derived from the adhesive wear mechanism. Material transfer is usually involved in adhesive wear. Sometimes the definition of 'adhesive wear' is also interchangeable with 'sliding wear'. Signs of adhesive wear include smearing, galling, scuffing, scoring, or seizure [120].

During the adhesive wear process, adhesive transfer particles can be formed by shear or cracking [131]. A series of shear bands are formed during the sliding motion, when the critical limit of cracking a shear band is reached, a crack is generated or the existing crack continues to grow until the new shear band is formed; the progress eventually detaches the particle from the surface [123]. Experiments shown that brittle materials allow comparatively little deformation and produce fewer particles than ductile materials [132].

Another important feature of adhesive wear is the transfer of films (i.e. tribolayers), with plate-like wear debris generated [123]. The film could greatly alter the wear process, for

example the smooth sliding wear may be interrupted by thick regions of the surface films, such that in some extreme situations detachment may not occur, leading to total seizure of the surfaces.

2.8.3 Fatigue Wear

Fatigue wear occurs in scenarios where the local stress is high, due to repeated sliding or rolling [123]. Wear of the surfaces is usually caused by fracture, including the initiation and growth of cracks. The occurrence of fatigue wear phenomenon is very common in bearings, with localised 'pitting' or 'flaking' arising from the cyclic loading as its main feature [133]. In this instance both surface and sub-surface cracks may be generated. The surface cracks are usually nucleated at some weak point and propagate downward, forming a 'secondary-crack' and then continue to grow through crack coalescence. For sub-surface cracks, which are generated at regions where the stress field is high, they often form a few microns below the contact surface. Inclusions, voids, flaws, or pre-existing cracks are usually the sites for initiation.

2.8.4 Wear of Cemented Carbide and Cermets

Cemented carbides and cermets have relatively high hardness when compared to metals, and are used extensively in wear resistant environments. It was found that when subjected to 'hard abrasion', plastic deformation can occur in both the carbide phase and the binder; a smaller binder mean free path, a measure of the metal ligament size, gives a higher wear resistance [134]. When 'soft abrasion' occurs, the carbide and binder phase are slightly removed by abrasive particles, leading to binder extrusion, carbide grain-removal and cracking by a fatigue mechanism [134].

The wear mechanisms for WC-Co 'hardmetals' have been conducted extensively, with suggested mechanisms including plastic deformation [135-137] or plastic grooving [135,136], binder phase extrusion and removal [135,138-141], fracture of WC grains [136-138] and Palmqvist cracking and subsequent material spalling [141]. Gee [142-147] *et al.* offered a large amount of researches on both two-body and three-body abrasive wear of various hardmetals. Cemented carbides with various grain sizes were used at either dry or wet environment [142]. Various types of abrasive tests [145], binder content, and different

geometries [146] were also studied. This low binder content hardmetal was found to have damage on the WC grains, also with binder extrusion; high binder hardmetal were dominated with mechanisms such as ploughing, fracture and re-embedment. The studies [144-147] suggested that the fracture of WC grains and plastic deformation were the main mechanisms but re-embedding of the fragments is also important. Debonding between the WC grains and the binder matrix were also found, with a tribolayer formed [144-146]. Cracks were found in the grains on the surface, but do not propagate through multiple grains, therefore a fatigue mechanism is preferred rather than the previous proposed indentation mechanism [144-146].

Wear of cermets, especially with TiC- and Ti(C,N) as the ceramic phase were also largely reported in the past decade. A family of the TiC-based cermets with various binder content and grain sizes under different wearing conditions were studied [148]. It was found that TiC-FeNi alloys appeared to have a better wear resistance for both abrasive and adhesive wear than the TiC-NiMo cermets at the same hardness. With proper selection of the binder content and microstructure, the TiC-based cermets could compete the WC-Co cemented carbides [148]. Pirso and colleagues [149-152] have conducted a series of studies on the two-body, three-body wear behaviour of TiC-based cermets. For two-body abrasive wear [150], they studied TiC-NiMo (6.1 to 34.4 vol.% binder) cermets under 20 N of load and compared the Cr_3C_2-Ni (with binder contents of 7.7 to 24.5 vol.%) and WC-Co (10 to 31.6 vol.% binder) under the same condition. Three-body abrasive wear [151,152] were conducted on TiC-NiMo (with binder content 20 -60 wt.%), Cr_3C_2-Ni (with binder contents of 10-30 wt%) and WC-Co (6-15 wt.% binder) under 40 and 200N of load, and studied the effect of hardness of abrasive particles on the material. If the hardness of the particles are significantly higher than that of material, plastic deformation would occur and lead to binder extrusion, carbide fracture and delamination; if the hardness of the particles are lower, binder removal followed by grain pull-up are favoured. Studies on the same family of materials loaded 3 N of force, confirmed that for abrasive and adhesive wear is mainly controlled by the stiffness of the material, which is the governed by elastic (Young's modulus) and the plastic (proof stress) strain [153,154]. The wear response is also mainly depending on the binder content and grain size than the composition. Binder extrusion, microcutting, ploughing and transgranular cracking were also found [153,154].

Reciprocating wear tests were conducted on TiC- and Ti(C,N)-based cermets with 20-40 vol.% Ni_3Al as binder, with load applied ranging from 20 to 80 N for 120 minutes [155]. It has shown that the mean coefficient of friction is stable for TiC-Ni_3Al cermets and independent of load throughout the test time, the reported specific wear rate ranges between 1.5 and 10×10^{-7} mm^3/Nm [155]. Same testing condition was applied on a series of Ti(C,N) cermets with the same amount of binder, and it appeared that the wear resistance of the Ti(C,N) cermets is lower than that of TiC-based cermets [156]. Increasing the nitrogen content would decrease the hardness and increase the fracture toughness [156]. Both studies [155,156] shown a transition in the wear mechanism occurred during the process, a two- and three-body wear generated wear debris and accumulated at the end of the wear track. A further transition to adhesive wear was confirmed as a uniform oxide layer, which was found on both the cermet and the counter-face sphere [155,156]. Stewart [157] *et al.* studied the Ti(C,N) based cermets tested with the same geometry has a specific wear rate of $0.5\text{-}5\times10^{-7}$ mm^3/Nm. Focused ion beam technique was applied to study the subsurface damage, a tribolayer with a thickness of 1.5-2.5 μm was found. Further investigation [158] of the system introduced Mo_2C to improve the densification behaviour up to 10 vol.%, however the content has increased the specific wear rate. TiC-based stainless steel cermets were also studied. Previous research [159] of TiC-304-L stainless steel cermets with 10-30 vol.% binder show specific wear rate 1.07×10^{-4} mm^3/Nm, and TiC-316L stainless steel cermets with fine- and coarse-grained have specific wear rates ranging from 5 to $\sim65\times10^{-7}$ mm^3/Nm [159].

2.9 References

1. J.R. Tinklepaugh, W.B. Crandall (Ed.), Cermets, Reinhold Publishing Corporation, New York, 1960.
2. P. Schwarzkopf, R. Kieffer, Refractory hard metals: borides, carbides, nitrides, and silicides; the basic constituents of cemented hard metals and their use as high-temperature materials, The Macmillan Company, New York, 1953.
3. E.K. Storms. The refractory carbides. Academic Press, New York, 1967.
4. H.O. Pierson. Handbook of refractory carbides & nitrides: properties, characteristics, processing and applications, Noyes Publications, New Jersey, 1996.

5. D. Moskowitz, M. Humenik Jr, Cemented titanium carbide cutting tools, In Modern Developments in Powder Metallurgy (1966) 83-94.
6. N. Durlu, Titanium carbide based composites for high temperature applications. J. Eur. Ceram. Soc. 19 (1999) 2415-2419.
7. J. Kim, Mo. Seo, S. Kang, Microstructure and mechanical properties of Ti-based solid-solution cermets, Mater. Sci, Eng,: A 528.6 (2011) 2517-2521.
8. A. Rajabi, M. J.Ghazali, J. Syarif, A. R. Daud, Development and application of tool wear: A review of the characterization of TiC-based cermets with different binders. Chem. Eng. J. 255 (2014) 445-452.
9. D. Miller. Liquid-phase sintering of TiC-Ni composites, J. Am. Ceram. Soc. 66 (1983) 841-846.
10. P. Lindahl, P. Gustafson, U. Rolander, L. Stals, H.O. Andrén, Microstructure of model cermets with high Mo or W content. Int. J. Refract. Met. Hard Mater. 17 (1999) 411-421.
11. J. Kübarsepp, H. Annuka, H. Reshetnyak, Characteristics of steel-bonded cermets and their applications, 1996 European Conference on Advaces in hard materials Procudtion, (1996) 523- 529.
12. F. Akhtar, S.J. Guo, Microstructure, mechanical and fretting wear properties of TiC-stainless steel composites. Mater. Charact. 59 (2008) 84-90.
13. B. Lograsso, R. German. Liquid Phase sintered Titanium carbide-tool steel composites for high temperature service, Prog. Powder Metallurgy. 43 (1987) 415-439.
14. G. Krauss, Steels: Processing, structure, and performance, ASM International, 2005.
15. J. H. Magee, Wear of stainless steels, 10th edition, ASM International, Materials Park, 1995.
16. F. Bülbül, H. Altun, V. Ezirmik, Ö. Küçük, Investigation of structural, tribological and corrosion properties of electroless Ni–B coating deposited on 316L stainless steel. Proc. Inst. Mech. Eng. Part J – J. Eng. Tribology 227 (2013) 629-639.
17. D.B. Marshall, R. F. Cook, N.P. Padture, M.L. Oyen, A. Pajares, J.E. Bradby, I.E. Reimanis, R.Tandon, T.F. Page, G.M. Pharr, B.R. Lawn, The compelling case for

indentation as a functional exploratory and characterization cool. J. Am. Ceram. Soc. 98(2015) 2671-80.

18. National Research Council Canada, Associate Committee on Tribology (Wear, Friction and Lubrication), A strategy for tribology in Canada: Enhancing reliability and efficiency through the reduction of wear and friction NRC. Ottawa, 1987.
19. M. Anderson, S. Chiovelli, S. Hoskins. Improving reliability and productivity at Syncrude Canada ltd. through materials research: Past, present, and future. CIM Bulletin 97 (2004) 1-5.
20. P. Ettmayer. Hardmetals and cermets. Annu. Rev. Mater. Sci. 19 (1989) 145-164.
21. S. Zhang. Titanium carbonitride-based cermets: Processes and properties. Mater. Sci, Eng.: A 163(1993) 141-148.
22. P. Ettmayer, W. Lengauer, The story of cermets, Powder Metall. Int. 21 (1989) 37-38.
23. J.B. Holt, Z.A. Munir, Combustion synthesis of titanium carbide: Theory and experiment. Springer J. Mater. Sci. 21 (1986) 251-259.
24. ASM handbook, ASM International, Handbook Committee, Materials Park, OH, 1990.
25. E. Rudy, D.P. Harmon, C.E. Brukl, AFML-TR-65-2, Part I, Vol II, Air Force Materials laboratory, Research and Technology Division, Air Force Systems Command, Wright-Patterson, A.F.B., Ohio, 1965.
26. D.B. Miracle, H.A. Lipsitt, Mechanical properties of fine-grained substoichiomebic titanium carbide, J. Am. Ceram. Soc. 66 (1983) 592-597.
27. W. Shimer, Proc.Roy.Soc. 42 (1887) 89.
28. H. Moissan, Compt. Rend., 120 (1895) 290.
29. H. Moissan, Comp. Red. 125 (1897) 839.
30. V.P. Elyutin, P.F. Merkulova, Yu. Pavlov, Proizv. i Obrabotka Stali I Splavov, Moskov. Inst. Stali im I..V. Stalina, Sb. 38 (1958) 79.
31. G.V. Samsonov, N.S. Rozinova, Bull. Sect. Phys. Chem. 34 (1956) 963-969
32. V.S. Kutsev, B.F. Ormont, Zh. Fiz. Khim 24 (1955) 597.
33. Meerson, G. A., O. E. Krein, Investigation of the mechanism of the formation of titanium carbide in vacuum. J. Appl. Chem. USSR 25 (1952) 143-56.

34. K. Ogawa, Y. Bando, Funtai Oyobi Funmatsuyakin 6 (1959) 160.
35. I. Campbell, C. Powell, D. Nowicki, B. Gonser, The Vapor-Phase deposition of refractory materials I. general conditions and apparatus. J. Electrochem. Soc. (1949) 318-333.
36. D. Schuler, Thesis, Tech. Hochschule, Zürich (1952).
37. R. Koc, J.S. Folmer, Carbothermal synthesis of titanium carbide using ultrafine titania powders. J. Mater. Sci. 32 (1997) 3101-3111.
38. W.D. Callister Jr., D.G. Rethwisch, Materials science and engineering: An introduction, 8th edition, John Wiley & Sons, New York, 2009.
39. H. Bhadeshia, R. Honeycombe, Steels: microstructure and properties, Butterworth-Heinemann, 2011.
40. G.J. Fischer, R.J. Maciag, The wrought stainless steels, Handbook of stainless steels, 1 (1977) 1.
41. M. Humenik, N.M. Parikh, Cermets: I, Fundamental concepts related to micro-structure and physical properties of cermet systems, J. Am. Ceram. Soc. 39 (1956) 60-63.
42. N.M. Parikh, M. Humenik, Cermets: II, Wettability and microstructure studies in liquid-phase sintering, J. Am. Ceram. Soc. 40 (1957) 315-320.
43. N.M. Parikh, Cermets: III, Modes of fracture and slip in cemented carbides, J. Am. Ceram. Soc. 40 (1957) 335-339.
44. H. Klaasen, J. Kübarsepp, F. Sergejev, Strength and failure of TiC based cermets, Powder Metall. 52 (2009) 111-115.
45. P.F. Becher, K.P. Plucknett, Properties of Ni_3Al-bonded titanium carbide ceramics, J. Euro. Ceram. Soc. 18 (1998) 395-400.
46. K.P. Plucknett, P.F. Becher, R. Subramanian, Melt-infiltration processing of TiC/Ni_3Al composites, J. Mater. Res. 12 (1997) 2515-2517.
47. K.P. Plucknett, P.F. Becher, S.B. Waters, Flexure strength of melt-infiltration processed TiC/Ni_3Al composites. J. Am. Ceram. Soc. 81 (1998) 1839-1844.
48. K.P. Plucknett, P.F. Becher, Processing and microstructure development of titanium carbide-nickel aluminide composites J. Am. Ceram. Soc. 84 (2001) 55-61.

49. R.B. Collier, K.P. Plucknett, Spherical indentation damage in TiC-Ni_3Al composites, Int. J. Refract. Met. Hard Mater. 30 (2012) 188-195.
50. P. Persson, A. Jarfors, S. Savage, Self-propagating high-temperature synthesis and liquid-phase sintering of TiC/Fe composites. J. Mater. Process. Technol. 127 (2002) 131-139.
51. T.L. Stewart, R.B. Collier, Z.N. Farhat, G.J. Kipouros, K.P. Plucknett. Melt-infiltration processing of titanium carbide-stainless steel cermets, Ceram. Eng. Sci. Proc. 31 (2010) 97-104.
52. R.M. German, Powder metallurgy of iron and steel, John Wiley & Sons, New York, 1998.
53. R.M. German, Powder metallurgy and particulate materials processing: the processes, materials, products, properties, and applications, 2nd edition, Metal Powder Indsutries Federation, Princeton, New Jersey, 2005.
54. R.M. German, Liquid Phase Sintering, Plenum, New York, 1985.
55. C. Toy, W. D. Scott, Ceramic-metal composite produced by melt infiltration, J. Am. Ceram. Soc. 73 (1990) 97-101.
56. E.J. Gonzalez, K.P. Trumble, Spontaneous infiltration of alumina by copper-oxygen alloys, J. Am. Ceram. Soc. 79 (1996) 114-120.
57. D. Muscat, K. Shanker, R.A.L. Drew, Al/TiC composites produced by melt infiltration, Mater. Sci. Technol. 8 (1992) 871-976.
58. N.A. Travitzky, N. Claussen, Microstructure and properties of metal infiltrated RBSN composites, J. Euro. Ceram. Soc. 9 (1992) 61-65.
59. J. Rodel, H. Prielipp, N. Claussen, M. Sternitzke, K.B. Alexander, P.F. Becher, J.H. Schneibel, Ni_3Al/Al_2O_3 composites with interpenetrating networks, Scripta. Metall. Mater. 33 (1995) 843-848.
60. H. Chandler (Ed.), Hardness testing, ASM international, 1999.
61. R.G. German, S.J. Park, Handbook of mathematical relations in particulate materials processing, John Wiley & Sons, New Jersey, 2008.
62. ASTM C1327-15, Standard Test Method for Vickers Indentation Hardness of Advanced Ceramics, ASTM International, West Conshohocken, PA, 2015.

63. C.E. Inglis, Stresses in a plate due to the presence of cracks and sharp corners, Trans. Inst. Nav. Archit. London 55 (1913) 219-230.
64. A.C. Fischer-Cripps, Introduction to contact mechanics, Springer, New York, 2000.
65. A.A. Griffith. The phenomena of rupture and flow in solids. Philos. Trans. R. Soc. London, Ser. A 221 (1920) 163-198.
66. G.R. Irwin, Fracture dynamic, Trans. Am. Soc. Met. 40A (1948) 147-166.
67. G.R. Irwin, Analysis of stresses and strains near the end of a crack traversing a plate, J. Appl. Mech. 24 (1957) 361-364.
68. J.B. Wachtman, W.R. Cannon, M.J. Matthewson, Mechanical properties of ceramics (2nd ed.), John Wiley & Sons, New York, 2009.
69. G.D. Quinn, R.C. Bradt, On the Vickers indentation fracture toughness test, J. Am. Ceram. Soc. 90 (2007) 673-680.
70. A.G. Evans, E.A. Charles, Fracture toughness determinations by indentation, J. Am. Ceram. Soc. 59 (1976) 371-372.
71. B.R. Lawn, M.V. Swain, Microfracture beneath point indentations in brittle solids, J. Mater. Sci 10 (1975) 113-122.
72. B.R. Lawn, E.F Fuller, Equilibrium penny-like cracks in indentation fracture, J. Mater. Sci. 10 (1975) 2016-2024.
73. B.R. Lawn, A.G. Evans, A model for crack initiation in elastic/plastic indentation fields, J. Mater. Sci. 12 (1977) 2195-2199.
74. B.R. Lawn, D.B. Marshall, Hardness, toughness, and brittleness: an indentation analysis, J. Am. Ceram. Soc. 62 (1979) 347-350.
75. B.R. Lawn, A.G. Evans, D.B. Marshall, Elastic/plastic indentation damage in ceramics: the median/radial crack system, J. Am. Ceram. Soc. 63 (1980) 574-581.
76. A.G. Evans, Quasi-static solid particle damage in brittle solids-I. Observations analysis and implications, Acta Metall. 24 (1976) 939-956.
77. D.J. Green, An introduction to the mechanical properties of ceramics, Cambridge University Press, 1998.
78. R.F. Cook, G.M. Pharr, Direct observation and analysis of indentation cracking in glasses and ceramics, J. Am. Ceram. Soc. 73 (1990) 787-817.

79. B.R. Lawn, R. Wilshaw, Indentation fracture: principles and applications, J. Mater. Sci. 10 (1975) 1049-1081.
80. D.B. Marshall, B.R. Lawn, Residual stress effects in sharp contact cracking, J. Mater. Sci. 14 (1979) 2001-2012.
81. G.R. Anstis, P. Chantikul, B.R. Lawn, D.B. Marshall, A critical evaluation of indentation techniques for measuring fracture toughness: I, direct crack measurements, J. Am. Ceram. Soc. 64 (1981) 533-538.
82. J. Lankford, Threshold microfracture during elastic-plastic indentation of ceramics, J. Mater. Sci. 16 (1981) 1177-1182.
83. K. Niihara, R. Morena, D. P. H. Hasselman., Evaluation of K_{IC} of brittle solids by the indentation method with low crack-to-indent ratios, J. Mater. Sci. Lett. 1 (1982) 13-16.
84. K. Niihara, A fracture mechanics analysis of indentation-induced Palmqvist crack in ceramics, J. Mater. Sci. Lett. 2 (1983) 221-223.
85. J. Lankford, Indentation microfracture in the Palmqvist crack regime: implications for fracture toughness evaluation by the indentation method, J. Mater. Sci. Lett. 1 (1982) 496-495.
86. D.K. Shetty, I.G. Wright, P.N Mincer, A.H. Clauer, Indentation fracture of WC-Co cermets, J. Mater. Sci. 20 (1975) 1873-1882.
87. D.K. Shetty, A.R. Rosenfield, W. H. Duckworth, Indenter Flaw Geometry and Fracture Toughness Estimates for a Glass-Ceramic, J. Am. Ceram. Soc. 68 (1985) 282-284.
88. D.K. Shetty, A.R. Rosenfield, W. H. Duckworth, Analysis of Indentation Crack as a Wedge-Loaded Half-Penny Crack, J. Am. Ceram. Soc. 68 (1985) 65-67.
89. D.K. Shetty, I.G. Wright, On estimating fracture toughness of cemented carbides from Palmqvist crack sizes, J. Mater. Sci. Lett. 5 (1986) 365-368.
90. M.T. Laugier, Palmqvist indentation toughness in WC-Co composites, J. Mater. Sci. Lett. 6 (1987) 897-900.
91. M.T. Laugier, Palmqvist toughness in WC-co composites viewed as a ductile/brittle transition, J. Mater. Sci. Lett. 6 (1987) 768-770.

92. M.T. Laugier, New formula for indentation toughness in ceramics, J. Mater. Sci. Lett. 6 (1987) 355-356.
93. I.M. Hutchings. Tribology: Friction and wear of engineering materials. Butterworth-Heinemann Ltd, 1992.
94. I.M. Hutchings, Mechanisms of wear in powder technology: A review, Powder Technol. 76 (1993) 3-13.
95. D.B. Marshall, B.R. Lawn, A.G. Evans, Elastic/plastic indentation damage in ceramics: the lateral crack system, J. Am. Ceram. Soc. 65 (1982) 561-566.
96. K.L. Johnson, One hundred years of Hertz contact, P. Ins. Mech. Eng. 196 (1982) 363-378.
97. B.R. Lawn, Indentation of ceramics with spheres: A century after hertz, J. Am. Ceram. Soc. 81 (1998) 1977-1994.
98. F.C. Roesler, Brittle fracture near equilibrium, P. Phys. Soc. Lond. B. 69 (1956) 981.
99. F. Auerbach, Measurement of hardness, An. Phy. Leipzig. 43 (1891) 61-100.
100. F. C. Frank, B.R. Lawn, On the theory of Hertzian fracture, Proceedings of the Royal Society of London A: Mathematical, Physical and Engineering Sciences. The Royal Society, 299 (1967)
101. B.R. Lawn, S.K. Lee, I.M. Peterson, S. Wuttiphan, Model of Strength Degradation from Hertzian Contact Damage in Tough Ceramics, J. Am. Ceram. Soc. 81 (1998) 1509-1520.
102. D. Tabor, The hardness of metals, Clarendon Press, Oxford, 1951.
103. M.V. Swain, B.R. Lawn, A study of dislocation arrays at spherical indentations in LiF as a function of indentation stress and strain, Phys. Status Solidi B 35 (1969) 909-923.
104. C. Hardy, C.N. Baronet, G.V. Tordion, The elasto-plastic indentation of a half-space by a rigid sphere, Int. J. Numer. Meth. Eng. 3 (1971) 451-462.
105. P.S. Follansbee, G.B. Sinclair, Quasi-static normal indentation of an elasto-plastic half-space by a rigid sphere-I: analysis, Int. J. Solids. Struct. 20 (1984) 81-91.
106. R.F. Hill, B. Storakers, A.B. Zdunek, A theoretical study of the Brinell hardness test, Proc. R. Soc. London, Ser. A 423 (1989) 301-330.

107. K. Komvopoulos, Finite element analysis of a layered elastic solid in normal contact with a rigid surface, J. Tribo. T. ASME. 110 (1989) 477-485.
108. K. Komvopoulos, Elastic-plastic finite element analysis of indented layered media, J. Tribo. T. ASME. 111 (1989) 430-439.
109. G. Care, A.C. Fischer-Cripps, Elastic-plastic indentation stress fieldsusing the finite-element method, J. Mater.Sci. 32 (1997) 5653-5659.
110. H. Cai, S. Kalceff, B.R. Lawn, Deformation and fracture of mica-containing glass-ceramics in Hertzian contacts, J. Mater. Res. 9 (1994) 762-770.
111. F. Guiberteau, N.P. Padture, B.R. Lawn, Effect of grain size on hertzian contact damage in alumina, J. Am. Ceram. Soc. 77 (1994) 1825-1831.
112. S.K. Lee, S. Wuttiphan, B.R. Lawn, Role of microstructure in Hertzian contact damage in silicon nitride: I, mechanical characterization, J. Am. Ceram. Soc.80 (1997) 2367-2381.
113. Y. Chiang, D. Birnie, W.D. Kingery, Physical ceramics: Principles for ceramic science and engineering, Johh Wiley & Sons, 1997.
114. A.G. Evans, Toughening mechanisms in zirconia alloys, Science and technology of zirconia II, 1983.
115. F. Guiberteau, N.P. Padture, B.R. Lawn, Indentation fatigue: A simple cyclic Hertzian test for measuring damage accumulation in polycrystalline ceramics, Philos. Mag. A 65 (1993) 1003-1016.
116. B.R. Lawn, N.P. Padture, H. Cait, F. Guiberteau, Making ceramics “ductile”, Science 263 (1994) 1114-1116.
117. N.P. Padture, B.R. Lawn, Toughness properties of a silicon carbide with an *in situ* induced heterogeneous grain structure, J. Am. Ceram. Soc. 77 (1994) 2518-2522.
118. A. Pajares, L. Wei, B.R. Lawn, D.B Marshall, Damage accumulation and cyclic fatigue in Mg-PSZ at Hertzian contacts, J. Mater. Res. 10 (1995) 2613-2625.
119. H.H.K. Xu, L. Wei, N.P. Padture, B. R. Lawn, Effect of microstructural coarsening on Hertzian contact damage in silicon nitride, J. Mater. Res. 30 (1995) 869-878.
120. Friction, lubrication, and wear technology, ASM International, Handbook Committee, 1992.

121. G.W. Stachowiak (ed.), Wear: Materials, mechanisms and practice, Johh Wiley & Sons, 2006.
122. K. Kato. Classification of wear mechanisms/models, Proceedings of the institution of mechanical engineerings, Part J: Journal of Engineering Tribology 216 (2002) 349-355.
123. ASTM G40-15 Standard terminology relating to wear and erosion, ASTM International, West Conshohocken, PA, 2015.
124. K. Kato, Wear mode transitions, Scripta Mater. 24 (1990) 815-820.
125. J. Archard, Contact and rubbing of flat surfaces, J. Appl. Phys. 24 (1953) 981-988.
126. J.K. Lancaster, The influence of substrate hardness on the formation and endurance of molybdenum disulphide films, 10 (1967) 103-117.
127. A.G. Evans. Abrasive wear in ceramics: An assessment, National Bureau of Standards-Ceramic Meeting, Gaithersburg, Washington, November 12, 1978.
128. K.H. Zum Gahr, Microstructre and wear of materials, Tribology Series, 10, Elsevier, 1987.
129. G. Stachowiak, A.W. Batchelor. Engineering tribology, Butterworth-Heinemann, 2013.
130. Glossary of Terms and Definitions in the Field of Friction, Wear and Lubrication (Tribology)Research Group on Wear of Engineering Materials, OECD, Paris, 1969.
131. T. Kayaba, K. Kato, The analysis of adhesive wear mechanism by successive observations of the wear process in SEM, Wear of materials (1979) 45-56.
132. F.P. Bowden, D. Tabor, The friction and lubrication of solids, Vol.2, 1964.
133. J.A. Williams, Wear and wear particles—some fundamentals, Tribol. Int. 38 (2005) 863-870.
134. J. Larsen-Basse, Resistance of cemented carbides to sliding abrasion: Role of binder metal, Science of Hard Materials (1983) 797-813.
135. J. Larsen-Basse, C.M. Shishido, P. Tanouye, Some features of abraded WC/Co surfaces, J. Australian Inst. Metals 19 (1974) 270-275.
136. H. Feld, P, Walter, Contribution to the understanding of mineral hard metal abrasive wear, Powder Metall. Int. 7 (1975) 188-190.

137. J. Larsen-Basse, N. Devnani, Binder extrusions as a controlling mechanism in abrasion of WC-Co cemented carbides, Science of Hard Materials (1984) 883-895.
138. J. Larsen-Basse, Wear of hard-metals in rock drilling: A survey of the literature, Powder Metall. 16 (1973) 1-32.
139. J. Larsen-Basse, C.M. Perrott, P.M Robinson, Abrasive wear of tungsten carbide-cobalt composites. I. Rotary drilling tests. Mater. Sci, Eng 13 (1974) 83-91.
140. J. Larsen-Basse, Binder extrusion in sliding wear of WC-Co alloys, Wear 105 (1985) 247-256.
141. S. F. Wayne, J.G. Baldoni, S.T. Buljan, Abrasions and erosion of WC-Co with controlled microstructures, Tribology transactions 33 (1990) 611-617.
142. M.G. Gee, Low load multiple scratch tests of ceramics and hard metals, Wear 250 (2001) 264-281.
143. A.J. Gant, M.G. Gee, Wear of tungsten-carbide-cobalt hardmetals and hot isostatically pressed high speed steels under dry abrasive conditions, Wear 251 (2001) 908-915.
144. A. J. Gant, M.G. Gee, B. Roebuck, Rotating wheel abrasion of WC/Co hardmetals, Wear 258 (2005) 178-188.
145. A.J. Gant, M.G. Gee. Abrasion of tungsten carbide hardmetals using hard countefaces. Int. J. Refract. Met. Hard Mater. 24 (2006) 189-198.
146. M. Gee, A. Gant, B. Roebuck, Wear mechanisms in abrasion and erosion of WC-Co and related hardmetals, Wear 263 (2007) 137-148.
147. M.G. Gee, L. Nimishakavi, Model single point abrasion experiments on WC/Co hardmetals, J. Int. Refract. Met. Hard Mater. 29 (2011) 1-9.
148. J. Kübarsepp, H. Klaasen, J. Pirso, Behaviour of TiC-base cermets in different wear conditions, Wear 249 (2001) 229-234.
149. J. Pirso, M. Viljus, S. Letunovits, Sliding wear of TiC-NiMo cermets, Tribol. Int. 37 (2004) 817-824.
150. J. Pirso, M. Viljus, K. Juhani, S. Letunovits, Two-body dry abrasive wear of cermets, Wear 266 (2009) 21-29.
151. J. Pirso, M. Viljus, K. Juhani, M. Kuningas, Three-body abrasive wear of TiC-NiMo cermets, Tribol. Int. 43 (2010) 340-346.

152. J. Pirso, M. Viljus, S. Letunovits, K. Juhani, R. Joost, Three-body abrasive wear of cermets, Wear 271 (2011) 2868-2878.
153. H. Klaasen, J. Kübarsepp, Abrasive wear performance of carbide composites, Wear 261 (2006) 520-526.
154. H. Klaasen, J. Kübarsepp, T. Roosaar, M. Viljus, R. Traksmaa, Adhesive wear performance of hardmetals and cermets, Wear 268 (2010) 1122-1128.
155. S. Buchholz, Z.N. Farhat, G.J. Kipouros, K.P. Plucknett, The reciprocating wear behaviour of TiC-Ni_3Al cermets, Int. J. Refract. Met. Hard Mater. 33 (2012) 44-52.
156. S. Buchholz, Z.N. Farhat, G.J. Kipouros, K.P. Plucknett, Reciprocating wear response of Ti(C,N)-Ni_3Al cermets, Can. Metall. Q. 52 (2013) 69-80.
157. T. L. Stewart. The characterization of TiC and Ti(C,N) based cermets with and without Mo_2C. MSc Thesis, Dalhousie University, Canada, 2014.
158. T.L. Stewart, K.P. Plucknett, The effects of Mo_2C additions on the microstructure and sliding wear of $TiC_{0.3}N_{0.7}$-Ni_3Al cermets, Int. J. Refract. Met. Hard Mater. 50 (2015) 227-239.
159. C.C. Onuoha, C. Jin, Z.N. Farhat, G.J. Kipouros, K.P. Plucknett. The effects of TiC grain size and steel binder content on the reciprocating wear behaviour of TiC-316L stainless steel cermets, Wear 350-351 (2016) 116-120.

Chapter 3 Materials and Experiments

This chapter provided details regarding the experimental procedures used in the current study, which were not fully presented in the following paper-based chapters. This includes powder characterisation, compaction and sintering. Basic microstructure of the sintered material is shown with the associated microstructure parameter calculations. A representative figure of the crystal structure analysis is also provided.

3.1 Materials

3.1.1 Titanium Carbide

The TiC powders (Lot#: PL20125339) used in the experiments were sourced from Pacific Particulate Materials Ltd. (Vancouver, BC, Canada). The morphology of the TiC particles was analysed using scanning electron microscopy (SEM; Model S-4700, Hitachi High Technologies, Tokyo, Japan), and a representative SEM image of the as-received powder is shown in Figure 3.1. The raw powders have a quoted manufacture particle size of ~1.3 μm, and subsequent particle size measurement reported the average particle size to be ~1.25 μm, with a bimodal distribution [1]. The particle size distribution of the powder is shown in Figure 3.2. In Table 3.1 the chemical composition of the TiC powder, provided by the manufacturer, is given.

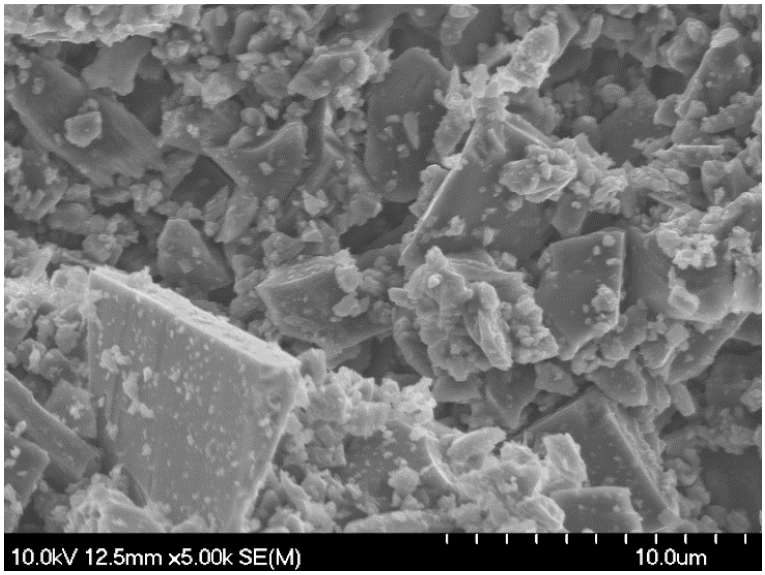

Figure 3.1: Representative SEM image of the as-received TiC powder.

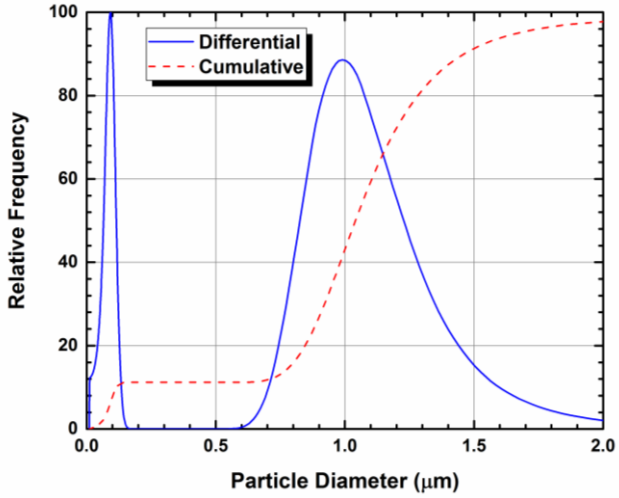

Figure 3.2: TiC Powder particle size distribution.

Table 3.1: Chemical composition of the as-received TiC powder.

	Total C	**Free C**	**Combined C**	**Fe**	**O**	**N**	**Ti**
(wt.%)	19.60	0.11	19.49	0.05	0.40	0.05	79.90

3.1.2 Stainless Steel

The three stainless steel powders used as the binder phases were sourced from Alfa Aesar (Ward Hill, MA, USA) grade 304-L (Stock # : 11085, Lot #: K19M09), 316-L (Stock # 11089, Lot # A04S008 and Lot#: F18W021), and 410-L (Stock #: 11085, Lot #: I23M43), each with a nominal particle size of -100 mesh. Figure 3.3 shows a representative SEM image of the 316-L powder, as-received. The chemical composition and particle size of the powder were provided for quality control purposes by the manufacturer, and are shown in Table 3.2 and Table 3.3 respectively. Table 3.4 lists the other property data provided by the manufacturer.

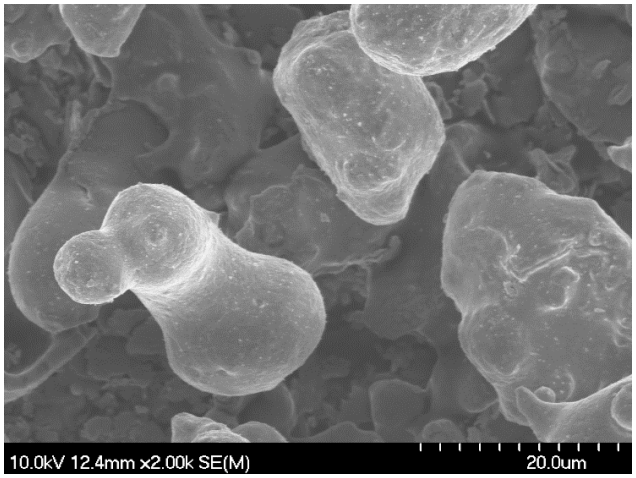

Figure 3.3: Representative SEM image of as-received 316-L stainless steel powder.

Table 3.2: Composition of the as-received stainless steel powders, provided by manufacturer.

(wt %)	Cr	Mo	Mn	S	Ni	Si	C	P	Fe
304L	18.75	--	0.15	0.008	11.47	0.71	0.022	0.013	68.877
316L	16.79	2.19	0.13	0.007	12.81	0.79	0.019	--	67.264
316L	16.82	2.19	0.09	0.01	13.35	0.86	0.02	--	66.660
410L	12.32	--	0.22	0.012	--	0.91	0.02	--	86.518

Table 3.3: Particle size distribution of the steel powders (in wt. %).

mesh	+100	+120	+140	+150	+200	+270	+325	-325
304L	4.0	4.3	6.8	16.5	--	25.2	7.4	35.8
316L	1.2	--	--	7.5	16.9	--	28.3	46.1
316L	2.0	--	--	9.1	17.7	--	28.3	42.9
410L	3.0	--	--	9.7	15.8	--	26.9	44.6

Table 3.4: Properties of the steel powders, provided by Alfa Aesar (tested with 1.0% lithium stearate).

Property	Powders			
	304L	**316L**	**316L**	**410L**
Apparent Density (Hall) (g/cm^3)	2.78	2.88	2.83	3.05
Flow Rate (Hall) (s/50g)	31	26.8	27.6	27.2
Green Strength (psi)	--	898	895	1830
Green Density (g/cm^3)	--	6.58	6.51	6.45
Transverse Rupture Strength (psi)	--	136707	130800	158500
Dimensional Change/ 2100ºF (%)	--	0.44-	0.52-	0.51-

3.2 Cermet Fabrication and Analysis

3.2.1 Sample Preparation

The TiC pellets were first pressed by using uniaxial compaction (Model S/N 41000-102, Carver Inc., Wabash, IN, USA) with ~7.35 g of powder in a hardened steel die (diameter: 31.75 mm), with approximately 0.6 mL of hexane (to reduce die wall friction), at a pressure of around 45 MPa. Then the samples were sealed and cold isostatically pressed (Model S/N-101462-1, Avure Technologies Inc., Franklin, TN, USA) at 208 MPa. Following compaction of the samples, a simple melt infiltration sintering technique was used to fabricate the densified sample. The pressed samples are placed in alumina crucibles, with different volume percentages of binder, ranging from 5 to 30 vol.%, placed on top. They were then sintered under various conditions to modify the final grain size: (i) 1475ºC for 15 minutes to get fine-sized TiC grains, (ii) 1550ºC for 60 minutes to get intermediate-sized grains (samples prepared for wear tests were sintered at 1500 ºC

for 60 minutes for the intermediated-grained), and (iii) 1550ºC for 240 minutes to get coarse-sized grains. Heating and cooling rates of 10ºC/min and 25ºC/min, respectively, were used. Samples were prepared under a dynamic vacuum (20 mTorr) inside a graphite resistance furnace (Materials Research Furnaces, Suncook, NH, USA).

The densities of the sintered cermets were calculated using Archimedes' immersion method in water, and the data showed the samples consistently reached densities higher than 95% of the theoretical value (calculated using the simple rule of mixtures). The cermets were then ground flat on both sides using a diamond peripheral wheel, and polished to a mirror-like finish (starting from a 125 μm diamond pad and finishing up with 0.25 μm diamond paste).

3.2.2 Microstructure Analysis

Microstructural characterization was carried using both optical microscopy (Model BX-51, Olympus Canada, Richmond Hill, Ontario, Canada) and scanning electron microscopy (SEM; Model S-4700, Hitachi High Technologies, Tokyo, Japan). The SEM allows the combined secondary and back-scattered electron signal to be recorded, using the Hitachi ExB 'in-column' detector, which can also be operated in a solely backscattered electron mode, with a negative bias applied to the detector to block out low energy secondary electrons. Backscattered electrons show a high sensitivity to differences in atomic number, and hence provide a valuable contrast mechanism based on changes in composition. A representative SEM image (Figure 3.4), demonstrates a typical TiC-316L cermet, with 10 vol.% of the stainless steel binder, produced by melt infiltration method. This sample was sintered at 1550 ºC for 60 minutes. Energy-dispersive X-ray spectroscopy (EDS; Model Inca X-Max^N, Oxford Instruments, Abingdon, UK) was used to determine the phase compositions for the TiC-stainless steel binder cermets.

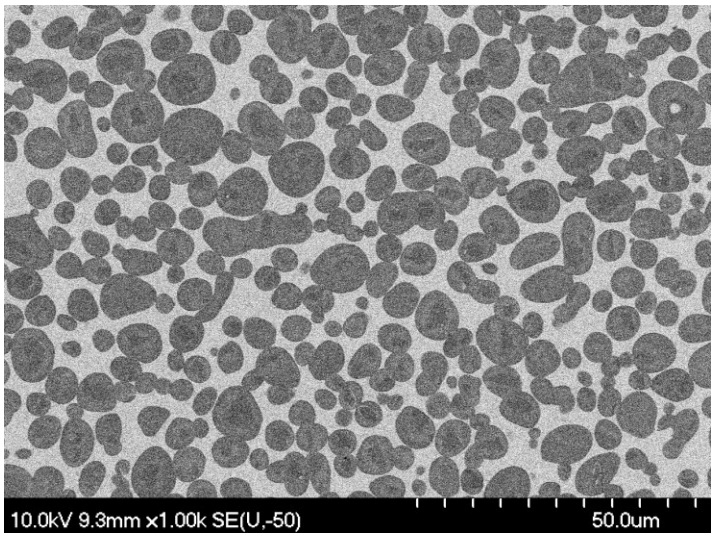

Figure 3.4: Typical microstructure of a TiC-316L stainless steel cermet, with 10 vol.% of binder. The backscatter electron mode is used to show the core-rim structure of the cermet, which arises from compositional changes.

The average TiC grain size, d_c, was measured using the linear intercept method [2], from digital SEM images, with a minimum of 300 TiC grains measured for each value of mean grain size that was determined. The contiguity, C, of the samples, were measured by counting the numbers of carbide/carbide and carbide/binder interfaces that were present on horizontal lines drawn through microstructural images of the corresponding samples. Contiguity was determined using the following equation [3]:

$$C = \frac{2N_{c/c}}{2N_{c/c} + N_{c/b}} \qquad \text{Equation 3.1}$$

where $N_{c/c}$ and $N_{c/b}$ are the number of TiC-TiC and TiC-steel interfaces intercepted, respectively [3]. The binder mean free path was then determined after obtaining the average grain size and contiguity of the sample, following [3]:

$$d_b = \frac{1}{1-C}\left(\frac{V_b}{V_c}\right)d_c \qquad \text{Equation 3.2}$$

3.2.3 X-Ray Diffraction Analysis

X-ray diffraction (XRD; Model Bruker D-9 Advance) was used to examine the crystalline phase of the samples. A cobalt source was used to minimise the Fe fluorescence. Figure 3.5 shows a typical sequence of XRD spectra for TiC-316L cermets.

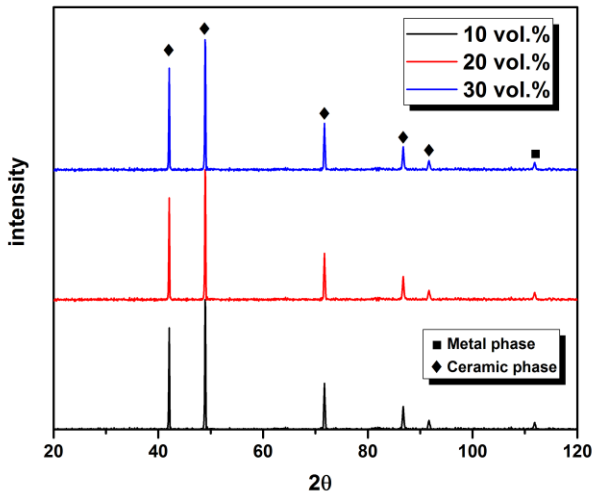

Figure 3.5: A typical XRD spectrum of an intermediate-grained TiC-316L cermet with various binder contents.

3.3 References

1. R.B. Collier K.P. Plucknett, Spherical indentation damage in TiC-Ni_3Al composites. Int. J. Refract. Met. Hard Mater. 30 (2012) 188-195.
2. M. I. Mendelson, Average grain size in polycrystalline ceramics, J. Am. Ceram. Soc. 52 (1969) 443-446.
3. J. Gurland, The measurement of grain contiguity in two phase alloys, Trans. Metall. Soc. AIME, 212 (1958) 452-455.

Chapter 4 Microstructure Instability in TiC-316L Stainless Steel Cermets

Chenxin Jin and Kevin P. Plucknett*

Dalhousie University, 1360 Barrington Street, Materials Engineering, Department of Process Engineering and Applied Science, B3H 4R2, Nova Scotia, Canada

Status: *Published:* International Journal of Refractory Metals and Hard Materials, 58 (2016) 74-83.

Abstract

Titanium carbide (TiC) based cermets are commonly used in wear and corrosion resistance applications. The microstructural evolution, and related compositional instability, of TiC-based cermets prepared with a 316-L stainless steel binder is described in the present work. Samples were fabricated using a simple vacuum melt-infiltration procedure, with 5 to 30 vol.% binder. Infiltration temperatures ranged from 1475°C to 1550°C, held for up to 240 minutes, typically resulting in sintered samples with densities in excess of 99 % of theoretical. It is demonstrated that irregularly shaped grains (concave/hollow) can arise after sintering, especially at 1475°C, which is discussed in terms of the 'instability of the solid-liquid interface' theory. It is demonstrated that a complex, multi-layer core-rim structure arose for the cermets, with accommodation of selected steel constituents into the rim of the TiC grains. In particular, it is shown that the Mo in the original 316-L stainless steel is essentially fully depleted from the metallic binder phase, forming a Mo-rich inner-rim layer on the TiC grain cores.

Keywords: Titanium carbide; Stainless steels; Cermets; Core-rim structure; Scanning electron microscopy; Focused ion beam microscopy

*Contact: kevin.plucknett@dal.ca

4.1 Introduction

Cermets are composite materials that combine hard, brittle ceramics with a ductile metallic binder phase. Compared with conventional 'hardmetals', such as tungsten carbide-cobalt (WC-Co), cermets are lighter in weight with high strength and toughness, combined with excellent wear and corrosion resistance [1-4]. Titanium carbide (TiC) is widely used as the ceramic component in cermets due to its high melting point (3065°C), hardness, and wear resistance [1-4]. Conventionally, TiC based cermets are mainly used as tooling and wear resistant materials, such as cutting tools, bearings, drawing dies, etc. Depending on the metallic binder phase employed, the applications can potentially be broadened to high-stress and high-temperature environments [5]. Several studies have been conducted assessing the effects of composition and microstructure on the behaviour cermets [6-12], particularly the role of the binder volume fraction. In addition to the binder fraction, the grain size and binder mean free path are also influence the physical properties [13].

Some common examples of the metallic phase used in TiC-based cermets include Ni and Fe [14,15]. Ni is the most commonly used metallic binder in these cermets, which is mainly due to the good wetting response during liquid phase sintering, combined with the reasonable mechanical properties of Ni [2]. More recently, TiC cemented with Ni-Mo alloys have proved to be applicable in cutting tools and severe wear conditions [4]. However, due to their relatively low cost and good mechanical properties, Fe alloys are being studied and applied as cermet binders. In particular, austenitic stainless steels have relatively high strength, which is maintained to moderately elevated temperatures, therefore offering potential for use as the binder phase in cermet systems [16-19]. This is combined with reasonable corrosion resistance when stainless steels are incorporated into a cermet structure [10].

It is well known that the addition of Mo or Mo_2C reduces the binder melt wetting angle with TiC to essentially zero when using Ni-based alloys, and typically a core-rim structure is generated, which can be beneficial to the mechanical properties of the cermet [20,21]. The core is invariably the original TiC, and the rim phase is an alloy of (Ti,Mo)C [22]. There can also be different types of rims generated in other specific systems,

particularly Ti(C,N) based cermets [23,24]. Oswald-ripening during the dissolution-reprecipitation process is invariably believed to form the core-rim structure [22-24], but diffusion of Mo into the TiC has also been suggested [25]. Similarly, Guo and colleagues examined the effects of Mo_2C addition when using a Fe binder for Ti(C,N)-based cermets [26]. They demonstrated an improvement in binder wettability, due to Mo_2C addition, and highlighted improved properties and the formation of a core-rim structure.

The aim of the present work was to study the effects of composition and sintering duration on the microstructure evolution of a range of TiC-316L stainless steel cermets, in order to obtain an understanding of the microstructure evolution and stability, and its potential influence on cermet properties.

4.2 Experimental Procedure

4.2.1 Sample Preparation

The TiC powder was obtained from Pacific Particulate Materials Ltd. (Vancouver, BC, Canada) with a quoted manufactured mean particle size of ~1.3 μm, which was confirmed through subsequent particle size analysis [27]. The TiC powder itself shows a bimodal distribution, with fine, nano-sized material (~90-100 nm) combined with coarser particles (from ~500 nm to ~2 μm) [27]. The austenitic stainless steel powder (grade 316L), used as the binder phase, was sourced from Alfa Aesar (Ward Hill, MA, USA), with a nominal particle size of -149 μm (-100 mesh). The melting response of the 316L powder was confirmed through differential scanning calorimetry (DSC; Model SDT Q600, TA Instruments, New Castle, DE, USA), heating at a rate of 20°C/min under a flowing Ar atmosphere. Using this approach the onset of the melting endotherm was confirmed by DSC to occur at ~1400°C. The chemical compositions of the TiC and 316L starting powders were confirmed using inductively coupled plasma optical emission spectroscopy (ICP-OES; Model Varian Vista Pro, CA, USA), for the principle elemental species. The C content of the as-received steel powder was determined using an inert gas fusion method (Model CS-444, Leco Instruments, Mississauga, ON, Canada). The

analyzed compositions of the TiC and 316L steel are presented in Table 4.1 and Table 2.2, respectively.

Table 4.1: Measured composition of the as-received TiC powder using ICP-OES. Note that the C content was not determined.

TiC powder	**Ti**	**Co**	**W**
Conc. (wt.%)	76.80	0.23	2.22

Table 4.2: Measured composition of 316-L as-received powder (in wt.%). Elements determined using ICP-OES, except for C, which is measured using inert gas fusion.

316-L	**Cr**	**Mo**	**Mn**	**S**	**Ni**	**Si**	**C**	**Fe**
Conc. (wt.%)	16.81	2.22	0.10	0.01	13.40	0.59	0.025	64.34

The TiC pellets (each ~7.4 g mass) were uniaxially compacted in a hardened steel die at a pressure of around ~45 MPa. The samples were then vacuum-sealed and further consolidated by cold isostatic pressing (CIPing) at ~208 MPa. This procedure generated TiC pellets with a green density of 59.2 ± 1.3 % of theoretical (i.e. ~40 vol.% porosity after CIPing), based on a TiC theoretical density of 4.93 g/cm^3. A simple melt-infiltration/sintering route was used to fabricate the samples, which has been discussed in detail in an earlier publication [28]. With this approach a pre-determined amount of 316-L stainless steel powder, to give nominal binder contents ranging from 5 to 30 vol.%, was placed on top of the CIPed TiC pellets, which were contained in an aluminium oxide (Al_2O_3) crucible on a bed of bubble Al_2O_3. The samples were sintered in a graphite resistance furnace (Materials Research Furnaces, Suncook, NH, USA) at 1475ºC/15 minutes to get a fine-grained structure, 1550ºC for 60 minutes to get intermediate-sized grains, and 1550ºC for 240 minutes to get coarse grains. Heating and cooling rates of 10ºC/min and 25ºC/min, respectively, were used under a dynamic vacuum (~20 mTorr).

4.2.2 Cermet Characterization

The densities of the sintered cermets were determined using Archimedes' immersion method, in water. For microstructural characterization, the cermets were initially ground flat on both sides using a diamond peripheral wheel, and then polished to a mirror-like finish (starting from a 125 μm diamond pad and finishing with 0.25 μm diamond paste). The samples were examined with optical microscopy (Model BX-51, Olympus Canada, Richmond Hill, Ontario, Canada) and scanning electron microscopy (SEM; Model S-4700, Hitachi High Technologies, Tokyo, Japan). The mean carbide grain size, d_c, was determined using the linear intercept method, from the digital SEM images, with a minimum 300 TiC grains measured per sample [29]. The contiguity values of each of the samples, C, were measured by counting the numbers of carbide/carbide ($N_{c/c}$) and carbide/binder ($N_{c/b}$) interfaces intercepted through horizontal lines on the digitized microstructural images, and determined following [30]:

$$C = \frac{2N_{c/c}}{2N_{c/c} + N_{c/b}} \qquad \text{Equation 4.1}$$

where $N_{c/c}$ and $N_{c/b}$ are the number of carbide-carbide and carbide-binder interfaces intercepted, respectively [28]. Based on information obtained for both the carbide grain size and contiguity, the binder mean free path (MFP), d_b, was then determined following [30]:

$$d_b = \frac{1}{1-C}\left(\frac{V_b}{V_c}\right)d_c \qquad \text{Equation 4.2}$$

where V_c and V_b are the volume fraction of carbide and binder. The binder MFP can be viewed as a measure of the dimensions of the metallic ligaments separating the carbide grains.

Compositional analysis of the cermets was performed in the SEM using energy-dispersive X-ray spectroscopy (EDS; Model Inca X-Max^N, Oxford Instruments, Abingdon, UK). X-ray diffraction (XRD; Model Bruker D-9 Advance) was used to examine the crystalline phases present in the samples, using a Co source to minimize Fe fluorescence. To assess the sub-surface structure of specific TiC grains, a focused ion

beam (FIB) microscope was used (Model 2000-A, Hitachi High Technologies, Tokyo, Japan), which utilizes Ga ions to 'micro-machine' the surface at site-specific locations.

4.3 Results and Discussion

4.3.1 Basic Cermet Microstructure

As shown in Figure 4.1, the TiC-316L stainless steel cermets sintered at 1475ºC for 15 minutes (i.e. fine-grained) had achieved densities in excess of 95 % of the theoretical estimates. The theoretical density was calculated using a simple rule of mixtures, based on the nominal volume fractions of the TiC and 316L stainless steel phases and their respective densities. The melt-infiltration/sintering procedure itself results in densification arising from two primary contributions, namely simple infiltration of the available porosity by the molten steel alloy and, perhaps more importantly, liquid phase sintering. In particular, when low binder contents are employed (i.e. 5 vol.%), the liquid phase sintering contribution is significant (leading to particle rearrangement, and dissolution/re-precipitation mechanisms), as pore filling alone would leave >30 vol.% porosity (the initial TiC preforms exhibit ~40 vol.% porosity after compaction).

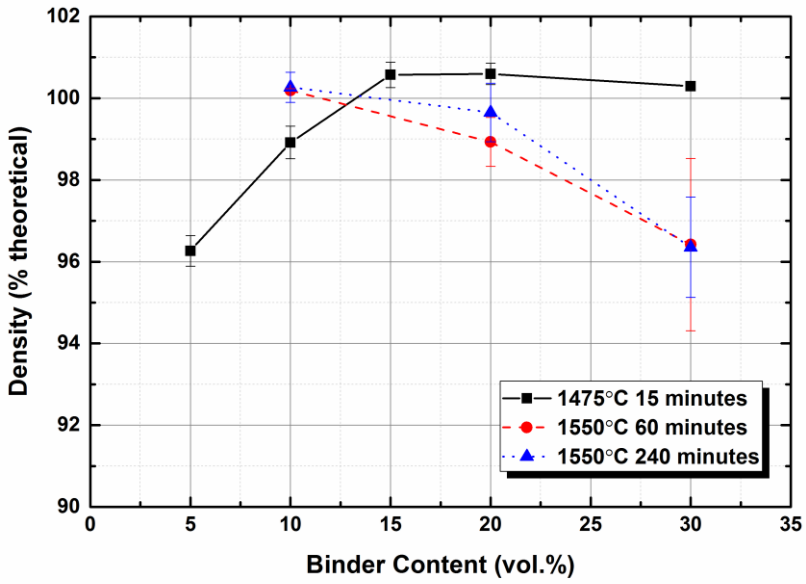

Figure 4.1: The effects of binder content and sintering temperature on the density of the cermets.

It is clear from Figure 4.1 that some densities have apparently exceeded 100 % of theoretical. This is, of course, based on the assumption that there are no compositional changes for either phase. As will be demonstrated in the following sections, compositional modifications do arise in terms of both of the constituent phases. It is also apparent in Figure 4.1 that the cermets prepared at 1550ºC, for both intermediate and coarse TiC structures, have apparently decreasing densities as the binder content is increased. It is proposed that this results from two factors, namely the compositional modification alluded to in the previous paragraph (discussed in greater detail in the following section (*Core-rim Structure and Binder Modification*)), and also through some limited degree of sample volatilization. In terms of the sintered samples, preferential volatilization of the steel binder phase would result in apparently decreased densities, as the higher density component is partially removed; consequently, the effective theoretical density will be lowered with less steel present. Looking specifically at the samples sintered at 1550 ºC for 240 minutes (coarse-grained TiC), the sintering weight losses recorded for 10 vol.% 316L binder were in the range of 1.2 to 1.5 wt.%, while the weight

loss increases to 2.0 to 3.0 wt.% for 20 vol.% 316L, and 4.0 to 5.0 wt.% for the highest 316L content (i.e. 30 vol.%).

In terms of the crystalline phase analysis, XRD spectra for the fine-grained cermets samples are presented in Figure 4.2, for 10 to 30 vol.% 316L content. The XRD demonstrates both a TiC-based ceramic phase and an Fe-based metallic phase to be present, with the metallic phase maintaining the austenitic structure after sintering. Not surprisingly, with an increase in the binder content, the intensity of the iron-based 'metal' phase slightly increases. No other intermediate or reaction phases were observed.

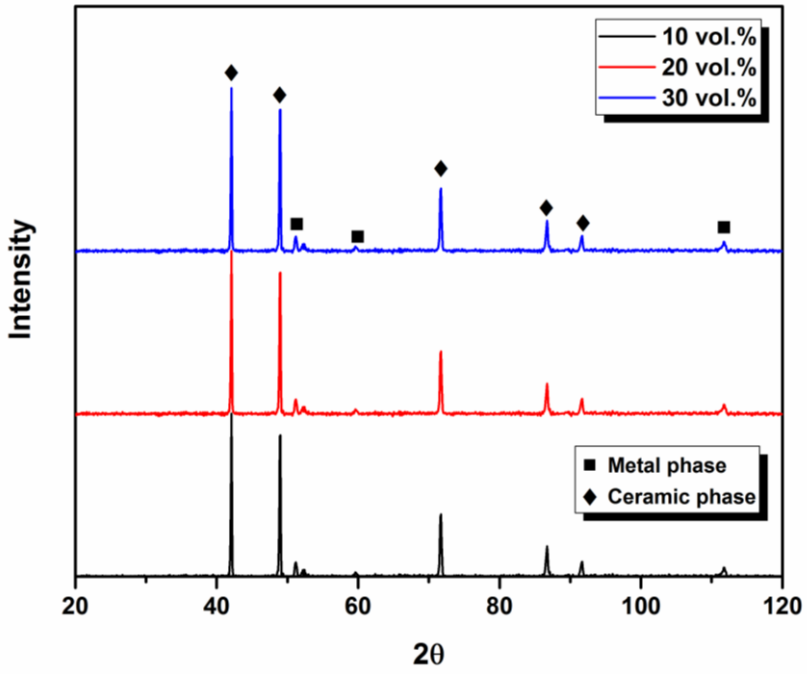

Figure 4.2: Representative XRD spectra obtained for the fine-grained cermets.

To assess the microstructure of the cermets, representative SEM images were primarily taken using back-scattered electrons (BSE), in order to highlight atomic number compositional contrast. Figure 4.3 shows the comparison of different sintering conditions for TiC cermets with the same 316L binder content (10 vol.%), together with the measured grain size distributions obtained under each condition. It can be seen that microstructures reveal a homogenous distribution of the TiC grains, and the cermets are essentially fully densified by melt infiltration. It is particularly apparent that a 'core-rim'

structure has arisen for the TiC grains sintered under the most extreme conditions, as shown in Figure 4.3 (c). In this instance the dark cores are surrounded by a slightly brighter inner rim phase, and a darker outer rim phase. Occasionally, some of the cores appear to be in direct contact with the liquid binder phase. From a microstructure point of view, the formation of the core-rim structure can enhance the wear resistance [31]. The formation mechanism for the core-rim structure in the present materials is discussed in detail in the following section (*Core-rim Structure and Binder Modification*).

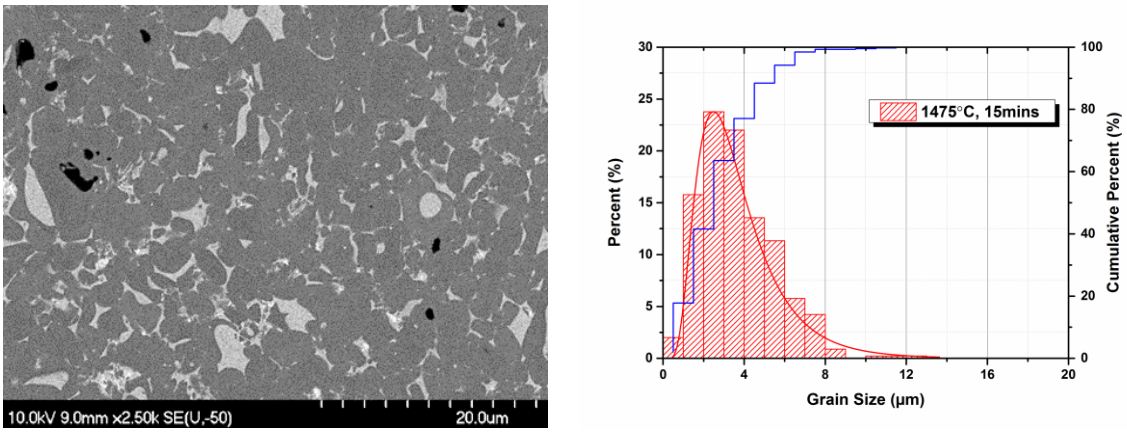

(a)

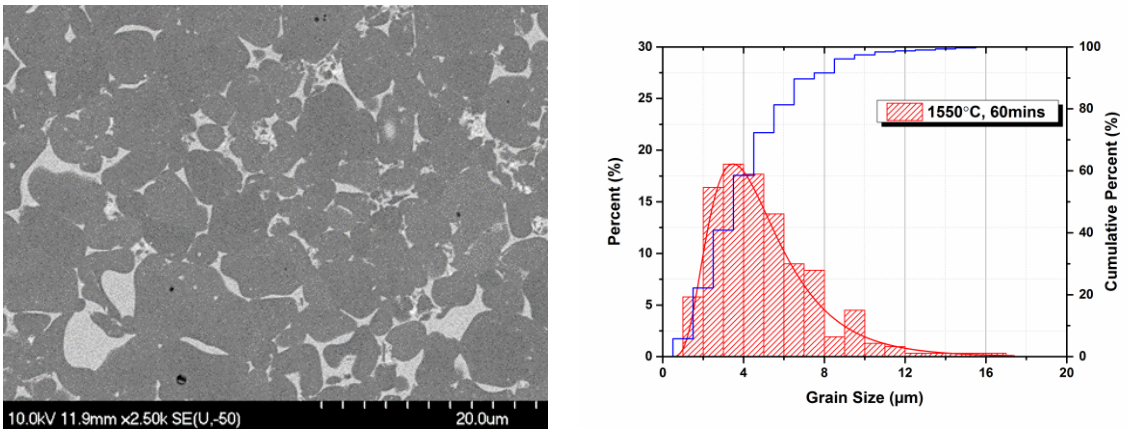

(b)

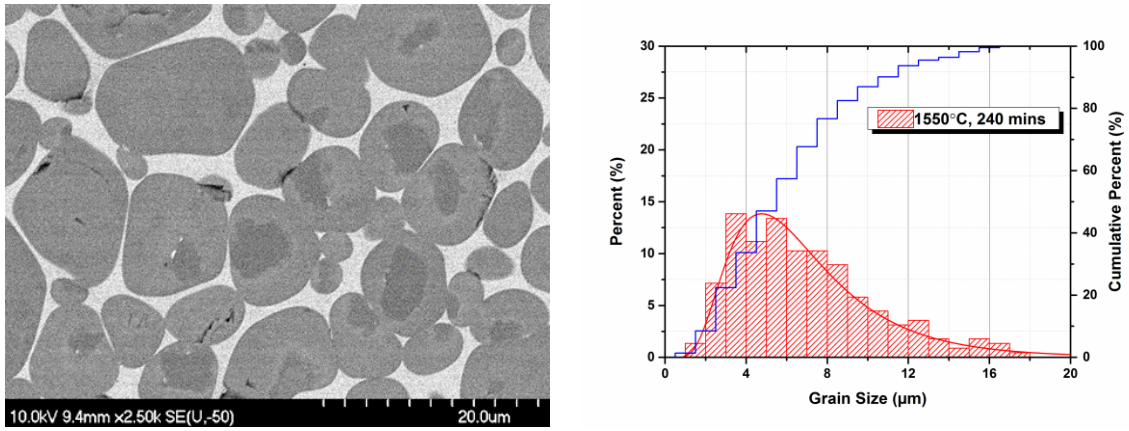

(c)

Figure 4.3: Representative SEM images of TiC cermets with 10 vol.% 316L binder content, and corresponding grain size distributions, for samples sintered at: (a) 1475°C/15 minutes (fine), (b) 1550°C/60 minutes (intermediate), and (c) 1550°C/240 minutes (coarse).

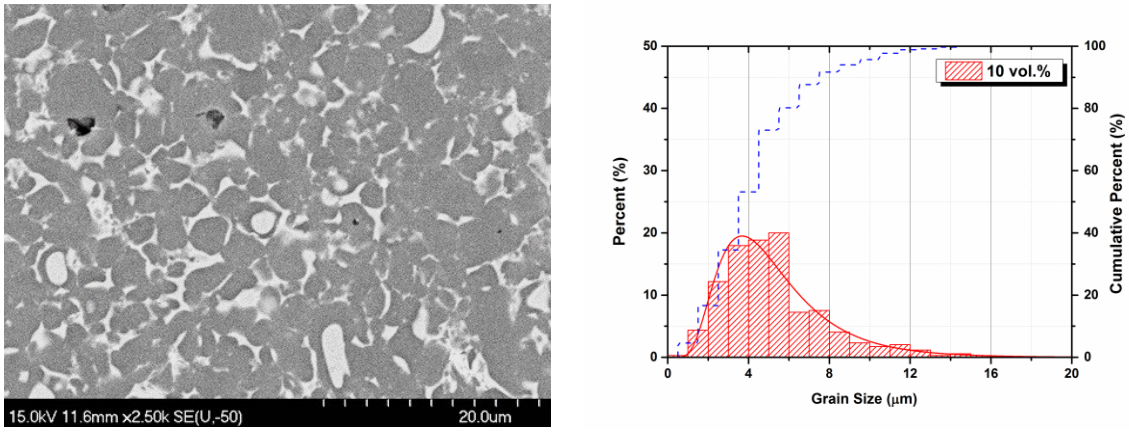

(a)

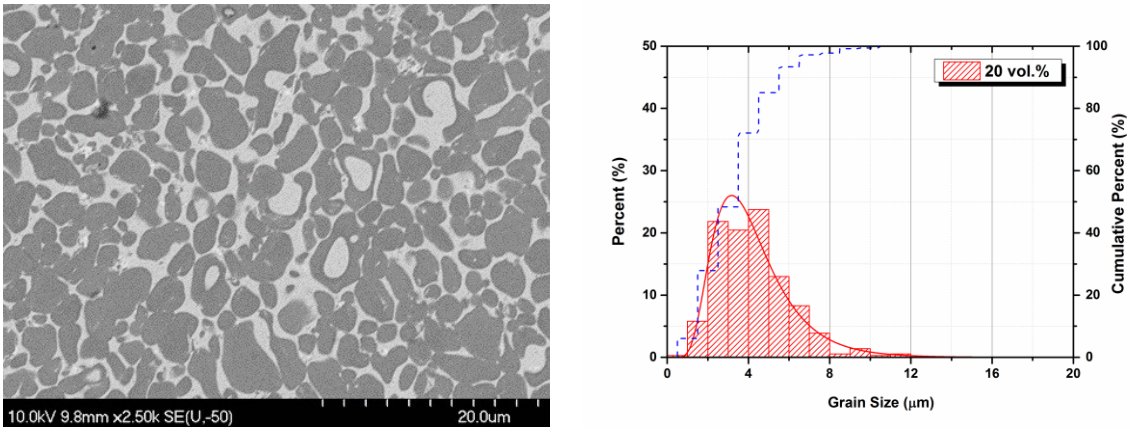

(b)

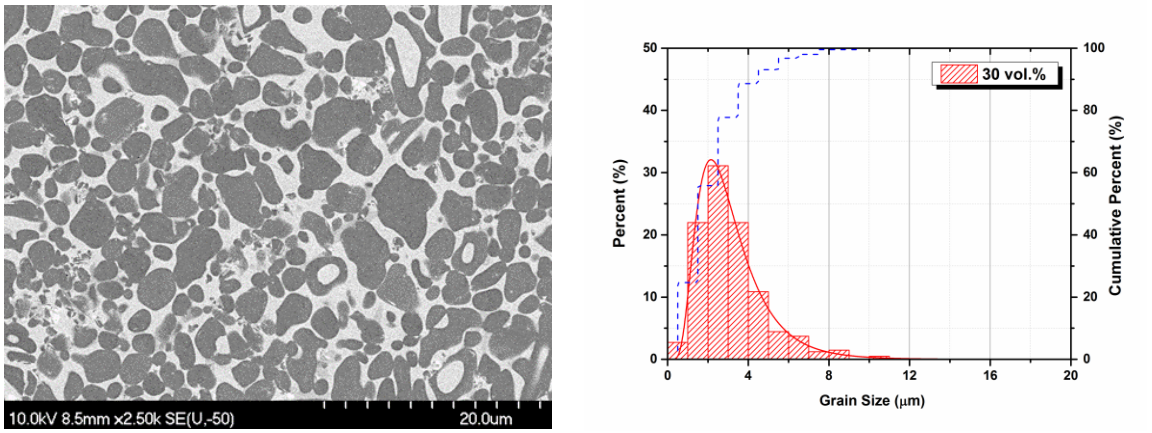

(c)

Figure 4.4: Representative SEM images of the fine-grained microstructures, and corresponding grain size distributions, for TiC cermets with 316L binder contents of: (a) 10 vol.%, (b) 20 vol.% and (c) 30 vol.%.

It can be observed that for the fine-grained structures (Figure 4.4), sintered at 1475°C/15 minutes, the morphology of the carbide grains is more irregular, rather than forming a facetted or spherical grain were the solid-liquid interface energy is minimized [19]. A moderate number of grains are present with either a 'C-shape' or 'O-shape' morphology; the O-shaped grains effectively have liquid trapped inside, which corresponds with some previous reports [19,25]. For the intermediate- and coarse-grained structures there were relatively few C-shape and O-shape grains observed, and the carbide phase is far more spherical in shape, indicating a minimization of the solid-liquid interfacial energy. The unusual concave shapes of the grains are very unstable from an energy point of view, and have been explained by the 'instability of solid-liquid interface' theory, which has been studied by a number of authors [32-35]. It is well established that the chemical free energy and interfacial energy are reduced through the dissolution and re-precipitation process of liquid-phase sintering (i.e. Oswald ripening), eliminating small grains with a high surface area and growing the large ones [19]. It was suggested that formation of equilibrium-shaped grains is inhibited when the dissolution rate on specific planes of the TiC particles are increased [19]. For the TiC-Fe system it was proposed that diffusion of Fe in the TiC particles would induce a thin layer of coherent strain at the dissolving surface, developing a tensile stress on the layer [19]. A later study of the TiC-Mo-Ni system [25], reported a similar instability during sintering. Due to the development of the negative curvature, it

was indicated that the increase in interfacial area causes the opposite effect of interfacial minimization, therefore the material transfer within a single grain plays a more important role than material transfer between grains [25]. In terms of confirming their actual morphology, selected O-shaped grains were sectioned *in-situ* within the FIB microscope, and then examined in the SEM. While these grains give the appearance of having the 316L melt phase trapped inside (i.e. creating the O-shaped morphology), it is possible that this is simply an artefact of the sectioning angle, with the grains actually exhibiting a 'cupped' shape (i.e. sectioning nominally at 90° to the C-shaped grains). Figure 4.5 presents an SEM image of a FIB cross-section of a TiC grain that initially appeared to be O-shaped (on the polished surface), which demonstrates that some of these grains are actually C-shape in nature. While this is not an exhaustive assessment of this morphology, several other FIB sectioned examples also showed a similar C-shaped structure below the surface.

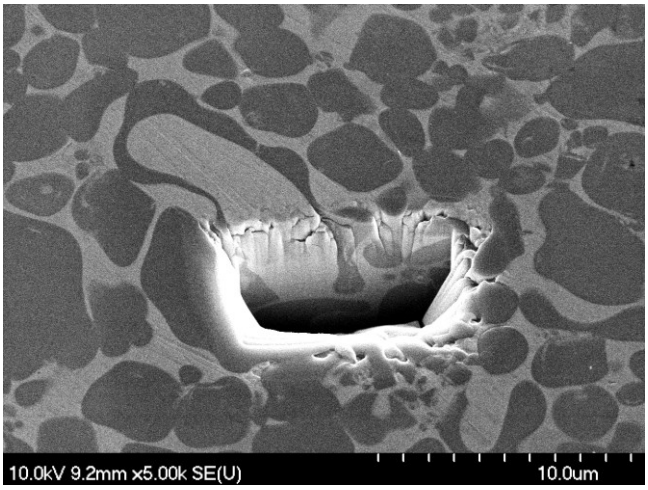

(a)

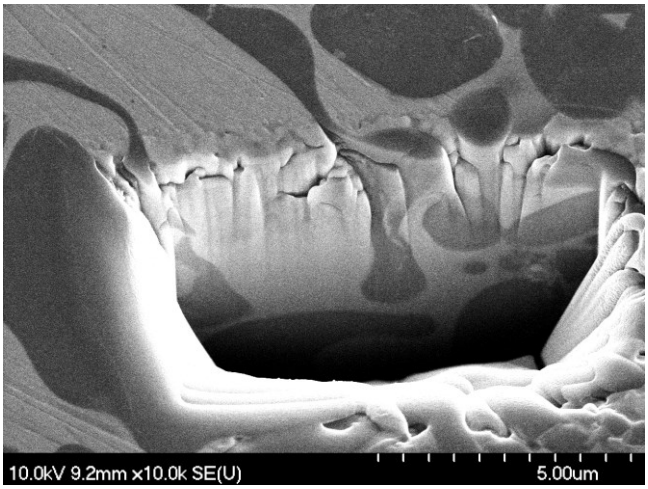

(b)

Figure 4.5: (a) Representative example SEM image of an O-shaped TiC grain following FIB micro-sectioning. (b) Higher magnification image of the grain showing an overall C-shape below the surface.

The grain size distributions, presented previously in Figure 4.3 and Figure 4.4, exhibit good fits to a logarithmic Gaussian distribution, which is common in both hardmetals and cermets [36,37]. With the increasing temperature and duration of the sintering process, there is appreciable growth of the TiC particles (Figure 4.3), and the grains become more rounded, with far fewer irregularly-shaped grains in the microstructure. It can also noted that there is less grain coalescence in the intermediate- and coarse-grained cermets. The logarithmic Gaussian distribution indicates there is no discontinuous grain growth occurring [36,37], although the size distribution becomes progressively broader, which is in agreement with previous studies [37]. Based on the data presented in Figure 4.3 and Figure 4.4, it can be concluded that the microstructural evolution of the grains is essentially uniform, and there is no evidence for abnormal grain growth.

It is important to characterize the various microstructural parameters of the cermets, as they give an indication of how the mechanical properties of the materials will be affected. For example, the hardness and toughness are, in part, related to the binder MFP dimension. In addition, the properties are dependent upon the ceramic phase particle size for a fixed ceramic-binder composition [38]. It has been noted that the hardness can be described by a modified rule of mixtures, although other parameters also need to be considered, and the fracture toughness is dependent on the binder mean free path [39]. In

Figure 4.6 (a) the mean grain sizes for the cermets are summarized, as a function of the 316-L stainless steel content, for the fine-, intermediate- and coarse-grained materials. It can be seen that the mean grain size increases with increasing sintering temperature, in accordance with the observations in Figure 4.3. For the fine- and coarse-grained structures, the mean grain size is largely independent of binder content, which broadly agrees with previous studies [40,41]. There is arguably a slight decrease with an increasing binder phase content, for the fine-grained material above 20 vol.% 316L, although the effect is small. For the intermediate grains, the mean grain size increases with the increasing volume of binder phase above 15 vol.% binder. The reason for this apparent discrepancy is not clear at the present time, although it may be related to the compositional modification that arises at the higher sintering temperature (discussed in the following section (*Core-rim Structure and Binder Modification*)). Compositional modification would be expected to affect both the diffusion rates in the melt and the TiC solubility at elevated temperatures.

The effects of processing variables on the contiguity and binder MFP of the cermets are presented in Figure 4.6 (b) and (c). The contiguity is a measure of the degree of contact between the hard ceramic particles [30], and is dependent on the fraction of binder content and the sintering conditions. The contiguities of the cermets are decreased with the increasing amount of binder, as expected, indicating less contact between the hard phase particles. It can also be expected that the hardness of the material will decrease as the contiguity decreases, as there is less load transfer between the high elastic modulus carbide particles. The contiguity also gives information on the interactions between the carbide and the binder phase, since reaction(s) will have occurred when the core-rim structure forms, and coarsening of the grains arises during the dissolution/re-precipitation Ostwald ripening process [39]. The binder mean free path is a measure of the characteristic binder ligament thickness between the carbide grains, and influences many of the mechanical properties (e.g. strength, indentation hardness and fracture toughness [30], since the mean free path is associated with the distance a dislocation can move in the metallic phase. In the current study, the binder mean free path increases with binder content, indicating the fracture toughness of the cermets should also increase. Based on

the data presented in Figure 4.6 (c) it can be anticipated that the coarse-grained cermets would have a higher value of the fracture toughness than the finer-grained materials.

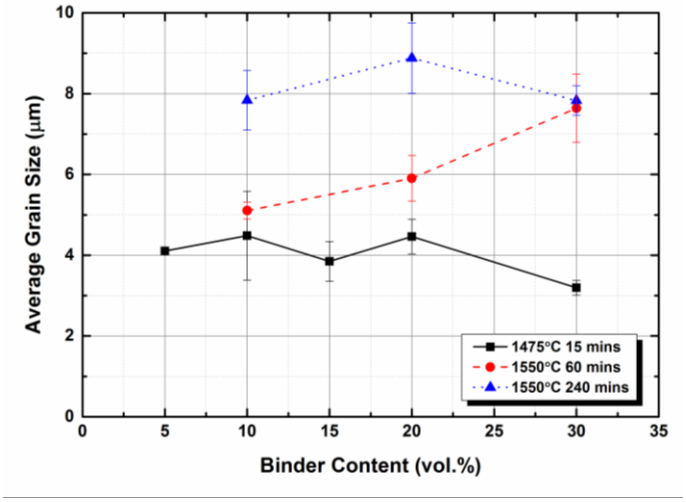

(a)

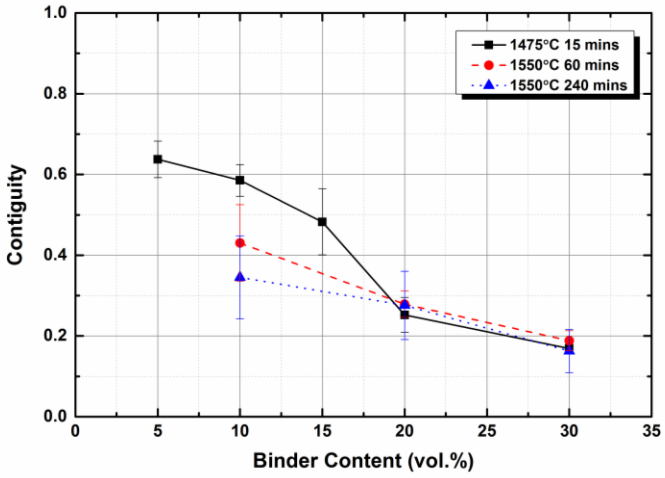

(b)

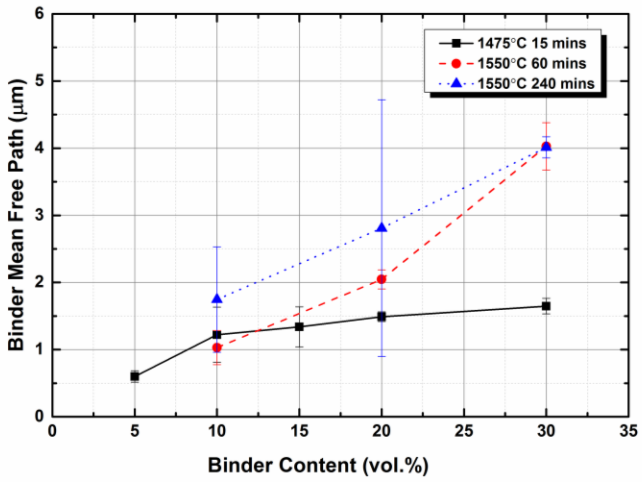

(c)

Figure 4.6: Microstructure analysis of the fine-, intermediate-, and coarse-grained TiC-316L cermets: (a) mean grain size, (b) carbide grain contiguity, and (c) binder MFP.

4.3.2 Core-rim Structure and Binder Modification

The addition of Mo or molybdenum carbide (Mo_2C) is known to improve the melt wettability during liquid phase sintering of TiC and Ti(C,N) based cermets, when using binders based on Ni alloys [20,21]. These additions also often generate a core-rim structure within the cermet [20,21,24,42,43]. It has generally been proposed that this core-rim structure arises as a result of dissolution of the carbide(s), with the dissolved material then re-precipitated onto the larger TiC or Ti(C,N) particles. The formation of a core-rim grains can significantly influence the properties of the materials [12,24]. As a consequence, a number of studies have been conducted to better understand the formation of the core-rim morphology in TiC and Ti(C,N) based cermets [24,44]. However, comparable studies on Fe-based binders are relatively scarce. A recent investigation by Guo and colleagues assessed the effects of Mo_2C additions on the microstructure and properties of Ti(C,N)-Fe cermets [26]. It was noted that Mo_2C improves both the wetting and mechanical response in this system, and also leads to the generation of a core-rim structure in the Ti(C,N) grains.

As shown in Figure 4.7, a moderately complex, core-rim structure can be generated in the present TiC-316L cermets; the corresponding EDS point analyses (in wt.%) for the

regions identified in Figure 4.7 are summarized in Table 4.3. The morphology of the TiC grains includes two rim regions, and additional areas of high atomic number contrast. It is apparent that these light contrast areas (region '3') exhibit a W-rich composition at the boundary with the core, which is often observed when W is present in the cermet composition [24,45]. W is not deliberately added in the present materials, and it is believed to arise from contamination of the TiC during the commercial preparation process, as confirmed through the chemical analysis of the starting TiC powder (Table 4.1). EDS analysis shows that the grain cores are essentially pure TiC, whereas the rim contains small amounts of Cr and Mo (Table 4.3), which were originally present in the stainless steel starting powder (Table 4.2). The current study confirms observations from prior work that the Ti is primarily detected within the grains, especially in the cores, while a small amount of Fe can be found in the grain rim but it mostly remains in the binder [46]. However, the Mo has clearly diffused into the rims as they are deposited onto the grain cores. In fact the Mo is predominantly found in the 'inner-rim' region, consequently depleting Mo from the binder phase. Both the dark and light rim regions of the grain contain some Mo, which could have an effect on the crack propagation [47]. ICP-OES tests have confirmed that the 316-L stainless steel powder initially contains approximately 2.21 wt.% of Mo, in accordance with standard specifications for this alloy. From the EDS data presented in Table 4.3 (relating to Figure 4.7), the analyses at both position '1' (rim) and '4' (binder) indicate that essentially all the Mo has diffused into the rim phase, and negligible Mo is retained in the binder. It should also be noted that, in relation to the weight losses observed for the more extreme sintering conditions (discussed previously in Section 3.1: *Basic cermet microstructure*), there is a very small decrease in the nominal Cr content of the steel binder. After processing at 1550°C/4 h, a mean Cr content of 14.6 (+/- 0.36) wt.% was determined for the 30 vol.% steel sample (which shows the highest weight loss under these sintering conditions). This is a moderate decrease from the starting content Cr content of ~16.8 wt.%, but a small Cr content was also detected in the rim of the TiC grains, as noted in Table 4.3.

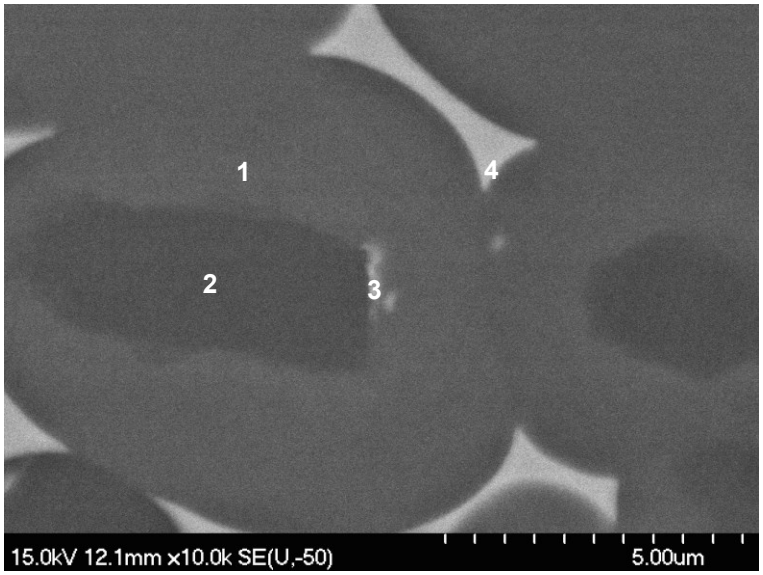

Figure 4.7: EDS point analysis regions for a core-rim grain in the 10 vol.% binder content, coarse-grained TiC-based cermet.

Table 4.3: EDS point analysis data for a 10 vol.% coarse grain cermet, for the areas previously highlighted in Figure 4.7.

Position	**Element concentration (wt. %)**							
	C	**Ti**	**Cr**	**Fe**	**Ni**	**Mo**	**W**	**Total**
1	22.16	72.02	0.72			2.36	2.75	100.00
2	20.01	79.99						100.00
3	20.02	69.22					10.76	100.00
4	7.44	13.56	7.26	54.95	16.80			100.00

In order to further understand the sintering mechanism(s) of the materials, cermets prepared at 1550ºC for 60 minutes, with binder phase contents of 15 and 30 vol.%, were compositionally assessed in more detail. As with the example in Figure 4.7, clear core-rim structures were formed, with a light contrast ‘inner’ rim and darker ‘outer’ rim. Points were selected in the cores, binder, inner rim and outer rim, in order to obtain the representative chemical compositions; mean values for each area type were then calculated, and these are summarised in Table 4.4. For the cermets with a binder content of 15 vol.%, qualitatively, a higher content of irregularly shaped TiC grains were observed, and the cores are often located on the negative curvature side of the grains. The

cermets with the higher binder content (i.e. 30 vol.%) reveal a more spherical shape to the grains, and the cores are often fully surrounded by the rims. This observation can be explained in terms of the *relative* solubility of the core and the rim phase. It is proposed that in this instance the cores are more soluble than the rim, and consequently preferential dissolution has caused the direct contact of the core to the metal binder. In a previous study examining the 'instability of the solid-liquid interface' phenomena [25], which is broadly similar to the current work, a comparable structural evolution was developed. Several theories were used to explain the microstructure evolution, including substitutional diffusion of Mo into TiC [22,38], precipitation of supersaturated melts [48], and dissolution of small grains into the liquid and re-precipitation on the large ones (Ostwald ripening) [49,50]. It has been suggested that the formation of a core-rim structure is mainly controlled by the dissolution of finer TiC grains into the melt, with material then re-precipitated from the melt on to the larger, remaining TiC grains once a saturation concentration is reached. The Ostwald ripening process and the coherency strain, causing the irregular grain shapes, are then competing in this process. In this case, the direct contact of the TiC cores with the binder, and the concave interface between them also supported the proposal that precipitation from the supersaturated melts during cooling is not sufficient to form the rim [25].

Table 4.4: Results of EDS analysis for the intermediate-grained samples with 15 and 30 vol.% 316L binder. All compositions are given in wt.%, with the standard deviation errors shown in parentheses.

	Element concentration (wt.%)							
	Core		**Rim (inner)**		**Rim (outer)**		**Binder**	
	15 vol.%	**30 vol.%**	**15 vol.%**	**30 vol.%**	**15 vol.%**	**30 vol.%**	**15 vol.%**	**30 vol.%**
C	20.08 (0.33)	19.31 (0.25)	22.30 (0.35)	21.79 (0.16)	19.85 (0.81)	20.76 (0.57)	2.21 (0.86)	1.69 (0.42)
Ti	78.11 (0.56)	78.27 (0.70)	67.35 (0.73)	68.94 (0.58)	62.78 (4.55)	69.59 (3.72)	4.29 (2.13)	6.37 (1.48)
Cr	0.06 (0.13)	0.25 (0.48)	0.76 (0.09)	0.66 (0.15)	2.15 (0.69)	1.11 (0.44)	11.48 (0.77)	13.54 (0.65)
Fe	1.75 (0.29)	1.89 (0.49)	1.51 (0.43)	1.84 (0.67)	10.81 (4.31)	4.45 (3.91)	70.37 (1.22)	69.89 (0.95)
Ni	--	--	--	--	0.80 (0.86)	0.17 (0.30)	11.67 (0.57)	11.50 (0.36)
Mo	--	--	4.88 (0.48)	4.06 (0.72)	1.65 (0.83)	2.11 (0.21)	--	--
W	--	0.28 (0.48)	3.21 (0.27)	2.72 (0.54)	1.96 (0.31)	1.82 (0.18)	--	--

As noted above, Table 4.4 lists the EDS element analyses for the intermediate microstructure cermets (1550°C/60 minutes) with 15 and 30 vol.% 316-L binder, showing the mean compositions of the TiC grain core, binder, light-contrast inner rim, and dark-contrast outer rim; it should be noted that the EDS analyses can be expected to have an error of approximately 1-2 at.%. The Ti, which originally exists solely in the TiC starting powder, has a decreasing gradient from the core to the rim, and was detected in low concentrations within the binder. The Cr, Ni and Mo, from the initial 316-L stainless steel powders, are all found in the rim to a greater or lesser extent. This indicates a dissolution/re-precipitation process during the liquid phase sintering stage of the melt infiltration treatment. The relative grey scale contrast of the BSE SEM images highlights the variations in mean atomic number of the various phases and regions, and the EDS

analysis further confirms these observations. The Cr is apparently found in a small amount in the core, with increasing gradient to the binder. The majority of the Fe remains in the binder phase, with a relatively large amount also found in the outer rim. Both Ni and Mo are detected in the rim phases, although the majority of the Ni remains in the binder, and could not be found in the inner 'light' rim. Some caution needs to be made with regards to low concentrations of Ni appearing in the outer rim, as this may simply arise as an artefact of the sub-surface interaction volume during EDS analysis. It is worth noting that essentially no Mo has been left in the binder phase and, for the intermediate-grained cermets, there is a localised, higher amount of Mo in the inner rim, when compared with the outer rim. Some studies suggested that the inner rims are actually formed during the heating stage of the sintering cycle, or through solid-state sintering, while the outer rims form during the dissolution/re-precipitation stage of liquid phase sintering [21,51,52]. In a prior study focused on Ti(CN) based cermets with a core-rim structure, it was proposed that the onset of inner rim formation occurs at the sintering temperature, and that the rim phase ultimately becomes unstable and dissolves at high temperature [24]. As a consequence, the early stage microstructure that is generated will differ from the final structure and composition. The ICP-OES results presented in Table 4.1 indicate ~2.22 wt.% W is present in the raw TiC powders used in the present work. After sintering, W was confirmed to be present in the rim structure, with a slightly higher amount occurring in the inner 'light' rim.

A composition analysis was also performed using an EDS line-scan, which was drawn across the particle, starting and ending in the binder phase. In each of the analyses, 25 points were chosen, as shown in Figure 4.8 (a); given the electron beam interaction volume these will be effectively overlapping analyses. In these figures, the elements present in relatively low concentrations (i.e. Cr, Ni, Mo, W) were plotted on an expanded scale for convenient comparison (Figure 4.8 (b)), with the higher concentration elements plotted full scale (Figure 4.8 (c)). This data further confirms that the Mo is not uniformly distributed within the core-rim structure, and is instead concentrated primarily within the light 'inner rim'. This likely indicates that Mo is rapidly removed from the 316-L binder during the early stages of sintering (after 316L melting has occurred), and incorporated

into the inner rim region. The DSC and melt-infiltration experiments highlight the steel phase is molten above ~1400°C.

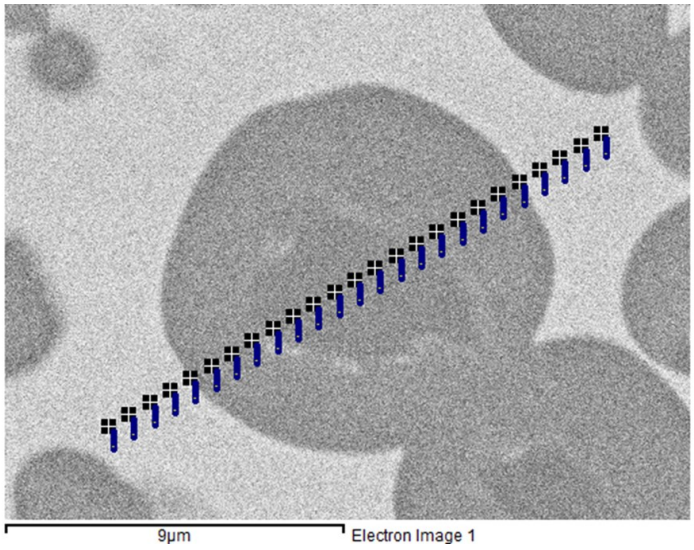

(a)

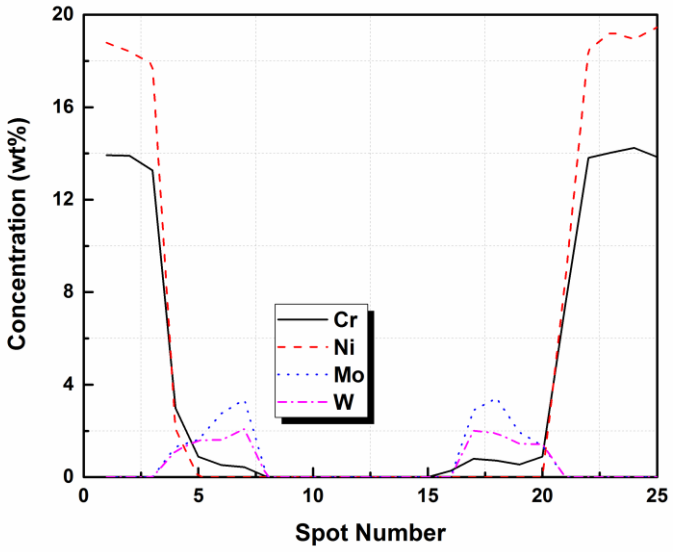

(b)

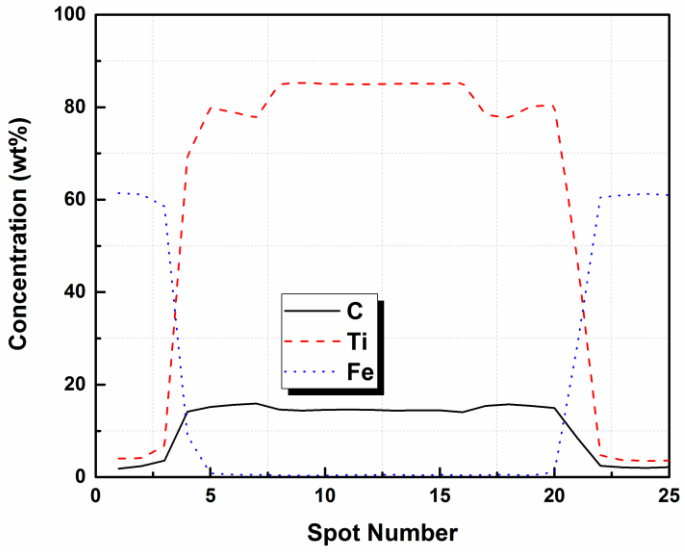

(c)

Figure 4.8: (a) Representative SEM image of an intermediate-sized TiC grain, with 15 vol.% of binder, showing the locations of EDS line profile analyses. (b,c) The EDS line profile data corresponding to the line shown in (a); note the differing concentration scale.

Based on the information that has been presented, it is possible to propose a simple model of the morphology evolution of the core-rim structure, which is illustrated by the schematic diagram presented in Figure 4.9. During the initial stages of wetting and infiltration the TiC particles are distributed in the metal binder (Figure 4.9 (a)), with the heavier element such as Mo (originally in the 316-L stainless steel) still present in the binder phase; impurity W is, at this point, confined to the surface of the TiC powder. As the temperature increases, some TiC dissolution into the melt occurs, and the heavier element such as Mo, W start to form an initial rim structure on the TiC particle cores through re-precipitation (Figure 4.9 (b)), as proposed previously for Ti(C,N) containing cermets [42]. This stage consumes much of the Mo from the 316L binder into the inner rim region. With continued sintering, Ostwald ripening is beginning to govern the process (Figure 4.9 (c)); the smaller TiC grains continue to dissolve into the liquid, reaching saturation in combination with other transition metal constituents, then re-precipitate back on to the larger TiC grain cores, generating a thin ‘outer’ rim containing additional

Cr and Ni. Finally, as proposed in Figure 4.9 (d), a complex 'core-rim' structure is generated, with a nominally pure TiC core, surrounded by an 'inner' rim with comparatively high Mo and W concentrations, and an 'outer' rim with the additional transition metal constituents. Cores are sometimes in direct contact with the binder phase, even with a relatively well developed rim, and some particles form irregular C- or O-shaped grains because of the instability during liquid phase sintering. It would be expected that the holding time (i.e. 240 minutes) would affect the growth of the grains, leading to a thicker 'outer' rim.

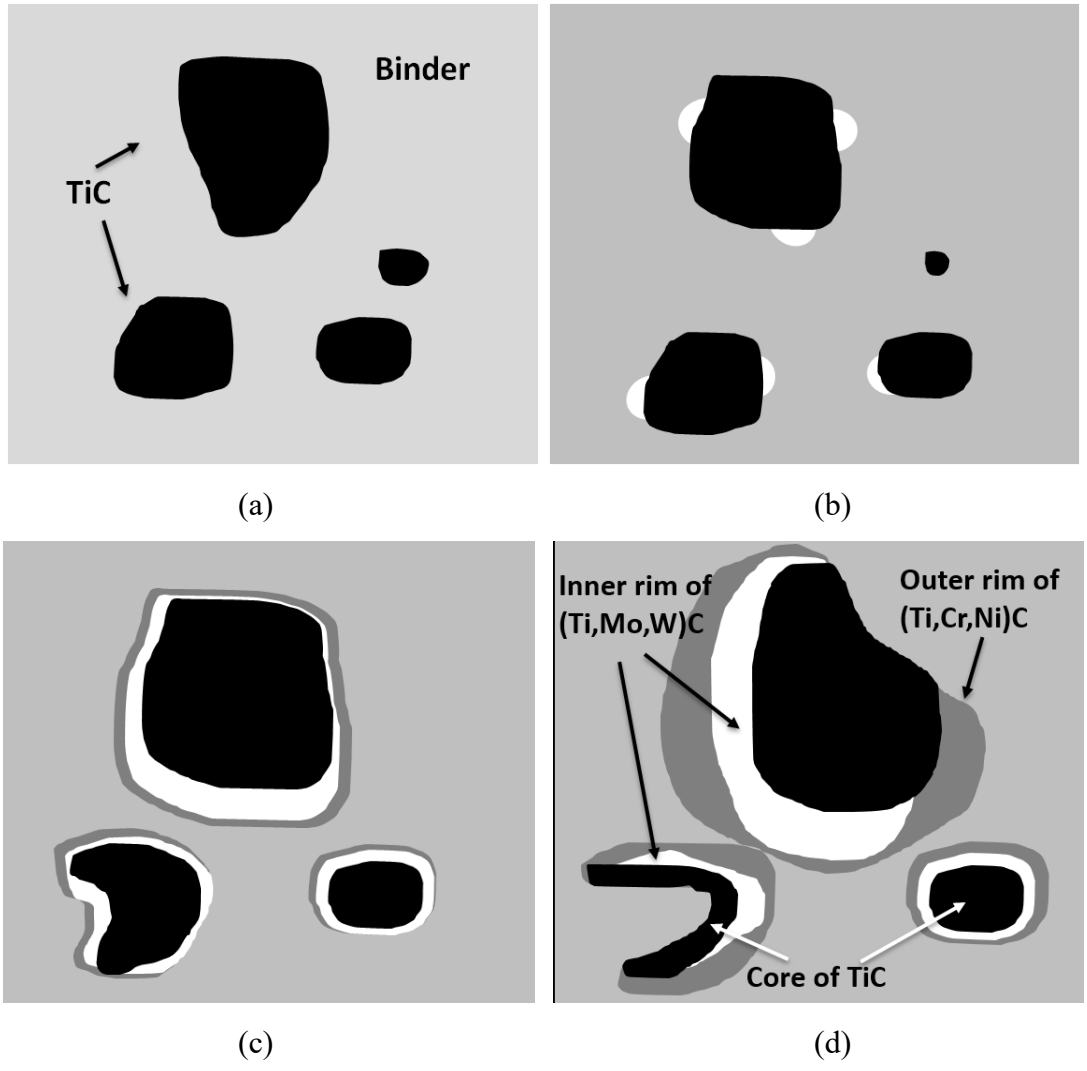

Figure 4.9: A simple schematic representation of the mechanism of multi-layer core-rim evolution.

4.4 Conclusions

In summary, TiC-316L stainless steel cermets with a range of binder contents were fabricated using a simple melt-infiltration/sintering process under three different sintering conditions. Following melt-infiltration, densities in excess of 95% of theoretical were achieved (typically close to 100%). The sintered cermets exhibit a somewhat irregular TiC grain morphology, especially at 1475 ºC for 15 minutes, with both C- and O-shaped grains present. This has been explained in terms of the 'instability of solid-liquid interface' theory. It is also shown that a complex core-rim structure has developed, which is believed to be a result of Ostwald ripening, with the dissolution of TiC into the liquid, and re-precipitation of (Ti,Mo,W)C back on to the TiC grains. The core-rim structure includes both 'inner' and 'outer' rims, which are shown to be compositionally different. The study of this specific material has indicated a competition of interfacial energy minimization and coherency strain energy during the liquid phase sintering process.

Acknowledgements

The authors would like to thank the Natural Sciences and Engineering Research Council of Canada (NSERC), for provision of funding through the Discovery Grants programme. The Canada Foundation for Innovation, the Atlantic Innovation Fund, and other partners who helped fund the Facilities for Materials Characterisation, managed by the Dalhousie University Institute for Materials Research, are also gratefully acknowledged. The authors also wish to thank Ms. Patricia Scallion for SEM and FIB assistance, and Mr. Dean Grijm for his support with sample machining.

4.5 References

1. S. Kang, Cermets, pp.139-181 in Comprehensive Hard Materials, Vol. 1 (Ed. V.K. Sarin), Elsevier Ltd., New York, 2014.
2. N. Durlu, Titanium carbide based composites for high temperature applications. J. Eur. Ceram. Soc. 19 (1999) 2415-2419.

3. H. Klaasen, L. Kollo, J. Kübarsepp, Mechanical properties and wear performance of compression sintered TiC based cermets. Powder Metall. 50 (2007) 132-136.
4. H. Klaasen, J. Kübarsepp, F. Sergejev, Strength and failure of TiC based cermets. Powder Metall. 52 (2009) 111-115.
5. K.P. Plucknett, P.F. Becher, S.B. Waters, Flexure strength of melt-infiltration processed TiC/Ni_3Al composites. J. Am. Ceram. Soc. 81 (1998) 1839-1844.
6. S. Norgren, J. García, A. Blomqvist, L. Yin, Trends in the P/M hard metal industry, Int. J. Refract. Met. Hard Mater. 48 (2015) 31-45.
7. H.O. Andren, Microstructure development during sintering and heat-treatment of cemented carbides and cermets. Mater. Chem. Phys. 67 (2001) 209-213.
8. S. Cardinal, A. Malchère, V. Garnier, G. Fantozzi, G. Microstructure and mechanical properties of TiC–TiN based cermets for tools application. Int. J. Refract. Met. Hard Mater. 27 (2009) 521-527.
9. H. Hosokawa, K. Kato, K. Shimojima, A. Matsumoto, A. Microstructures and mechanical properties of $(Ti_{0.8}Mo_{0.2})$C-30 mass% Ni without core-rim structure. Mater. Trans. 51 (2010) 1428-1432.
10. C.C. Onuoha, G.J. Kipouros, Z.N. Farhat, K.P. Plucknett, The effects of metal binder content and carbide grain size on the aqueous corrosion behaviour of TiC–316L stainless steel cermets. Int. J. Refract. Met. Hard Mater. 44 (2014) 129-141.
11. I. Hussainova. Effect of microstructure on the erosive wear of titanium carbide-based cermets. Wear 255 (2003) 121-128.
12. I. Hussainova, Microstructure and erosive wear in ceramic-based composites. Wear 258 (2005) 357-365.
13. J. Pirso, M. Viljus, S. Letunovits, Sliding wear of TiC–NiMo cermets. Tribol. Int. 37 (2004) 817-824.
14. D. Miller, Liquid-phase sintering of TiC-Ni composites. J. Am. Ceram. Soc. 66 (1983) 841-846.
15. K. Aigner, W. Lengauer, P. Ettmayer, Interactions in iron-based cermet systems. J. Alloy. Compd. 262-263 (1997) 486-491.

16. A. Farid, S. Guo, X. Yang, Y. Lian, Y. Stainless steel binder for the development of novel TiC-reinforced steel cermets. J. Univ. Sci. Technology Beijing, 13 (2006) 546-550.
17. B.W. Lograsso, R.M. German, Liquid phase sintered titanium carbide-tool steel composites for high temperature service. Prog. Powder Metall. 43 (1987) 415-439.
18. F. Akhtar, S.J. Guo, Microstructure, mechanical and fretting wear properties of TiC-stainless steel composites. Mater. Charact. 59 (2008) 84-90.
19. K.W. Chae, D.I. Chun, D.Y. Kim, Y.J. Baik, K.Y. Eun, Microstructural evolution during the infiltration treatment of titanium carbide-iron composite. J. Am. Ceram. Soc. 73 (1990) 1979-1982.
20. P. Lindahl, P. Gustafson, U. Rolander, L. Stals, H.O. Andrén, Microstructure of model cermets with high Mo or W content. Int. J. Refract. Met. Hard Mater. 17 (1999) 411-421.
21. Y.K. Kim, J. Shim, Y.W. Cho, H. Yang, J. Park, Mechanochemical synthesis of nanocomposite powder for ultrafine (Ti,Mo)C–Ni cermet without core-rim structure. Int. J. Refract. Met. Hard Mater. 22 (2004) 193-196.
22. D. Moskowitz, H.K. Plummer, Jr., Binder-carbide phase interactions in titanium carbide base systems, in: R. Viswanadham (Ed.), Science of Hard Materials, Springer-Verlag, Berlin, 1983, pp. 299-309.
23. S.Y. Ahn, S. Kang, Formation of core/rim structures in Ti(C,N)-WC-Ni cermets via a dissolution and precipitation process. J. Am. Ceram. Soc. 83 (2000) 1489-1494.
24. S. Kim, K.H. Min, S. Kang, S. Rim structure in $Ti(C_{0.7}N_{0.3})$-WC-Ni cermets. J. Am. Ceram. Soc. 86 (2003) 1761-1766.
25. D.I. Chun, D.Y. Kim, K.Y. Eun, Microstructural evolution during the sintering of TiC-Mo-Ni cermets. J. Am. Ceram. Soc 76 (1993) 2049-2052.
26. Z. Guo, J. Xiong, M. Yang, J. Wan, L. Su, Y. W, J. Chen, S. Xiong, Microstructure and properties of Ti(C,N)-Mo_2C-Fe cermets, Int. J. Refract. Met. Hard Mater. 27 (2009) 781-783.
27. R.B. Collier K.P. Plucknett, Spherical indentation damage in TiC-Ni_3Al composites. Int. J. Refract. Met. Hard Mater. 30 (2012) 188-195.

28. K.P. Plucknett, P.F.Becher, Processing and microstructure development of titanium carbide-nickel aluminide composites prepared by melt infiltration/sintering (MIS). J. Am. Ceram. Soc. 84 (2001) 55-61.
29. M.I. Mendelson, Average grain size in polycrystalline ceramics. J. Am. Ceram. Soc. 52 (1969) 443-446.
30. J. Gurland, The measurement of grain contiguity in 2-phase alloys. T. Metall. Soc. AIME (1958) 452-455.
31. J.R. Davis, General guidelines for selecting cutting tool materials, in: ASM Speciality Handbook: Tool Materials, ASM International, Materials Park, 1995, pp. 3-9.
32. D.N. Yoon, Chemically induced interface migration in solids. Ann. Rev. Mater. Sci. 19 (1989) 43-58.
33. W.H. Rhee, D.N. Yoon, The instability of solid-liquid interface in Mo-Ni alloy induced by diffusional coherency strain. Acta Metall. 35 (1987) 1447-1451.
34. S. Ahn, S. Kang, Effect of various carbides on the dissolution behavior of Ti($C_{0.7}N_{0.3}$) in a Ti($C_{0.7}N_{0.3}$)-30Ni system, Int. J. Refract. Met. Hard Mater. 19 (2001), 539-545.
35. S. Ahn, S. Kang, Dissolution phenomena in the Ti($C_{0.7}N_{0.3}$)-WC-Ni system, Int. J. Refract. Met. Hard Mater. 26 (2008) 340-345.
36. D. Mari, S. Bolognini, G. Feusier, T. Cutard, C. Verdon, T. Viatte, W. Benoit, TiMoCN based cermets Part I. Morphology and phase composition, Int. J. Refract. Met. Hard Mater. 21 (2003) 37-46.
37. N. Liu, W. Yin, L. Zhu, Effect of TiC/TiN powder size on microstructure and properties of Ti(C.N)-based cermets, Mater. Sci. Eng. A 445-446 (2007) 707-716.
38. D. Moskowitz, M. Humenik, Jr., Cemented titanium carbide cutting tools, in: H.H. Hausner (Ed.), Modern Developments in Powder Metallurgy, Development and Future Prospects, vol. 3, Springer, New York, 1966, pp. 83–94.
39. H.E. Exner, Qualitative and quantitative interpretation of microstructures in cemented carbides, in: R. Viswanadham, D.J. Rowcliffe and J. Gurland (Eds.), Science of Hard Materials, Springer-Verlag, Berlin, 1983, pp. 233-262.
40. C.C. Onuoha, G.J. Kipouros, Z.N. Farhat, K.P. Plucknett, K. P. The reciprocating wear behaviour of TiC–304L stainless steel composites prepared by melt infiltration. Wear 303 (2013) 321-333.

41. K.P. Plucknett, P.F. Becher, Processing and microstructure development of titanium carbide-nickel aluminide composites J. Am. Ceram. Soc. 84 (2001) 55-61.
42. P.P. Li, J.W. Ye, Y. Liu, D.J. Yang, H.J. Yu, Study on the formation of core–rim structure in Ti(CN)-based cermets. Int. J. Refract. Met. Hard Mater. 35 (2012) 27-31.
43. N. Liu, Y.D. Xu, Z.H. Li, M.H. Chen, G.H. Li, L.D. Zhang, Influence of molybdenum addition on the microstructure and mechanical properties of TiC-based cermets with nano-TiN modification. Ceram. Int. 29 (2003) 919-925.
44. H. Kwon, S. Kang, S. Microstructure and mechanical properties of TiC–WC–(Ti,W)C–Ni cermets. Mater. Sci. Eng. A 520 (2009) 75-79.
45. Y. Li, N. Liu, X.B. Zhang, C.L. Rong, Effect of Mo addition on the microstructure and mechanical properties of ultra-fine grade TiC-TiN-WC-Mo_2C-Co-cermets. Int. J. Refract. Met. Hard Mater. 26 (2008) 190-196.
46. L.E. Murr, Interfacial phenomena in metals and alloys, Addison-Wesley Publishing Company, Reading (1975).
47. I. Hussainova, A. Kolesnikova, M. Hussainov, A. Romanov, Effect of thermo-elastic residual stresses on erosive performance of cermets with core–rim structured ceramic grains. Wear 267 (2009) 177-185.
48. H. Suzuki, K. Hayashi, O. Terada, Mechanisms of surrounding structure formation in sintered TiC-Mo_2C-Ni alloy. J. Jpn. Inst. Metal. 35 (1971) 936-942.
49. O. Rodiger, O., H.E. Exner, Application of basic research to the development of hard metals. Powder Metall. Int. 8 (1976) 7-13.
50. L. Lindau, K.G. Stjemberg, Grain growth in TiC-Ni-Mo and TiC-Ni-W cemented carbides. Powder Metall. 19 (1976) 210-213.
51. J.K. Yang, H. Lee, Microstructural evolution during the sintering of a Ti(C,N)-Mo_2C-Ni alloy. Mater. Sci. Eng. A 209 (1996) 213-217.
52. J. Zackrisson, H. Andren, Effect of carbon content on the microstructure and mechanical properties of (Ti,W,Ta,Mo)(C,N)–(Co,Ni) cermets. Int. J. Refract. Met. Hard Mater. 17 (1999) 265-273.

Chapter 5 The Effect of Microstructure on Vickers Indentation Damage in TiC-316L Stainless Steel Cermets

Chenxin Jin, Kevin Plucknett

Dalhousie University, 1360 Barrington Street, Materials Engineering, Department of Process Engineering and Applied Science, B3H 4R2, Nova Scotia, Canada

Status: *Submitted*: International Journal of Refractory Metals and Hard Materials

Abstract

Titanium carbide (TiC) based cermets are commonly used as wear resistance and corrosion resistance components. In the present work, the effects of microstructure of TiC-316L stainless steel cermets are assessed in terms of Vickers indentation damage, with both the steel binder content and TiC grain size varied. Binder contents from 5 to 30 vol. % were examined, with samples fabricated using a simple vacuum melt-infiltration procedure at temperatures between 1475°C and 1550°C (held for up to 240 minutes). Two primary Vickers indentation-cracking patterns arise in these materials, namely median or Palmqvist cracks, and this response relates to both the volume fraction of ductile metal binder present and the binder ligament dimension. Focused ion beam microscopy has been utilised for sub-surface evaluation of the cracks, to confirm the anticipated crack patterns.

Keywords: Vickers hardness; indentation size effect; indentation fracture resistance; Palmqvist cracking; scanning electron microscopy

*Contact author: kevin.plucknett@dal.ca

5.1 Introduction

Cermets are composite materials that combine a high volume fraction of hard but brittle ceramic particles with a ductile metallic binder, which helps to impart toughness in the composite. Compared with conventional 'hardmetals', such as tungsten carbide-cobalt (WC-Co), cermets are lighter in weight with high strength and toughness, combined with excellent wear and corrosion resistance [1-3]. Due to its high melting point and low density, titanium carbide (TiC) based cermets are used in a variety of industries. Common examples of the metallic binder phase utilised for TiC-based cermets include Ni, Co and Fe alloys [4,5]. While the mechanical properties of these traditional cermet system have been studied relatively widely, there has been comparatively little assessment of TiC-based cermets with stainless steel binders [6]. With this in mind, indentation testing is one of the most convenient ways to assess a material's mechanical properties, and is particularly relevant for scenarios where impact damage may arise from impact damage by foreign objects. For 'brittle' ceramics and cermets, it is typical to employ Vickers indentation, which allows determination of the hardness and indentation fracture resistance (IFR).

The fracture toughness of a material is an important property that effectively describes the 'resistance' to fracture. A number of experimental techniques are available to determine the fracture toughness, including single-edge notched beam (SENB), single-edge V-notched beam (SEVNB), chevron-notch (CN), and double-cantilever-beam (DCB) tests, etc. [7]. The Vickers IFR test has also found broad usage for this purpose, and it can be regarded a convenient way to estimate the toughness using relatively small samples [8]. Evans and Charles [9] originally proposed the concept of indentation fracture toughness in the mid-1970s, and there have been extensive subsequent studies on using this method for evaluating the fracture toughness of brittle materials. As a consequence, numerous equations have been developed to estimate the toughness based on Vickers indentation.

The Vickers indentation technique was introduced to determine fracture toughness values through characterising the crack patterns. Among the different crack patterns generated, there are two types that generally viewed as the most important, the fully developed

median/radial crack (i.e. 'halfpenny') and the Palmqvist crack (Figure 5.1). It has been demonstrated that cracks are generated for a wide range of contact loads, and Palmqvist cracks are often not of the ideally elliptical shape inferred in Figure 5.1(b), and the cracks may actually penetrate deeper than the indentation itself [10]. It has been experimentally shown that, at low loads, the cracks tend to only remain at the surface, and transform into median cracks at high loads [11].

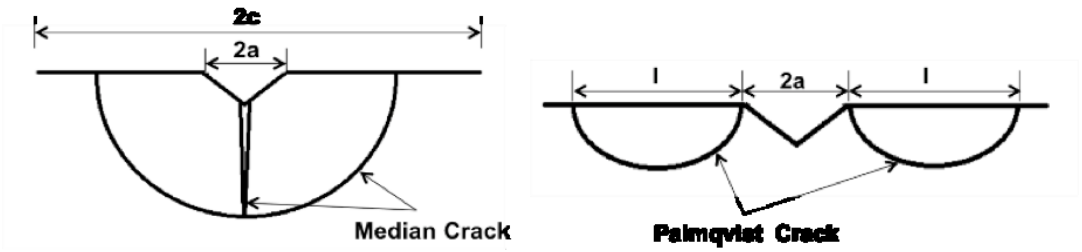

(a) (b)

Figure 5.1: Schematic figures of (a) the median crack system and (b) the Palmqvist crack system.

The aim of the present work was to study the effects of microstructure on the indentation response of a range of TiC-stainless steel cermets. The indentation size effect (ISE) was investigated by applying both Meyer's law and the proportional specimen resistance (PSR) model. The Vickers IFR was also analysed, not to prove the validity of the test, but rather as a predictive approach for determining the crack system generated. IFR values were then calculated using various models, with the associated sub-surface crack systems that were generated studied using a focused ion beam (FIB) milling technique.

5.2 Experimental Procedure

5.2.1 Sample Preparation and Microstructure Assessment

The TiC powder used for cermet preparation was sourced from Pacific Particulate Materials Ltd. (Vancouver, BC, Canada), with a quoted particle size of ~1.3μm. The austenitic stainless steel powder (grade 316L) to be used for the binder phase was obtained from Alfa Aesar (Ward Hill, MA, USA), and had a nominal particle size of -100

mesh. For cermet fabrication, TiC pellets were first formed by uniaxial compaction of ~7.35 g of TiC powder in a hardened steel die of 31.75 mm in diameter at ~45 MPa. The pellets were then further compacted by cold isostatic pressing at ~208 MPa. A simple melt infiltration sintering procedure was then used to fabricate the cermet test samples. The compacted TiC pellets are placed in an alumina crucible on a bed of bubble alumina, with different amounts of the steel binder, ranging from 5 to 30 vol.%, placed carefully on top the samples. The combined melt infiltration sintering cycle was then conducted at temperatures of 1475ºC (held for 15 minutes) to get fine grains, 1550ºC (for 60 minutes) to get intermediate grains, and 1550ºC (for 240 minutes) to get coarse grains. A heating rate of 10ºC/min and cooling rate of 25ºC/min were used for all experiments, under a dynamic vacuum (20 mTorr), inside a graphite resistance furnace (Materials Research Furnaces, Suncook, NH, USA).

The densities of the sintered cermets were calculated using Archimedes' immersion method in water; all samples reached a nominal density exceeding 95% of the theoretical values. The cermets were then ground flat on both sides using a diamond peripheral wheel, and polished to a mirror-like finish (starting from 125 μm diamond pad and finishing up with 0.25 μm diamond paste). Microstructural characterisation of the densified cermets was conducted using both optical microscopy (OM; Model BX-51, Olympus Canada, Richmond Hill, Ontario, Canada) and scanning electron microscopy (SEM; Model S-4700, Hitachi High Technologies, Tokyo, Japan). The SEM is equipped with both an upper, 'in-column' ExB electron detector (to which a bias can be applied for observation of solely back-scattered electrons (BSE)) and a lower, off-axis Everhart-Thornley detector that allows greater observation of topographic features.

5.2.2 Vickers Indentation Assessment

Vickers indentation was conducted using a pyramidal diamond indenter, with loads of 1, 5, 10, and 30 kgf, holding under load for 15 seconds (Model V-100A, Leco, St. Joseph, MI, USA). To determine the mean hardness, a minimum of 5 indents were made per load per sample, following the ASTM standard [12], and the indent sizes were then confirmed

by OM and SEM. The Vickers hardness, in GPa, was computed using following equation [12]:

$$HV = 0.0018544(\frac{P}{d^2}) \quad \text{Equation 5.1}$$

where P is the load (N), and d (mm) is the average length of the two diagonals of the indentation. The Vickers hardness number is also computed, using the following equation [12]:

$$HV = 1.8544(\frac{P}{d^2}) \quad \text{Equation 5.2}$$

The IFR was determined for the cermets using various applied loads of 1, 5, 10 and 30 kgf, with at least 5 indents measured per load per sample. Depending upon whether median or Palmqvist-type cracking was observed, the IFR values were then calculated using either the Anstis *et al.* [13] or Shetty *et al.* [14] approach. The transition between median/Palmqvist cracking was predicted based on the measured value of the ratio *c:a*, where *c* is the total distance from the centre of the indents to the crack tip, and *a* is the half-diagonal length of the indent. For median/radial type of crack, the IFR was calculated according to Anstis *et al.* [13] following:

$$K_{\mathrm{IC}} = 0.016(\frac{E}{H})^{1/2} \times \frac{P}{c^{3/2}} \quad \text{Equation 5.3}$$

where E is the Young's modulus (GPa) and H is the hardness (GPa). For Palmqvist type cracks, the IFR value was calculated using a modified version of the Shetty *et al.* equation [14]:

$$K_{\mathrm{IC}} = 0.0319P/(al^{\frac{1}{2}}) \quad \text{Equation 5.4}$$

where l is the indentation crack length (mm). To determine the IFR, the indented samples were examined using SEM for accurate measurement of the cracks generated from the corners of the indents.

To study the crack system generated for different applied loads and cermet microstructures, the cracks were cross-sectioned *in-situ* using a FIB microscope (Model F-2000A, Hitachi High Technologies, Tokyo, Japan). In the present work, typically three 'staircase' FIB milled regions were examined, at the beginning, middle and end of the

crack, as shown in Figure 5.2. The dimensions of FIB milled cut were a length of 15 μm and a width of 8 μm wide. For the cermet materials examined the FIB cuts were made to a total depth of ~8 μm. SEM observation of the FIB milled regions was then conducted after each cut.

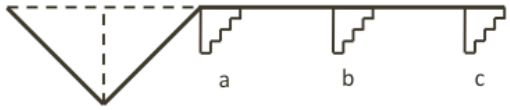

Figure 5.2: Schematic representation of the location of FIB 'staircase' cuts relative to the indentation crack.

5.3 Results and Discussions

5.3.1 Microstructure of the Cermets

Figure 5.3 shows representative SEM images of the 'as-fabricated' structures of cermets following the sintering. Here the cermets have been processed under three different conditions, with a nominally constant binder content of 30 vol.%. It can be seen that the microstructural evolution is considerable; the cermets sintered for 1475ºC for 15 minutes, show 'C'- and 'O'-shaped grains, due to the instability of the solid-liquid interface during the initial liquid phase sintering stage, which causes a coherency strain on the grains. For the cermets sintered at higher temperatures, the grains are more spherical in shape. There is also an obvious 'core-rim' structure generated in the cermets, which results from a 'solution/re-precipitation' process. The mean grain sizes for these examples are presented in Table 5.1, highlighting the extent of grain coarsening. The 'instability of the interface' phenomenon occurs during liquid phase sintering, together with the formation of a 'core-rim' structure which is seen in many TiC-based cermets [16,17].

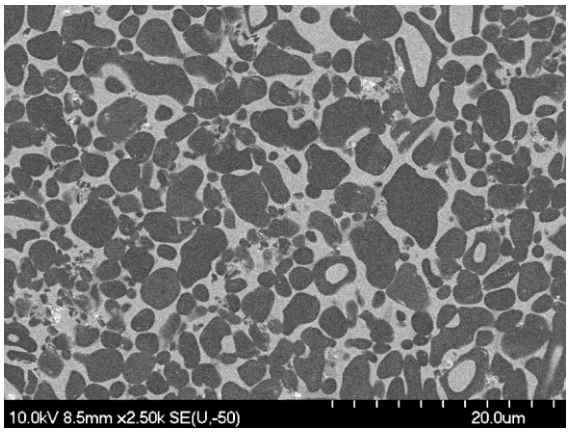

(a)

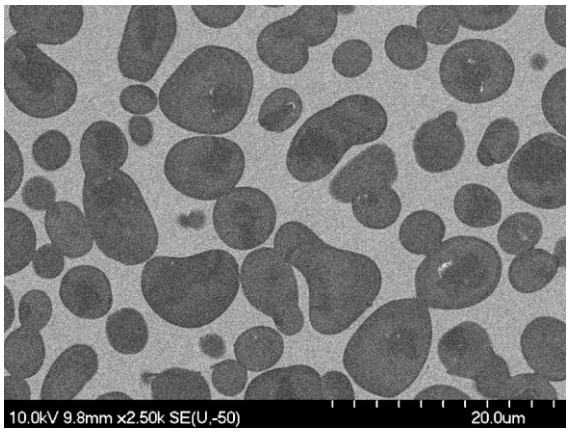

(b)

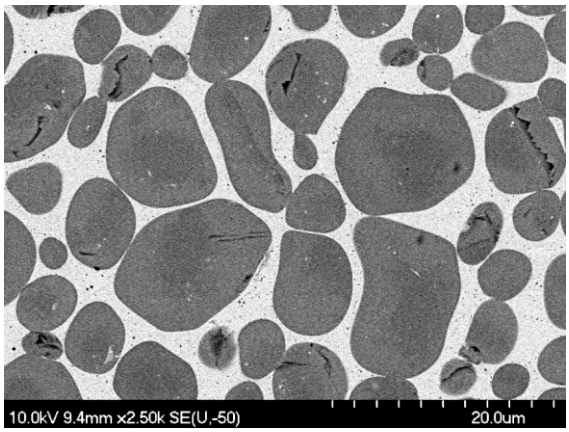

(c)

Figure 5.3: Representative BSE SEM images of the cermets sintered at: (a) 1475ºC for 15 minutes, (b) 1550ºC for 60 minutes, and (c) 1550ºC for 240 minutes.

Table 5.1: The mean grain size of the cermets shown in Figure 5.3, determined using the linear intercept method.

Sintering Condition	Mean grain size (μm)
1475 ºC/15 minutes (fine)	3.19 ± 0.18
1550 ºC/60 minutes (intermediate)	7.64 ± 0.84
1550 ºC/240 minutes (coarse)	7.83 ± 0.36

5.3.2 Hardness and the Indentation Size Effect

For cemented carbides and cermets the hardness is invariably related to the erosion/wear response of the material [18,19]. The bulk hardness of a cemet depends on the composition (i.e. the volume fraction of constituents), the ceramic grain size and the binder mean free path [14,20]. OM images, using Nomarski differential contract imaging (DIC), was used to study the indentation feature of the cermets. Figure 5.4 shows example DIC images of the fine-grained cermets with 5 vol.% steel binder, subjected to applied loads of 1 and 30 kgf. The Vickers indentations show cracks radiating from the indent corners at 30 kgf, with no sign of spalling. The optical microscopy images have revealed that the degree of material 'uplift' around the sides of the indents is significant [21].

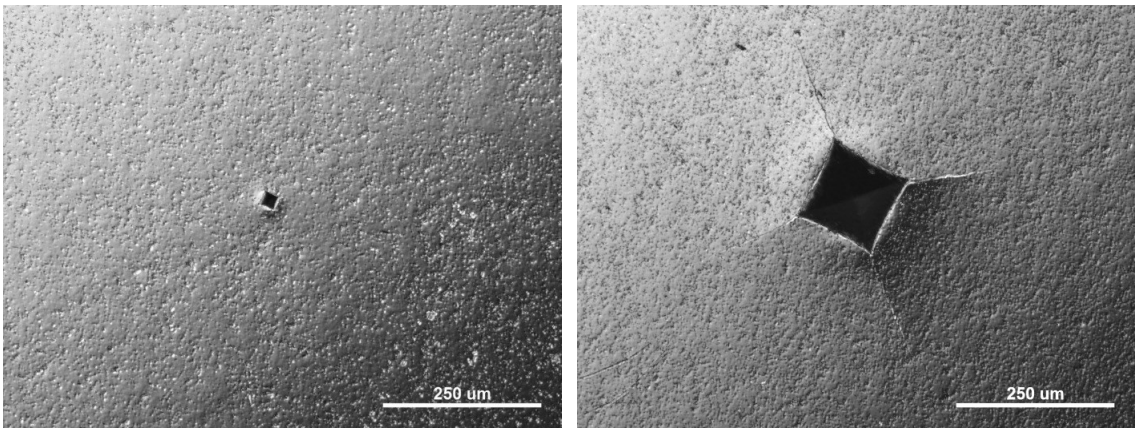

(a) (b)

Figure 5.4: Nomarski DIC images showing the Vickers indentation patterns of fine-grained (1475ºC/15minutes) cermets with 5 vol.% of binder using: (a) 1 kgf and (b) 30 kgf applied loads.

Figure 5.5 shows representative SEM images of typical indentation tests, at various applied loads, for the intermediate grain size cermets prepared with 30 vol.% binder. Higher magnification SEM images of detailed features at the corners of indents are presented in Figure 5.6. It is apparent that the binder phase has been pressed out of the sample surface, indicating a 'binder-extrusion' phenomenon, since the metal binder phase is more significantly plastic than the ceramic phase. The plastic deformation of the indents affects the surrounding area up to ~20 μm from the indent. The hard, brittle ceramic particles under the indenter are severely damaged, showing micro-cracks, while grains at the edge of the indents are often pushed out. From Figure 5.6, it should be noted that negligible corner cracks were generated for 30 vol.% binder content samples.

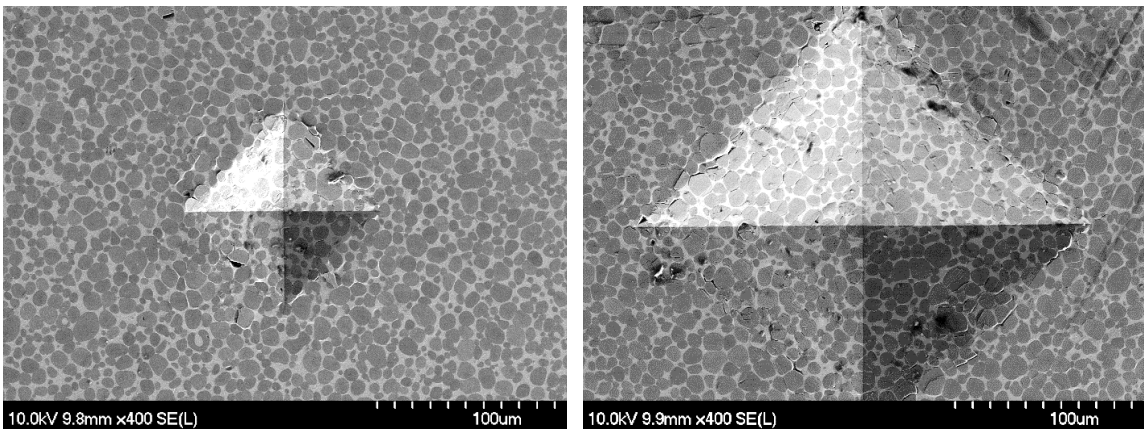

(a) (b)

Figure 5.5: Representative SEM images showing intermediate-grained (1550ºC/60 minutes) cermet with 30 vol.% of binder subjected to applied indentation loads of: (a) 5 kgf, and (b) 30 kgf.

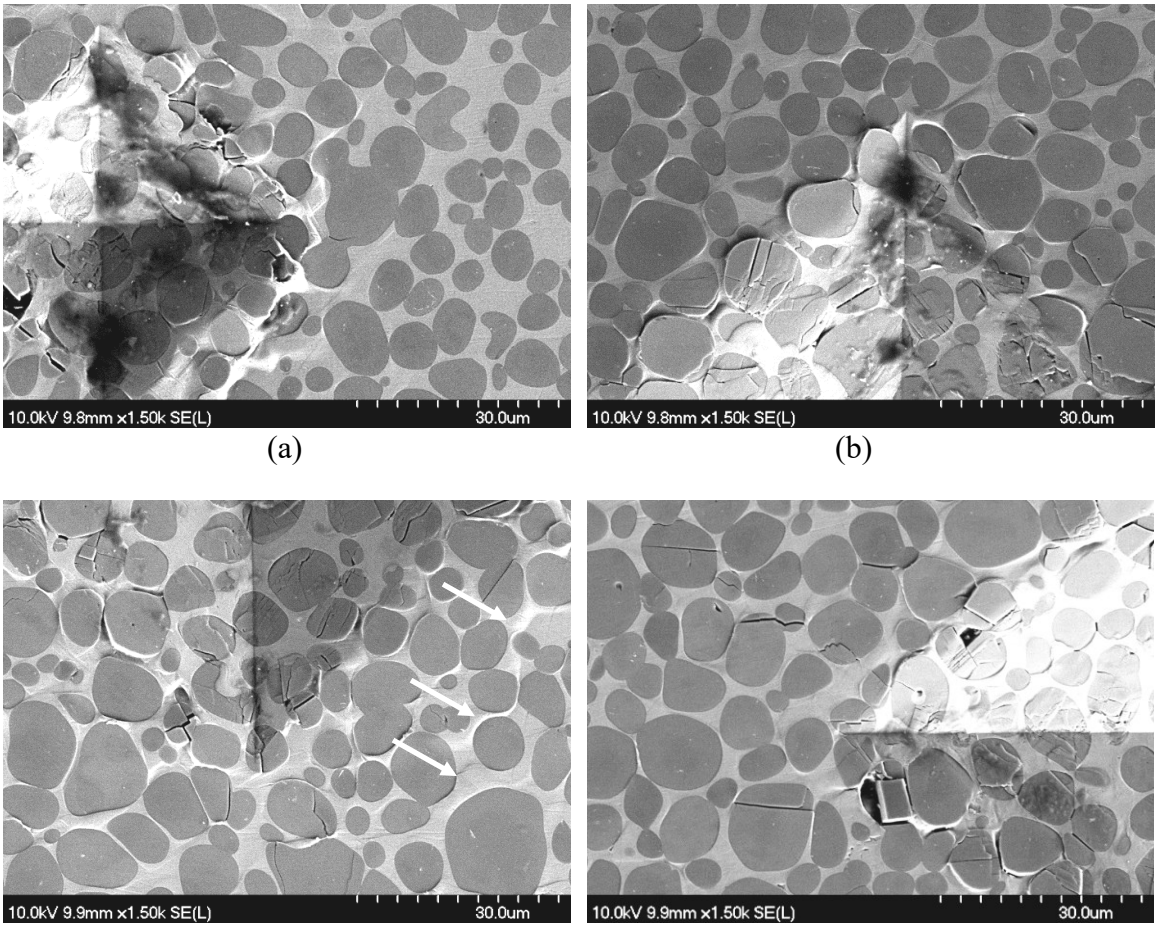

Figure 5.6: SEM images of Vickers indentations in intermediate-grained cermets with 30 vol.% steel binder. Indentations were subject to: (a) 1 kgf, (b) 5 kgf, (c) 10 kgf, and (d) 30 kgf applied load. An ‘off-axis’ lower-detector was used in the SEM to highlight surface topography, particularly the 'binder extrusion' features around the indents, as arrows shows in (c).

The Vickers hardness values were determined using Equation 5.1 and Equation 5.2, respectively. Figure 5.7 shows the effects of binder content on the hardness for both the fine- and intermediate-grained cermets. In each case the general trends are of hardness decreasing with both increasing applied load and steel binder content. The relatively low hardness with 5 vol.% binder for the fine-grained cermet (1475°C/15 minutes) is the result of retained porosity after sintering (< 95 % of theoretical density). For an equivalent binder content, the hardness values of the intermediate-grained cermets are slightly lower than those of the fine-grained equivalents, with the exception of the 5 vol.% samples, due to their increased sintered density.

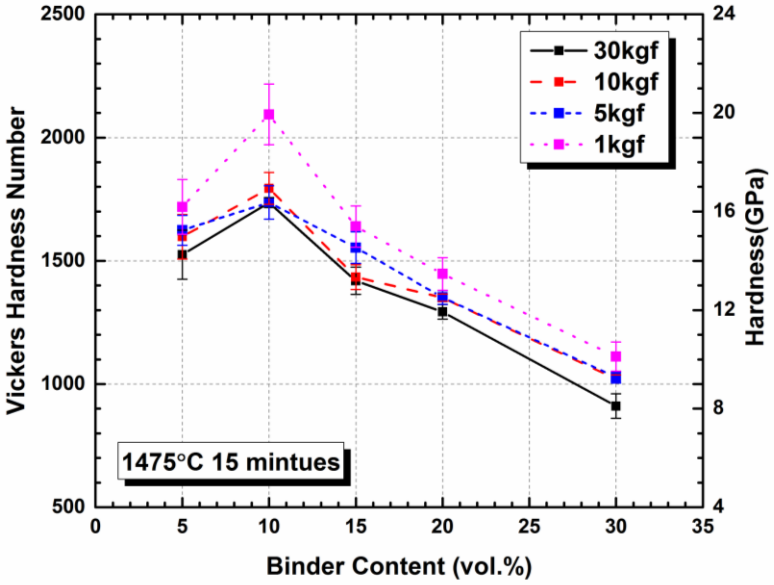

(a)

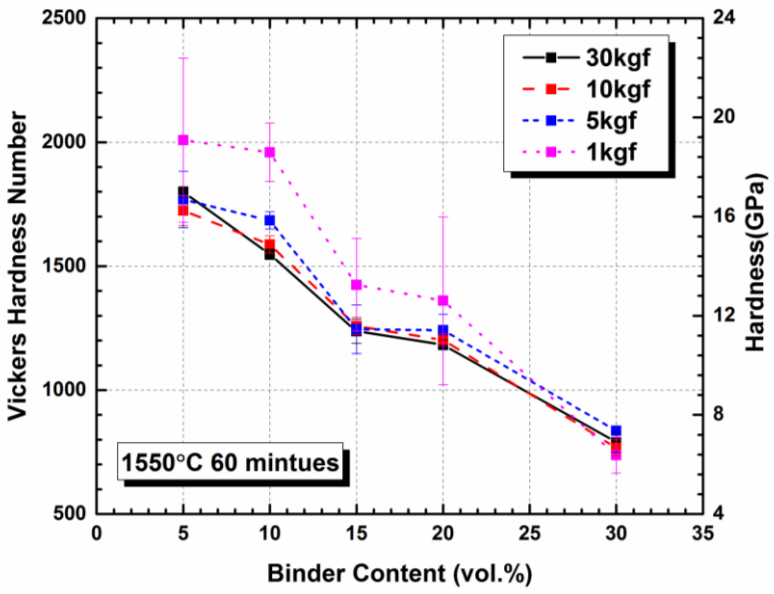

(b)

Figure 5.7: The hardness of TiC-cermets as a function of binder content: (a) fine-grained (1475ºC/ 15 minutes), and (b) intermediate-grained (1550ºC/60 minutes). Error bars indicate the standard deviation of the calculated hardness values.

It was shown previously that the binder mean free path values of the intermediate-grained cermets are slightly higher than for the fine-grained cermets [22]. Taking the Hall-Petch relationship into account, it can therefore be expected that the hardness should be lower when the ligament dimension is increased. A comprehensive study on the microstructure and erosive wear of a series of cermets/hardmetals was conducted by Hussainova [23], comparing the hardness of the composites assessed with a 5 kg indentation load. TiC-based cermets, with 60 to 80 wt.% of ceramic phase and an austenitic steel binder, have been reported with hardness values from 1060 to 1440 HV.

For many materials the hardness is load dependent when using a low load [7-9], which is often referred as the “indentation size effect” (ISE). In this instance the hardness increases with decreasing load applied. Potential explanations of the ISE have been proposed by many researchers, including indentation elastic recovery [24], work hardening during indentation [25,26], surface dislocation pinning [27,28], plastic deformation band spacing [29], an activation energy for dislocation nucleation [30], and the load required to initiate plastic deformation [31].

The hardness of the fine- and intermediate-grained cermets, as a function of the applied indentation load, are presented in Figure 5.8. It can be seen that the hardness decreases with increasing applied load, especially for the lower loads, below 10 kgf. Similar results have been seen for WC-Co cermets for loads between 0.025 and 40 kgf [32]. It was demonstrated that the hardness of both nanostructured and conventional composites decreases as the applied load increases, and stabilises when the load is higher than 10 kgf. It was suggested that the changes in hardness are the result of micro-cracking and work-hardening [32]; since the work-hardening effect is small in the low deformation region, the hardness changes more significantly.

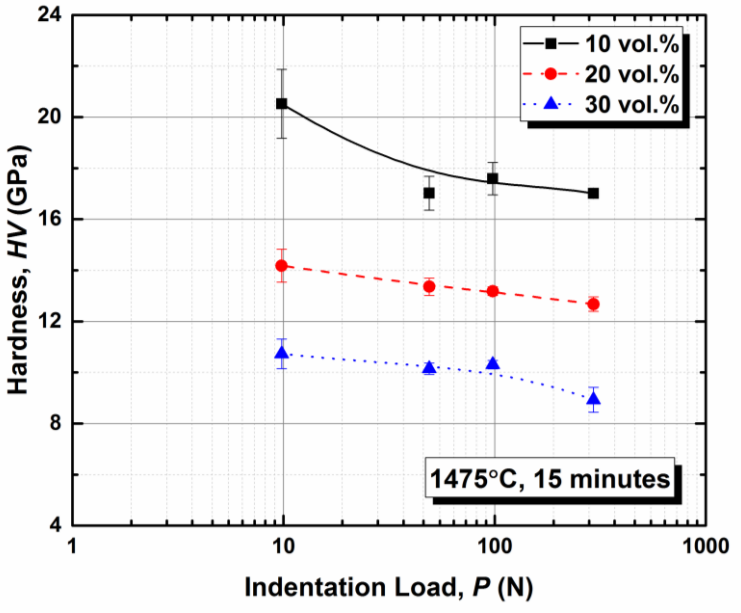

(a)

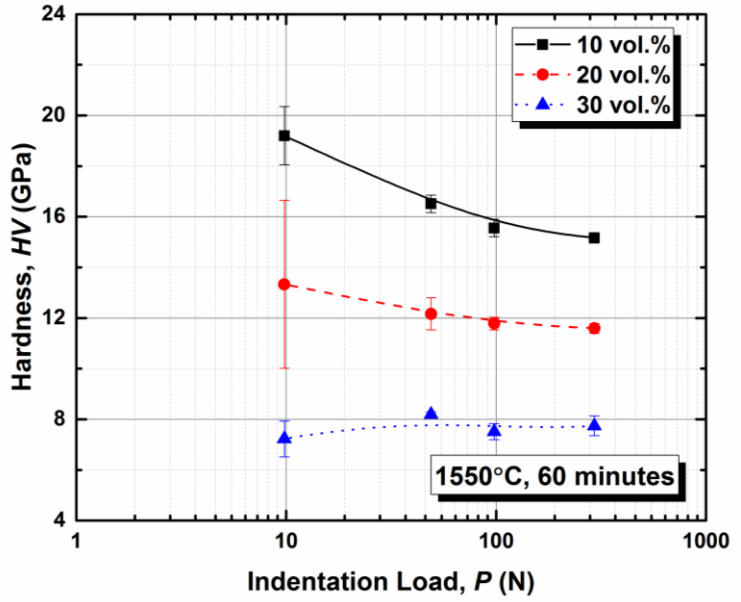

(b)

Figure 5.8: Vickers hardness as a function of load and binder content for: (a) fine-grained and (b) intermediate-grained cermets. Error bars indicate the standard deviation of the hardness values.

Traditionally, the ISE is described using Meyer's law [33], giving an expression for the load and size of the indentation:

$$P = Ad^n \qquad \text{Equation 5.5}$$

where regression can be applied to calculate A and n. When $n < 2$, the material shows an ISE behaviour, and when $n = 2$, the hardness is independent of the applied load.

This model has been applied to a variety of materials, including glass [34], ceramics [35,36], refractory carbides [37], and cermets [38]. A straightforward indication of the existence of an ISE for each material is then based on the value of the n exponent. For the current materials, by applying Meyer's law, the values for the exponent n were calculated. The values are presented in Table 5.2 for the fine-grained and intermediate-grained cermets with 10, 20 and 30 vol.% binder. It can be seen that the fine-grained cermets exhibit an ISE, with a decreasing exponent n as the binder content increases. This indicates that the high binder content cermets exhibit a greater ISE. For the intermediate-grained cermets, the ISE is less obvious, and the exponent n actually increases with the binder content. In fact, the measured values suggest that the 30 vol.% intermediate-grained cermets do not show an ISE.

Table 5.2: The values of n and A calculated using Meyer's Law [34].

Binder Content (vol.%)	**Fine**		**Intermediate**	
	n	**log *A***	***n***	**log *A***
10	1.96 ± 0.02	3.94	1.93 ± 0.02	3.86
20	1.94 ± 0.01	3.79	1.96 ± 0.01	3.77
30	1.84 ± 0.02	3.58	2.00 ± 0.04	3.64

The indentation size effect (ISE) has also been analysed by other models, using mostly empirical analytical equations, e.g. the Hays-Kendall model [31], Li and Bradt's proportional specimen resistance (PSR) model [34,35], and the modified PSR model [38-40]. The proportional specimen resistance model was developed based on the study of TiO_2 and SnO_2 ceramics; both compounds exhibit the rutile structure, and single crystal variants were examined. The PSR model is in fact an improved version of the Hays-Kendall model, which is based on the concept of 'effective indentation load'; here a minimum test load is proposed, below which plastic deformation does not occur, only

elastic deformation (this is also referred to as test-specimen resistance). As a consequence, the effective indentation load can be expressed by:

$$P_{eff} = P - W = Kd^2 \qquad \text{Equation 5.6}$$

where K is a constant, P is the applied load, and d is the indentation diagonal length. However, in contrast to the Hays-Kendall model, where the test-specimen resistance, W, is a constant, Li and Bradt suggest that the W is proportional to indentation size, and should be written as:

$$W = a_1 d \qquad \text{Equation 5.7}$$

Similar to the Hays-Kendall model, the equation can then be modified to:

$$P_{eff} = P - W = a_2 d^2 \qquad \text{Equation 5.8}$$

or, alternatively:

$$P = a_1 d + a_2 d^2 \qquad \text{Equation 5.9}$$

where the a_1 and a_2 terms are determined by polynomial regression. This equation can then be written as a linear regression in the form of P/d versus d:

$$P/d = a_1 + a_2 d \qquad \text{Equation 5.10}$$

Therefore, the a_1 and a_2 term are used to express the elastic and plastic portions of the hardness, with the a_1 term suggested to be related to the degree of cracking, and a_2 is sometimes referred as the 'true-hardness', which is the resistance to crack-free deformation [41-43]. Calculation based on the PSR model, for a_1 and a_2, are listed in Table 5.3, for both fine- and intermediated-grained cermets. The a_1 terms for the fine-grained cermets are generally higher than intermediate-grained cermets, and 30 vol.% intermediate-grained cermets even show a negative value.

It is generally proposed that the ISE is caused by crack formation under and around the indents [36,43]. Larger a_1 values indicate greater cracking damage through the indentation motion. Therefore, it can be concluded that the fine-grained cermets suffered more from cracking, and show a more pronounced ISE; this agrees with the analysis using Meyer's law, outlined previously. It should be noted that the complex microstructures (i.e. concave and 'hollow' grains) of the fine-grained cermets exhibit lower binder mean free

path values [22]. When subjected to a 'sharp' Vickers indenter, the cracking in the intermediate-grained cermets should be reduced, as the binder mean free path is basically a measure of the 'binder ligament size'. It can be found that the 'true-hardness', a_2 (N/mm^2, which is MPa), is significantly lower than that of measured values. As a_2 denotes only the pure resistance of plastic deformation, the higher measured hardness values are likely related to the micro-crack toughening of the cermets.

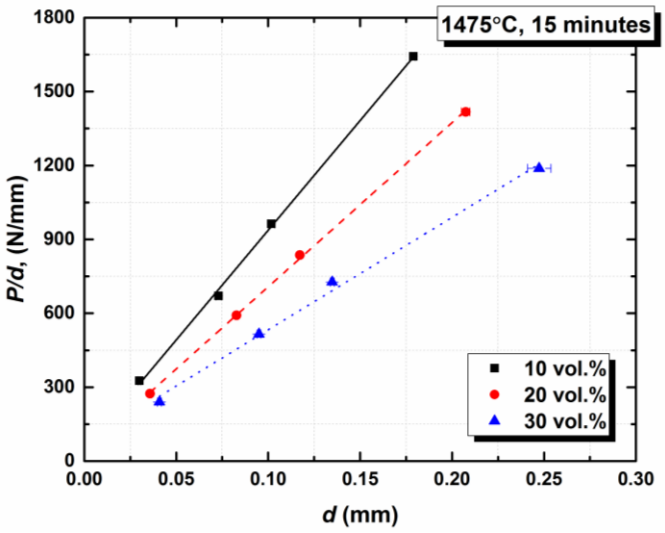

(a)

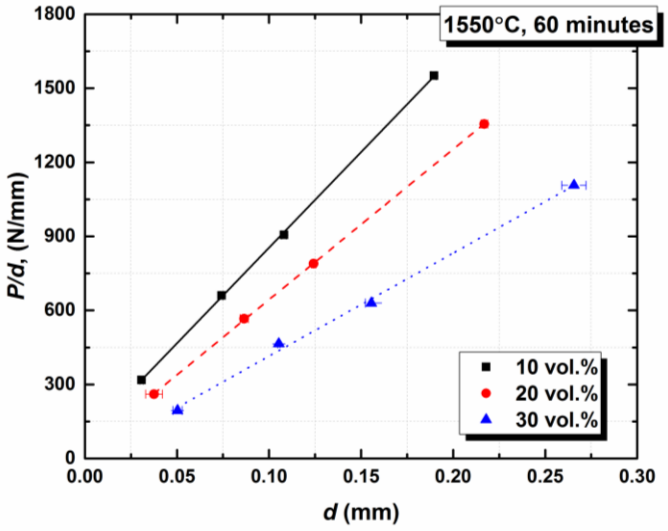

(b)

Figure 5.9: PSR model plots of P/d versus d, for various binder contents, for (a) fine-grained and (b) intermediate-grained cermets.

Table 5.3: Parameter analysis based on the PSR model developed by Li and Bradt (linear) [36].

Binder Content (vol.%)	**Fine**		**Intermediate**	
	a_1 **(N mm^{-1})**	a_2 **(N mm^{-2})**	a_1 **(N mm^{-1})**	a_2 **(N mm^{-2})**
10	46.40	8904.22	79.29	7744.21
20	41.05	6664.94	34.24	6093.43
30	76.50	4564.79	-2.59	4173..48

5.3.3 Indentation Fracture Resistance and Crack System Identification

The determination of fracture toughness by indentation test was first developed by Palmqvist in the 1950s, and it was not until the mid-1970s that Evans and Charles [9] evolved this into a viable Vickers indentation fracture toughness procedure. They also presented a generalized equation that appeared to apply to many different materials with either Palmqvist cracks or median cracks. Subsequently, other authors have developed similar curve fitting methods and analyses from Vickers indention to assess the fracture toughness for both of the crack geometries [44-49]. Many of these equations are the

products of dimensional analyses, modified with experimentally derived calibration factors. Marshall and Evans refined the original equation and then published one that was further simplified. Anstis *et al*. [13] and Chantikul *et al*. [50] then followed with two papers presenting further indentation toughness research. Niihara [51] focused particularly on Palmqvist cracks. Another equation was developed by Miyoshi [52], for median cracks, which is derived from Anstis *et al*. [13], while further equations were introduced by Li *et al.* [53] and Ghosh *et al*. [54], a list of the equations were summarised by Ponton and Rawlings [15].

There has been considerable study on the load-dependence of indentation cracking, with some of these focusing on the microstructure. Palmqvist-type cracking was observed for WC-Co hardmetals, which was revealed through detailed sequential polishing through the indentation [14]. In the current research, a combination of predictive equations (i.e. Anstis and Shetty's equation) and focused ion beam techniques are employed to study the crack system, and to further identify the transition of one crack geometry to the other.

The indentation fracture resistance, measured under various loads, for the fine-, intermediate- and coarse-grained cermets are shown in Figure 5.10, as a function of binder content. Figure 5.10(b) highlights the IFR data for the lower range of binder content. The fracture resistance values were calculated for scenarios were either the Palmqvist [14] or median [13] cracking equations were anticipated. For each of the figures, the open symbols indicate what is predicted as a 'median crack' system, while the closed symbols indicate a 'Palmqvist' crack system is predicted. In Table 5.4 the predicted crack types are listed, based on the *c:a* ratio [15]. It is apparent that the cracking geometry tends to be of the median type for low binder contents, where $c:a > 2$, and Palmqvist-type cracks at high binder content, where $c:a < 2$ [15] . The transition from median to Palmqvist cracking, under a 30 kgf applied load, for these types of cermet is predicted to occur between 10 vol.% and 15 vol.% steel binder. The transition in the predicted crack geometry drops down to between 5 vol.% and 10 vol.% binder with a lower applied load (5 kgf). The cracking geometries are predicted to be all Palmqvist-type when the cermets are subjected to 1 kgf. It should be noted that some limited cracking still exists in high binder content cermets, even at 1 kgf, although it is restricted to TiC grains immediately in contact with the indenter corners.

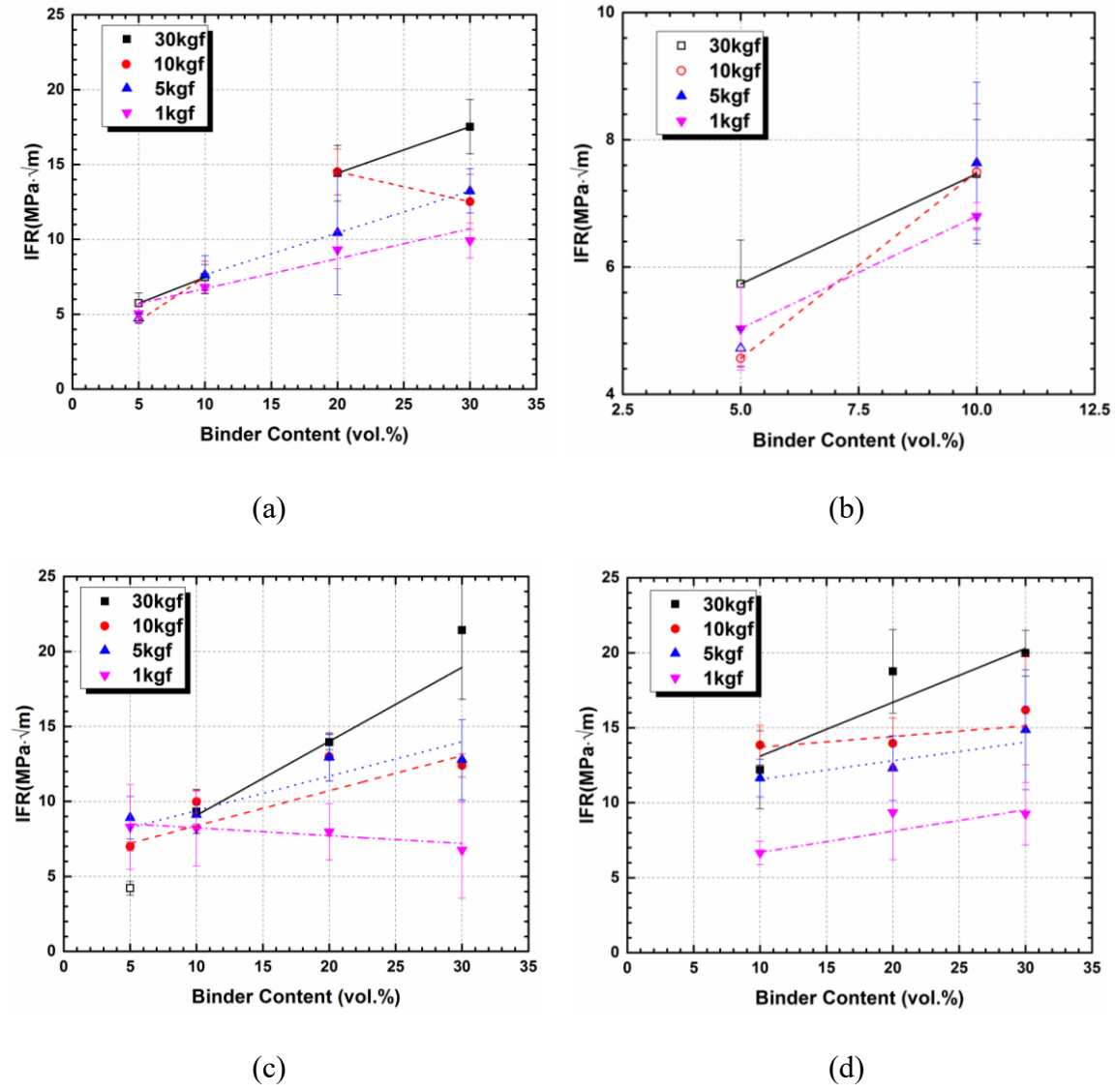

Figure 5.10: The indentation fracture resistance of the cermets as a function of binder content, measured for a series of different applied loads and determined for both median and Palmqvist cracking. Samples were sintered at: (a) 1475ºC/15 minutes, (b) inset of data from (a) for the transition of two cracks, (c) 1550ºC/60 minutes, and (d) 1550ºC/240 minutes. Error bars indicate the standard deviation of the indentation fracture resistance values. Open symbols denotes the 'median' cracking, closed symbols indicates the 'Palmqvist' cracking. The two types of cracks were fitted independently.

Table 5.4: The crack system predicted for fine-grained cermets (1475ºC/15minutes), as a function of indention load and steel binder content.

	30kgf	**5kgf**	**1kgf**
5 vol.%	Median	Median	Palmqvist
10 vol.%	Median	Palmqvist	Palmqvist
20 vol.%	Palmqvist	Palmqvist	Palmqvist
30 vol.%	Palmqvist	Palmqvist	Palmqvist

While the indentation fracture resistance theory and VIF method has been accepted by a number of researchers, it has also been suggested that it is not a valid characterisation of the fracture toughness of brittle materials, leading to debate of the validity of the measurement [8,55]. The main issues arise with the crack growth during VIF testing for different ceramic materials. They may first form as Palmqvist-type cracks, which later extend to form median cracks, or alternatively median cracks may form directly from the deformation beneath the indenter [8]. With increasing applied loads, a transition in the cracking response has also been observed [8]. The indentation begins as crack-free pyramidal micro-hardness impression, and then evolves to an impression with individual corner cracks apparent at the surface, but there is also a crack pattern hidden beneath the surface. As recently summarised by Quinn [8], from the previous researches, many different equations (up to ~30) can be applied to calculate the fracture resistance with same crack lengths in a ceramic material, but the resultant K_{IC} can be widely different. Furthermore, when the various equations are applied to estimate the fracture resistance from the indentation crack lengths, the fracture resistance can appear to increase and then sometimes decrease with crack length for the same material, which clearly generates confusion in terms of potential analysis.

The indentation crack systems arising from a ‘sharp’ Vickers indenter are well established in brittle materials, and have been studied extensively. In the current work, in order to determine the sub-surface cracking response FIB microscopy was applied to the cermets for all loads and binder contents. Representative SEM images of the fine-grained cermets, presented in Figure 5.11 , give a comparison of the indentions obtained under

the same load, but with different binder contents. Similarly, Figure 5.12 presents indentations formed for the same binder content, but subjected to different loads, again for the fine-grained cermets. The SEM images were taken using back-scattered electrons to better reveal the cracking, and the selected images are for the FIB 'staircase' cuts located at the beginning of the crack, with respect to the indent corner. It can be seen from Figure 5.11 , that the nominally 'brittle' cermet (i.e. 10 vol.% binder) shows multiple cracking in the sub-surface region, while the 'ductile' cermet (i.e. 30 vol.% binder) shows a single crack. The cracks follow a 'transgranular' path, which is favoured from a fracture mechanics perspective, since the more will be absorbed by a crack traversing the ductile binder content (hence it is easier for the crack to follow a path through the brittle ceramic phase). For the same binder content, as shown in Figure 5.12 for the brittle cermet with 5 vol.% binder, the sub-surface region near the indent corner shows a number of cracks, indicating the damage arising from the high load, which is 30 kgf in this case. In comparison, the cracking arising from a 1 kgf force reveals clear evidence of single crack, with some slight evidence of 'intergranular cracking', since the binder content is very low.

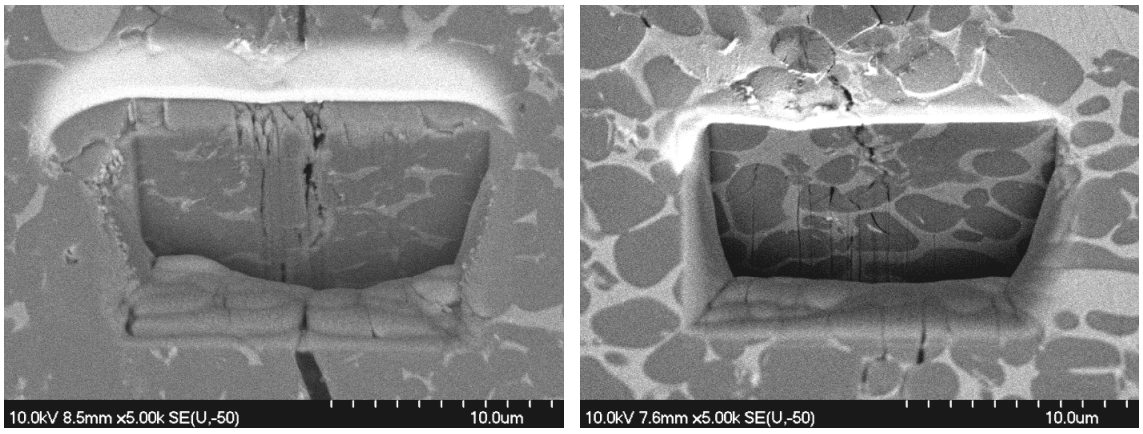

(a) (b)

Figure 5.11: SEM images of FIB staircase cuts at the beginning (with respect of the corner) of an indentation crack, for fine-grained cermets (1475ºC/15 mintues) with: (a) 10 vol.% and (b) 30 vol.% steel binder. The samples were subjected to 30 kgf applied load, and show 'median' and 'Palmqvist' cracking, respectively.

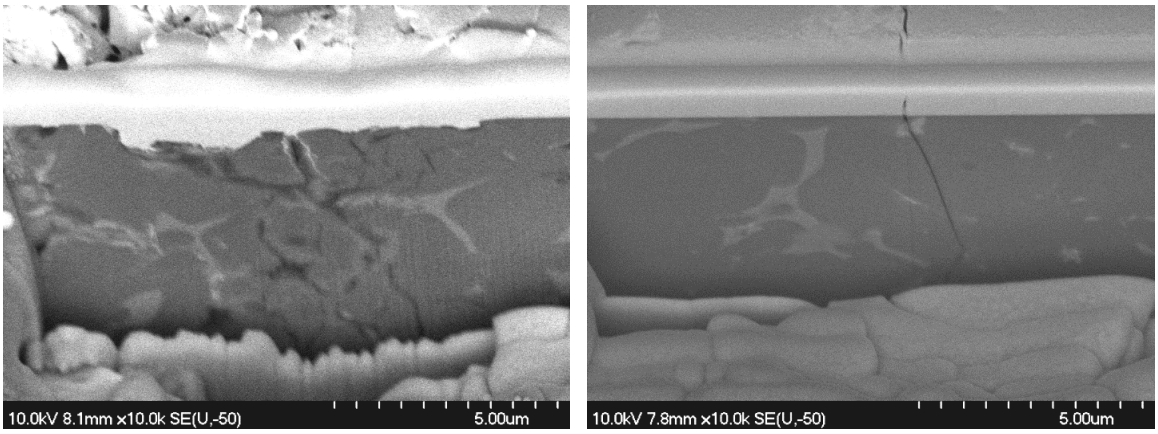

(a) (b)

Figure 5.12: SEM images of FIB staircase cuts at the beginning (with respect of the corner) of an indentation crack for sample with 5 vol.% steel binder, sintered at 1475ºC for 15 minutes, with: (a) 30 kgf and (b) 1 kgf applied load. Samples show 'median' and 'Palmqvist' type of cracks, respectively.

The same study has also extended to the intermediate- and coarse-grained cermets. The SEM images obtained for the same binder content (in this case 10 vol.% steel), for the three different sintering conditions (creating fine-, intermediate- and coarse-grained TiC), subjected to 30 kgf of force, are presented in Figure 5.13. It can be seen that the fine-grained cermet exhibits multiple ‘thin’ cracks, while the intermediate-grained cermet shows one single ‘thick’ crack. In comparison, the coarse-grained cermet only shows a shallow, sub-surface Palmqvist-type of cracking.

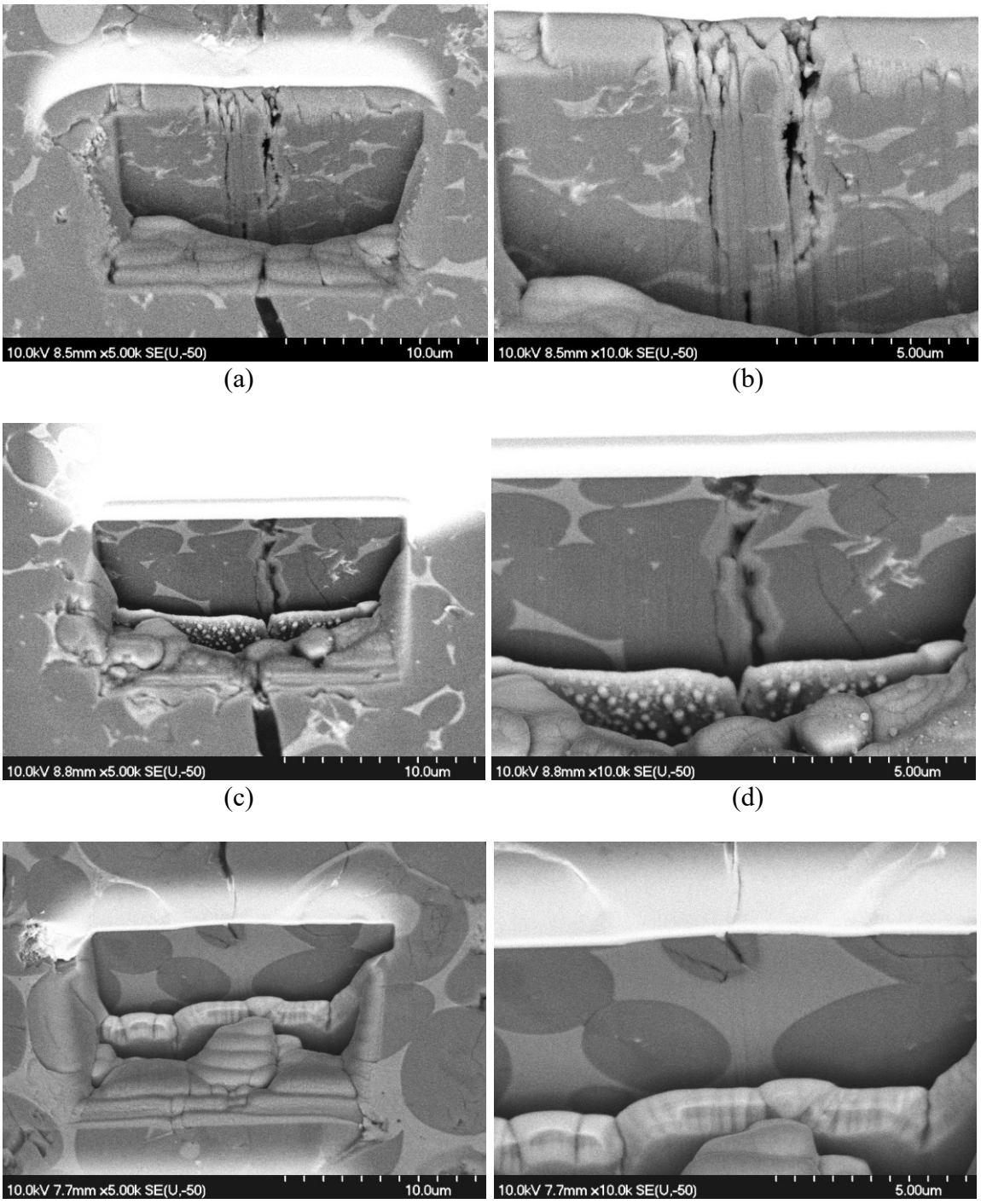

Figure 5.13: SEM images of FIB staircase cuts at the beginning (with respect of the corner) of an indentation crack for sample with 10 vol.% of binder subjected to 30 kgf applied load, with: (a,b) fine-grained (1475ºC/15 minutes), (c,d) intermediate-grained (1550ºC/60 minutes), and (e,f) coarse-grained (1550ºC/240 minutes) microstructures.

A ‘stitched’ series of SEM images of a surface radial crack is shown in Figure 5.14. Again the crack pattern shows a transgranular tendency, and some ductile ligament bridging is also evident. The indentation site shows extensive damage, with small cracks generated from the edge of the impression into the surrounding region; this again reveals the complex cracking behaviour of the cermets.

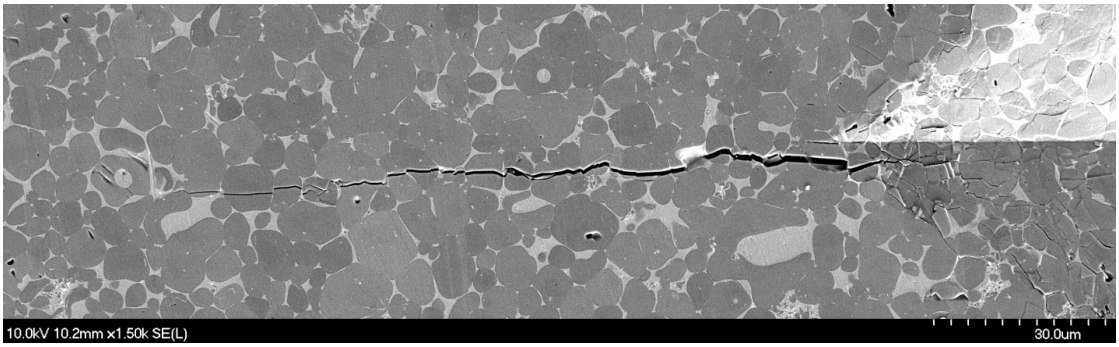

Figure 5.14: ‘Stitched’ sequence of SEM pictures of a radial crack formed in the intermediate-grained cermet with 10 vol.% binder (1550ºC/60 minutes), subjected to Vickers indentation with 30 kgf applied load, showing transgranular cracking.

5.4 Conclusions

TiC based cermets, with 316L stainless steel as the binder phase, were fabricated using a melt infiltration/sintering method. The cermets were sintered at 1475ºC for 15 minutes, 1550ºC for 60 minutes and 1550ºC for 240 minutes, in order to get fine-, intermediate- and coarse-grained microstructures. The sintered materials are homogeneous, with a ‘core-rim’ structure generated through sintering. The fine-grained cermets show a high concentration of complex ‘C-shape’ and ‘O-shape’ grains, while the intermediate- and coarse-grained cermets microstructure are more rounded. The sintered samples were subjected to a series of indentation loads using a ‘sharp’ Vickers indenter, ranging from 1 to 30 kgf. The OM images show a surface ‘uplift’ phenomenon around the indents. Further SEM observation revealed extensive damage within the indents and an apparent ‘binder extrusion’ occurring between TiC grains around the indents. The Vickers hardness values of the cermets were calculated, and it was shown that the hardness values decreased with increasing binder content. The hardness values of the fine-grained cermets

were higher than that of the intermediate-grained materials, since the binder mean path values are lower (effectively showing a Hall-Petch type response).

The cermets also demonstrated an indentation size effect (ISE), as the hardness values were higher when subjected to lower loads. The ISE was analysed using both Meyer's law and the proportional resistance specimen (PSR) model. It was shown that the fine-grained cermets exhibited a more pronounced ISE, and suffered more from cracking, because of their low binder mean free path. The sub-surface crack patterns arose were calculated by either 'median-radial' or 'Palmqvist' model equations, based on the measured indentation fracture resistance (IFR), when subjected to different applied loads with various binder contents. It was found for a fixed binder content (especially for low binder contents), that low loads generally produced 'Palmqvist' type of cracking, while 'median-radial' cracks were favoured at high loads. Similarly, low binder content cermets were more likely to have 'median-radial' cracks, while high binder content samples more typically exhibit 'Palmqvist' type of cracks. FIB micro-sections were used to study the sub-surface crack patterns for the cermets, which confirmed the findings from the analytical results.

Acknowledgements

The authors gratefully acknowledge financial support from the Natural Sciences and Engineering Research Council of Canada (NSERC), through both the Collaborative Research and Development programme (grant #CRDPJ381565-09) and the Discovery Grants programme (grant #283311-2011), and Petroleum Research Atlantic Canada (PRAC), under grant C09-10. The Canada Foundation for Innovation, the Atlantic Innovation Fund, and other partners who helped fund the Facilities for Materials Characterisation, managed by the Dalhousie University Institute for Materials Research, are also appreciated. The authors would also like to thank Dean Grijm and Patricia Scallion for their technical assistance.

5.5 References

1. N. Durlu, Titanium carbide based composites for high temperature applications. J. Eur. Ceram. Soc. 19 (1999) 2415-2419.
2. H. Klaasen, L. Kollow, J. Kübarsepp, Mechanical properties and wear performance of compression sintered TiC based cermets. Powder Metall. 50 (2007) 132-136.
3. H. Klaasen, J. Kübarsepp, F. Sergejev, Strength and failure of TiC based cermets, Powder Metall. 52 (2009) 111-115.
4. J. LaSalvia, D. Kim, M. Meyers, Effect of Mo on microstructure and mechanical properties of TiC-Ni-based cermets produced by combustion synthesis-impact forging technique, Mat. Sci. Eng. A. 206 (1996) 71-80.
5. A. Farid, S. Guo, X. Yang, Y. Lian. Stainless steel binder for the development of novel TiC-reinforced steel cermets, J. Univ. Sci. Technol. B. 13 (2006) 546-550.
6. F. Akhtar, S.J. Guo, Microstructure, mechanical and fretting wear properties of TiC-stainless steel composites. Mater. Charact. 59 (2008) 84-90.
7. J.B. Wachtman, W.R. Cannon, M.J. Matthewson, Mechanical properties of ceramics (2nd Ed.) John Wiley & Sons, New York, 2009.
8. G.D. Quinn, R.C. Bradt, On the Vickers indentation fracture toughness test, J. Am. Ceram. Soc. 90 (2007) 673-680.
9. A.G. Evans, E.A. Charles, Fracture toughness determinations by indentation, J. Am. Ceram. Soc. 59 (1976) 371-372.
10. R. Warren, H. Matzke, Indentation testing of a broad range of cemented carbides, pp. 563-582 in Science of Hard Materials (Eds. R.K. Viswandham, D.J. Rowcliffe, J. Gurland), Plenum Press, New York, NY, USA (1983).
11. J. Lankford, Indentation microfracture in the Palmqvist crack regime: implications for fracture toughness evaluation by the indentation method, J. Mater. Sci. Lett. 1 (1982) 496-495.
12. Standard test method for Vickers indentation hardness of advanced ceramics, ASTM C1327, C28.01 (2008).
13. G.R. Anstis, P. Chantikul, B.R. Lawn, D.B. Marshall, A critical evaluation of indentation techniques for measuring fracture toughness: I, Direct crack measurements, J. Am. Ceram. Soc. 64 (1981) 533-538.

14. D.K. Shetty, I.G. Wright, P.N Mincer, A.H Clauer, Indentation fracture of WC-Co cermets, J. Mater. Sci. 20 (1975) 1873-1882.
15. C.B. Ponton, R.D. Rawlings. Vickers indentation fracture toughness test Part 1: Reviews of literature and formulation of standardized indentation toughness equations, Mater. Sci. Technol. 5 (1989) 865-872.
16. K.W. Chae, D.I. Chun, D.Y. Kim, Y.J. Baik, K.Y. Eun, Microstructural evolution during the infiltration treatment of titanium carbide-iron composite. J. Am. Ceram. Soc. 73 (1990) 1979-1982.
17. D.I. Chun, D.Y. Kim, K.Y. Eun, Microstructural evolution during the sintering of TiC-Mo-Ni cermets. J. Am. Ceram. Soc. 76 (1993) 2049-2052.
18. D.K. Shetty, I.G. Wright, J.T. Stropki, Slurry erosion of WC-Co cermets and ceramics, ASLE Trans. 28 (1985) 123-133.
19. D.K. Shetty, I.G. Wright, A.H Clauer, Effects of composition and microstructure on the slurry erosion of WC-Co cermets, Wear 114 (1987) 1-18.
20. D. Moskowitz, M. Humenik Jr., Cemented Titanium Carbide cutting tools, Modern developments in powder metallurgy (1966) 83-94.
21. G.D. Quinn, Fracture toughness of ceramic by the Vickers indentation crack length method: A critical review, Ceram. Eng. Sci. Proc. 27 (2008) 45-62.
22. C. Jin, K.P. Plucknett, Microstructure instability in TiC-316L stainless steel cermets, Int. J. Refract. Met. Hard Mater. 58 (2015) 74-83.
23. I. Hussainova, Microstructure and erosive wear in ceramic-based composites, Wear 258 (2005) 357-365.
24. D.R. Tate, A comparison of microhardness indentation tests, Trans. ASM, 35 (1945) 374-384.
25. H. O'Neill, The hardness of metals and its measurement, Chapman & Hall, Ltd., 1934.
26. B.W. Mott, Micro-indentation hardness testing, Butterworths Scientific Publications, 1956.
27. S.A. Varchenya, F.O. Muktepavel, G.P. Upit, Dependence of hardness and length of dislocation rosette ray on indentor load in LiF crystals, Sov. Phys. Sol. Stat. 11 (1970) 2300-2303.

28. J.J. Gilman, J.H. Westbrook, H. Conrad, The science of hardness testing and its research applications, American Society of Metals, Metals Park, Ohio, 54 (1973).
29. S.J. Bull, T.F. Page, E.H. Yoffe, An explanation of the indentation size effect in ceramics, Philos. Mag. Lett. 59 (1989) 281-288.
30. N. Gane, J.M. Cox, The micro-hardness of metals at very low loads, Philos. Mag. 22 (1970) 881-891.
31. C. Hays, E.G. Kendall, An analysis of Knoop microhardness, Metallography 6 (1973) 275-282.
32. K. Jia, T. Fischer, B. Gallois, Microstructure, hardness and toughness of nanostructure and conventional WC-Co composites, Nanostruct. Mater. 10 (1998) 875-891.
33. E. Meyer, Investigations of hardness testing and hardness, Phys. Z. 9 (1908) 66.
34. L. Hong, R.C. Bradt, The indentation load/size effect and the measurement of the hardness of vitreous silica, J. Non-Cryst. Solids 146 (1992) 197-212.
35. H. Li, R.C. Bradt, The microhardness indentation load/size effect in rutile and cassiterite single crystals, J. Mater. Sci. 28 (1993) 917-926.
36. J. Wade, S. Ghosh, P. Claydon, H. Wu, Contact damage of silicon carbide ceramics with different grain structures measured by Hertzian and Vickers indentation, J. Eur. Ceram. Soc. 35 (2015) 1725-1736.
37. A. Nino, A. Tanaka, S. Sugiyama, H. Taimatsu, Indentation size effect for the hardness of refractory carbides, Mater. Trans. 51 (2010) 1621-1626.
38. J. Gong, J. Wu, Z. Guan, Examination of the indentation size effect in low-load Vickers hardness testing of ceramics, J. Eur. Ceram. Soc. 19 (1999) 2625-2631.
39. Z. Peng, J. Gong, H. Miao, On the description of indentation size effect in hardness testing for ceramics: Analysis of the nanoindentation data, J. Eur. Ceram. Soc. 24 (2004) 2193-2201.
40. L. Curkovic, M. Lalic, S. Solics, Analysis of the indentation size effect on the hardness of alumina ceramics using different models, Kovove Materialy - Metallic Materials 47 (2009) 89-93.
41. H. Li, R.C. Bradt, The effect of indentation-induced cracking on the apparent microhardness, J. Mater. Sci. 31 (1996) 1065-1070.

42. M.V. Swain, M. Wittling, Fracture mechanics of ceramics, Plenum Press, New York, 11(1996) 379.
43. J.B. Quinn, G.D. Quinn, Indentation brittleness of ceramics: a fresh approach, J. Mater. Sci. 32 (1997) 4331-4346.
44. B.R. Lawn, M.V. Swain, Microfracture beneath point indentations in brittle solids, J. Mater. Sci 10 (1975) 113-122.
45. B.R. Lawn, E.F Fuller, Equilibrium penny-like cracks in indentation fracture, J. Mater. Sci. 10 (1975) 2016-2024.
46. B.R. Lawn, A.G. Evans, A model for crack initiation in elastic/plastic indentation fields, J. Mater. Sci. 12 (1977) 2195-2199.
47. B.R. Lawn, D.B. Marshall, Hardness, toughness, and brittleness: An indentation analysis, J. Am. Ceram. Soc. 62 (1979) 347-350.
48. B.R. Lawn, A.G. Evans, D.B. Marshall, Elastic/plastic indentation damage in ceramics: the median/radial crack system, J. Am. Ceram. Soc. 63(1980) 574-581.
49. A.G. Evans, Quasi-static solid particle damage in brittle solids-I. Observations analysis and implications, Acta Metall. 24 (1976) 939-956.
50. P. Chantikul, G.R. Anstis, B.R. Lawn, D.B. Marshall, A critical evaluation of indentation techniques for measuring fracture toughness: II, Strength method J. Am. Ceram. Soc. 64 (1981) 539-543.
51. K. Niihara, A fracture mechanics analysis of indentation-induced Palmqvist cracks in ceramics, J. Mater. Sci. Lett. 2 (1983) 221-223.
52. T. Miyoshi, N. Sagawa, T. Sassa, Study on fracture toughness evaluation for structural ceramics, Trans. Jap. Soc. Mech. Eng. 51 (1985) 2489-2497.
53. Z. Li, A. Ghosh, A.S. Kobayashi, R.C. Bradt, Indentation fracture toughness of sintered Silicon Carbide in the Palmqvist crack regime, J. Am. Ceram. Soc. 72 (1989) 904-911.
54. A. Ghosh, A.S. Kobayashi, Z. Li, C.H. Jr. Henager, R.C. Bradt, Vickers microindentation toughness of a sintered SiC in the median-crack regime, Report No. PNL-SA-16927, Pacific Northwest Lab, Richland, WA, 1991.
55. D.B. Marshall, R.F. Cook. N.P. Padture, M.L. Oyen, A. Pajares, J.E. Bradby, I.E. Reimanis, R. Tandon, T.F. Page, G.M. Pharr, B.R. Lawn, The compelling case for

indentation as a functional exploratory and characterization tool, J. Am. Ceram. Soc. 98 (2015) 2671-2680.

Chapter 6 Hertzian Indentation Damage in TiC-316L Stainless Steel Cermets

Chenxin Jin, Kevin Plucknett

Dalhousie University, 1360 Barrington Street, Materials Engineering, Department of Process Engineering and Applied Science, B3H 4R2, Nova Scotia, Canada

Status: To be submitted to Ceramic Engineering and Science Proceedings

Abstract

Titanium carbide (TiC) based cermets are commonly used in mining and tooling industries because of high hardness, strength and wear resistance. The present work is focused on the Hertzian indentation damage of TiC-316L stainless steel cermets. Samples were fabricated using a vacuum melt-infiltration procedure, at temperatures between at 1550°C for 60 and 240 minutes, with steel binder contents ranging from 10 to 30 vol.%. Various diameter WC-Co spheres, ranging from 1.19 mm to 3.97 mm, were used for indentation, with applied loads ranging from 250 N to 2000 N. A standard 4140-4142 steel was also prepared and tested for comparison. Indentation stress-strain curves were plotted to study the effects of differences in the cermet microstructure and the loading condition. 'Ideal' Hertzian elastic responses were also calculated, to demonstrate the deviation of the curves. It is shown that the materials perform in a 'quasi-plastic' manner, with evidence of 'strain-hardening' phenomena.

Keywords: Quasi-plasticity; scanning electron microscopy; optical microscopy; elastic modulus

6.1 Introduction

The indentation of materials with spheres was first studied by Hertz in the 1880s, when he was observing two lenses that came into contact. The contact induced damage, including deformation and cracking are important in many related engineering applications, such as bearings, engine components, etc. Over the past 100 years the contact mechanics of advanced materials has been studied extensively, especially for the case of brittle materials. Cone crack formation in brittle materials is driven by the tensile stress that is generated, which is just *outside* of the contact region [1-4]. Beginning in the 1990s, the study of contact mechanics in brittle materials has been extended to investigate heterogeneous 'toughened' ceramics, which have so-called 'quasi-plastic' behaviour [5-11]. This quasi-plasticity is driven by the shear components in the applied stress field, generating faults or microcracks in the sub-surface [12-15], and that type of damage is generated *beneath* the contact zone. Quasi-plasticity is usually related to materials that exhibit an '*R*-curve' behaviour, where the fracture toughness of the material actually increases with increasing crack length. The quasi-plasticity of the material is often determined through the evaluation of indentation stress-strain curves, which provide information on the mechanism of deformation and help in predicting the material's performance, such as for bearings in contact, wear [16,17], and erosion and/or fatigue [18-20]. For a sphere contacting on a flat surface, the mean contact pressure is given by:

$$p_m = \frac{P}{\pi a^2} \qquad \text{Equation 6.1}$$

where P is the applied load, and a is the measured indent radius (i.e. the contact radius). The equation can be also expressed as:

$$p_m = \frac{3E}{4\pi k}\frac{a}{R} \qquad \text{Equation 6.2}$$

where the E is the Young's modulus of the material (in the present case a ceramic-metal composite, or cermet), R is the sphere radius and k is the elastic mismatch constant, which is given by:

$$k = \frac{9}{16}[(1-\nu^2) + \frac{E}{E'}(1-\nu'^2)] \qquad \text{Equation 6.3}$$

where E and E' are the Young's modulus and ν and ν' are the Poisson's ratios of the specimen and the indenter, respectively. Therefore, the left hand side of Equation 6.2 is the so-called 'indentation stress', and a/R, is the 'indentation strain'.

Over the past few decades, a technique referred to as the 'bonded interface method' has been widely employed to study the sub-surface quasi-plastic damage zone arising from Hertzian-type indentation [7,8,15,21-23]. The shape, location and microstructure within the damage zones has provided a lot of information regarding the 'quasi-plastic' response of the materials being evaluated. The 'bonded interface method' is sometimes used in conjunction with numerical or computational approaches (e.g. the finite element method (FEM)), since there are no exact analytical models to explain the indentation response of ceramics and cermets, or even the contact between a ceramic and a metal [24,25]. As a consequence, FEM is a powerful tool to evaluate the contact between two materials. Fischer-Cripps and colleagues have conducted extensive studies on the fracture [2], elastic-plastic [13,14] and quasi-plastic [15] indentation response of ceramics in relation to Hertzian contact geometries. The quasi-plastic FEM analysis incorporated strain-hardening effects into the elastic-plastic constitutive model, and was able to simulate the indentation stress-strain curves and the size/location of the deformation zones [15].

The purpose of the current study is to assess the 'quasi-plastic' behaviour of TiC-stainless steel cermets, compare the effects of microstructural changes on the indentation response of the materials, and provide experimental data for future finite element modelling. The effects of the applied indentation load and indenter sizes were also investigated. Optical profilometry was utilised to measure the final residual 'indentation depth', such that the 'elastic recovery' of the indentation can then be determined.

6.2 Experimental Procedure

6.2.1 Sample Preparation and Characterisation

The TiC powder used in the current study was sourced from Pacific Particulate Materials Ltd. (Vancouver, BC, Canada). The 316-L grade, austenitic stainless steel powder used as the binder phase was obtained from Alfa Aesar (Ward Hill, MA, USA). TiC pellets were obtained by uniaxial compaction in a hardened steel die, using with ~7.35g of powder at a pressure of approximately 45 MPa. The TiC samples were then bagged and subsequently further compacted by cold isostatic pressing at 208 MPa. The pressed samples were placed in alumina crucibles, on a bed of bubble alumina. Different volume percentages of the steel binder powder, ranging from 10 to 30 vol.%, were placed on top of the TiC preforms. Melt-infiltration/sintering was conducted under a dynamic vacuum (~20 mTorr) inside a graphite resistance furnace (Materials Research Furnaces, Suncook, NH, USA) at 1550ºC for either 60 or 240 minutes, in order to vary the grain size. The nominal heating and cooling rates were 10ºC/min and 25ºC/min, respectively, although a natural furnace cool occurred below ~900ºC.

The densities of the sintered cermets were calculated by Archimedes' immersion method in water, and the data shows the samples reached higher than 95% of the theoretical densities. The cermets were then ground flat on both sides, using a diamond peripheral wheel, and subsequently ground and polished to a 'mirror-like' surface finish (starting with a 125 μm diamond impregnated pad and concluding with 0.25 μm diamond paste). Characterization of the microstructure of both sintered and indented samples was conducted with both optical microscopy (Model BX-51, Olympus Canada, Richmond Hill, Ontario, Canada), with a Nomarski differential interference contrast (DIC) capability, and scanning electron microscopy (SEM; Model S-4700, Hitachi High Technologies, Tokyo, Japan).

6.2.2 Hertzian Indentation Testing

The configuration of the Hertz indentation frame, designed in previous work [23], is a simple system that can be easily inserted and removed from a servo hydraulic test frame

(5594-200 HVL Satec Series, Instron, Norwwod, MA, USA). A linear variable differential transform (LVDT) displacement sensor system is attached to the system to monitor the indenter sphere displacement during testing. The indentation stylus was designed to hold a variety of WC-Co sphere sizes. The WC-6Co spheres were procured from McMaster Carr (Aurora, OH, USA), with the properties of this grade of WC-Co listed in Table 6.1. A schematic representation of the configuration used for Hertzian indentation is shown in Figure 6.1. Both the indentation stylus and the frame were made of 4140 high strengh steel, while the support frame was machined from 1040 carbon steel. The sliding ring holding the stylus is made from brass to enable smooth movement of the indenter head.

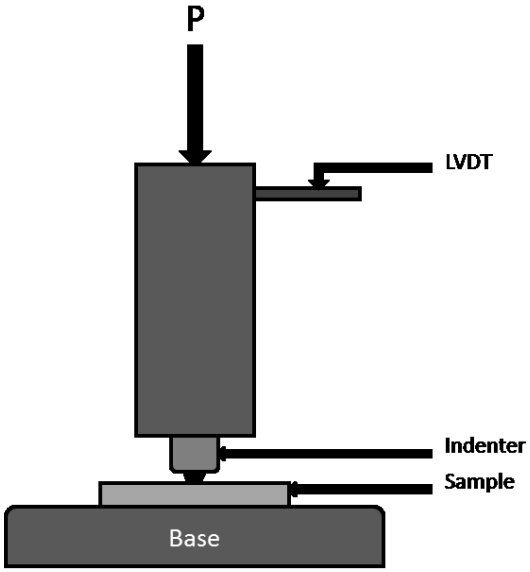

Figure 6.1: Schematic figure of the Hertz indentation configuration.

Table 6.1: Properties of WC-Co spheres [23] .

Property	Value
Composition	C2 Grade-6% Co, 94% WC
Density	14.95 g/cm^3
Diameter	±0.001”
Sphericity	±0.000025”
Vickers Hardness	1620
Surface Roughness	0.05 μm
Young’s Modulus	650 GPa
Compressive Strength	5.17 GPa
Impact Strength	1.36 Nm
Grain Size	~1.0 μm

In order to study the cermet response to Hertz indentation, six different sizes of WC-6Co spheres were chosen, as listed in Table 6.2. Samples were indented with a series of applied loads (250 N, 500 N, 1000 N and 2000 N). During the test, the frame was placed under the hydraulic press, with the LVDT attached. The sample is securely clamped and holding plates are screwed into place to eliminate any sample movement. They were automatically loaded at the rate of 5 N/s to the prescribed load, which was monitored with a 50 kN load cell. The load and deflection are recorded throughout the tests. The load was applied until the peak was reached, which was then held for 10 seconds and released. The WC-6Co spheres were invariably checked in the SEM after testing, since they may encounter cracking or damage during the tests. The spheres were changed after each set of experiment.

Table 6.2: WC-Co sphere sizes and designations.

Designation	Sphere Size (in)	Sphere Size (mm)
Green	3/64	1.19
Red	1/16	1.59
Black	5/64	1.98
Blue	3/32	2.38
Grey	1/8	3.18
White	5/32	3.97

After testing, the indentations were observed and measured using DIC imaging, on the optical microscope, to determine the indent radius, *a*. This was achieved using Image-Pro Plus software (version 6.3, Media Cybernetics, USA), from calibrated digital micrographs. An optical profilometer system was then used to determine the depth, h_r, of the Hertzian indentation marks. The optical profilometer system uses a high resolution chromatic confocal sensor including controller and the optical pen (STIL Initial 4.0, STIL, France) with axial resolution of 130 nm. The scan was completed with a step size of 5 μm, in both the *x* and *y* directions. The three-dimensional feature observation and depth calculations were performed using the software package SPIP 6.3.5 (Image Metrology A/S, Horsholm, Denmark). Peak deflection values, δ, obtained from the extensometer were then compared with the residual indentation depths, in order to analyse the elastic recovery of the materials. After the residual depths were obtained, the final volume of the indents, or the indent's plastic deformation, can be calculated as (assuming there are no 'pile-up' or 'sink-in' phenomena):

$$V = \frac{\pi h_r (3a^2 + {h_r}^2)}{6} \qquad \text{Equation 6.4}$$

where *V* the volume of the final indent, h_r is the 'indentation depth', or more precisely the 'depth of the residual impression' determined using the profilometer, and *a* is the contact radius, measured by DIC optical microscopy, six indents were used to calculate the average and standard deviation of the contact radius.

6.3 Results and Discussions

6.3.1 Microstructure and Residual Indents Analysis

The microstructure of the melt-infiltration processed samples were initially analysed using SEM, prior to indentation testing. Representative SEM images of the cermets, prepared with 30 vol.% steel binder under both sintering conditions, are shown in Figure 6.2. It can be seen that the TiC grains within the cermets have formed a 'core-rim' structure, which was believed to be a result of Oswald ripening during the dissolution/re-precipitation process of the liquid phase sintering and incorporation of constituents from the steel into the TiC. The basic microstructural parameters were calculated (detailed information of the calculation was published in a recent paper [26]), and are presented in Table 6.3. The cermets sintered for 60 minutes have a slightly lower grain size, higher contiguity and relatively similar binder mean free path to those processed for 240 minutes. It can be predicted that the mechanical properties, such as hardness, fracture toughness and other behaviour of the cermets might therefore be very similar at a fixed binder content.

It has been reported that cemented carbide-type cermets exhibit a 'quasi-plastic' behaviour [21-23], which is suggested partly due to the formation of microcracks [21,22]. However the plasticity of the metal binder phase should also plays an important role. Lawn and Marshall [27] have determined the correlation between strain hardening and microcrack formation, by measuring the density and size of the microcracks, which is given as:

$$\alpha = 1/(1 + 2Nl^3) \qquad \text{Equation 6.5}$$

where α is the strain hardening factor, N is the number of microcracks density, and l is the size of the microcrack. When $2Nl^3 << 1$, it is a fully elastic response, when $2Nl^3 >> 1$, it is a fully plastic response. This has indicated that the microstructural variables such as grain size, contiguity, binder mean free path and binder content are all important in evaluating the indentation phenomena arising in cermets. Previous research [28] reported a correlation between microcrack densities and the microstructural parameters, and has demonstrated that the densities increases with increasing grain size, and hence binder mean free path, and decreases with increasing contiguity. This response is similar to the trend of fracture

toughness with these microstructure parameters. It has also been shown that the microcrack density increases with increasing binder content (i.e. increasing fracture toughness, decreasing hardness), indicating that it is the microcracks that are dissipating the energy and shielding the long-crack formation [28]. Since the cermets in the current study show similar trends in hardness and fracture toughness (or 'indentation fracture resistance', IFR) [26], in comparison to that prior work, it can be concluded that the microcracks are also likely to be formed in the current material.

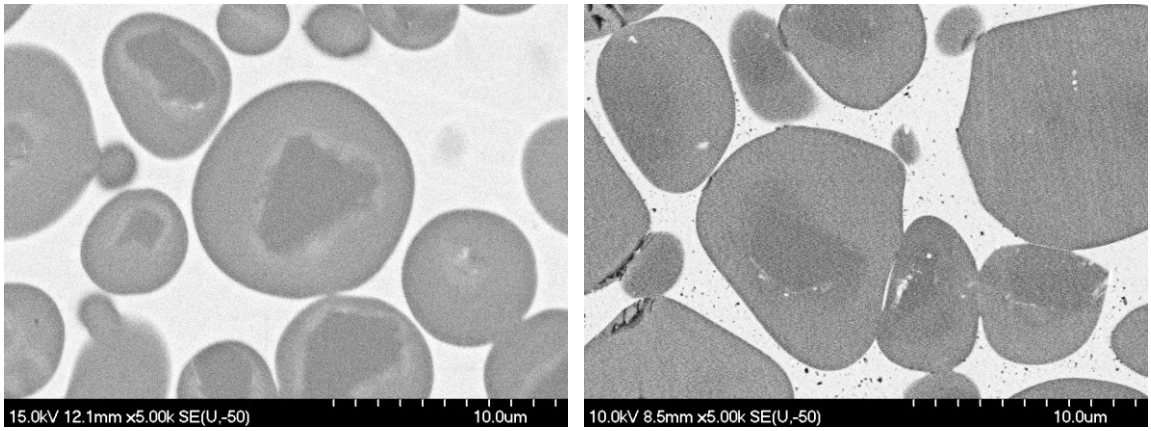

(a) (b)

Figure 6.2**:** Representative SEM images of the sintered TiC-30 vol.% cermets, after (a) 60 and (b) 240 minutes.

Table 6.3: Microstructure parameters of the cermets.

Binder content (vol.%)	**Mean grain size (µm)**		**Contiguity**		**Binder mean free path (µm)**	
	60 min	240 min	60 min	240 min	60 min	240 min
10	5.11 ± 0.21	7.84 ± 0.73	0.43 ± 0.10	0.35 ± 0.10	1.03 ± 0.25	1.75 ± 0.78
20	5.91 ± 0.56	8.88 ± 0.87	0.28 ± 0.03	0.28 ± 0.08	2.05 ± 0.14	2.81 ± 1.91
30	7.64 ± 0.84	7.83 ± 0.36	0.19 ± 0.02	0.16 ± 0.05	4.03 ± 0.35	4.01 ± 0.16

The impressions of the indents were first characterised with a DIC optical microscope. Figure 6.3 shows an example of TiC-30 vol.% cermet, sintered for 60 minutes, when using a 1.98 mm indenter loaded with 250 N and 2000 N of applied stress. It can be seen that the radius of the indents increases with applied load, and the material exhibits a slight 'pileup' effect around the indentation edge at the higher load. The representative indentation radius versus the applied load(s) is shown in Figure 6.4, and fitted with a

second order polynomial function. For the sake of easier presenting the data, only four indenters are shown out of total six (1.59 mm, 1.98 mm, 2.38 mm, 3.18 mm) in the figures (coloured symbols are indicated in the legends as red, black, blue, and grey, the same as the indenter designation colours).

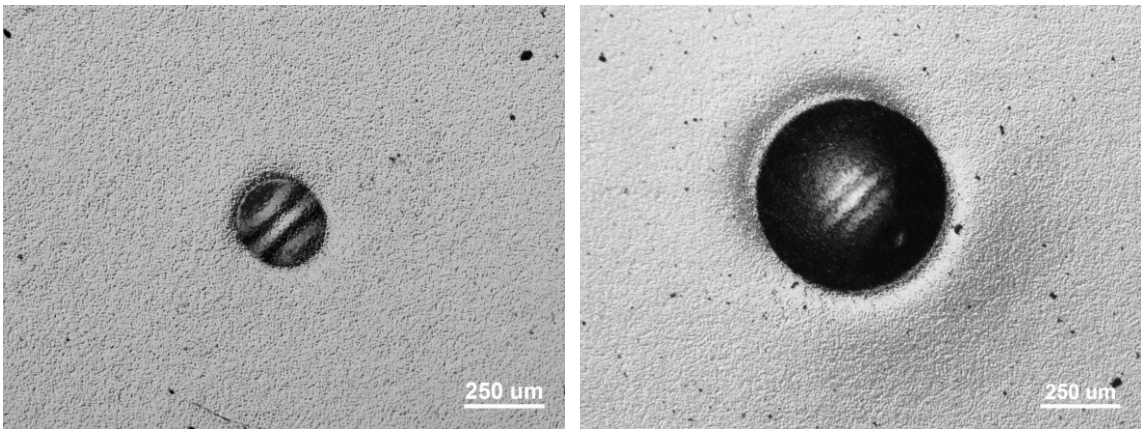

(a) (b)

Figure 6.3: Optical microscope images of a sample with 30 vol.% of binder sintered for 60 minutes, indented with a 1.98 mm indenter, for (a) 250 N and (b) 2000 N of load.

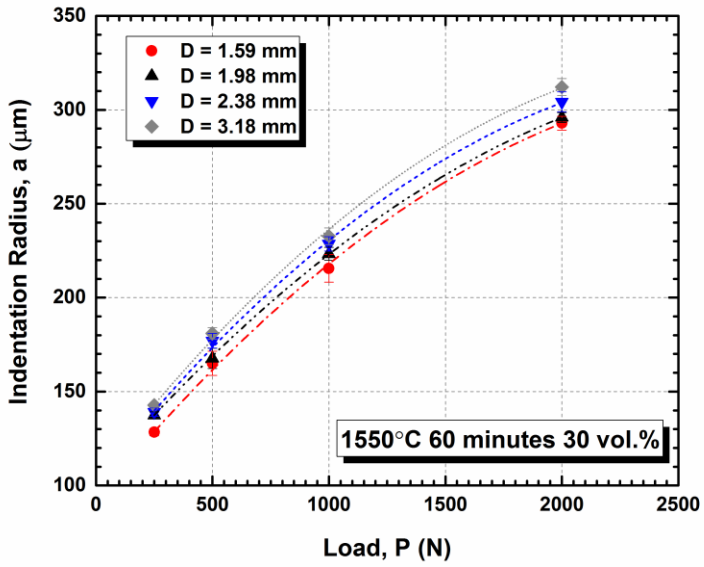

Figure 6.4: Indentation radius as a function of testing load for TiC- 30 vol.% cermet sintered for 60 minutes.

The effects of binder content on the residual indentation radius were also studied. Figure 6.5 shows a cermet sintered for 60 minutes, tested with a 1.98 mm indenter, with 10 vol.% and 30 vol.% steel binder. The indentation radius has increased slightly with the increasing binder content, as has the indentation depth. Further characterisations of the indentation depth will be discussed in the following section. Figure 6.6 shows the indentation radius variation as a function of binder content, for both of the cermets tested, using a 250 N applied load. The use of a larger indenter yields a larger indentation radius, as would be expected. The radius difference between the indents for both the cermets (i.e. 60 and 240 minutes sintering time) does not show a significant difference when the same indenter is used at the same binder content. The effects of the indenter sizes are also demonstrated. For a 1.59 mm indenter, as an example, the indentation radius has increased ~25 μm, when the binder content increased from 10 vol.% to 30 vol.%. This shown that the cermet has undergone a more severe deformation when applied with same loading conditions (indenter radius and applied load) at a higher binder content. Figure 6.7 gives a comparison of a cermet indentation versus one in a 4140/4142 steel sample.

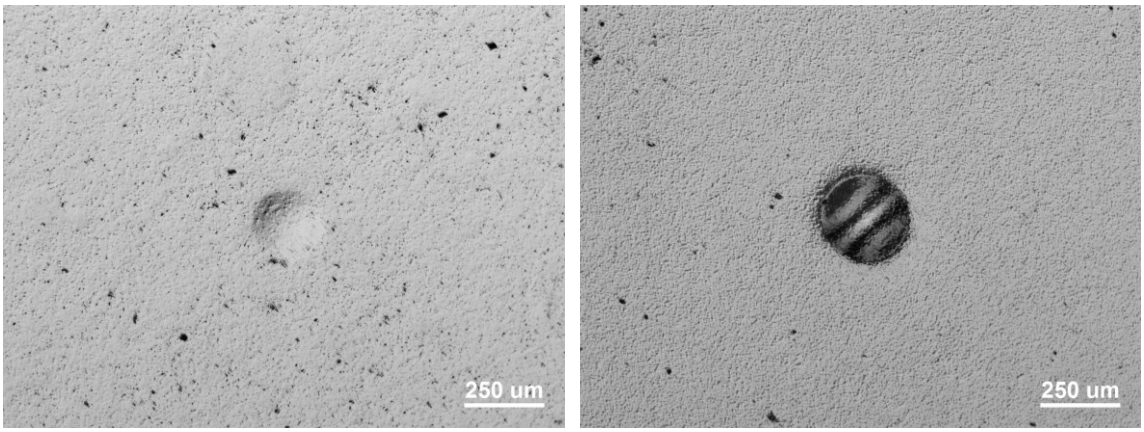

(a) (b)

Figure 6.5: Optical microscope images of a sample indented with a 1.98mm indenter, for (a) 10 vol.%/60 minutes, (b) 30 vol.%/60 minutes.

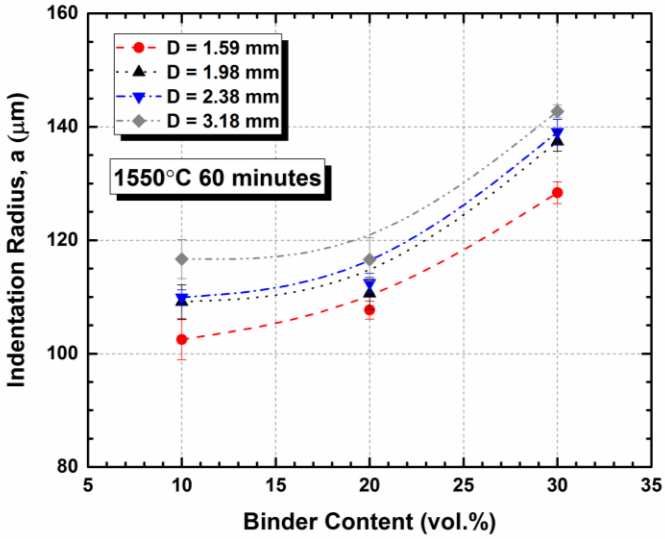

(a)

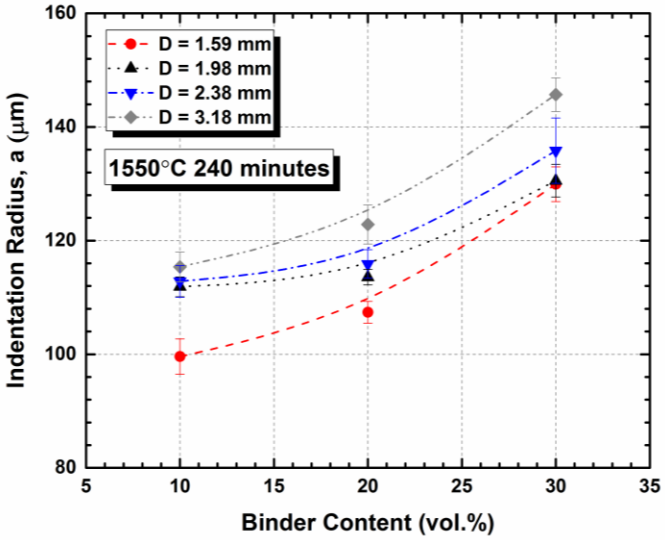

(b)

Figure 6.6: Indentation radius variation of the cermets as a function of the binder content, tested under 250 N applied load. The cermets were sintered for: (a) 60 minutes and (b) 240 minutes.

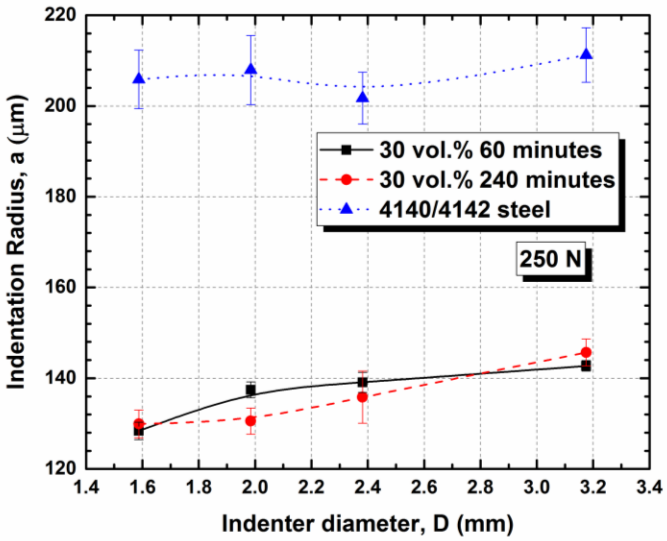

Figure 6.7: Indentation radius as a function of the indenter diameter used; only four different indenter sizes are shown in the figure for clarity. The test was performed under 250 N applied load. Note the difference between the current cermets and the steel.

6.3.2 Indentation Stress-Strain curves

As stated earlier, investigation the indentation stress-strain behaviour can help in evaluating the material's performance, understanding potential damage mechanisms, and possible even predicting the material's operational lifetime. The indentation stress is determined by Equation 6.2, the indentation strain is the ratio of contact radius to the sphere radius, a/R. The Young's modulus of the cermet was calculated based on a simple rule of mixtures, based on the constituent phases, while the cermet Poisson's ratio was estimated following Budiansky's equation [29].

The indentation stress-strain curves for both 60 minutes and 240 minutes sintering time are presented in Figure 6.8. These tests were conducted using a 250 N applied load, with various binder contents. The indenter sizes are not differentiated in these figures. The dashed lines are the Hertzian elastic response calculated according to Equation 6.2 and Equation 6.3. The materials shows an 'pseudo-elastic' response at the beginning of the curves, and then at some point begin to deviate, in a manner not disimilar to 'yielding' in a metal. For example, for the cermet sintered for 60 mintues with 10 vol.% binder, deviatation from elastic begins at ~5 GPa, while for the 30 vol.% binder sample, deviatation occurs at ~1 GPa; the corresponding hardness values for these samples are

presented in Table 6.4. With strain further increasing, the indentation stress increases as well, showing a phenomenon similar to 'strain hardening'. At this stage, the material presents an apparent 'quasi-plastic' response.

In terms of the Hertz elastic stress field [30], the maximum shear tress is located at a distance of ~0.5a beneath the surface, with a value of:

$$\tau_m = 0.48 p_m \qquad \text{Equation 6.6}$$

The 'yielding' starts when the shear stress reaches (if either Tresca or von Mises shear stress criteria are applied [30]) and value of:

$$\tau_m = Y/2 \qquad \text{Equation 6.7}$$

where Y is the yield stress of the material, and often related to the hardness, as:

$$H = cY \qquad \text{Equation 6.8}$$

where c is a 'constraint factor'; for typical metals, $c \approx 3$ [31].

Therefore, plastic deformation is expected to occur at:

$$p_m \approx 1.1Y \qquad \text{Equation 6.9}$$

According to Fischer-Cripps [15,30], the shape of a shear driven plastic zone depends on the ratio of E/Y. For high E/Y values, such as in metals, the material shows "fully plastic" behaviour, where the indentation stress-strain curve does not increase any further with continuing increasing strain. The plastic zone expands beneath and outside of the contact area, therefore more shear driven deformation is taking over, and pushing away the material from the loading axis. This is exhibited in the form of the 'pileup' phenomenon, outlined earlier. It can be shown from using 'bonded interface' samples that the deformation zone is considerably larger than the contact circle [15]. For a lower value of the ratio E/Y, the elastic portion are starting to dominate the response. The 'pileup' is less pronounced compared to the previously described example, and an 'expanding cavity' model [31-34] has been used to describe the mechanism. For relatively low E/Y values, such as in ceramics, the subsurface damage is largely constrained within the contacting surface, showing a hemispherical shape. For the current study, the 'yield stress' of the cermet could not be obtained from the relationship shown in Equation 6.8, where c = 3,

since the model is specifically for metals. Previous research [13,35] has suggested that it is adequate to determine the 'yield stress' from the point of deviation from linearity, therefore for a TiC-10 vol.% cermet, the 'yield stress' was estimated as ~5 GPa. the Young's modulus, determined from rule of mixtures is ~415 GPa, hence the ratio E/Y = 83, which is close to the value of a commercial "Macor" glass-ceramic [13] (i.e. E/Y = 85). This value is considered to be low in comparison to metals. It can be therefore be assumed that the sub-surface damage zones of TiC-stainless steel cermets also exhibit a 'hemispherical' shape, constrained within the contact area. A prior study of WC-Co cemented carbides tested three kinds of WC-Co with different grain sizes [21], indented with a polycrystalline diamond sphere radius of 5.09 mm, under testing loads ranging from 0.1 to 26 kN. That work confirmed the 'near-hemisphere' damage zone shape underneath the indenter contact, which was effectively retained in the contact circle diameter in terms of its dimension. However, this study also reported that no 'pileup' was found, since the E/Y ratio is low (value was not indicated).

A previous study [15] compared the indentation stress-strain curves obtained for a variety of materials, loaded with WC-Co spheres ranging from 1.98 to 12.7mm. The evaluated materials included a glass-ceramic (HV = 2.8 GPa), a yttria-doped HIPed silicon nitride ceramic (HV = 15 GPa), mild steel (HV = 1.1 GPa), and even the same WC-Co material as the indenter itself (HV = 19 GPa). For the silicon nitride sample (grain size ~2.0μm), yielding started around ~7.8 GPa (determined by sequential load experiments [31,36]). SEM images demonstrated that when loaded using a 1.98 mm sphere, with loads varied from 1000 N to 3000 N, the sample shows no apparent evidence of pileup, but clear ring cracks were formed on the top surfaces. The 'bonded interface' SEM images showed that the sub-surface damage expands when the load increases. The sub-surface damage zones did not expand outside of the contact area, either at the top surface or underneath. In addition, there was no evidence of ring cracks developing into cone cracks from the side view.

As outlined previously, the maximum shear stress of the indentation is expected to be located at depth of ~0.5a beneath the surface. Therefore, for a TiC-30 vol.% steel cermet, the estimated maximum shear is ~2 GPa, which will be located at a depth of ~68 μm below the surface under a 250 N applied load with a 1.98 mm diameter indenter. A

previous study applied a 'bonded interface' method to study the subsurface damage [23]. With a low applied load and high binder content, subsurface 'elastic-plastic' damage was evident; for a TiC-40 vol.% Ni_3Al sample, this occurred ~50 μm below the surface when the same test condition is applied. The difference in maximum shear stress location is potentially arising because of the significant difference in the yield strength of the binder phase. In that prior work, for TiC-20 vol.% Ni_3Al cermets, no cone cracks were observed under 1000 N applied load, for a 1.98 mm indenter. The study also found two regions of severe deformation, located directly under the indenter and deeper within the material at where the maximum shear stress is located [23]. The TiC grains were separated from the binder phase, showing interfacial debonding because of the significant deformation of the matrix. Evidence of transgranular cracking in the deformation zone is also found [23].

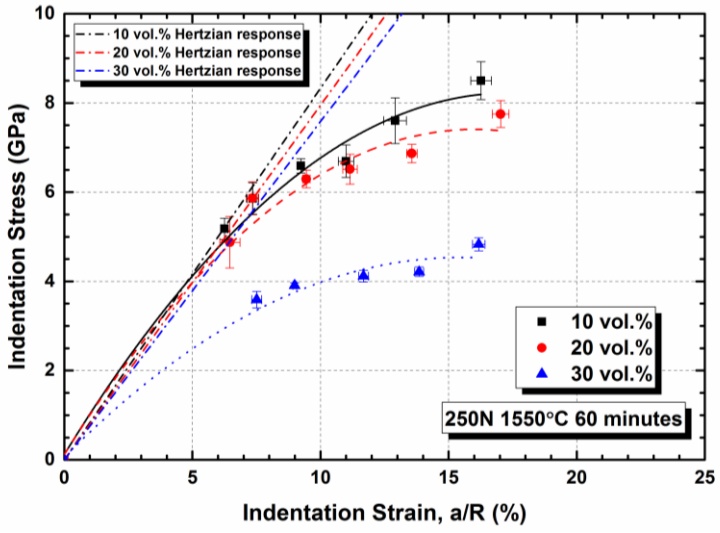

(a)

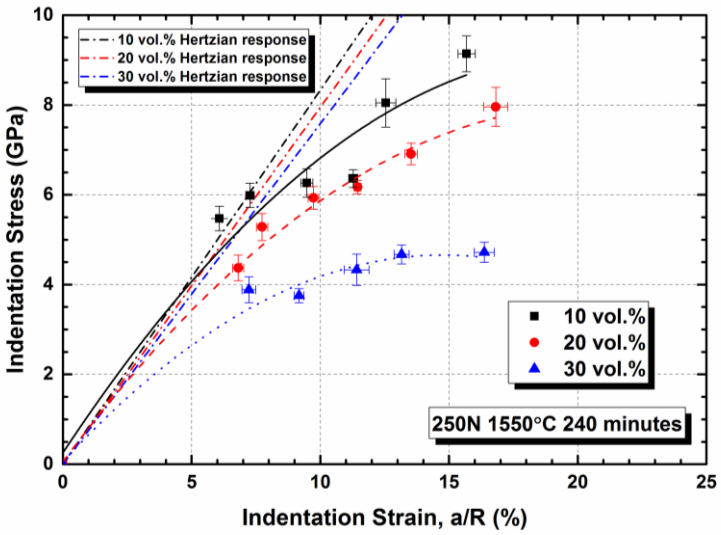

(b)

Figure 6.8: The indentation stress-strain curve and calculated Hertzian responses for cermets sintered for: (a) 60 minutes, and (b) 240 minutes. Data is from multiple indenter sizes and is not differentiated in terms of the various sizes.

Table 6.4. Hardness values of the cermets.

Binder content (vol.%)	**Hardness (GPa)**	
	1550 °C 60 minutes	**1550 °C 240 minutes**
10	19.20 ± 1.15	17.77 ± 0.80
20	13.33 ± 3.32	14.16 ± 1.12
30	7.22 ± 0.71	10.59 ± 0.83

To compare the effects of applied load on the same sample, a representative indentation stress-strain curve for TiC-30 vol.% cermet, sintered for 60 minutes, is shown in Figure 6.9(a). It can be seen that with a higher applied load, the indentation stress-strain curve deviates more severely, indicating that the relatively high amount of ductile stainless steel binder has introduced a greater amount of 'plasticity' into the system. A comparison is shown in Figure 6.9(b), between the cermet sintered after 60 minutes and the 4140/4142 steel, both loaded to 250 N and 500 N. It can be observed that even with the highest binder content (i.e. 30 vol.%), the indentation stress-strain curves of the cermets are still much 'steeper' than that of steel. Note the dashed and dot-dashed straight lines on the left

hand side of the figure, which are the 'Hertzian elastic response' curves of each of the materials, calculated according to the equation given previously.

Another important method to determine the 'quasi-plastic' response of the material is by calculating the 'brittleness index', as studied by Rhee and colleagues [4]. For brittle fracture, the maximum tensile stress is responsible for the generation of cone cracks, therefore the critical load is determined from Auerbach's law [37-40]:

$$\frac{p_c}{R} = \frac{AT^2}{E} = \text{constant} \qquad \text{Equation 6.10}$$

where T is the fracture toughness of the material ($T = K_{IC}$).

For quasi-plasticity, the critical contact load, p_Y, at yield is [41]:

$$\frac{p_Y}{R^2} = DH(\frac{H}{E})^2 = \text{constant} \qquad \text{Equation 6.11}$$

where D is:

$$D = (\frac{1.1\pi}{c})^3[\frac{3(1-\nu^2)}{4}]^2 \qquad \text{Equation 6.12}$$

Therefore, a 'brittle index' can be derived [4] as follows:

$$\frac{p_Y}{p_C} = (\frac{D}{A})(\frac{H}{E})\left(\frac{H}{K_{IC}}\right)^2 R \qquad \text{Equation 6.13}$$

When $p_Y/p_C > 1$, the material is brittle, and $p_Y/p_C < 1$, it is quasi-plastic. This indicates a correlation of the indentation behaviour with the materials' hardness and fracture toughness. A somewhat stronger dependency is observed on the hardness compared to the fracture toughness. This equation also suggests a more brittle behaviour will be observed when a larger indenter is used. Spherical indentation on the WC-Co hardmetals adapted this method [21]. Samples were loaded with incremental indentation loads, such that the initiation of the fracture, p_C, is determined as when a quarter of the circle of a ring crack is formed. The onset of plastic deformation is then measured by a mechanical profilometer, when a preset value is reached for the axial displacement, the corresponding load is p_Y.

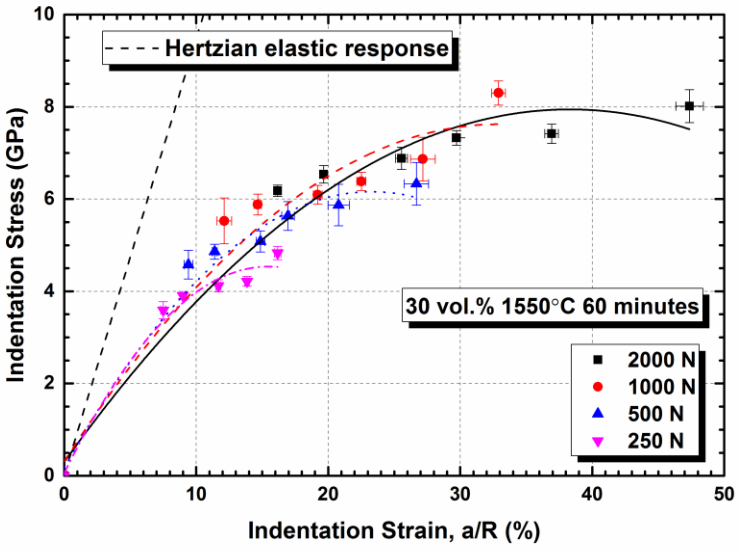

(a)

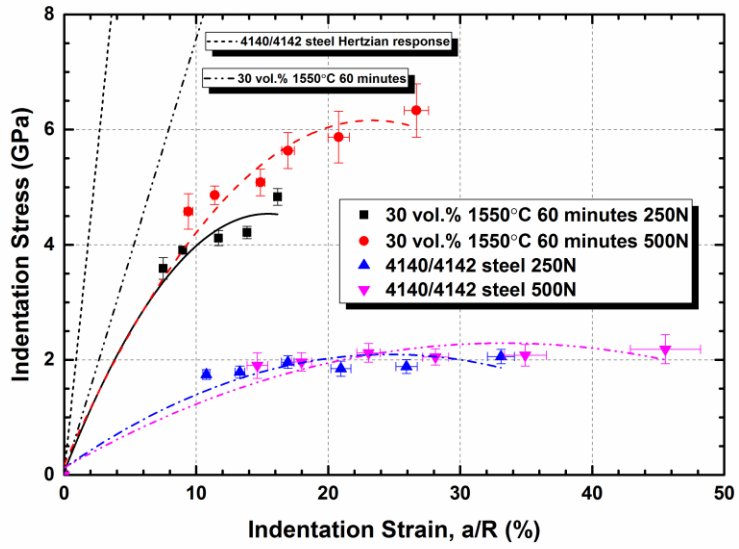

(b)

Figure 6.9: (a) Indentation stress-strain curve and calculated Hertzian response for TiC-30 vol.% cermet sintered for 60 minutes, under various testing loads, (b) Indentation stress-strain curve of TiC-30 vol.% cermet and a 4140/4142 steel sample, both tested with 250 N and 500 N of loads.

6.3.3 Contact Damage, Deformation and the Materials Response

It is important to study the contact damage and deformation of materials to fully understand the indentation mechanism and response. The optical microscopy images

presented in Figure 6.10 show the damage arising in a TiC-30 vol.% cermet, sintered for 60 minutes, with an applied load of 2000 N; the smallest (1.19 mm) and largest (3.97 mm) indenters are shown here, to provide a clear comparison. From the optical microscopy images, the 1.19 mm indenter shows a clear impression, with numerous radial cracks. Further characterisation was conducted using the SEM, and is shown in Figure 6.10(c) and (d). Higher magnification images show the edge of each indent (Figures 6.10(e) and (f)). Use of the 1.19 mm indenter generates extensive damage within the indent, with transgranular radial cracks propagating from the edge of the indentation. A very subtle 'ring' crack can be seen at the edge of the indentation site. It can be expected that, under the same load, but with a lower binder content, a more obvious 'ring' crack would be generated. The 3.97 mm indenter does not show any significant sign of cracking, but binder extrusion can be observed. The SEM images in Figure 6.10(g) and (h) show higher magnification images of the damage at the indent edge and within the contact zone of Figure 6.10(c). The radial cracks were not propagating from the edge of the contact as individual long cracks, but rather in a 'tangle' of multiple short cracks. They propagate through the TiC grains while the steel binder ligaments remain intact. However, the crack trajectories travelling through the steel binder phase can be seen, providing clear evidence of the toughening effects of the ductile phase. The damage at the centre of the contact zone shows extensive cracking of the TiC grains. Very few intergranular cracks can be observed, suggesting a shear driven mechanism. The binder phase is clearly extruded from between the TiC grains.

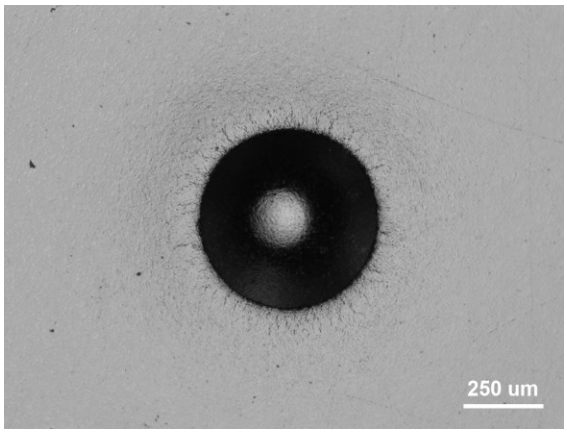
250 um

(a)

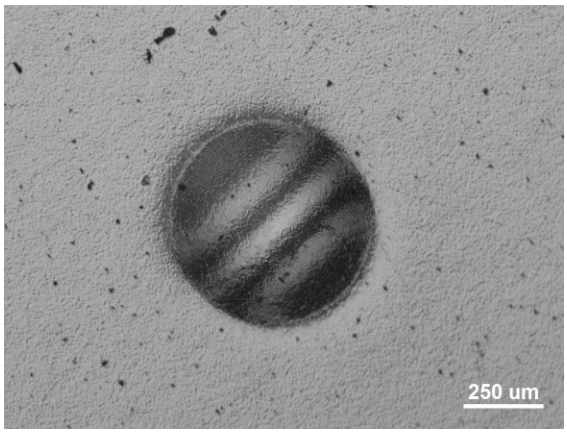
250 um

(b)

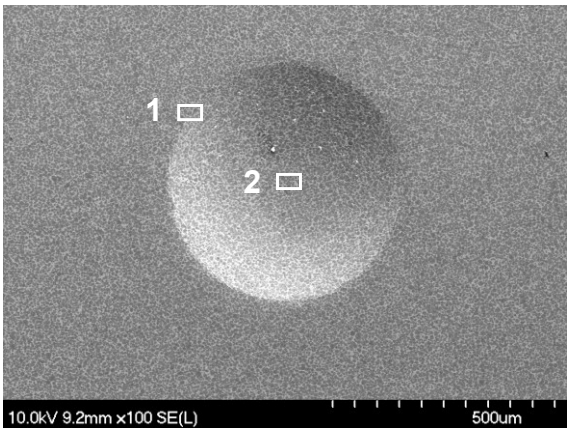
1
2
10.0kV 9.2mm x100 SE(L)
500um

(c)

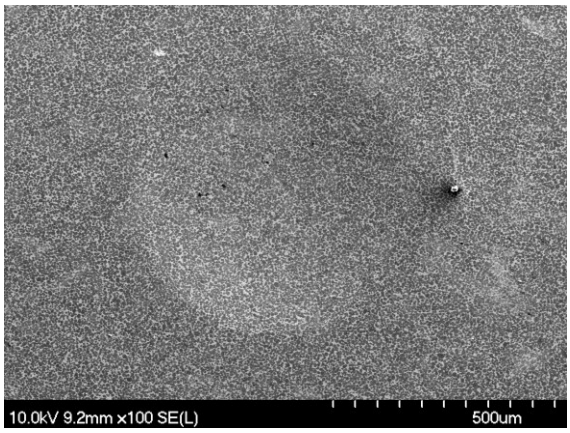
10.0kV 9.2mm x100 SE(L)
500um

(d)

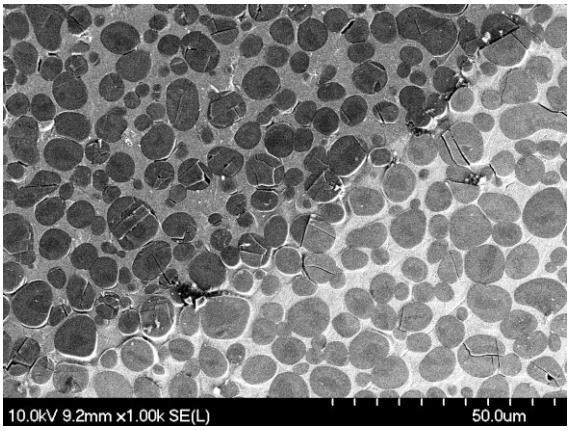
10.0kV 9.2mm x1.00k SE(L)
50.0um

(e)

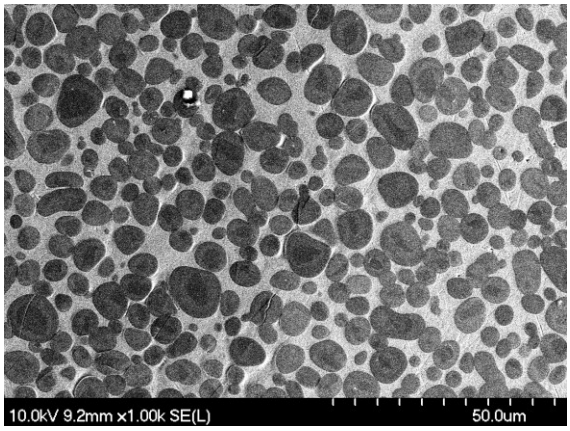
10.0kV 9.2mm x1.00k SE(L)
50.0um

(f)

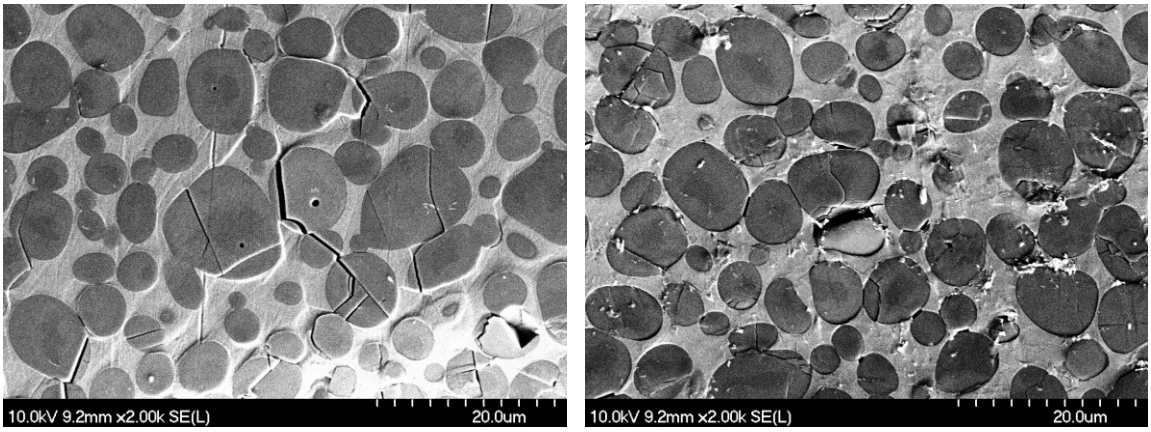

(g) (h)

Figure 6.10: Optical microscopy images of a TiC-30 vol.% cermet, indented with a 2000 N applied load, using a: (a) 1.19 mm, and (b) 3.96 mm indenter. (c,d) SEM micrographs of the indents shown in (a) and (b), respectively. (e,f) Higher magnification SEM images of the edge areas for the corresponding images for (c) and (d), respectively; the region 'inside' the indent are shown in the left top corner for both of the images. (g,h) Radial crack at the edge and at the centre of the contact, respectively, for the TiC cermet sample shown in (c) as region '1' and '2'.

Further analysis was conducted using the optical profilometer in order to determine the indentation depth and to calculate the indentation volume of the impressions. Representative, pseudo three-dimensional images from both the 1.19 mm and 3.97 mm indenters are shown in Figure 6.11. It should be noted that the aspect ratio of the images is 1:1:6 in the X:Y:Z axes, respectively, in order to give a clear indication of the difference in depth for the Z direction. In this instance, the measured top (plane) to bottom depth for the 1.19 mm indenter, is ~ 46.86 μm and ~14.67 μm for the 3.97 mm indenter. The correlation between the indentation depth and the applied load is shown in Figure 6.12. The depth increased linearly with increasing load, in agreement with a previous study [42].

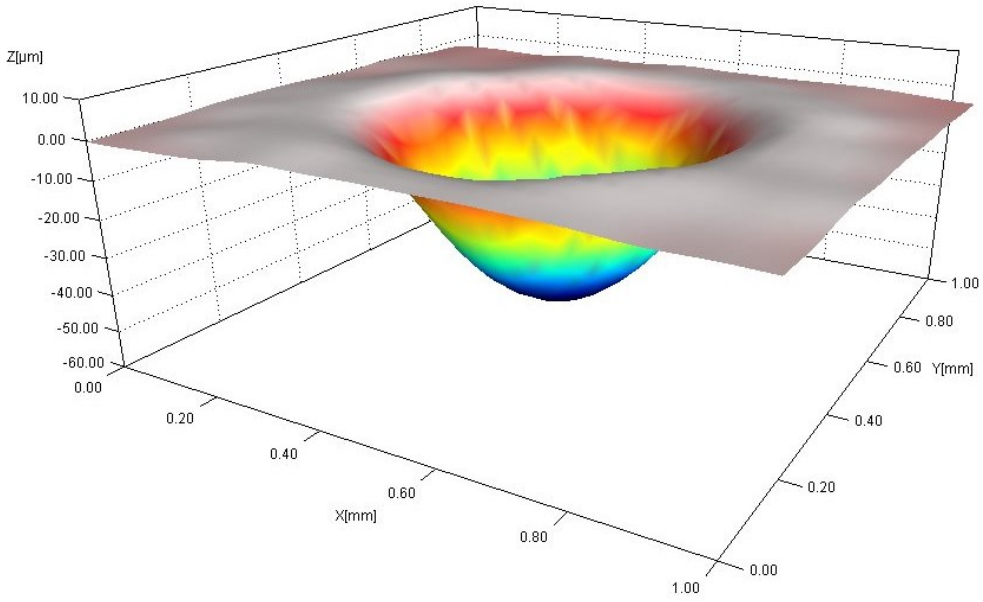

(a)

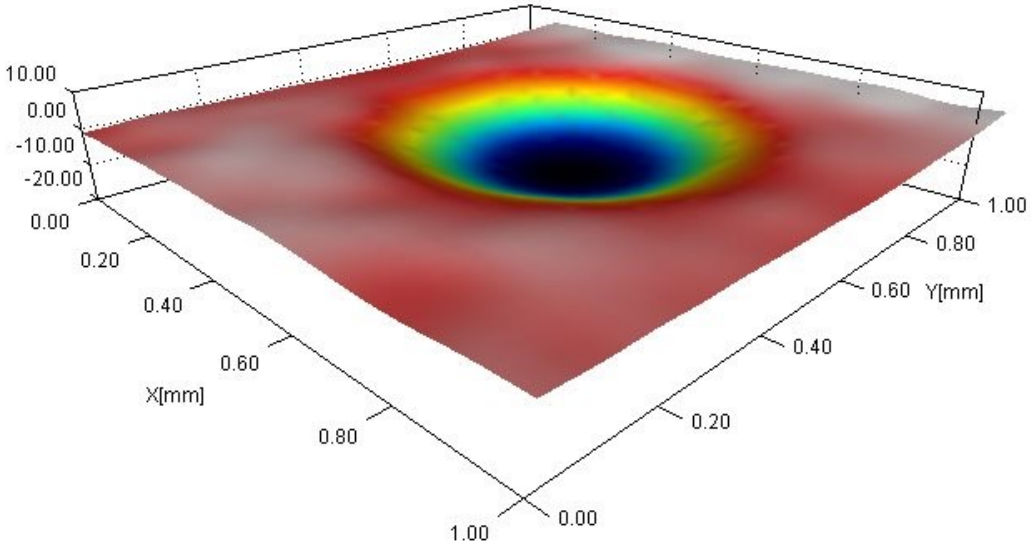

(b)

Figure 6.11: Pseudo colour 3D images of the indents in Figure 6.10.

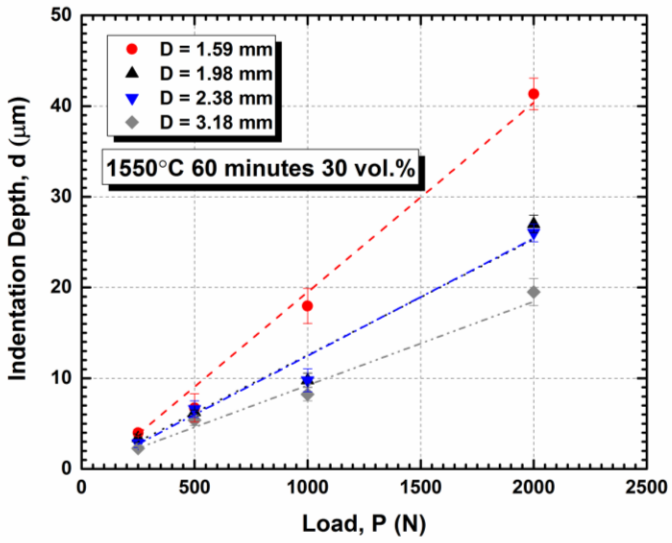

Figure 6.12: Representative curves of the indentation depth and applied load, with various indenters.

As mentioned earlier, the peak deflections, δ, that occur during each indentation test were recorded, therefore a comparison between the residual impression (i.e. the final indentation depth) and the peak deflection can be undertaken. This information is provided in Figure 6.13(a,b) for cermets sintered at 60 minutes, as a representative example. It can be seen that the peak deflections are significantly larger than the final residual indents; for some of the indenters it is essentially an order of magnitude higher. This shows the majority of the material deformation is elastic, and is mostly recovered after unloading. A small portion of the residual deformation is plastic. The indentation depth increases with increasing binder content, as anticipated, since the fraction of high elastic modulus TiC phase has decreased. The indent depths also exhibit an inverse relationship with the indenter size. However, for the peak deflections, these changes are less obvious.

According to the original Hertz theory, if the contact bodies are elastic, the deflection, δ, is given as:

$$\delta = \frac{a^2}{R} \qquad \text{Equation 6.14}$$

As an example, for a TiC-10 vol.% cermet, loaded to 250 N with a 1.98 mm indenter, the recorded peak deflection is ~28 μm and the measured 'contact radius' is ~109 μm. If the

contact is fully elastic, for the 1.98 mm indenter (R = 992 µm), the deflection should be ~12 µm, which is less than half of the recorded value. This confirms that the material is showing an apparent 'elastic-plastic' behaviour. The elastically deformed material will try to return to the original shape, but is constrained by the plastic deformation zone, and a residual stress is left within the loaded material [30]. It has been previously demonstrated that the contact radius between fully loaded and fully unloaded remain virtually the same [30,43], therefore the difference between depth is due to the elastic recovery of the material [30]. A schematic representation of elastic-plastic contact with a sphere is shown in Figure 6.14. It can be seen that the difference between the total depth and the residual impression depth is noted as an elastic displacement, h_e.

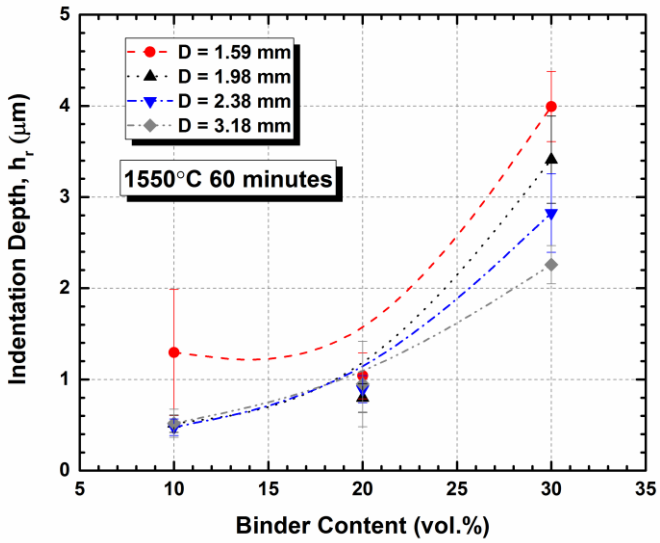

(a)

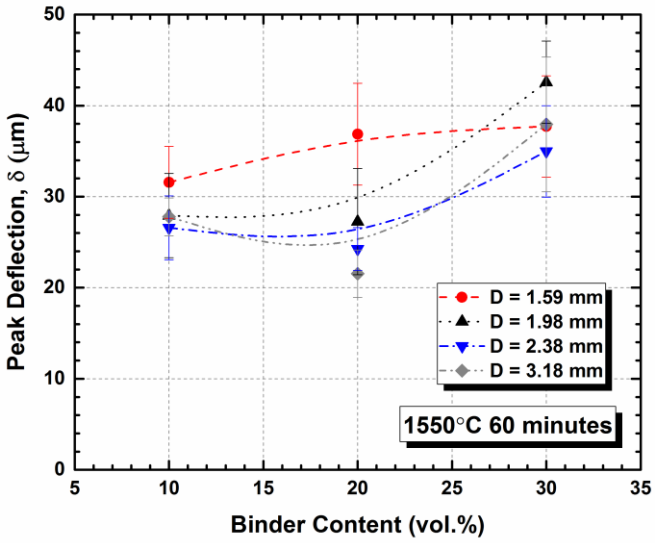

(b)

Figure 6.13: (a) The indentation depth or the 'depth of residual impression', h_r, as a function of binder content (cermets sintered for 60 minutes, after loading to 250 N), and (b) The peak deflection, δ, as a function of binder content (cermets sintered for 60 minutes, after loading to 250 N).

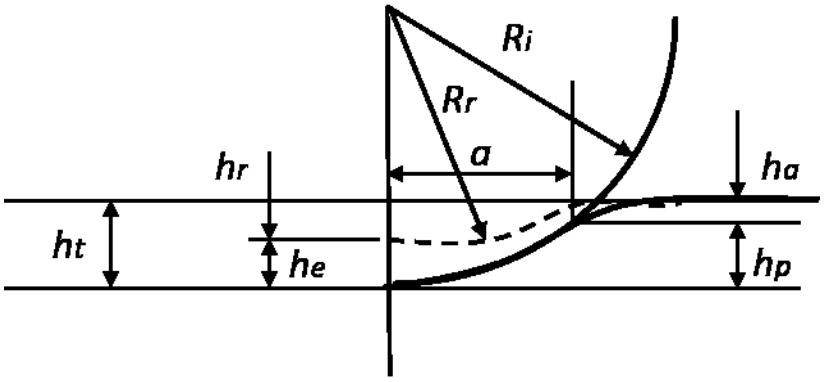

Figure 6.14: Schematic figure of an elastic-plastic indentation, using a spherical indenter: h_t is the total indentation depth, h_r is the depth of the residual indents, h_e is the depth with the elastic unloading, and h_p is the depth at full loading.

With the indentation depth obtained, the indentation volume for each sample was determined. Figure 6.15 shows a comparison for the cermets sintered for 60 and 240

minutes, loaded to 250 N. It is shown that for a fixed binder content, a smaller indenter tends to produce a larger indentation volume. The cermets sintered for 60 minutes appear to have smaller indentation volume at 10 and 20 vol.% of binder content, but the volume increased dramatically with a higher binder content, and finally they have a larger indent volume than the cermets sintered for 240 minutes.

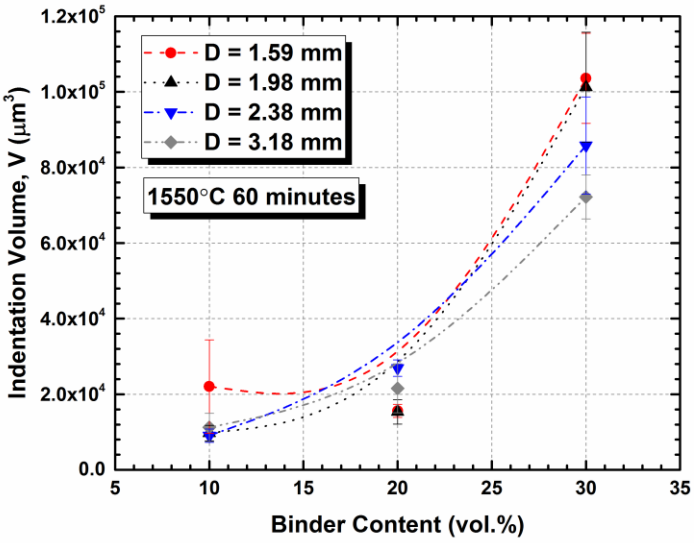

(a)

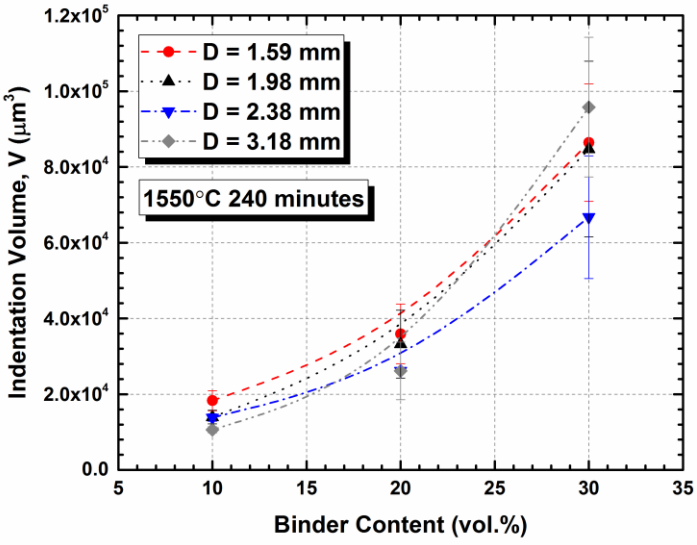

(b)

Figure 6.15: Indentation volume as a function of binder content for cermets sintered for: (a) 60 minutes and (b) 240 minutes. All samples were loaded to 250 N.

6.4 Conclusions

The current study has provided experimental data for the case of Hertzian contact between WC-Co spheres and TiC-316-L cermets. A standard 4140/4142 steel sample was also tested to provide a baseline. The sintered samples were characterised with SEM. Microstructure parameters were calculated as they are important in evaluating mechanical properties, it was found that the values were close for cermets sintered at 1550 ºC for 60 and 240 minutes. After loaded with a series of indenter and load for cermets binder phase ranging from 10 to 30 vol.%, the indented samples were examined with DIC optical microscope, and a slight 'pileup' effect was found for samples subjected at high load with high binder content. The contact radius of the residual impressions were recorded and increased with applied load, binder content, and the size of the indenter used. Indentation stress-strain curves of the cermets were plotted, and the Hertzian elastic responses of the materials were also plotted for comparative purposes. The 'quasi-plastic' behaviour of the cermets was categorised into three regions, when studying the indentation stress-strain curves of the materials: (i) pseudo-elastic, (ii) elastic-plastic, and (iii) fully pseudo-plastic. The 'quasi-plastic' behaviour of the cermets is due to the formation of microcracks in the TiC grains and the plasticity of the steel binder phase. Optical microscopy and SEM were used to observe the residual indentation sites, the cermets shows 'ring' cracks at low binder content, and radial cracks propagates from the edge of the contact. Cracks trajectories also suggested the toughening effects of the binder. An optical profilometry system was used to quantify dimensional features of the indents. Indentation depths were obtained from the optical profilometer and was found increases with both binder content and applied load. Further calculations were made to assess the residual indentation volume, which follows the same trend. The peak deflection recorded by the extensometer and the measured residual indentation depth were compared, and was found significant larger than the final impression depth, which indicate the material shows elastic recovery. Peak deflection for 'ideal' elastic response was also calculated and compared with the indentation depth, and confirmed the 'quasi-plastic' behaviour of the current material, which is due to the microcrack formation and plasticity of the metal binder phase.

6.5 References

1. A.C. Fischer-Cripps, R.E. Collins, The probability of hertzian fracture, J. Mater.Sci. 29 (1994) 2216-2230.
2. A.C. Fischer-Cripps, Predicting Hertzian fracture, J. Mater. Sci. 32 (1997) 1277-1285.
3. B.R. Lawn, Indentation of ceramics with spheres: A century after Hertz, J. Am. Ceram. Soc. 81 (1998) 1977-1994.
4. Y. Rhee, H. Kim, Y. Deng, B.R. Lawn, Brittle fracture versus quasi plasticity in ceramics: A simple predictive index, J. Am. Ceram. Soc. 84 (2001) 561-565.
5. B.R. Lawn, N. P. Padture, H. Cait, F. Guiberteau, Making ceramics "ductile", Science 263 (1994) 1114-1116.
6. F. Guiberteau, N. P. Padture, H. Cai, B.R. Lawn, Indentation fatigue, Philos. Mag. A 68 (1993) 1003-1016.
7. H. Cai, M. A. S. Kalceff, B. R. Lawn, Deformation and fracture of mica-containing glass-ceramics in Hertzian contacts, J. Mater. Res. 9 (1994) 762-770.
8. F. Guiberteau, N.P. Padture, B.R. Lawn, Effect of grain size on Hertzian contact damage in alumina, J. Am. Ceram. Soc. 77 (1994) 1825-1831.
9. N.P. Padture, B.R. Lawn, Toughness Properties of a silicon carbide with an *in Situ* induced heterogeneous grain structure, J. Am. Ceram. Soc. 77 (1994) 2518-2522.
10. A. Pajares, L. Wei, B.R. Lawn, D.B. Marshall, Damage accumulation and cyclic fatigue in mg-PSZ at Hertzian contacts, J. Mater. Res. 10 (1995) 2613-2625.
11. H.K. Xu, L. Wei, N.P. Padture, B.R. Lawn, Effect of microstructural coarsening on Hertzian contact damage in silicon nitride, J. Mater. Sci. 30 (1995) 869-878.
12. A.C. Fischer-Cripps, B.R. Lawn, Indentation stress-strain curves for “quasi-ductile” ceramics, Acta Mater. 44 (1996) 519-527.
13. A.C. Fischer-Cripps, Elastic-plastic behaviour in materials loaded with a spherical indenter, J. Mater. Sci. 32 (1997) 727-736.
14. G. Care, A.C. Fischer-Cripps, Elastic-plastic indentation stress fields using the finite-element method, J. Mater. Sci. 32 (1997) 5653-5659.
15. A.C. Fischer-Cripps, B. R. Lawn, Stress analysis of contact deformation in quasi-plastic ceramics, J. Am. Ceram. Soc. 79 (1996) 2609-2618.

16. H.K. Xu, S. Jahanmir, Y. Wang, Effect of grain size on scratch interactions and material removal in alumina, J. Am. Ceram. Soc. 78 (1995) 881-891.
17. H.K. Xu, S. Jahanmir, Scratching and grinding of a machinable glass-ceramic with weak interfaces and rising *T*-curve, J. Am. Ceram. Soc. 78 (1995) 497-500.
18. H. Cai, S.M.A. Kalceff, B.M. Hooks, B.R. Lawn, K. Chyung, Cyclic fatigue of a mica-containing glass-ceramic at Hertzian contacts, J. Mater. Res. 9 (1994) 2654-2661.
19. N.P. Padture, B.R. Lawn, Contact fatigue of a silicon carbide with a heterogeneous grain structure, J. Am. Ceram. Soc. 78 (1995) 1431-1438.
20. N.P. Padture, B.R. Lawn, Fatigue in ceramics with interconnecting weak interfaces: A study using cyclic Hertzian contacts, Acta Metall. Mater. 43 (1995) 1609-1617.
21. H. Zhang, Z.Z. Fang, J.D. Belnap, Quasi-plastic deformation of WC-co composites loaded with a spherical indenter, Metall. Mater. Trans. A. 38 (2007) 552-561.
22. H. Zhang, Z.Z. Fang, Characterization of quasi-plastic deformation of WC-co composite using Hertzian indentation technique, Int. J. Refract. Met. Hard Mater. 26 (2008) 106-114.
23. R.B. Collier, K. P. Plucknett, Spherical indentation damage in TiC–Ni_3Al composites, Int. J. Refract. Met. Hard Mater. 30 (2012) 188-195.
24. D.A. Doman, R. Bauer, A. Warkentin, Optical microscopy-aided indentation tests, J. Eng. Mater. Technol. 130 (2008) 011008.
25. D. Anderson, A. Warkentin, R. Bauer, Simulation of deep spherical indentation using Eulerian finite element methods, J. Tribol. 133 (2) 021401.
26. C. Jin, K. P. Plucknett, Microstructure instability in TiC-316L stainless steel cermets, Int. J. Refract. Met. Hard Mater. 58 (2016) 74-83.
27. B.R. Lawn, D.B. Marshall, Nonlinear stress-strain curves for solids containing closed cracks with friction, J. Mech. Phys. Solids 46 (1998) 85-113.
28. H. Zhang, Q. Lu, L. Zhang, Z. Z. Fang, Dependence of microcrack number density on microstructural parameters during plastic deformation of WC–Co composite, Int. J. Refract. Met. Hard Mater. 28 (2010) 434-440.
29. B. Budiansky, On the elastic moduli of some heterogeneous materials, J. Mech. Phys. Solids 13 (1965) 223-227.

30. A.C. Fischer-Cripps, Introduction to contact mechanics, Springer, New York, 2000.
31. D. Tabor, The hardness of metals, Clarendon Press, Oxford, 1951.
32. R. Hill, The mathematical theory of plasticity, Clarendon Press, Oxford, 1950.
33. D.M. Marsh, Plastic flow and fracture of glass, P. Roy. Soc. Lond. A. Mat. 282 (1964) 33-43.
34. K.L. Johnson, Contact mechanics, Cambridge University Press, Cambridge, UK, 1985.
35. M.V. Swain, J. T. Hagan, Indentation plasticity and the ensuing fracture of glass, J. Phys. D. Appl. Phys. 9 (1976) 2201-2214.
36. R.M. Davies, The determination of static and dynamic yield stresses using a steel ball, P. R. Soc. A. Math. Phy.197 (1949) 416-432.
37. F. C. Frank, B.R. Lawn, On the theory of Hertzian fracture, P. R. Soc. A. Math. Phy. 299 (1967) 291-306.
38. B.R. Lawn, R. Wilshaw, Indentation fracture: Principles and applications, J. Mater. Sci. 10 (1975) 1049-1081.
39. R. Mouginot, D. Maugis, Fracture indentation beneath flat and spherical punches, J. Mater. Sci. 20 (1985) 4354-4376.
40. C. Kocer, R. E. Collins, Angle of Hertzian cone cracks, J. Am. Ceram. Soc. 81 (1998) 1736-1742.
41. R. Mouginot, Blunt or sharp indenters: A size transition analysis, J. Am. Ceram. Soc. 71 (1988) 658-661.
42. Sergejev, F., M. Petrov, and J. Kübarsepp, Determination of the mechanical properties of the carbide composites by spherical indentation, Proc. 8th International DAAAM Baltic Conference “INDUSTRIAL ENGINEERING. 2012.
43. K.L. Johnson, The correlation of indentation experiments, J. Mech. Phys. Solids 18 (1970) 115-126.

Chapter 7 The Effects of TiC Grain Size and Steel Binder Content on the Reciprocating Wear Behaviour of TiC-316L Stainless Steel Cermets

Chukwuma C. Onuoha[+@], Chenxin Jin[+], Zoheir N. Farhat, Georges J. Kipouros[#] and Kevin P. Plucknett*

Dalhousie University, 1360 Barrington Street, Materials Engineering Program, Department of Process Engineering and Applied Science, B3H 4R2, Nova Scotia, Canada

Status: *Published*: Wear, 350-351 (2016) 116-129.

Abstract

TiC-based cermets are heavily utilised in applications demanding good resistance to both wear and corrosion. In the current work, TiC-stainless steel (grade 316L) cermets have been developed, with the TiC grain size varied through heat-treatment, for steel binder contents between 10 and 30 vol. %. Microstructural analysis showed mean TiC grain sizes of ~4 and 10 μm, respectively, for fine- and coarse-grained cermets, with the grain size nominally consistent as a function of binder content. Sliding wear resistance was assessed in a reciprocating motion, using a WC-Co counter face sphere paired against the TiC cermets. Overall, the fine-grained cermets exhibit better wear resistance and hardness. The specific wear rate was seen to increase with applied load and/or binder content, for both fine- and coarse-grained materials. SEM and FIB microscopy were used to assess the microstructural changes occurring during wear. A two- to three-body abrasive wear transition was apparent, together with the formation of a surface tribolayer, which highlights a further evolution to an adhesive wear mechanism. The tribolayer showed incorporation of a high concentration of O, which increased with the applied load, together with a predominance of the binder constituents.

Keywords: Cermets; Abrasive wear; Adhesive wear; Tribolayer; Dry sliding; Scanning electron microscopy; Focused ion beam microscopy

[+]These authors contributed equally to the work

*****Contact author email: kevin.plucknett@dal.ca

[@]Now at PureHM (Hunter McDonnell Pipeline Services Inc), Edmonton, AB, Canada

[#]Now at University of Saskatchewan, Saskatoon, SK, Canada

7.1 Introduction

Ceramic-metal composites, or cermets, are used in a broad variety of industries, including chemical processing, aerospace, automotive, pulp and paper, oil and gas, etc, due to the high wear resistance. Titanium carbide (TiC) based cermets show considerable potential for substitution into applications where tungsten carbide-cobalt (WC-Co) based materials are more commonly used [1-3]. TiC-based cermets benefit significantly from reduced mass and better high temperature properties, in comparison to WC-Co. Although adding the secondary ductile phase results in a reduction of the hardness [4], the improvement in toughness and wear resistance significantly outweighs this. It is generally assumed that the wear behaviour of cermets is a direct function of both the hardness and toughness of the composite, and that optimum wear behaviour is obtained when both of these properties are fully maximised [3-5].

In terms of specific TiC-based cermet systems, a wide variety of metallic binders have been employed. However, only limited attention has been paid to steel variants, particularly stainless steels. For example, 316-grade stainless steel has excellent corrosion resistance, combined with good mechanical (i.e. tensile) properties. However, the wear resistance is relatively poor, as the steel has a low hardness, and 316 is therefore susceptible to many common forms of wear and contact damage, which limits use in tribological applications [6,7]. In order to enhance the wear resistance of stainless steels, several authors have reported an improvement through the incorporation of carbide particles, such as TiC, to form metal matrix composites [8-10].

The cermet microstructural features that influence the mechanical and tribological behaviour include the metal binder content, the average carbide grain size, the binder mean free path (i.e. the thickness of the binder ligaments) and the contiguity of the carbide grains [11]. Decreasing either the binder content or the carbide grain size typically increases the hardness of the cermet; an increase in hardness is invariably accompanied by decrease in bulk fracture toughness [12-15]. For instance, it has been shown that carbide size influences the abrasive and erosive wear rate and, when comparing an equivalent carbide volume fraction of fine- and coarse-grained particles, cermets prepared with fine-

grained carbide particles provide superior wear resistance, as the binder mean free path is decreased [3,9,10,16].

To date, studies of the effects of grain size on the wear behaviour of cermets have primarily been conducted on WC-Co [11,17-24]. Typically, an improvement in hardness and wear resistance with a decrease of the carbide grain size and Co binder content is observed, while the fracture toughness invariably shows the opposite trend [11,17,22,23]. If the carbide size is decreased for a fixed binder content, the binder mean free path is also reduced, resulting in greater constraint against deformation, increased hardness and a reduced tendency for binder phase extrusion. These features invariably result in an increase in the wear resistance. Conversely, an improvement in fracture toughness with increased in carbide grain size or binder mean free path is attributed to a decrease in the constraint that limits plastic deformation of the metallic binder ahead of the propagating crack [11,18,19].

In order to devise an alternative route to further improve the wear performance of novel TiC-316L steel based cermets, which could potentially be used as an wear and/or corrosion resistant coating or facing (especially in the mining, oil and gas, or aerospace industries), the present study is aimed at investigating the effects of grain size on the dry reciprocating wear behaviour of these new materials. Melt infiltration has been employed to fabricate the cermets, with processing conditions varied to give both fine- and coarse-grained TiC, with the stainless steel binder content varied from 10 to 30 vol. %.

7.2 Experimental Procedure

7.2.1 Sample Preparation

The TiC powder was obtained from Pacific Particulate Materials Ltd. (Vancouver, BC, Canada), and had a mean particle size of ~1.25 μm [25]. The 316L stainless steel used for the binder was sourced in powder form from Alfa Aeser (Ward Hill, MA, USA), with a nominal particle size of -100 mesh. Disk-shaped TiC pellets (~31.75 mm diameter by ~4 mm thick) were first prepared by uniaxial pressing at ~35 MPa, then vacuum bagged, and subsequently compacted by cold isostatic pressing at ~220 MPa. Following compaction,

the TiC disks were weighed and a pre-determined amount of 316L stainless steel was added on top of the pellet. This approach allows control of the steel binder volume fraction, which was varied from 10 to 30 vol. %. The TiC preforms and steel powder were held in a closed alumina crucible on bubble alumina during melt infiltration. Two different vacuum heat-treatment cycles were developed in order to produce the fine- or coarse-grained microstructures. For the fine-grained cermets melt infiltration was performed at 1475°C for 15 minutes, while for the coarse-grained materials it was conducted at 1550°C for 240 minutes. The heating cycle was performed under a dynamic vacuum (better than 20 milliTorr), inside a graphite resistance furnace (Materials Research Furnaces, Suncook, NH, USA). The nominal heating and cooling rates were 10°C/min and 25°C/min, respectively.

7.2.2 Materials Characterisation Procedure

Following melt-infiltration, the densities of the TiC-316L cermets were determined in water using the immersion method. The cermets were initially diamond ground, and then polished to a 0.25 μm surface finish using diamond paste. Microstructure assessment was conducted using a field emission scanning electron microscope (SEM; Model S-4700, Hitachi High Technologies, Tokyo, Japan), with chemical analysis performed in the SEM using energy dispersive X-ray spectroscopy (EDS; Model X-Max/Inca, Oxford Instruments, Concord, MA, USA).

The TiC grain size, d_c, was determined using the linear intercept method [26], from digital SEM images, with ~300 grains measured for each compositional/grain size variant. In addition, the contiguity, C, and binder mean free path length (or binder intercept distance), d_b, were calculated from these micrographs. The contiguity is a measure of the ratio of carbide-carbide to carbide-binder interfaces, and was determined following [27]:

$$C = \frac{2N_{c/c}}{2N_{c/c} + N_{c/b}} \qquad \text{Equation 7.1}$$

where $N_{c/c}$ and $N_{c/b}$ are the number of carbide/carbide (TiC/TiC) and carbide/binder (TiC/316L) interfaces that are intercepted per unit length, respectively. Based on the

contiguity and grain size information, the binder mean free path can then be determined following [27]:

$$d_b = \frac{1}{1-C}\left[\frac{V_b}{V_c}\right]d_c \qquad \text{Equation 7.2}$$

where V_b and V_c are the respective volume fractions of 316L binder and TiC. The hardness of the densified cermets was determined using Vickers indentation (Model V-100A, Leco Corporation, St. Joseph, MI, USA), with a 1 kg load used in order to avoid sample cracking at the corners of the indenter; a minimum of 6 indentations were made for each composition.

7.2.3 Wear Testing and Evaluation

The reciprocating wear response of the cermets was assessed using a universal micro tribometer (Model UMT-1, Bruker Corp., Campbell, CA, USA), with a 6.35 mm diameter WC-Co counter-face sphere (Grade 25 with 6 wt. % Co (~10.2 vol.% Co), subsequently referred to as WC-6Co; McMaster-Carr, Aurora, OH, USA) sliding against a flat test sample in a reciprocating motion. The use of WC-6Co presents an aggressive counter face pairing, resulting in measurable specific wear rates for these wear resistant materials, and allows comparison with a variety of other studies also using WC-Co as the pairing material. A fixed stroke length of 5.03 mm was utilised, oscillating at a frequency of 20 Hz; the sliding geometry was selected to mimic a number of industrial applications, for example the coatings used in aircraft landing gear components (as replacement for hard chromium plating) and wing flap tracks. Wear testing was performed at room temperature (21 ± 2ºC), under a relative humidity of 40-55%. Applied loads of 20 to 80 N were used for the reciprocating tests, held for a period of two hours; this results in a total sliding distance of ~1.45 km. Further details regarding the wear testing procedure are outlined in previous publications [28,29]. The wear tracks were examined using optical profilometry (Model PS50 Optical Profilometer, Nanovea, Irvine, CA) to quantify the

volume of material removed. Based on the volumetric wear loss, the specific wear rate, *k*, was then determined following the basic Lancaster relationship [30]:

$$k = \frac{V}{PD} \qquad \text{Equation 7.3}$$

where V is the volume of material removed (in mm^3), P is the applied load (in N), and D is the total sliding distance (in m). While single tests were performed in the present work, a separate study using the same wear testing system and counter face material showed a maximum standard deviation of ~25 % for sets of three repetitions [31]. SEM/EDS was then used to assess microstructural features of the wear tracks and related wear debris, along with the WC-6Co counter face sphere. Localised, sub-surface damage was examined by micro-machining using a focused ion beam microscope (FIB; Model FB-2000A, Hitachi High Technologies, Tokyo, Japan). In this instance a tungsten protective strip is first deposited next to the area of interest, and then the adjacent surface region is milled using gallium ions (30 kV accelerating voltage) within the FIB. This allows subsequent examination of the immediate sub-surface region within the SEM, with the FIBed samples viewed at 30° tilt relative to the original FIB orientation.

7.3 Results and Discussion

7.3.1 Densification, Microstructure and Hardness of the Composites

Using melt-infiltration, the cermets were invariably sintered to greater than 99 % of theoretical density (Figure 7.1). In this instance the values determined for the theoretical densities were based on a simple rule-of-mixtures for the initial component phases. It is apparent that some densities appear to exceed 100 % of theoretical. This is likely due to compositional modification during sintering, which would slightly change the theoretical density. The apparent decrease in density for the coarse-grained cermets is due to a combination of compositional change and volatilisation losses (up to ~1.5 wt.% for the highest binder contents in the present samples); these general aspects are discussed in more detail in a recent paper focusing on microstructural instability in similar TiC-316L

cermets [32]. Typical SEM images of the TiC-316L cermets, as a function of both binder content and carbide grain size (i.e. fine- and coarse-grained), are shown in Figure 7.2, and confirm the high sintered densities. The microstructure for both the fine- and coarse-grained cermets is characteristically uniform, with no evidence for abnormal growth of the TiC grains. The homogeneous distribution of the TiC particles within the steel binder helps to ensure isotropic mechanical properties and uniform distribution of stresses in the sintered cermets [3]. It is apparent from Figure 7.2 that sintering at 1475°C for 15 minutes results in a relatively complex, non-equilibrium grain morphology (i.e. a clear deviation from moderately spheroid grains), with irregular shapes and even hollow 'O' and 'C'-shaped grains. This deviation from nominally spherical TiC grains will result in a higher interfacial area between the carbide and binder phases when processing under such conditions.

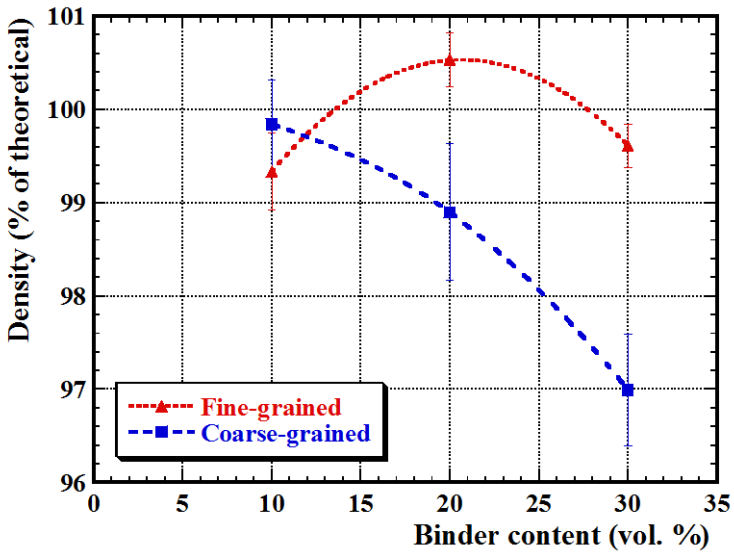

Figure 7.1: The measured densities of the fine- and coarse-grained TiC-316L cermets, as a function of the binder content (theoretical densities were estimated using a simple rule-of-mixtures for the constituent phases).

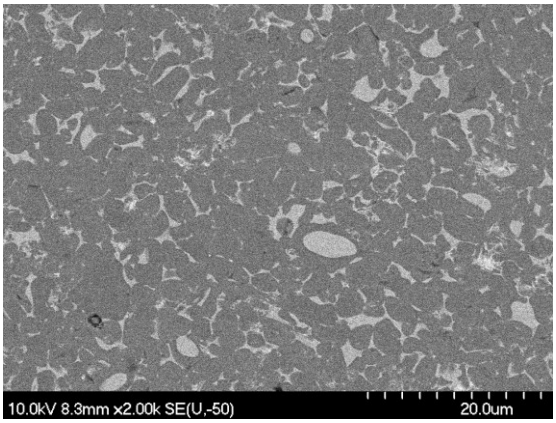

(a)

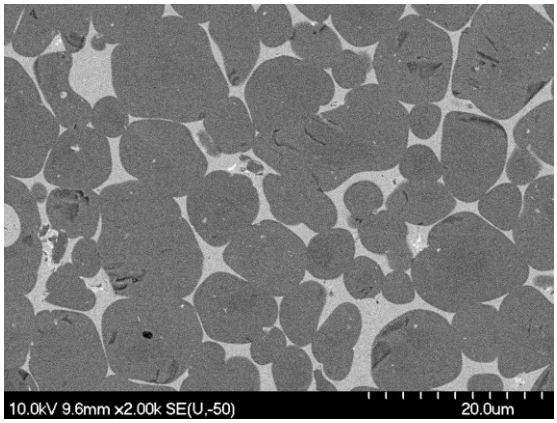

(b)

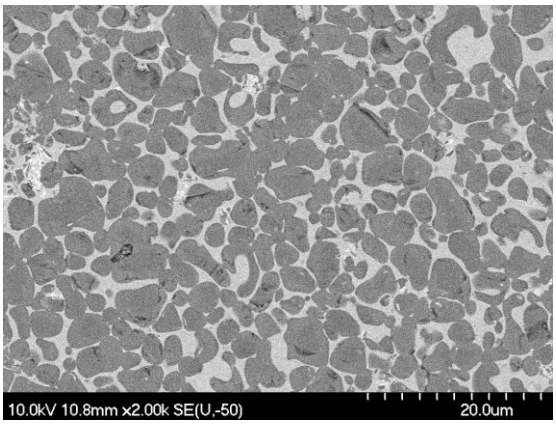

(c)

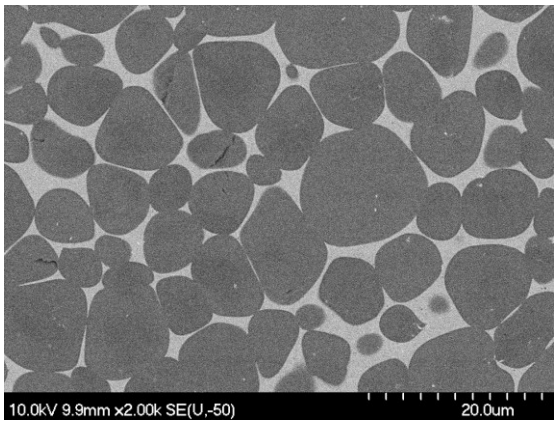

(d)

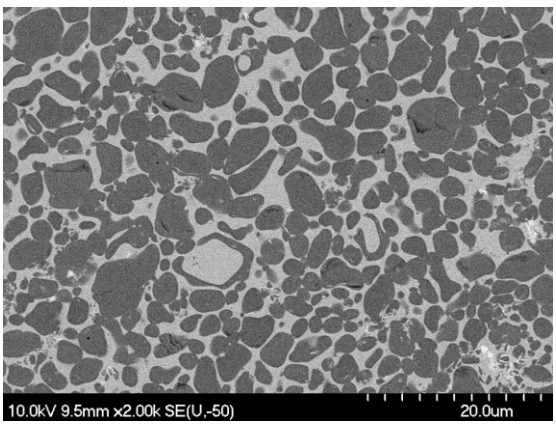

(e)

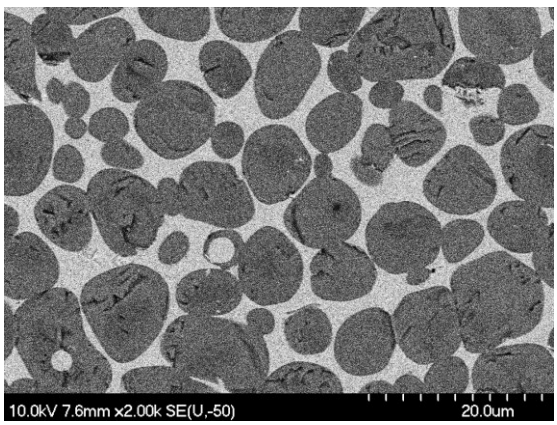

(f)

Figure 7.2: Representative SEM images of fine- and coarse-grained TiC-316L cermets prepared with: (a) 10 vol. %/fine, (b) 10 vol. %/coarse (c) 20 vol. %/fine, (a) 20 vol. %/coarse, (e) 30 vol. %/fine, and (f) 30 vol. %/coarse.

The average grain size, contiguity and binder mean free path of both the fine- and coarse-grained cermets are presented in Figure 7.3. The grain size is largely independent of binder content (Figure 7.3 (a)), with only a slight decrease seen with increasing binder content. This is broadly similar to observations with other TiC-based cermet systems, and highlights the likelihood of an interface-controlled grain growth response [33], where the rate-limiting step is transport of Ti and C across the interface between the metallic binder and the TiC, rather than diffusion through the steel melt. As can be seen from Figure 7.3 (b), the contiguity decreases with increasing binder content, which is similar to the results of prior studies [33]. It is apparent for the coarse-grained cermets that the mean free path length increases with binder content (Figure 7.3 (a)), in agreement with prior studies on TiC-based cermets [33]. However, for the fine-grained cermets the behaviour is more complex, actually showing a slight reduction in mean free path for the 20 vol. % 316L samples, in comparison to 10 and 30 vol. %. This response is not fully understood, however it is clear from Figure 7.2 that sintering at 1475°C for 15 minutes results in a relatively complex, non-equilibrium grain morphology (i.e. a clear deviation from moderately spheroid grains). As a consequence, this deviation from a nominally spherical morphology will result in a higher interfacial area between the carbide and binder phases when processing under such conditions, which likely leads to the anomalous mean free path data presented in Figure 7.3 (b).

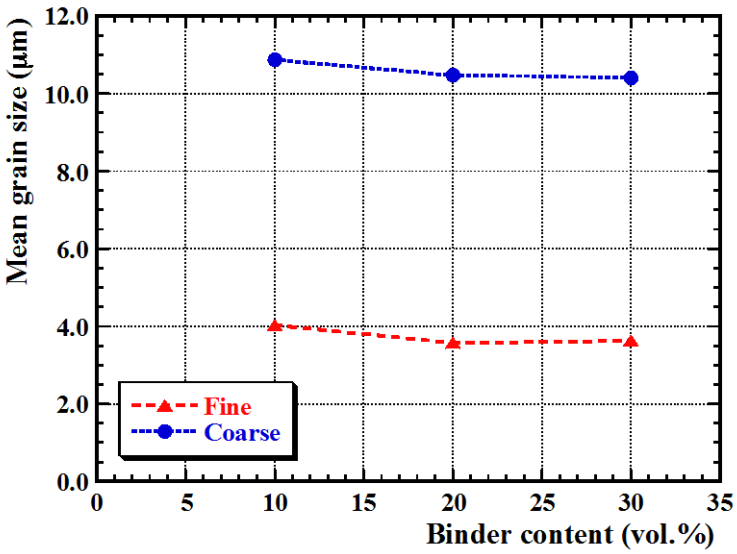
Mean grain size (μm)
12.0
10.0
8.0
6.0
4.0
2.0
0.0
0
5
10
15
20
25
30
35
Binder content (vol.%)
Fine
Coarse

(a)

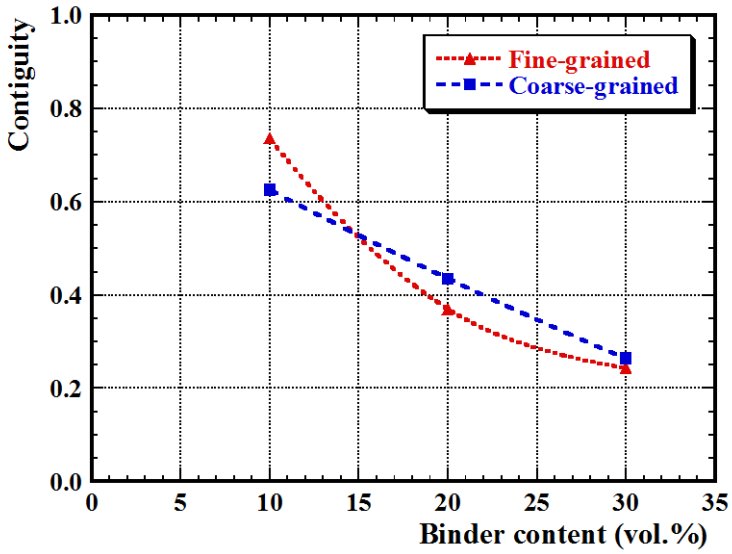
Contiguity
1.0
0.8
0.6
0.4
0.2
0.0
0
5
10
15
20
25
30
35
Binder content (vol.%)
Fine-grained
Coarse-grained

(b)

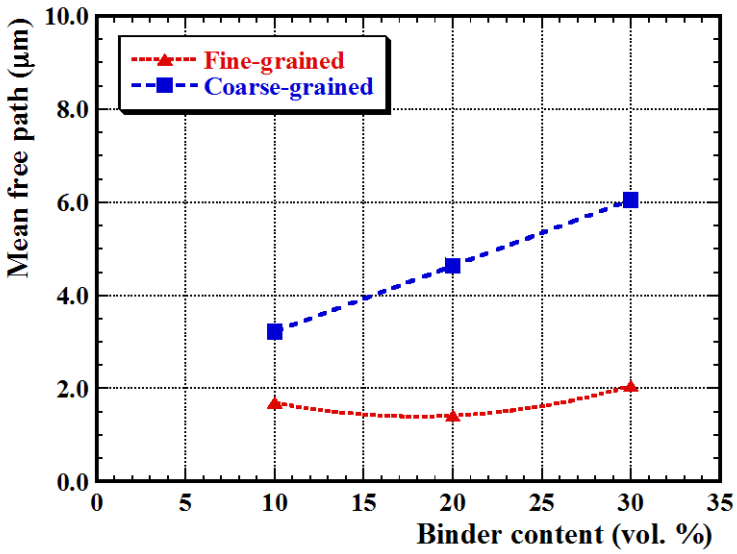

(c)

Figure 7.3: The variation of microstructural parameters as a function of binder content, for both fine- and coarse-grained TiC-316L cermets: (a) mean grain size, (b) contiguity, and (c) binder mean free path.

Image analysis measurements of the binder volume fractions showed a consistently lower binder content when compared to the nominal starting compositions for the coarse-grained cermets (Figure 7.4), confirming some potential volatilisation of the steel binder. Typically the discrepancy was small, with the main exception to this trend being the coarse-grained TiC-30 vol.% 316L cermets, where the mean binder volume fraction was determined to be 25.6 ± 1.9 vol.% (the average of 20 repeat measurements). More detailed SEM examination, using back scattered electron imaging and EDS analysis demonstrated the presence of a core-rim structure for these materials [32]; in this instance the grains possessed a TiC core, surrounded by a rim invariably containing some Mo, Cr and W (an impurity from the TiC powder), in addition to the primary Ti and C. Such core-rim structures are common in TiC and related Ti(C,N) cermets, especially when Mo is present in some form. The 316L steel is therefore effectively depleted of these elemental species (Mo and Cr), so that the measured TiC volume fraction is increased (now a (Ti,Mo,Cr,W)C alloy in the rim) and there is a concurrent reduction in the (higher density) steel content. As a consequence, the theoretical density is effectively reduced.

The steel binder volatilisation, combined with core-rim formation, therefore results in a decrease in the *actual* theoretical density, resulting in the discrepancy noted in Figure 7.1(based on a simple rule-of-mixtures value for the theoretical density).

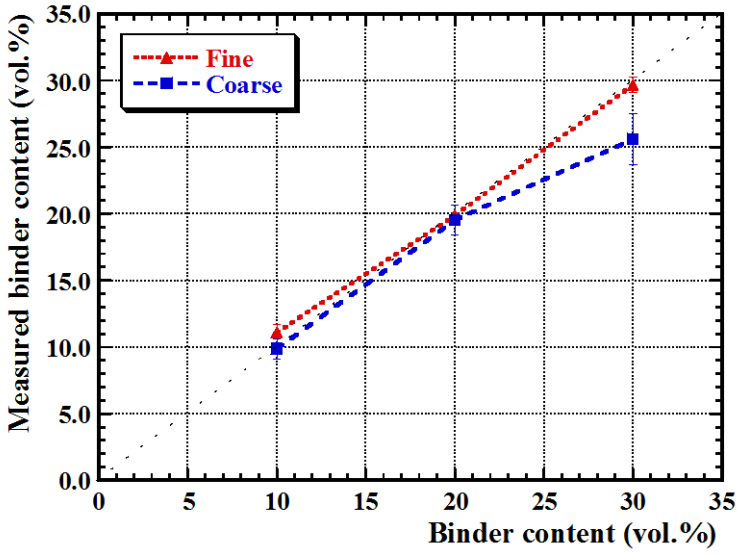

Figure 7.4: The measured area fractions of 316L binder, as function of the initial cermet binder contents during melt-infiltration processing. Each data point was determined from 20 individual image analyses on digitised micrographs.

Vickers hardness measurements for both the fine- and coarse-grained TiC-316L cermets are shown in Figure 7.5, highlighting the superior hardness of the fine-grained cermets. The hardness of the composite is seen to decrease with increasing binder content for both the fine- and coarse-grained materials. This observation is in agreement with our prior studies, examining a TiC-304L cermet system [28], and is related to the relative elastic moduli of the individual constituents (TiC: ~439 GPa and 316L: ~193 GPa). The reason for the improved hardness, as the grain size is reduced, is attributed to the decrease in the thickness of the binder phase ligaments (Figure 7.3(c)). Consequently, the movement of dislocations within the binder phase is hindered due to the reduced ligament dimensions, in a manner similar to the Hall-Petch response for polycrystalline metals; in this instance the ligament widths effectively represent the functional 316L 'grain size' between TiC crystals.

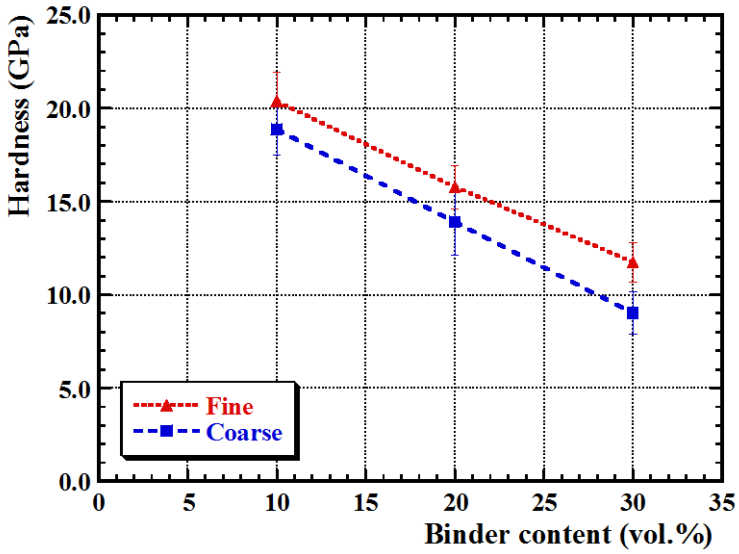

Figure 7.5: The hardness of fine- and coarse-grained TiC-316L cermets as a function of steel binder content (measured with a 1 kg load).

7.3.2 Reciprocating Wear Testing

Typical dynamic coefficient of friction (COF) curves for selected samples are shown in Figure 7.6. Generally, although not always, the curves show a decreasing COF with increasing applied load. There is invariably an initial transition period, typically lasting 15 to 30 minutes, where the COF is relatively unstable, after which the COF tends to stabilise. These initial instabilities likely mark changes in the wear mechanisms, which are discussed in more detail in subsequent sections. Figure 7.7 presents the variation in the COF of the fine- and coarse-grained cermets with the applied load (determined after 120 minutes of dry sliding). It can be seen that the COF for all the fine- and coarse-grained cermets evaluated ranges from 0.25 - 0.42, which is broadly similar to the COF values recorded for a comparable TiC-304L cermet examined in an earlier study [28].

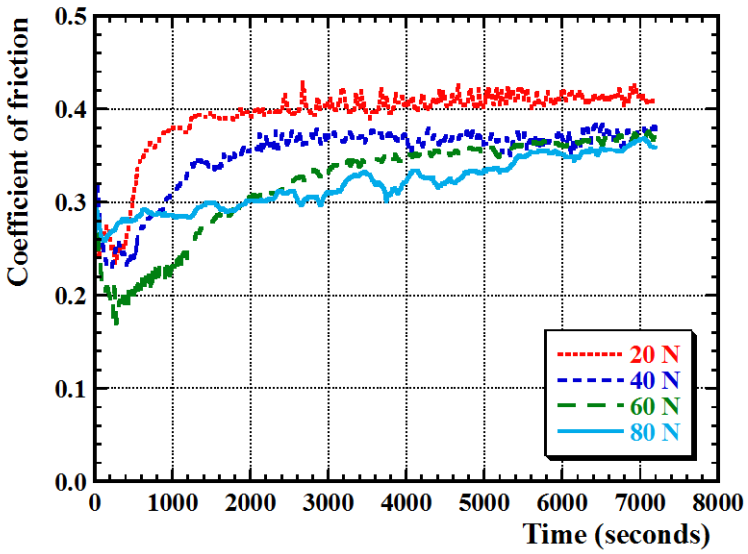

(a)

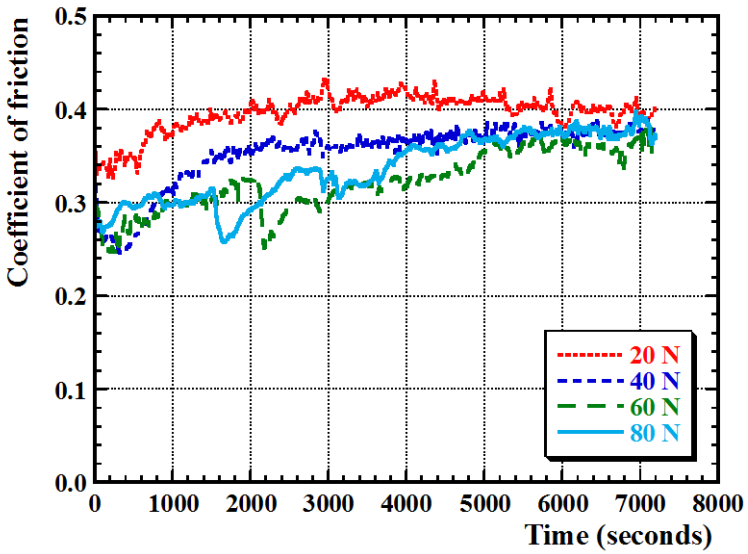

(b)

Figure 7.6: Typical examples of the dynamic COF curves obtained for the TiC-316L cermets: (a) 20 vol.% 316L/fine, and (b) 30 vol.% 316L/coarse.

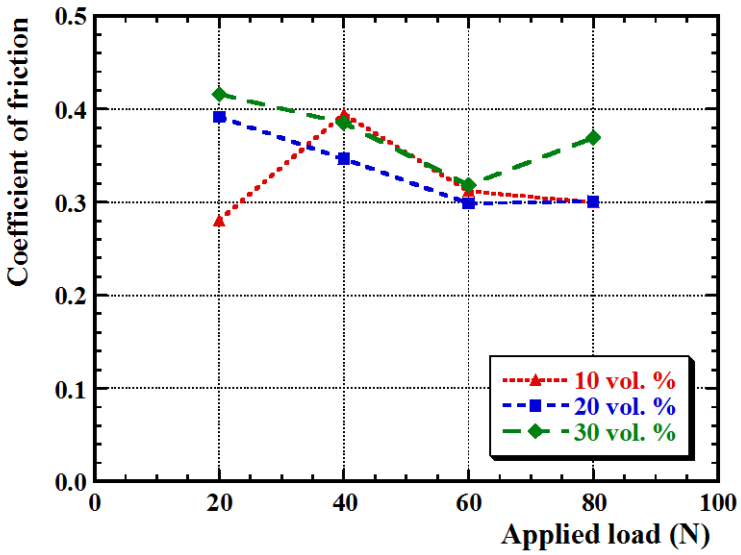

(a)

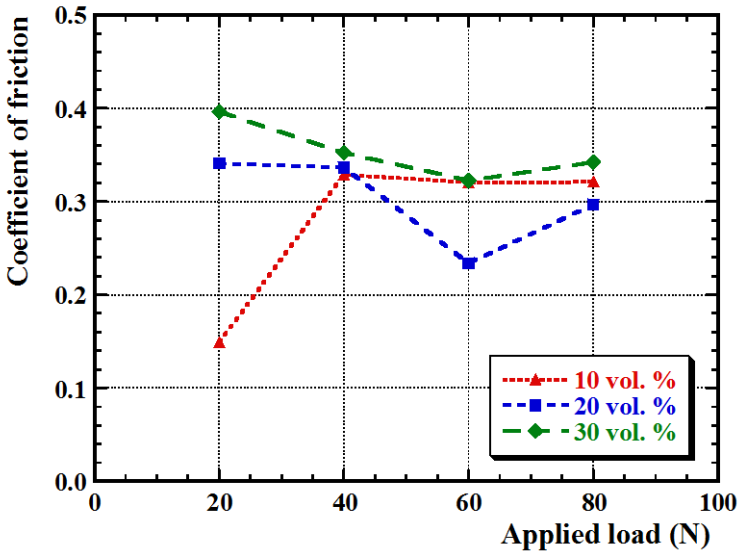

(b)

Figure 7.7: The COF for the TiC-stainless steel cermets after 120 minutes of dry sliding, as a function of the applied load and steel binder content: (a) fine- and (b) coarse-grained.

Looking critically at Figure 7.6 and Figure 7.7, it can be seen that the COF shows a slight dependence on applied load, broadly decreasing with increasing load. This slight variation of COF could depict that the wear mechanism may be gradually changing from

an initially two-body to a three-body abrasive wear scenario, which slightly lowers the COF. The transitions between 60 N and 80 N load may relate to the formation of a tribolayer (these microstructural features are discussed in more detail in the following section (*3.3 Microstructural Development Following Wear Testing*)). With an increase in friction between the TiC cermet and WC-Co counter face sphere, the degree of frictional heating can be expected to rise, resulting in a small temperature increase; previous work highlighted such increases to typically be up to ~100°C [29]. Comparing the COF of fine- and coarse-grained cermets, there is no clear dependence on the TiC grain size. This observation is in general agreement other studied cermet systems [23,34]. A slight increase in COF with binder content is apparent for both the fine- and coarse-grained cermets, inferring that the steel volume fraction plays some role in the measured COF. Previous studies have documented moderately high COF values for stainless steels under dry sliding conditions. For example, O'Donnell, in comparing the wear performance of carburized and un-carburized 316L stainless, reported a COF of 0.58 to 0.61 for an untreated 316L stainless steel dry sliding against a WC sphere [35]. In that case the applied load was 5 N, although severe adhesive/abrasive wear was reported, with a specific wear rate of 4.25×10^{-4} mm^3/Nm [35]. Similarly, Dogan and colleagues reported a mean COF of 0.679 for 316L stainless steel, dry sliding against an Al_2O_3 counter sphere under a relatively conservative load of 1N [36]. The range of COF values observed for the present TiC-316L cermets is comparable with other TiC-based cermet systems recently studied. For instance, in our previous publications, we reported a COF of 0.2 to 0.36 for TiC-304L cermets sliding against an identical WC-6Co sphere to the present work [28]. Buchholz and colleagues reported a mean COF of ~0.32 to 0.35 for TiC cermets, prepared by melt-infiltration with between 20 and 40 vol. % Ni_3Al (alloy IC50) binder, sliding against an identical WC-6Co sphere [37]. Interestingly, similar TiC-Ni_3Al and Ti(C,N)-Ni_3Al cermets prepared through a reaction sintering method, rather than melt infiltration, exhibited somewhat higher COF values around 0.5 [29]. It was shown in that work that the recorded steady state COF was essentially independent of both the ceramic phase composition and the volume fraction of the binder phase, contrary to the present study with a steel binder.

Figure 7.8 presents the variation of specific wear rate, as a function of both the applied load and steel binder content, for both fine- and coarse-grained TiC-316L cermets. At the lowest loads (i.e. 20 N), the specific wear rates are consistent for all the compositions and binder contents (at ~5 x 10^{-7} mm^3/Nm). However, the specific wear rate is then seen to increase with either increasing binder content or applied load. It should be noted that the specific wear rate is normalised by the load (units of mm^3/Nm), and might be expected to be invariant with applied load if the same mechanism operates across the entire load range. Consequently, the increasing specific wear rate as a function of applied load indicates the likelihood of changes arising in the operative wear mechanism(s), which are discussed in more detail in *Section 3.5: Wear Mechanisms*. The response shown in Figure 7.8 infers that the specific wear rate is dependent on the TiC content (and consequently the steel binder volume fraction), and hence has a nominally linear dependence with hardness (Figure 7.5); similar observations on the effects of TiC content were also reported in our previous studies on a TiC-304L [28]. Figure 7.8 demonstrates that for the lowest binder content (i.e. 10 vol. %) the response of the fine- and coarse-grained cermets is quite similar, showing comparable specific wear rates, and a gradual increase with increasing load in each case. However, for the higher binder contents the behaviour deviates considerably, demonstrating the influence of the softer, ductile metallic phase on the wear response. Firstly, the extent of increase in the specific wear rates is greater with each stepped increase in binder content. Secondly, at the highest applied loads, the fine-grained cermets have clearly lower specific wear rates than the coarse-grained equivalents, typically by a factor of ~2.

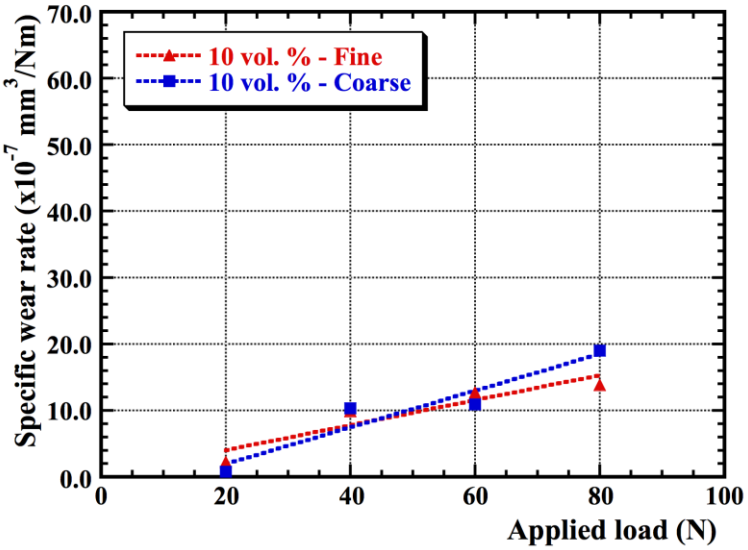
10 vol. % - Fine
10 vol. % - Coarse
Specific wear rate (x10^{-7} mm^3/Nm)
Applied load (N)
0.0
10.0
20.0
30.0
40.0
50.0
60.0
70.0
0
20
40
60
80
100

(a)

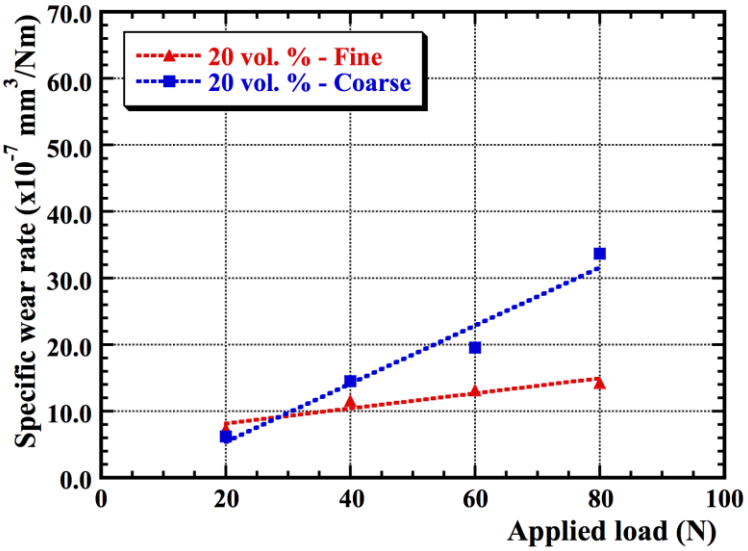
20 vol. % - Fine
20 vol. % - Coarse
Specific wear rate (x10^{-7} mm^3/Nm)
Applied load (N)
0.0
10.0
20.0
30.0
40.0
50.0
60.0
70.0
0
20
40
60
80
100

(b)

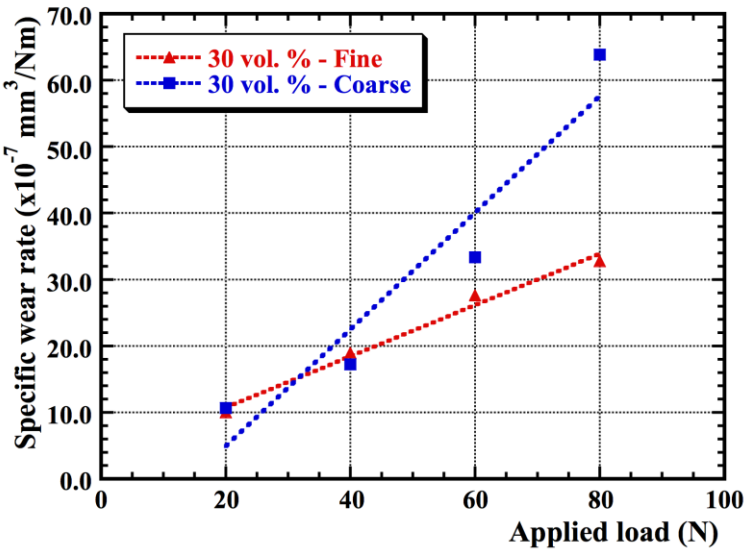

(c)

Figure 7.8: Comparison of the specific wear rate of the fine- and coarse-grained TiC-316L stainless steel cermets as a function of applied load, for: (a) 10 vol.% binder, (b) 20 vol.% binder, and (c) 30 vol.% binder.

When the TiC cermet and WC-Co counter-face sphere are brought into sliding contact initially, the soft ductile steel metal binder between TiC particles can be anticipated to undergo plastic deformation under the Hertzian contact stress. At the lowest loads this effect is relatively small, but increases significantly with applied load. The deformed steel metal binder is then extruded under compression. This binder extrusion can be anticipated to be easier in the coarse-grained structures, where the binder mean free path (and hence ligament dimension) is greater. Then micro-cracking, fragmentation, and/or pull-out of the TiC particles occurs; the extent of this response increases with several variables, notably applied load, steel binder content and/or TiC grain size. The degree of deformation/damage is reduced in severity as both the size of the TiC grains and the steel binder content are reduced. For the higher TiC contents, and at low loads, deformation of the binder and associated material removal is minimised by the high TiC grain contiguity. In this instance, there is an extensive, contacting network of the high modulus ceramic particles, which can resist the Hertzian contact loading, minimising the binder extrusion. In terms of the microstructure of the cermets, it is apparent that the wear resistance

increases with increasing contiguity, but decreases with an increasing binder mean free path. Hence, the improvement of the wear resistance (i.e. lower specific wear rate) and hardness for the fine-grained cermets over the coarse-grained cermets, at constant 316L content, is attributed to the decrease in the binder mean free path. This leads to greater constraint of the binder ligaments against deformation, due to the higher contact area between the high modulus TiC grains, and a reduced tendency for steel binder phase extrusion, making shear and associated dislocation motion more difficult [22]. It can also be expected that this will promote a greater degree of dislocation pile-up during deformation, due to the reduced ligament dimension, effectively increasing the yield strength of the binder. Although the test geometry and conditions are slightly different for the present study, comparing the data presented in Figure 7.8 with reported specific wear rates for 316L in dry sliding against a similar WC sphere (i.e. 4.25×10^{-4} mm^3/Nm [35] and 8.20×10^{-4} mm^3/Nm [7]), it is seen that the TiC-316L cermets exhibit a roughly three orders of magnitude decrease in the specific wear rate over the steel alone.

When comparing the specific wear rates determined in the present work to other cermets, it can be seen that the current materials compare favourably. For instance, Juhani *et al* examined the dry abrasive wear of fine-grained Cr_3C_2-Ni cermets using a block-on-disc geometry at 20 N load, with the cermets sliding against an abrasive Al_2O_3 wheel [38]. They reported a specific wear rate of 2.6×10^{-4} mm^3/Nm, rising to 7.4×10^{-4} mm^3/Nm, for Ni binder contents varied from 10 to 30 wt.%, which are much higher values than observed in the present work. Similarly, Pirso and colleagues determined the dry abrasive wear of Cr_3C_2-Ni, TiC-NiMo and WC-Co cermets using the identical test geometry and condition similar to Juhani *et al.*, and reported specific wear rates for WC-Co from ~5×10^{-7} mm^3/Nm (10 vol. % Co), increasing up to ~80×10^{-7} mm^3/Nm (31.5 vol. % Co) [1]. For the Cr_3C_2-Ni cermets they reported specific wear rates ranging from ~8×10^{-7} mm^3/Nm to ~95×10^{-7} mm^3/Nm, with the respective Ni content increasing from 7.6 to 24.5 vol.% [1]. Bonny and co-workers examined a variety of WC-Co based materials, dry sliding against a WC-6Co counter face, using a pin-on-disk geometry [39,40]. They recorded typical specific wear rates from 0.2 to 4.5 x 10^{-7} mm^3/Nm. It is apparent from these prior studies that both the fine- and coarse-grained cermets developed in the present work compare favourably with these other cermet systems.

7.3.3 Microstructural Development Following Wear Testing

Typical SEM images of the edges of wear tracks for the fine- and coarse-grained cermets are presented in Figure 7.9. There is a minimal amount of build-up of ploughed material apparent around the edges or ends of the wear tracks, while the presence of a tribolayer is also noted. Two-body wear may be associated with ploughing deformation of the material [41]. In addition, uplift and material deposition can occur at the wear track edges [41], which can be observed as pronounced ridges around the wear track. Material deposited at the wear track ends indicates two-body wear, while the absence of any significantly raised 'lip' on the wear track would indicate a three-body wear mechanism. These wear modes indicate abrasive wear is occurring in the cermets. However, the added formation of a tribolayer highlights a mode of tribo-chemical, or adhesive, wear. The wear process is initially two-body in character, with the fine- or coarse-grained cermet sliding against the counter-face. This leads to debris formation between the surfaces, as binder is extruded out from between the carbide grains, and the grains themselves crack and fragment under the high Hertzian contact stress; this process can be anticipated for both of the materials in the tribo-couple due to their high elastic moduli. There is consequently a mechanism transition from two- to three-body wear, with the wear debris creating the third body.

The tribolayer forms through continued cyclic loading, as the third body particles are rolled back and forth between the tribo-pair surfaces. Severe mechanical attrition arises, and there is significant refinement in the third-body particle size, which eventually forms a homogeneous thin film in the wear track. As the wear process and loading continue, the small fragments of TiC and WC particles are then embedded within the mix of extruded binder, and become part of the tribolayer. Compositional analysis of the tribolayer is discussed in the following section (*3.4 Characterization of the Tribolayer and Sub-surface Damage*). It is clear that the wear behaviour of these cermets is rather complex; previous studies have indicated that the wear of cermets is initiated by the removal and extrusion of the ductile binder phase, followed by plastic deformation, grain fragmentation and micro-abrasion [11,18,41].

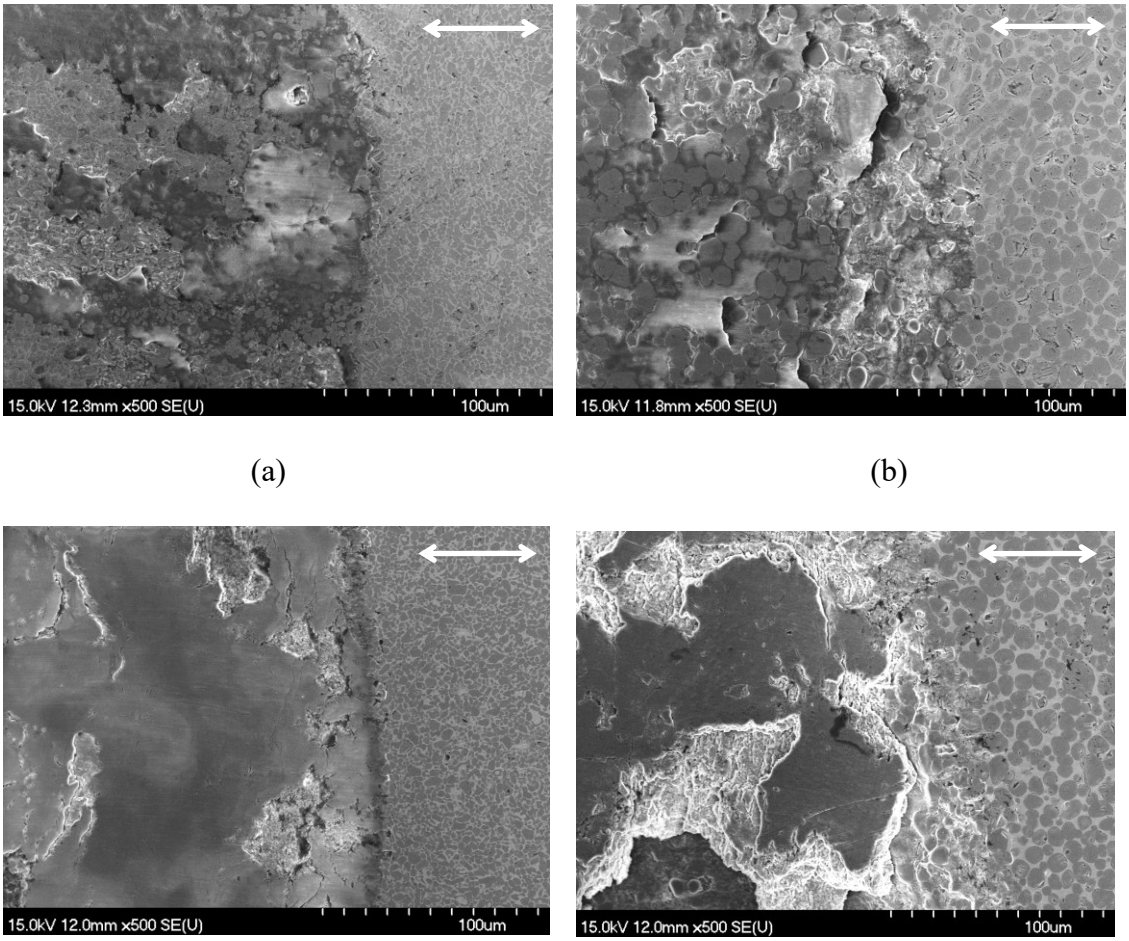

Figure 7.9: SEM images of the ends of the wear track formed on the fine- and coarse-grained TiC-30 vol. % 316L after testing using 20N and 80 load for 2 hours duration; the sliding direction is shown for all images. (a) fine-grained/20 N load, (b) coarse-grained/20N load, (c) fine-grained/80N load, and (d) coarse-grained/80 load. The unworn region is present on the right hand side of each image (c.f. the as-fabricated material presented in Figure 7.2).

When examining the evolution in the microstructure at higher magnification several features can be seen, especially when looking at the coarse-grained cermets. Figure 7.10 to Figure 7.12 track the effects of increasing load on the wear track structure for a single composition (coarse-grained TiC with 20 vol.% 316L binder). Figure 7.10 shows the end of a wear track, developed under the lowest applied load (i.e. 20 N). While the majority of TiC grains are retained, there is some initial evidence for damage occurring in these grains. It is also apparent that much of the 316L steel binder has been removed from

between the TiC grains, and a tribolayer is beginning to be generated. The tribolayer itself is deposited between the TiC grains, and laminar cracks are apparent in the tribolayer, highlighting its brittle nature. As the applied load is increased, the extent of tribolayer formation also increases, as shown in Figure 7.11. Here large areas of tribolayer are observed to have spalled away (particularly on the left hand side of Figure 7.11 (a)), leaving a rough surface with isolated, exposed TiC grains (Figure 7.11 (b)). At the highest load, the wear track ends are largely covered by the tribolayer (Figure 7.12). The tribolayer will continue to fail through spalling, but in this instance this region is still largely intact (Figure 7.12 (a)). Isolated TiC grains are still visible in the tribolayer, along with some imbedded TiC grain fragments, and there is significant crack formation perpendicular to the sliding direction (Figure 7.12 (b)). Clearly, with continued sliding some of the regions of tribolayer will ultimately spall off and be ejected from the wear couple as fine debris.

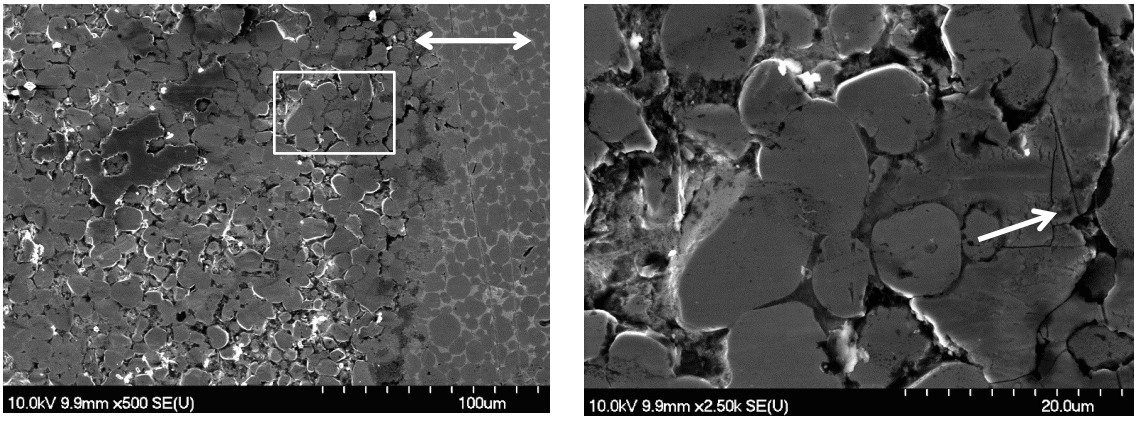

Figure 7.10: (a) SEM image of the end of the wear track of a coarse-grained cermet, with 20 vol.% 316L binder, tested under an applied load of 20 N for 2 hours (sliding direction is shown by the arrow, with the unworn region on the right hand side of the image). (b) Inset region of (a), adjacent to the end of the wear track, highlighting the initial formation of the tribolayer, and laminar cracks being generated perpendicular to the sliding direction (arrowed).

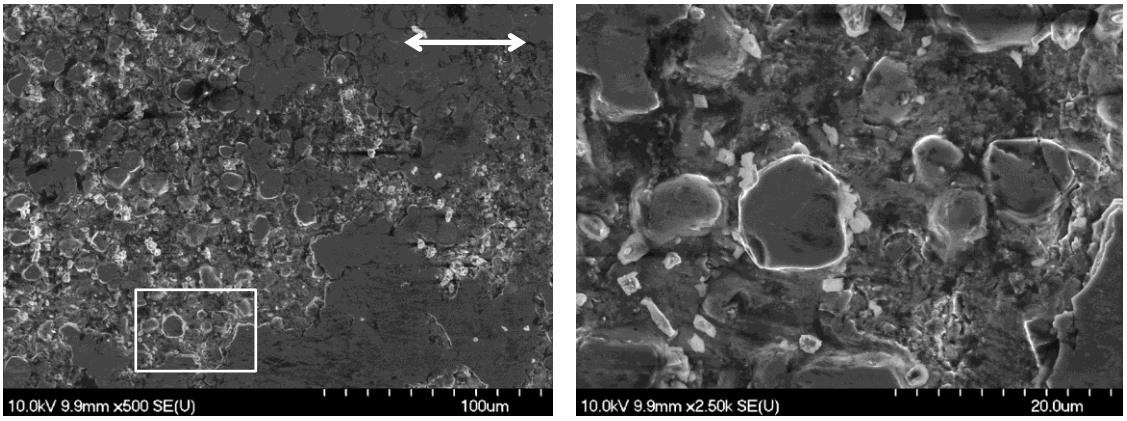

Figure 7.11: (a) SEM image near the end of the wear track of a coarse-grained cermet, with 20 vol.% 316L binder, tested under an applied load of 40 N for 2 hours (sliding direction is shown by the arrow). (b) Inset region of (a), highlighting considerable spalling.

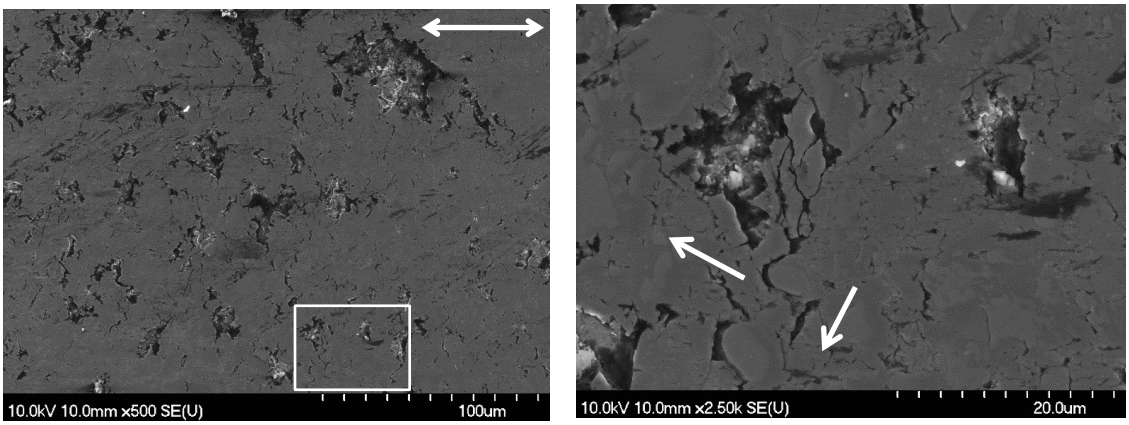

Figure 7.12: (a) SEM image of the end of the wear track of a coarse-grained cermet, with 20 vol.% 316L binder, tested under an applied load of 80 N for 2 hours (sliding direction is shown by the arrow). Note that the surface was largely covered by the tribolayer, w which is still mostly intact. (b) Inset region of (a), highlighting significant tribolayer cracking perpendicular to the sliding diraction. Note that there are some TiC grains that can still be clearly observed within the tribolayer (arrowed), as well as some grain fragments.

SEM micrographs of representative third body wear debris examples, generated for both the fine- and coarse-grained TiC-20 vol.% 316L cermets, at 20 N and 40 N loads, respectively, are presented in Figure 7.13; these particles are recovered material that was ejected from the wear track during testing. As the wear process proceeds, it would be expected that there is increasing extrusion of the metallic binder phase, micro-cracking

and fragmentation of the TiC particles, and an increasing degree of tribolayer formation. This layer is then removed from the surface periodically through spallation (the tribolayer exhibits brittle characteristics, as noted previously), potentially taking some of the damaged sub-surface cermet material with it, creating exposed damage regions on the surface. In other words, the entrapped debris particles produce further damage on both surfaces in a three-body scenario, and the debris itself undergoes further fragmentation during sliding, resulting in the formation of fine particles even at lower loads. At the higher load the wear debris appears coarser, and exhibits a 'plate-like' morphology. This is likely to be the result of successive adhesion and transfer of relatively round debris, composed of material from both sliding surfaces (observed at lower load), which ultimately forms part of the tribolayer and is then released by spallation.

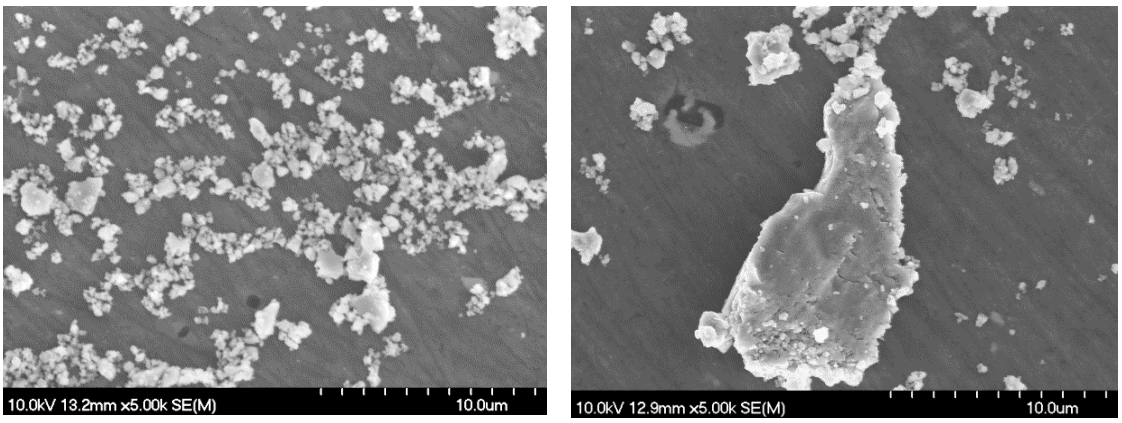

(a) (b)

Figure 7.13: Representative SEM micrographs of the wear debris recovered after testing both fine- and coarse-grained TiC-20 vol. % 316L. (a) coarse-grained/20 N load, and (b) fine-grained/40 N load.

7.3.4 Characterization of the Tribolayer and Sub-surface Damage

To further understand the wear mechanisms of the fine- and coarse-grained TiC-316L cermets, tribolayer compositional analysis was conducted in the SEM using EDS, while examples of the tribolayer were also micro-sectioned using the FIB. Figure 7.14 presents representative SEM EDS images, and the associated elemental maps, recorded at the edges of wear tracks for the current cermets; both samples were tested at an applied load

of 80 N. In each case, a significant portion of the wear track exhibits tribolayer build up. Table 7.1 and Table 7.2 present typical mean EDS compositions for the fine- and coarse-grained cermets respectively, for both 20 N and 80 N applied loads. These examples confirm that a O forms a major chemical component within the tribolayer, which is likely to be in the form of oxides associated with the steel binder constituents (i.e. Fe, Cr, Ni and Mo), as well as Ti from the TiC, and trace W and Co arising from the counter face material. Tribolayer formation increases with load, forming through continued mechanical attrition and refinement of the third body particles. Consequently, fresh surfaces are constantly being created, which results in repeated passivation of the exposed surfaces and an increasing O incorporation. The EDS chemical analyses of the tribolayers presented in Table 7.1 and Table 7.2confirm that the oxygen content increases with applied load, indicating that the scale of the tribolayer is being refined (i.e. smaller particles with a higher surface area).

As noted earlier, it is possible to examine the near sub-surface region of the wear tracks by sectioning through the tribolayer with Ga ions in the FIB microscope. With this approach a variety of features can be observed in terms of the wear behaviour, both within and below the tribolayer, through subsequent examination in the SEM; the sample tilt in the SEM is 30° for all of the FIB prepared images that are presented. Figure 7.15 shows a sequence of images at increasing magnification, following micro-sectioning within an intact region of tribolayer (Figure 7.15 (a)). At higher magnification it is apparent that the tribolayer is relatively thick (Figure 7.15 (b)); taking in to account the tilt angle, the thickness can be estimated to be ~6 to 8 μm. The tribolayer itself is highly damaged, showing a significant concentration of fine scale cracks (Figure 7.15 (c)), and confirming the “composite” nature alluded to earlier, with TiC grain fragments mixed in to the layer.

Figure 7.16 highlights a region where the tribolayer has largely spalled away, leaving the rough cermet microstructure fully exposed. Just below the surface both the TiC grains and the 316L binder are still present (Figure 7.16 (b)), while at higher magnification it is apparent that cracking and failure is occurring at the interface between the TiC grains and the steel binder (Figure 7.16 (c)). There is even clear evidence of crack propagation through the steel binder itself, between the TiC grains. Here the ligament dimension is

extremely thin, and it can be anticipated that the local Hertzian stress has exceeded the yield stress of the 316L, which likely has become more brittle through dislocation pile-up due to the small dimensions. In Figure 7.17, a FIB section has been taken right at the edge of the wear track, where both retained tribolayer and unworn material are present. In the boxed area to the left hand side of Figure 7.17 (a), a heavily fragmented TiC grain is present below the tribolayer (Figure 7.17 (b)). There is extensive cracking within this grain, which is most probably only retained while there is still tribolayer present to hold the fragments in place. The boxed area on the right hand side of Figure 7.17 (a) shows two TiC grains in very close proximity, where shear between the grains has occurred under the Hertzian contact loading, resulting in a crack being generated between them.

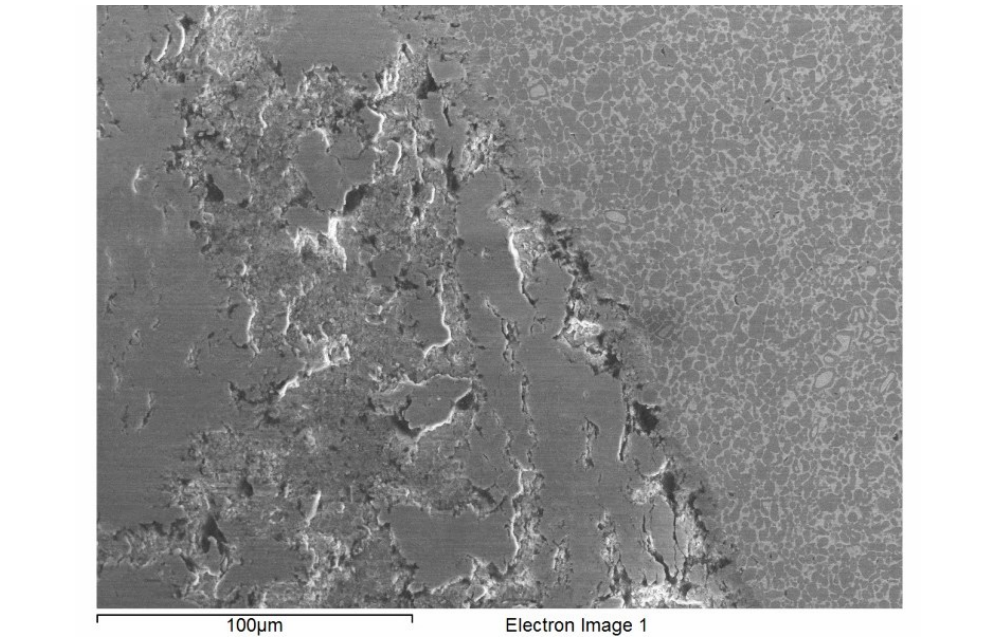

(a)

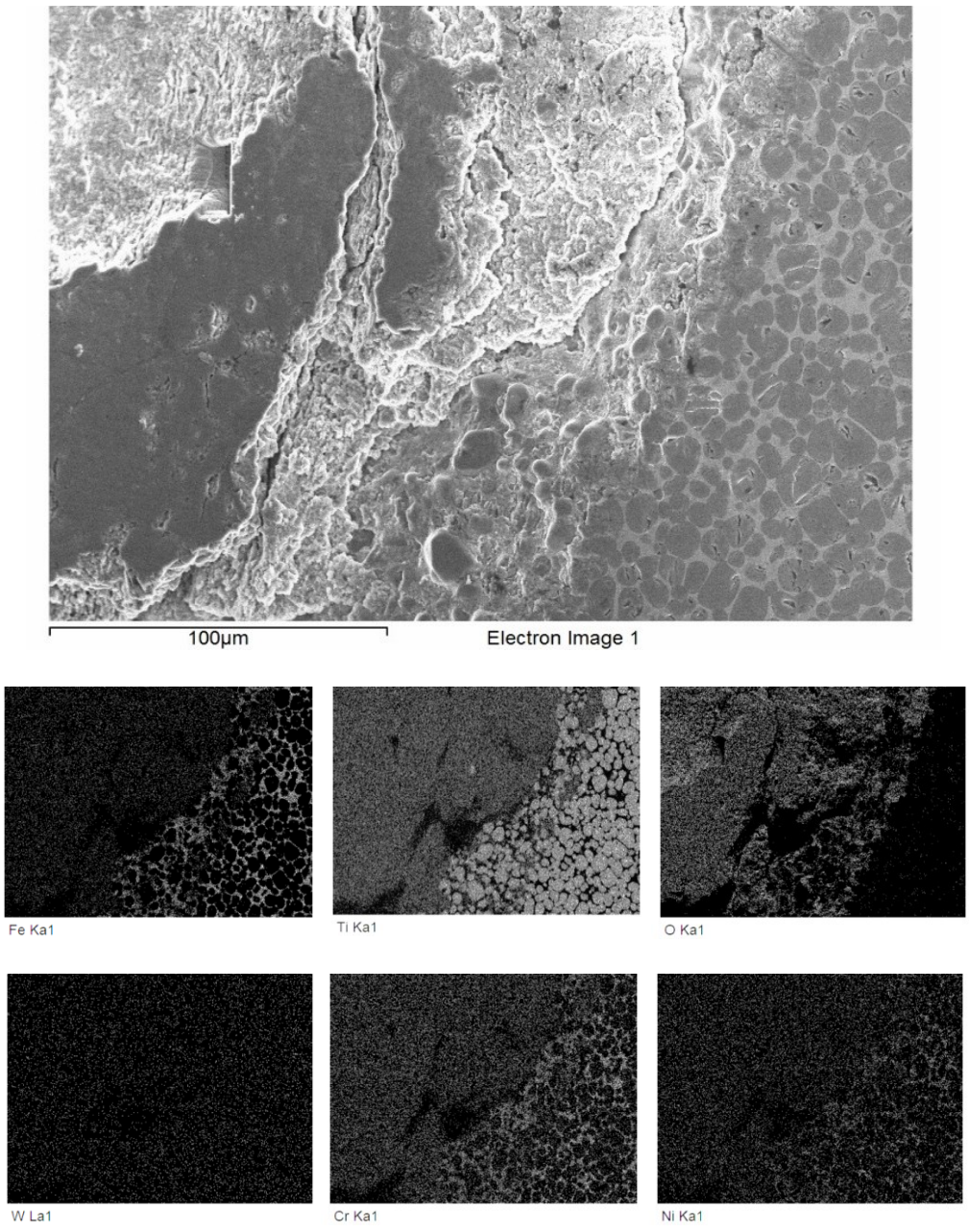

(b)

Figure 7.14: EDS SEM images and associated elemental maps of the ends of the wear tracks for both fine- and coarse-grained TiC- 30 vol. % 316L cermets, following wear testing (80N applied load for 2 hours) for: (a) fine-grained, and (b) coarse-grained microstructures. Note that the unworn region of the cermet is shown on the right hand side of both SEM images (c.f. the as-fabricated materials presented in Figure 7.2).

Table 7.1: Typical tribolayer compositions determined using EDS analysis, for the fine-grained TiC-20 vol. % 316L cermets, after sliding for 2 hours, under 20 and 80 N loads.

Element (KLM line)	**Load**	
	20 N	**80 N**
C(K)	11.46	7.02
O(K)	22.44	31.92
Ti(K)	43.99	35.32
Cr(K)	3.11	3.84
Fe(L)	14.83	15.93
Ni(L)	1.58	2.06
Mo(L)	0.15	0.50
W(M)	2.23	3.18

Table 7.2: Typical tribolayer compositions determined using EDS analysis, for the coarse-grained TiC-20 vol. % 316L cermets, after sliding for 2 hours, under 20 and 80 N loads.

Element (KLM line)	**Load**	
	20 N	**80 N**
C(K)	11.63	9.48
O(K)	21.23	26.12
Ti(K)	51.52	42.54
Cr(K)	1.71	2.62
Fe(L)	9.42	13.85
Ni(L)	1.31	2.38
Mo(L)	0.16	0.28
W(M)	2.79	2.41

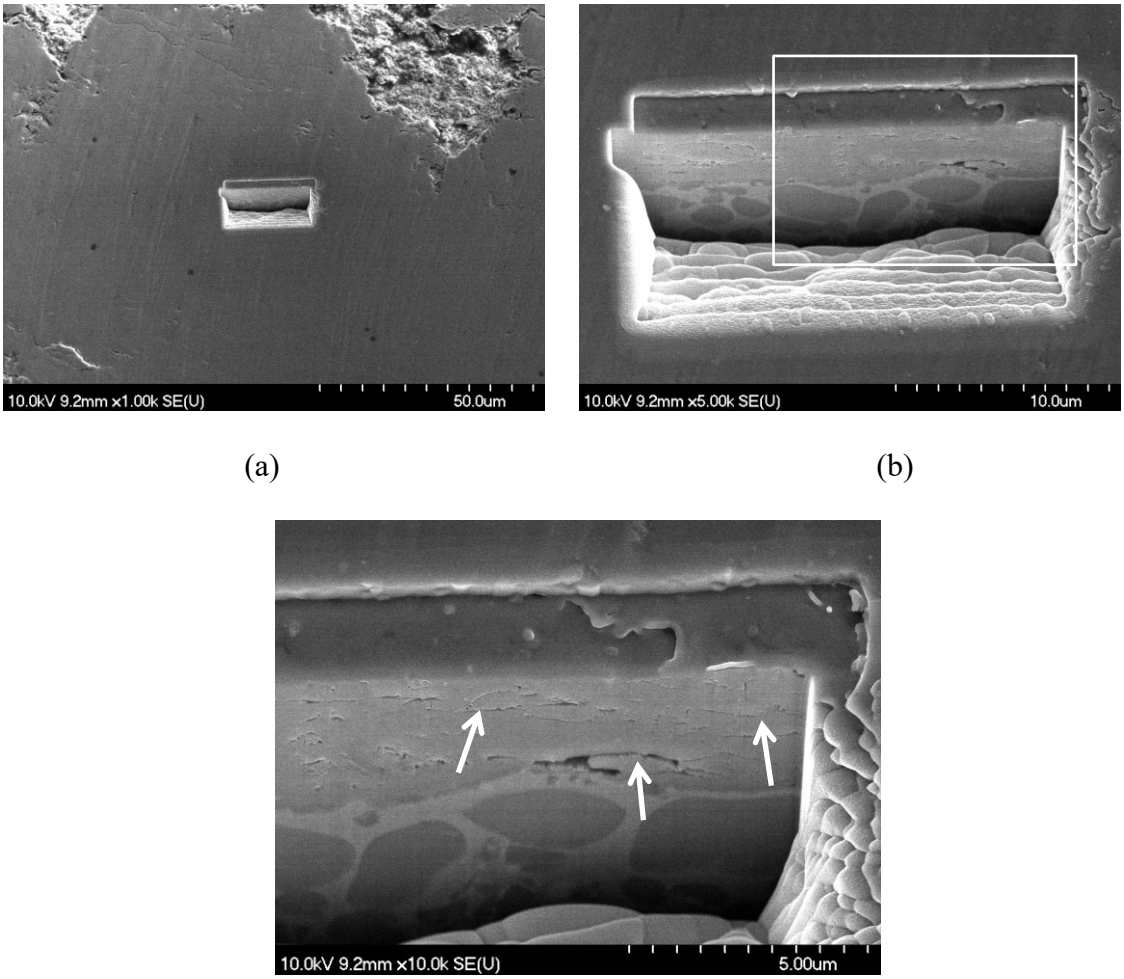

Figure 7.15: SEM images of a FIB micro-section through the tribolayer of a TiC-30 vol.% 316L cermet (fine-grained), tested under an applied load of 80 N for 2 hours. (a) Overview of the micro-machined area of the tribolayer. (b) Image of the full FIB cut through th through the tribolayer. (c) Higher magnification image of the inset area from (b), highlighting cracking of the brittle tribolayer (arrowed).

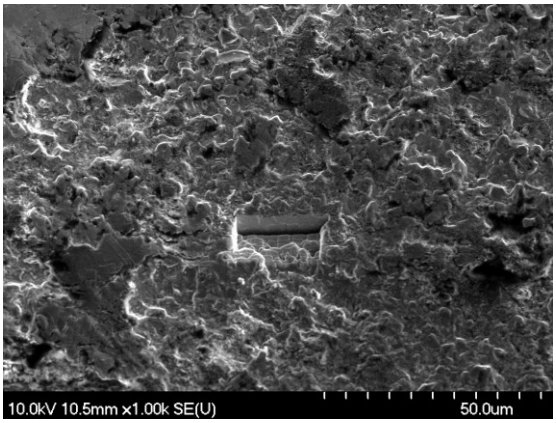

(a)

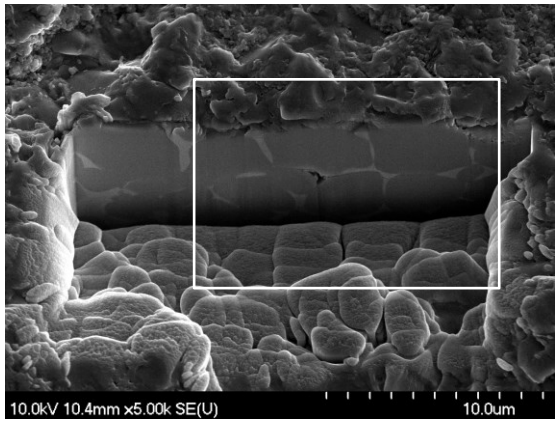

(b)

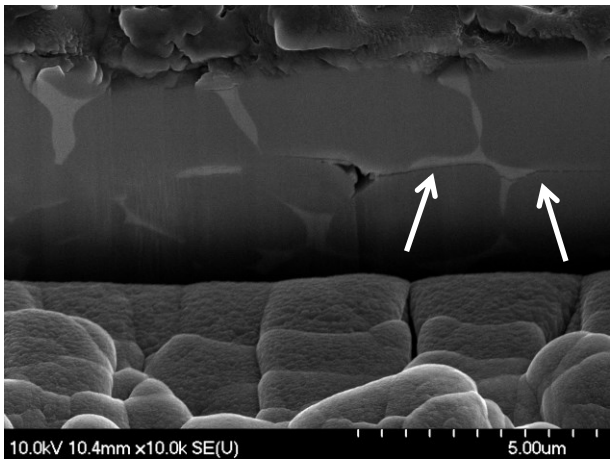

(c)

Figure 7.16: SEM images of a FIB micro-section through the tribolayer of a TiC-10 vol.% 316L cermet (fine-grained), tested under an applied load of 80 N for 2 hours. (a) Overview of the micro-machined area of the tribolayer, showing significant spalling of the tribolayer surface. (b) Image of the full FIB cut through the tribolayer. (c) Higher magnification image of the inset area in (b), highlighting sub-surface cracks occurring between the TiC grains and the narrow 316L steel ligaments (arrowed).

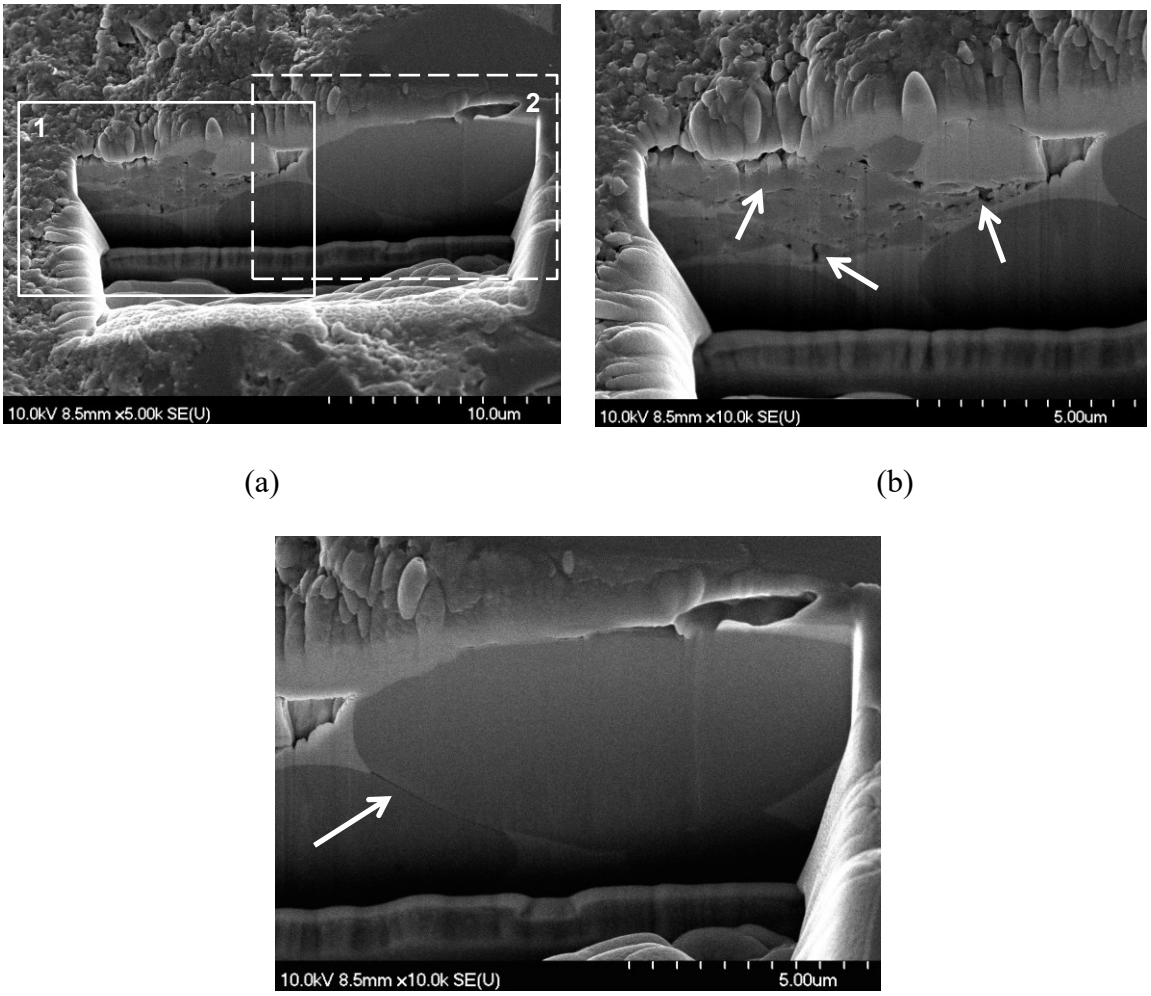

Figure 7.17: SEM images of a FIB micro-section at the edge of the tribolayer/unworn material for a TiC-10 vol.% 316L cermet (fine-grained), tested under an applied load of 80 N for 2 hours. (a) Image of the full FIB cut through the tribolayer/undeformed cermet. (b) Higher magnification image of inset area #1 in (a), highlighting extensive sub-surface cracking occurring in a TiC grain. (c) Higher magnification image of inset area #2 in (a), highlighting cracking occurring between two TiC grains (arrowed), and indicating likely shear deformation.

7.3.5 Wear Mechanisms

Through assessment of the wear behaviour and the resulting response in terms of the microstructural evolution of the TiC-316L cermets, it is apparent that the wear mechanisms are moderately complex in the present materials. Initially, two-body abrasive

wear occurs, with the WC-6Co sphere contacting directly on the surface of the TiC cermet. However, it is evident that that there is a fairly rapid transition from two-body abrasive wear to a predominantly three-body abrasive wear mechanism. This arises through binder extrusion from the surface, under the high Hertzian contact load, and subsequent TiC grain fragmentation when the surrounding constraint is reduced or removed. This extent of this behavior is increased through increasing the applied load, the steel binder content and/or the TiC grain size, as demonstrated by the increasing specific wear rates.

In terms of the mechanism transitions, eventually there is an associated adhesive component to the wear response, as evidenced through the formation of a tribolayer. The generation of a highly homogeneous tribolayer arises from continued attrition of the third-body wear debris, which constantly incorporates O into its structure as new surfaces are exposed through fracture. Ultimately the tribolayer has a high O content, and is essentially brittle in nature; several examples of regions of spalled tribolayer are apparent, especially near the wear track ends. The degree of binder extrusion is more severe for the coarse-grained cermets, relative to the finer-grained structures, although the underlying mechanisms are broadly the same; the fine-grained materials typically exhibit specific wear rates approximately half those of the coarse-grained materials at the highest loads, combined with thinner tribolayers. Both the fine- and coarse-grained cermets show an improvement in the wear resistance with an increase in the TiC content, which is in agreement with a number of previous wear studies on TiC based cermets [1,10,27,34]. Due to the lessened binder extrusion and fragmentation phenomena, the fine-grained cermets showed superior wear resistance relative to their coarse-grained counterparts, which mirrors observations in related studies on WC-Co materials [17,22,23].

As noted earlier, the observed transitions in wear mechanism, from two-body to three-body, and then to adhesive wear correspond with the observed increases in specific wear rate as a function of load (rather than a specific wear rate that is independent of load). The extent of this load dependency increases with both the steel binder content and the TiC grain size (as demonstrated by the increasing gradients of the specific wear rate curves in Figure 7.8), and it can be expected that the ease of binder extrusion and TiC grain fracture will increase in a similar manner for these materials. It is also apparent

from Figure 7.8 that the lowest dependency of specific wear rate on load occurs with the finer-grained cermets, particularly those with the lower binder contents. In this instance the refined microstructure is more resistant to both binder extrusion and TiC grain fragmentation (under identical Hertzian loads), particularly at the highest applied loads, where the extent of wear is most severe.

7.4 Conclusions

In the present work, a simple melt-infiltration technique has been employed to develop high-density fine- and coarse-grained TiC-316L cermets. The dry sliding wear response of these materials has been assessed under reciprocating conditions, and the resulting effects of wear testing on the microstructure have been evaluated. The following conclusions can be drawn:

(1) The fine- and coarse-grained TiC cermets showed improvement in hardness with a decrease in the 316L binder content, as the lower modulus steel is replaced with TiC. In comparing the two sets of cermets, the fine-grained cermets had a higher hardness overall, which likely arises from a reduced binder ligament dimension for the fine-grained materials, and the greater tendency towards dislocation pile-up and an associated increase in the yield stress.

(2) The fine-grained cermets also exhibited superior wear resistance to the coarse-grained materials (i.e. lower specific wear rates), for an equivalent binder content and applied load. The specific wear rate for both fine- and coarse-grained cermets increases with load and 316L binder content. Binder extrusion and TiC grain fragmentation arise during the sliding wear process, indicating a transition from an initially two-body abrasive wear mechanism to one involving three-body wear.

(3) A tribolayer is also generated during testing, confirming the further transition to an adhesive, tribo-chemical wear mechanism. The extent of tribolayer generation increases with load and, to a lesser extent, with the 316L binder content. The tribolayer was shown to contain a high O content, which increases with applied load.

This was attributed to extensive mechanical attrition of the third-body particles, creating new surfaces, which then passivate in the air environment of the tests.

(4) The specific wear rates for both the fine- and coarse-grained cermets were invariably in the range of 10^{-7} mm^3/Nm, which compares favorably with data for other TiC- and WC-based cermets found in the open literature.

(5) Examination of the wear tracks, following FIB micro-machining, highlighted that a variety of sub-surface damage mechanisms were occurring in the cermets, including extensive tribolayer cracking, TiC grain fragmentation and Hertzian loading induced shear.

Acknowledgements

The authors gratefully acknowledge financial support from the Natural Sciences and Engineering Research Council of Canada (NSERC) and Petroleum Research Atlantic Canada (PRAC). The Canada Foundation for Innovation, the Atlantic Innovation Fund, and other partners who helped fund the Facilities for Materials Characterisation, managed by the Dalhousie University Institute for Materials Research, are also appreciated. The authors are also grateful to Dean Grijm and Patricia Scallion, who provided technical assistance.

7.5 References

1. J. Pirso, M. Viljus, K. Juhani, S. Letunovits, Two-body dry abrasive wear of cermets, Wear 266 (2009) 21-29.
2. M. Komac, S. Novak, Mechanical and wear behaviour of TiC cemented carbide, Int Refract. Hard Mater. 4 (1985) 21-26.
3. I. Hussainova, Effect of microstructure on the erosive wear of titanium carbide-based cermets, Wear 255 (2003) 121-128.
4. H. Reshetnyak, J. Kübarsepp, Mechanical properties of hard metals and their erosive wear resistance, Wear (1994) 177-185.

5. I. Hussainova, J. Kübarsepp, The effect of impact angle on the erosion of cermet, Wear 250 (2003) 818-825.
6. J. H. Magee, Wear of stainless steels, 10th edition, ASM International, Materials Park, 1995.
7. F. Bülbül, H. Altun, V. Ezirmik, Ö. Küçük, Investigation of structural, tribological and corrosion properties of electroless Ni–B coating deposited on 316L stainless steel. Proc. Inst. Mech. Eng. Part J – J. Eng. Tribology 227 (2013) 629-639.
8. E. Pagounis, V.K. Lindroos, Processing and particulate reinforced steel matrix composites, Mater. Sci. Eng. A 246 (1998) 221-234.
9. O. N. Dogan, J.A. Hawk, J. H. Tylczak, R. D. Wilson, R. D. Govier, Wear of titanium carbide reinforced metal matrix composites, Wear 225 (1999) 758-769.
10. F. Akhtar, S.J. Guo, Mechanical and fretting wear properties of TiC-stainless steel composites, Mater. Char. 59 (2008) 84-94.
11. A. Mukhopadhyay, B. Basu, Recent developments on WC-based bulk composites, J. Mater Sci. 46 (2011) 571-589.
12. J. Gurland, The fracture strength of sintered tungsten carbide-cobalt alloyst in relation to composition and particle spacing, Trans. AIME, 227 (1963) 1146-1150.
13. H.E. Exner and J. Gurland, A review of parameters influencing some mechanical properties of tungsten carbide-cobalt alloys, Powder Metall. 13 (1970) 13-30.
14. J. Larsen-Basse, Effect of composition, microstructure and, service conditions on the wear of cemented carbides, J. Metals, 35 (1983) 35-42.
15. E.A. Almond, B. Roebuck, Identification of optimum binder phase compositions for improved WC hardmetals, Mater. Sci, Eng A. 105 (1988) 237-248.
16. J. Chermant, A. Deschanvres, F. Osterstock, Abrasive wear of brittle solids, Powder Met. 20 (1977) 63-69.
17. K. Jia, T.M. Fischer, Abrasion resistance of nanostructured and conventional cemented carbides, Wear 200 (1996) 206-214.
18. K. Jia, T.E. Fischer, Sliding wear of conventional and nanostructured cemented carbides, Wear 203 (1997) 310-318.

19. P. Chivavibul, M.Watanabe, S. Kuroda, K. Shinoda, Effects of carbide size and Co content on the microstructure and mechanical properties of HVOF-sprayed WC–Co coatings, Surf. Coat. Tech. 202 (2007) 509-521.
20. K. Jia, T.E. Fischer, B. Gallois, Microstructure, hardness, and toughness of nanostructures and conventional WC–Co composites, Nanostruct. Mater. 10 (1998) 875–891.
21. R.A. Cutler, A.V. Virkar, The effect of binder thickness and residual stresses on the fracture toughness of cemented carbide, J. Mater Sci, 20 (1985) 3557-3573.
22. C. Allen, M. Sheen, J. Williams. V.A. Pugsley, The wear of ultrafine WC-Co hardmetals, Wear 250 (2001) 604-610.
23. Q. Yang, T. Senda, A. Ohmori, Effect of carbide grain size on microstructure and sliding wear behaviour of HVOF-sprayed WC-12% Co coatings, Wear 254 (2003) 23-34.
24. M. Gee, A. Gant, B. Roebuck, Wear mechanisms in abrasion and erosion of WC-Co and related hardmetals, Wear 263 (2007) 137-148.
25. R.B. Collier, K.P. Plucknett, A comparison of anionic and cationic polyelectrolytes for the aqueous colloidal processing of titanium carbide ceramics, Int. J. Refract. Met. Hard Mater. 29 (2011) 298-305.
26. M. I. Mendelson, Average grain size in polycrystalline ceramics, J. Am. Ceram. Soc. 52 (1969) 443-446.
27. J. Gurland, The measurement of grain contiguity in two phase alloys, Trans. Metall. Soc. AIME, 212 (1958) 452-455.
28. C.C. Onuoha, Z.N. Farhat, G.J. Kipouros, K.P. Plucknett, The reciprocating wear behaviour of TiC-304L stainless steel composites prepared by melt infiltration, Wear 303 (2013) 321-333 (2013).
29. T.L. Stewart, K.P. Plucknett, The sliding wear of TiC- and Ti(C,N) cermets prepared with a stoichiometric Ni_3Al binder, Wear 318 (2014) 153-167.
30. J. K. Lancaster, The influence of substrate hardness on the formation and endurance of molybdenum disulphide films, Wear 10 (1967) 103-107.

31. T.L. Stewart, K.P. Plucknett, The effects of Mo_2C additions on the microstructure and sliding wear of $TiC_{0.3}N_{0.7}$-Ni_3Al cermets, Int. J. Refract. Met. Hard Mater. 50 (2015) 227-239.
32. C. Jin, K.P. Plucknett, Microstructural Instability in TiC-316L Stainless Steel Cermets, submitted to Int. J. Refract. Met. Hard Mater. (2015).
33. K.P. Plucknett, P.F. Becher, Processing and microstructure development of titanium carbide-nickel aluminide composites prepared by melt-infiltration/sintering (MIS), J. Am. Ceram. Soc. 84 (2001) 55-61.
34. A. K. Mukhopadhyay, Y. W. Mai, Grain size effects and abrasive wear mechanisms in alumina ceramic, Wear (1993) 258-268.
35. L.J. O'Donnell, Tribology of 316L Austenitic Stainless steel carburized at low temperature, MSc Thesis, Case Western Reserve University, USA, 2010.
36. H. Dogan, F. Findik, O, Morgul, Tribology properties of coated ASME 316L SS and comparison with a substrate, Industrial Lubrication and Tribology (2004) 5-10.
37. S. Buchholz, Z.N. Farhat, G.J. Kipouros, K.P. Plucknett, The reciprocating wear behaviour of TiC-Ni_3Al cermets, Int. J. Refract. Met. Hard Mater. 33 (2012) 44-52.
38. K. Juhani, J. Pirso, M. Viljus, S. Letunovits, Two-body dry abrasive wear of Cr_3C_2-Ni cermets, Proc. Estonian Acad. Sci. Eng. 12 (2006) 368-376.
39. K. Bonny,P. DeBaets, W. Ost, S. Huang, J. Vleugels, W.Liu, B. Lauwers, Influence of electrical discharge machining on the reciprocating sliding friction and wear response of WC-Co cemented carbides, Int. J. Refract. Met. Hard Mater. 27 (2009) 350-359.
40. K. Bonny, P. DeBaets, J. Quintelier, J. Vleugels, D. Jiang, O. Van der Biest, B. Lauwers, W. Liu, Surface finishing: impact on tribological characteristics of WC-Co hardmetals, Tribol. Int. 43 (2009) 40-54.
41. A. J. Gant, M.G. Gee, B. Roebuck, Rotating wheel abrasion of WC/Co hardmetals, Wear 258 (2005) 178-188.

Chapter 8 Reciprocating Wear Behaviour of TiC-Stainless Steel Cermets

Chenxin Jin, Chukwuma C. Onuoha, Zoheir N. Farhat, Georges J. Kipouros, and K.P. Plucknett*

Dalhousie University, 1360 Barrington Street, Materials Engineering Program, Department of Process Engineering and Applied Science, B3H 4R2, Nova Scotia, Canada

Status: *Submitted:* Tribology International

Abstract

TiC based cermets have been prepared with three different grades of stainless steel binder (304L, 316L and 410L). The cermets were densified by vacuum melt infiltration, at 1500°C, which allows the steel binder content to be readily varied from 5 to 30 vol.%. The cermets were assessed for their hardness and indentation fracture resistance using Vickers testing. The reciprocating wear response was evaluated using a ball on flat geometry, with a WC-Co counter face sphere. It was shown that the coefficient of friction increases with increasing steel binder content, and also with increasing load and wear time. Similarly, the specific wear rate increases with both steel binder content and applied load, but was largely independent of the steel grade used.

Keywords: Abrasive wear; adhesive wear; coefficient of friction; optical profilometry

*Author for correspondence: kevin.plucknett@dal.ca

8.1 Introduction

Many demanding applications in the chemical, aerospace, automotive, mining, and oil and gas industries require the use of materials that show a good combination of wear and corrosion resistance. Invariably, ceramic-metal composites, or cermets, are employed in these industries due to their unique combination of high wear resistance, hardness, and strength characteristics, combined with good aqueous corrosion resistance [1-3]. The most widely employed cermet-type materials are the tungsten carbide-cobalt (WC-Co) cemented carbides, or 'hardmetals', which have been extensively used as cutting tools, and also in the drilling and mining industries [4,5]. WC-Co based coatings are also widely used as hard chrome replacements [6,7]. However, cemented carbides based on WC suffer from having exceptionally high densities (~13-15 g/cm^3), relatively poor mechanical properties at elevated temperatures, and only moderate oxidation and corrosion resistance. Titanium carbide (TiC) based cermets have proven to be a good substitute for these conventional 'hardmetals' in many applications, due to having low densities (less than 50% of WC-Co), high chemical and thermal stability, relatively high hardness, and good wettability with many metallic binder materials. Several metals have been utilised as ductile binders with TiC, such as Ni, Mo and Fe [8-11]. Due to the relatively low cost, potential for heat-treatment, and good strength and ductility, Fe-based alloys are now being studied and applied more widely [9,12,13]. TiC based cermets have been reported to show high abrasive wear resistance [14]. Degnan and colleagues noted that it is the load bearing capability of the TiC retained at the sliding surface of the composite, and its ability to reduce metal to metal contact during sliding, that is responsible for the improved wear performance of TiC composites at low level of ceramic loading [15].

When thinking specifically about ferrous alloys, stainless steels are widely used for their corrosion resistance, while they also typically possess good mechanical properties. However, one significant limitation of austenitic stainless steels (e.g. 316L) is their poor wear resistance. These materials are generally quite soft, and thus are susceptible to many common forms of wear and contact damage [16]. For wear driven applications, ferritic or martensitic stainless steels are better choices [17]. Because of this drawback in tribological applications, several authors have investigated ways to improve the wear behaviour of

stainless steels. Pagounis and co-workers reported that the wear resistance of stainless steel can be improved dramatically through the incorporation of ceramic particles such as carbides and oxides [18]. Akhtar and Guo reported that a 50%-70% TiC addition to a stainless steel binder, therefore generating a cermet structure, led to improvement in wear resistance [17]. Tjong and Lau also reported a significant improvement in the micro hardness, sliding wear and abrasion wear resistance by addition of 20 vol.% of a related material, titanium diboride (TiB_2), to 304L stainless steels [19].

For the present study, we have developed a family of TiC-based cermets utilising a variety of austenitic and martensitic stainless steels as binder (i.e. grades 304L, 316L, and 410L), using a simple melt infiltration/sintering technique, with the binder contents varied from 5 to 30 vol.%. The primary aim of this study is to investigate the microstructure, mechanical, and wear behaviour of these new TiC stainless steel composites. A companion paper will report in more detail on the microstructural effects of the wear process in terms of damage accumulation [20].

8.2 Experimental Procedures

8.2.1 Sample Preparation

The general details of the melt infiltration process for production of the cermets has been reported in detail previously [21-23], and will only be briefly outlined here. The TiC powder used in the current study was obtained from Pacific Particulate Materials Ltd. (Vancouver, BC, Canada), and had a manufacturer quoted mean particle size of ~1.3 μm; this was confirmed through independent particle size analysis, with a measured mean of ~1.25 μm, and a clear bimodal distribution [24]. The 304L (Stock #: 11085, Lot #: K19M09), 316L (Stock #: 11089, Lot #: A04S008) and 410L (Stock #: 11088, Lot #: I23M43) stainless steel powders were all obtained from Alfa Aesar (Ward Hill, MA, USA), and each had a nominal particle size of -100 mesh. Chemical composition analysis of the as-received TiC powder, determined using inductively coupled plasma optical emission spectroscopy (ICP-OES; Model Varian Vista Pro, CA, USA) is presented in Table 8.1. The W and Co constituents are believed to arise from a milling stage used by the manufacturer for particle size reduction. ICP-OES was also used to analyse the

metallic constituents of the three stainless steel powders, as demonstrated in Table 8.2. In this instance the powders match the specifications typically reported for these steel grades. The C and N contents were determined using combustion infrared (Model Leco CS-444, Leco Instruments, St. Joseph, MI, USA) and inert gas fusion methods (Model Leco TC-436, Leco Corporation, St. Joseph, MI, USA), respectively.

Table 8.1: ICP-OES chemical analysis of the TiC powders used in the present work (in wt.%). C comprises the balance.

Element	**Ti**	**W**	**Co**	**Fe**	**Ta**	**Ni**	**Cr**
Concentration	76.79	2.22	0.23	0.17	0.026	0.024	0.014

Table 8.2. A summary of themical analysis results for the nominal compositions (in wt.%) of the three stainless steel powders used in the present study. Fe comprises the balance.

Alloy	**Cr**	**Ni**	**Mo**	**Mn**	**S**	**Ti**	**Si**	**V**	**Co**	**C**	**N**
304L	17.56	10.92	0.073	0.130	0.005	< 0.01	0.427	0.028	0.034	0.023	0.034
316L	16.28	12.81	2.21	0.12	0.01	< 0.01	0.56	0.0177	0.0836	0.03	0.03
410L	11.91	0.078	0.0155	0.1578	0.0106	< 0.01	0.6354	0.0154	0.0131	0.021	0.026

In order to fabricate the cermets, TiC powder pellets were uniaxially compacted in a hardened steel die at ~45 MPa (using ~7.35 g of powder), and then vacuum sealed in polyethylene bags and cold isostatically pressed at ~208 MPa. After compaction, a known amount of steel powder is applied on top of the pressed disks (held in alumina crucibles), which were then melt-infiltration/sintered in a graphite resistance furnace (Materials Research Furnaces, Suncook, NH, USA). The vacuum sintering cycle was conducted at 1500°C, held for 60 minutes, with nominal heating and cooling rates of 10°C/min and 25°C/min, respectively. Using this approach, samples with 5 to 30 vol.% steel content could be prepared for each of the steel grades.

8.2.2 Materials Characterisation

The sintered densities of the cermet samples, as a percentage of theoretical, were determined using Archimedes immersion method in water. For subsequent microstructural evaluation and wear testing, the samples were first ground flat using a coarse grit diamond peripheral wheel, and then polished to a mirror-like finish (starting with a 125 μm diamond impregnated pad and finishing with 0.25 μm diamond paste). Microstructural assessment was then conducted using both optical microscopy (Model BX-51, Olympus Canada, Richmond Hill, Ontario, Canada) and scanning electron microscopy (SEM; Model S-4700, Hitachi High Technologies, Tokyo, Japan), equipped with energy dispersive X-ray spectroscopy (EDS; Model Inca X-Max^N, Oxford Instruments, Abingdon, UK) for chemical microanalysis. The mean TiC grain size in the sintered materials was determined using the linear intercept method [25] from digital SEM images, while both the TiC-TiC contiguity and steel binder mean free path (MFP) were determined using Gurland's method [26]. The hardness of the materials was determined using Vickers indentation (Model V-100A, Leco Corporation, St. Joseph, MI, USA) with a 1 kgf applied load, held for 15 seconds, in order to avoid any sample cracking. The indentation fracture resistance (IFR) of the various cermets was determined using Vickers indentation method, with a 50 kgf applied load. Both median and Palmqvist-type sub-surface cracking patterns can be anticipated for these materials, depending on the load and binder volume fraction. For median cracking, IFR values were determined using the equation developed by Anstis and colleagues [27]. For the Palmqvist-type cracking a modified version of the equation formulated by Shetty and co-workers was employed [28], consistent with our recent work [29]. To ensure the validity of the measurements of both hardness and IFR values, a minimum of six indentations were made for each test procedure and material.

8.2.3 Reciprocating Wear Testing

A reciprocating wear test procedure, using a ball-on-flat geometry, was employed in the present study, and is consistent with our recent publications on related cermet systems [22,29]. The tests were conducted using a universal micro tribometer (Model UMT-1,

Bruker Corp., Campbell, CA, USA) on cermet samples prepared with 10, 20 and 30 vol.% of each of the three steel grades. A 6.35mm diameter WC-Co counter-face sphere (Grade 25 with 6 wt.% Co, equivalent to ~10.2 vol.% Co) was used, sliding against the sample in a reciprocating motion. The wear tests have a fixed stroke length of 5.03 mm, while an oscillating frequency of 20 Hz is used. The tests were conducted at room temperature (21 ± 2°C), with a relative humidity of 40-55 %. The effects of applied load were assessed using fixed duration tests (120 minutes total sliding time, for a sliding distance equivalent to ~1.45 km), with loads of 20, 40, 60 and 80 N. The effects of test duration were determined with 40 and 80 N applied loads, for total test times of 15, 30, 60 and 120 minutes.

After wear testing the samples were assessed using optical profilometry (Model PS50 Optical Profilometer, Nanovea, Irvine, CA), to observe the general wear track features in three dimensions, but more importantly to determine the volume of material removed from within the track itself. The wear loss is then used to calculate the specific wear rate, k, based on the Lancaster relationship [30].

$$k = \frac{V}{PD} \qquad \text{Equation 8.1}$$

where V is the volume removed in mm^3, P is the applied load in N, and D is the total sliding distance in m.

8.3 Results and Discussion

8.3.1 Microstructure Characterisation

It is generally assumed that the wear behaviour of cermet materials is a direct function of both the material hardness and toughness [31], and that an optimum wear response is obtained when both of these properties are fully maximized [32]. In view of this, the processing techniques used in the production of TiC-based cermets should be careful selected. A method that minimises residual porosity and effects a homogenous distribution of the carbide phase within the metallic binder phase, with no interfacial debonding, should be employed. These benefits are achieved when using vacuum melt-

infiltration/sintering in the production of the TiC stainless steel cermets, which ensures highly dense cermets (>98 % of theoretical density), even when very low amounts of binder are employed (even as low as 5 vol.%).

Based on a simple rule of mixture, the densities of the sintered samples were assessed as a percentage of theoretical. It can be seen from Figure 8.1 that all of the cermets have achieved process densities greater than 98 % of theoretical. It is also noted that densities apparently *exceeded* 100% of theoretical in some instances. This arises from the use of a simple rule of mixtures calculation and the assumption that there is no change in composition (and hence theoretical density) of either constituent during sintering. However, in reality there is a high probability of modified compositions, to a greater or lesser extent, after sintering; for example, some limited solubility of the ceramic phase in the steel melt is a requirement for liquid phase sintering to proceed. It can also be observed from Figure 8.1 that there is an apparently small decrease in the sintered densities as the binder content increases. This phenomenon has been discussed in our recent work [33], and arises due to a combination of minor volatilisation of the steel constituent, and some limited compositional change of the phases (i.e. the formation of a 'core-rim' structure in the TiC, and the reduction of Mo contents in selected steel grades).

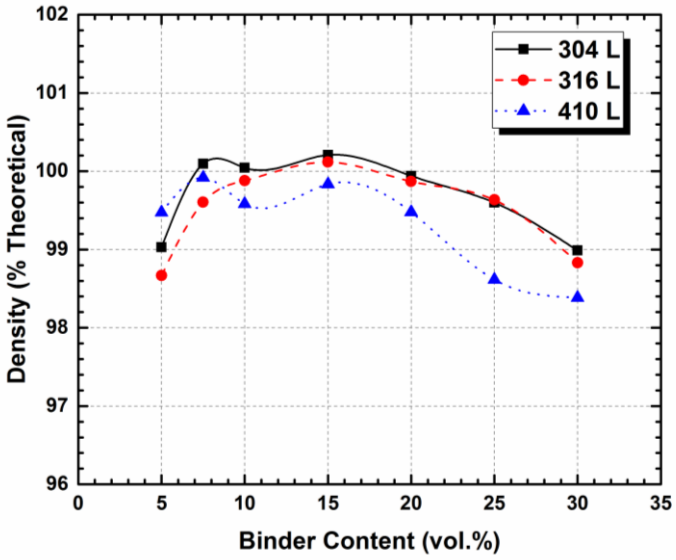

Figure 8.1: The effects of steel binder content on the density of the melt-infiltration/sintered TiC-stainless steel cermets.

A typical optical microscopy image of TiC with 20 vol.% 410L steel binder is presented in Figure 8.2(a). The microstructure of the sintered samples is homogeneous, with negligible evidence of residual. A representative SEM image of TiC with 10 vol.% 316L binder is shown in Figure 8.2(b), while Figure 8.2(c) highlights the microstructure of a small region in Figure 2 (b) where a W-rich area is present. There is no evidence of interface debonding in the cermets, which show good wettability of the molten stainless steel binder with the TiC particles during melt-infiltration/sintering. A homogenous distribution of TiC in the binder phase and an absence of interface debonding can be expected to enhance the tribological and mechanical properties of the composites.

It can be observed that there are some concave grains in the image, which is often observed in TiC-based cermets [34,35], which can be explained through the 'instability of solid-liquid interface' theory [33]. A 'core-rim' structure has also developed in the cermets after the sintering, with a dark 'core' of pure TiC surrounded by a lighter 'outer rim'. With the 316L binder, the core-rim structure is relatively clear, with a thin, light contrast 'inner rim' as well as the darker TiC core and outer rim. For TiC with either 304L or 410L as binders, the structures are subtler in nature. This arises because of the relative chemical compositions of the 'core-rim' structure itself; the backscattered electron detector emphasises contrast based on average atomic number differences. For 316L

cermets, the outer rim is mainly (Ti,Mo,Cr,W)C, as heavier elements precipitate onto the particle as a complex carbide; here there is also a greater concentration of W present in a thin, inner rim region. For the 410L containing cermets, there is no Mo content in the original steel powder, and the outer rim is (Ti,W)C, based on the EDS analysis. It is interesting to find some 'localized' white areas in the SEM images of these cermets, it appears that the particle is surrounded by high amount of W. The W arises as contamination in the TiC powder, presumably from an attrition stage used by the manufacturer, when milling the powders to a finer size.

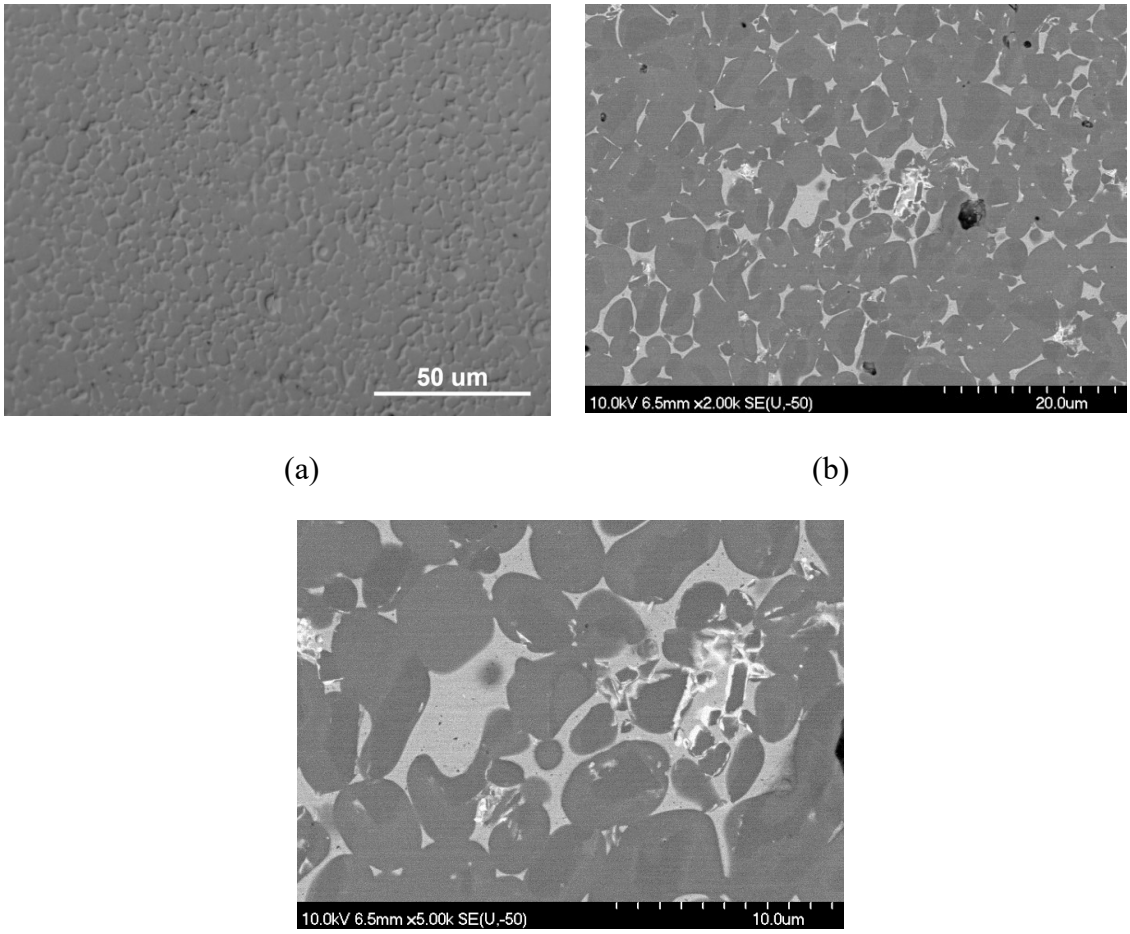

(a) (b)

(c)

Figure 8.2: DIC optical microscopy image of TiC cermet with 20 vol.% 410L stainless steel binder. (b) SEM image of TiC cermet with 10 vol.% 316L stainless steel binder. (c) Higher magnification image shows a W concentrated area from (b).

The characteristic microstructural parameters are important in determining the ultimate material properties, such as hardness, fracture toughness, etc. In particular, the binder MFP is effectively a measure of the steel ligament dimensions between TiC particles. This will dictate the distance over which a dislocation can move in the binder [36], and hence have an influence on altering the binder yield stress in a manner equivalent to the Hall-Petch effect. The various microstructural parameters that were examined (i.e. mean grain size, contiguity, and binder MFP), as a function of steel binder content, are presented in Figure 8.3. For the mean grain size of the cermets, shown in Figure 8.3(a), the standard deviation values were obtained from measuring the mean values from individual distributions for multiple samples. It appears that the grain size is essentially independent of the binder content, which is consistent with previous observations of TiC-based cermets, indicating an interface-controlled grain growth mechanism likely predominates [22,37]. Figure 8.3(b) presents the contiguity of the cermets, and highlights that this parameter decreases with increasing steel binder content. Not surprisingly, as the binder content increases, due to its wetting ability there is a tendency for lowered TiC-TiC contact, and hence a reduced contiguity. In terms of the binder MFP, there is a generally trend of increasing ligament dimension with increasing binder content (Figure 8.3(c)). The slight increase in binder MFP at low binder volume fractions is likely due to the complex carbide morphology that develops (i.e. ‘C’ and ‘O’ shaped TiC grains). For cermets and hardmetals, a small binder mean free path can be expected to lead to higher abrasion resistance [38]. Comparing the three cermets, TiC-316L invariably has the lowest binder mean free path values, which likely arises due to Mo depletion from the steel (effectively lowering the true binder volume fraction).

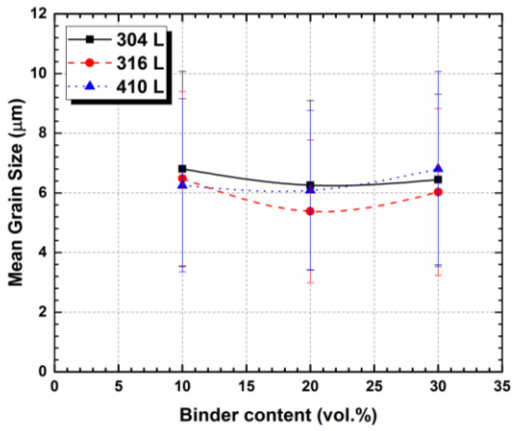

(a)

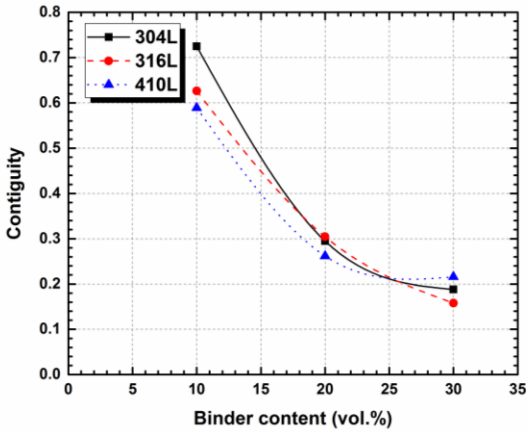

(b)

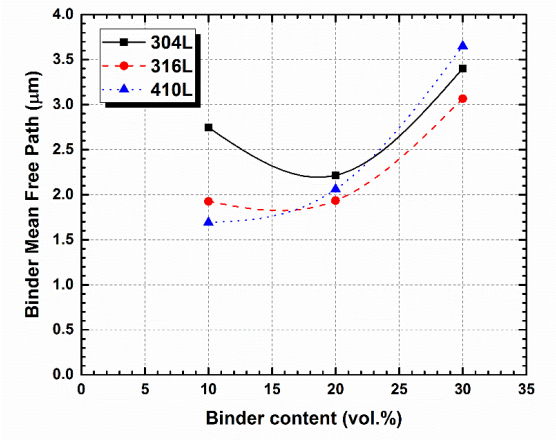

(c)

Figure 8.3: Microstructural parameters determined for the TiC-stainless steel cermets: (a) mean grain size, (b) contiguity, and (c) binder MFP.

8.3.2 Hardness and Indentation Fracture Resistance

High hardness, respectable strength and fracture toughness, combined with relatively low production costs make TiC based materials attractive and widely used wear resistant composites [31]. According to conventional definitions, the structure of one or both surfaces and the component(s) that may be present between the sliding surfaces (which can contain hard particles), can be viewed as leading to 'abrasive wear'. Processes resulting in abrasive wear are usually through brittle fracture or plastic deformation [38,39]

To predict the wear mechanism and to study the wear response, two important bulk material properties are often assessed, namely the hardness and fracture toughness.

Vickers hardness measurements of the present cermets, as a function of binder content, are presented in Figure 8.4. The hardness values are plotted as both the Vickers hardness number and also in GPa. Overall, the hardness values obtained are relatively consistent for each of the steel binders, but it appears that the 316L steel grade provides the highest hardness for a fixed binder content, while the 304L cermets exhibits the lowest; these observations broadly confirmed the previous prediction from the binder MFP values. The hardness is observed to decrease as the binder content increases, which relate to the reduced amount of elastic phase (i.e. ceramic) with the cermet structure. Increasing the binder ligament size (i.e. the binder MFP) has effectively increased the dimensions a dislocation could move within the ligaments, which can be ultimately expected to reduce the yield stress.

A number of equations have been developed to determine the wear rate of advanced materials, one of which is the Archard equation [40], originally developed based on sliding wear scenarios, which is given as:

$$V = \frac{k_1 PL}{H} \qquad \text{Equation 8.2}$$

where V is the material volume loss, in mm^3, k_1 is the wear coefficient or wear rate, which will be determined, P is the applied load, in N, L is the sliding distance, in m, and H is the Vickers hardness number of the material. This can be compared with the Lancaster relationship, outlined earlier in Equation 8.1. It has been demonstrated that hardness is an important mechanical parameter in terms of the wear resistance of materials. According to Hutchings [38,39], for wear by plastic deformation, such as in metals, the specific wear rate of the material is dependent upon the hardness. When the contact pressure exceeds the hardness of the surface, fully plastic deformation would occur. The ratio of hardness of the abrasive (H_a) and the hardness of the wearing surface (H_s), gives an indication of the type of wear; when $H_a/H_s > \sim 1.2$ it is often called 'hard abrasion', and when $H_a/H_s < \sim 1.2$, it can be termed 'soft abrasion' [38]. The actual hardness value of the WC-Co counter-face ball was tested in the current study with 1 kgf,

and a value of HV 1668 ± 92 was determined. Comparing this to the hardness of the present cermets, the hardness values are higher than the counter-face for low binder phase contents. At this stage the wear of the material is dominated by the elastic-plastic response; this phenomenon is common in ceramics, cermets, hardmetals (i.e. WC-Co), and hardened steels [41]. For the present materials the transition from 'hard abrasion' to 'soft abrasion' is expected to occur at approximately 25 vol.% of binder content; a nominally fully plastic deformation response can then be anticipated at high binder phase contents (i.e. 30 vol.%).

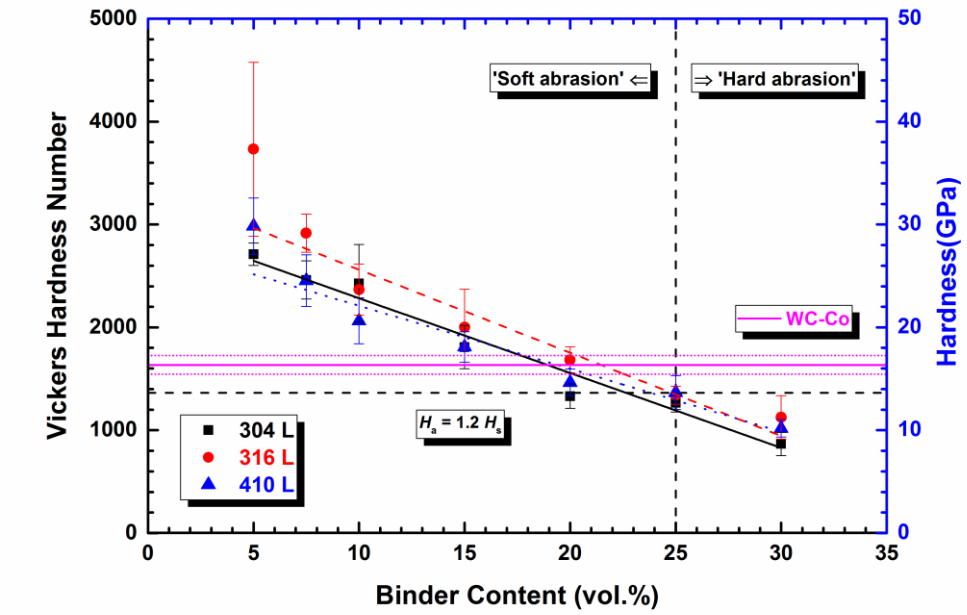

Figure 8.4: TiC cermet hardness values, as a function of steel binder content, for the three steel grades, measured using 1 kgf of applied load.

When it comes to brittle materials, the wear behaviour is usually dominated by fracture. As a consequence, the fracture toughness of the material also plays an important role. Though the elastic moduli of ceramics are usually relatively high, plastic deformation can occur, which is invariably followed by crack formation. Many models have been developed to estimate the abrasive wear for brittle materials, one of which is the 'plastic groove' model, formulated by Evans and colleagues [42], where the volume wear rate per unit sliding distance for all particles is Q and the equation is given as:

$$Q = \alpha_1 N \frac{\left(\frac{E}{H}\right) P^{9/8}}{K_c^{3/4} H^{1/2}}$$ Equation 8.3

where N is the number of particles in contact with the surface, α is a material-independent constant, E is the elastic modulus, K_c is the fracture toughness, and H is the hardness. This equation has taken into account both the hardness and the fracture toughness of the material.

This relationship was subsequently further adapted by Evans [43]:

$$Q = \alpha_2 N \frac{P^{5/4}}{K_c^{3/4} H^{1/2}}$$ Equation 8.4

and further can be written as:

$$Q = \alpha_3 \frac{W^{5/4} d^{1/2}}{A^{1/4} K_c^{3/4} H^{1/2}}$$ Equation 8.5

where W is the fixed load, A is the apparent contact area, d is the linear dimension where particles are in contact, and N is proportional to Ad^{-2}. These equations are all in a form where there is an inverse correlation of the wear rate with some power of the fracture toughness, indicating that the wear rate depends more predominantly on the material fracture toughness than its hardness. According to previous research, the predicted wear rates are invariably much higher than those that arise through plastic deformation alone [38,39]. This may relate to the fact that these models assume the cracks generated underneath the surface are based on an indentation mechanism.

For the cermets in the current study, at low binder phase content, the majority of the material is the hard TiC phase (up to 90 vol.%). As a consequence, the cermet fracture toughness is probably more important in predicting the wear response [38,44]. The indentation method, using a Vickers indenter, is widely used to 'estimate' the fracture toughness or 'fracture resistance' of brittle materials [45-48], and can be seen to be relevant under scenarios relating to low rate impact by sharp objects. The current study is not focused on the absolute validity of this method, but rather to give a comparative indication of the indentation fracture properties of the materials. The IFR values for the present cermets are shown in Figure 8.5, as a function of the steel binder content. It can

be seen that, through increasing the steel binder content, the IFR of the TiC cermets increases considerably. Generally, pure TiC exhibits a relatively low fracture toughness (i.e. K_{IC} = 2 to 3 MPa·m$^{1/2}$) [49]. By adding the steel binder into the cermet structure, a highly ductile phase is increasingly incorporated, thereby improving the fracture toughness. To show the different types of sub-surface cracks that are expected to be generated (i.e. 'median/radial' and/or 'Palmqvist'), and the transition point(s) for these crack patterns, the IFR values have been plotted as both open and closed symbols, indicating the usage of the two equations for median/radial (Anstis *et al*. [27]) and Palmqvist (Shetty *et al*. [28]) cracking, respectively.

Based on Figure 8.5 it can be seen that the transition from 'median' to 'Palmqvist' type cracks, for the composites with 304L and 316L stainless steel, occurs between 5 and 7.5 vol.% binder, while for the 410L stainless steel, this transition lies between 10 and 15 vol.% binder. Due to this crack mechanism transition, and the relative equations being used in each case, some of the IFR values appear to be lower for Palmqvist cracks than for median/radial cracks in the low binder content cermets (i.e. 10 vol.% binder for both 304L and 316L containing cermets). The main reason to assess the transition between operative crack systems is due to the suggestion that in the abrasive wear by brittle fracture, the lateral cracks, or 'Palmqvist' cracks, move vertically towards the loading direction upon unloading, and are therefore related to material removal during wear [38]. As a consequence, Figure 8.5 basically suggests that as more ductile phase material is added into the cermet system, the easier the formation of the lateral cracks becomes, leading to increased wear. Clearly, this seems contradictory. However, prior work on WC-Co and TiC-based cermets have indicated that what appear to be lateral cracks in the sub-surface are actually not the result of an 'indentation mechanism' at all, and that in this instance a fatigue mechanism is more likely to occur [50,51]. Further discussion of the sub-surface damage evolution for the current cermets is provided in a companion paper to the present study [20].

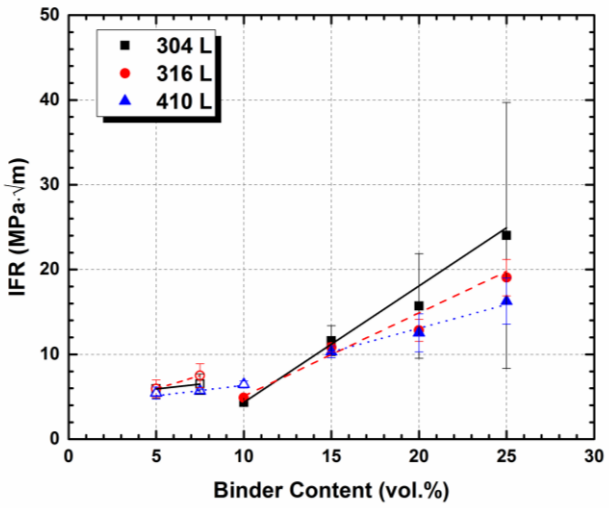

Figure 8.5: Measurement of IFR as a function of binder content for the three TiC-stainless steel cermet systems, highlighting the transition from median/radial cracking (open symbols) to Palmqvist cracking (filled symbols).

8.3.3 Reciprocating Wear Behaviour

8.3.3.1 Load Effects on the Wear Response

The cermet samples were initially tested under applied loads of 20, 40, 60 and 80 N, for a period of 120 minutes. Representative dynamic coefficient of friction (COF) curves, obtained under 20 and 40 N loads, are presented in Figure 8.6(a-c). For cermets with a low binder content (i.e. 10 vol.%), it is apparent that the applied load has an important influence on the COF (Figure 8.6(a)). The dynamic coefficient of friction initially increases with test time under 20 N applied load, and then stabilises after approximately 15 minutes. For the higher load (i.e. 40 N), the values tend to increase for the first ~60 minutes, and then stabilise and maintain an essentially steady state after that. For cermets with high binder content (i.e. 30 vol.%), the dynamic COF slightly decreases with increasing load, indicating a potential transition in wear mechanism.

Previous studies have suggested such a response may indicate a transition from two-body to three-body abrasive wear [22,23,29]. Here third-body particles are generated, through a combination of binder extrusion and micro-fracture of the ceramic phase, and the resultant particles are then free to roll back and forth between the tribopair surfaces. It appears that the dynamic COF for cermets with the austenitic steel binders (i.e. 304L and

316L) are also more sensitive to testing time, compared to the nominally martensitic steel binder (i.e. 410L). Figure 8.6(d) shows the dynamic COF curves of the TiC-410L cermet with 10 vol.% binder at four different loads. It can be seen that when the cermets were subjected to an applied load of 20 N the COF is relatively constant through the whole testing time, while for the other loads it gradually increased with time.

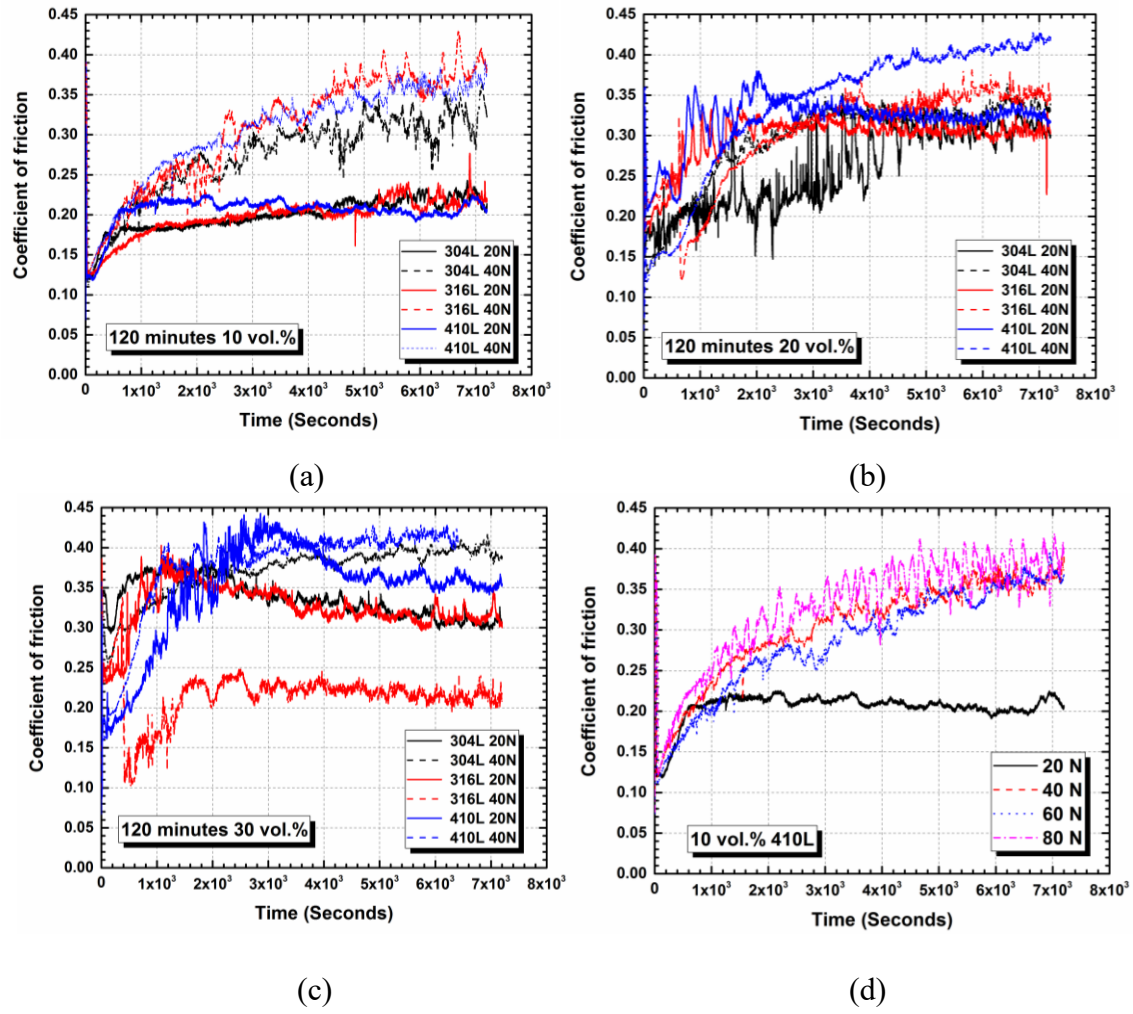

Figure 8.6: Dynamic coefficient of friction curves at 20 and 40 N for TiC cermets with binder contents of: (a) 10, (b) 20, and (c) 30 vol.% stainless steel. (d) The effects of applied load on the dynamic COF curves of TiC with 10 vol.% 410L stainless steel.

The mean COF values for the cermets, as a function of applied load, are presented Figure 8.7. It can be seen for all compositions that the mean COF ranges from ~0.18 to ~0.38. A

previous study has reported that using a 6 mm diameter WC-6Co sphere, dry sliding against a 304 stainless steel with 2.5 N applied load, has a coefficient of friction of 0.58-0.63 [52]. A separate study reported that by applying 5 N load, a 6 mm WC-Co sphere sliding against 304 stainless steel has a COF of ~0.65 after ~0.5 m total sliding distance [53]. Clearly, the incorporation of high TiC contents in the present work lowers the COF significantly.

When subjected to the same load, the mean COF generally increases with increasing binder content. At low binder contents (i.e. 10 vol.%), the high elastic modulus TiC particles resist deformation under the high Hertzian contact load; here it should be noted that the ceramic phase contiguity is high, and there are many TiC-TiC contacts. By increasing the steel binder content, there is an increase in the binder MFP, and a concurrent reduction in the contiguity. As a consequence, it becomes easier to extrude the significantly softer steel binder out from between the TiC grains, and the ductile steel can then be expected to present a greater contact area against the WC counter face sphere, raising the COF. It can be seen that the COF response generally agrees with the trend of hardness, and again relates to the ability to plastically deform the softer metallic phase. Ultimately, the extent of material removal from the binder or grain fragmentation/pull-out decreases with an increase in TiC content, which must be balanced against the more brittle fracture response of a lower toughness cermet.

There is typically a slight increase in COF with applied load, from 20 to 40 N, and then invariably a slight drop at highest load (80 N). Previous research has suggested this may be the result of formation of a tribolayer and its subsequent spallation [22]. In a related study on TiC-Ni_3Al cermets [23], typical maximum temperatures within the wear tracks were ~60˚C at 20 N, rising to ~100˚C for 60 N. As the extent of frictional heating increases the temperature, it can be anticipated that the COF also increases. The small drop in COF at the highest load (i.e. 80 N) may infer the formation of a more lubricious tribolayer, which by this stage has a fine, atomically mixed structure and relatively high oxygen content [20].

Unsurprisingly, the current mean COF values are similar to a previous study [29] on related TiC-316L stainless steel cermets, using an identical test geometry, with both fine

and coarse TiC grain structures; in that instance the mean COF values ranged from ~0.25 to ~0.42. In comparison, for a TiC-Ni_3Al cermet system, with 20 to 40 vol.% Ni_3Al binder (alloy IC-50), the mean COF was ~0.3 for *all* evaluated compositions [54], regardless of the binder content. It was also shown that the COF was stable and essentially independent of load throughout the test duration [54]. That response is clearly quite different from the present TiC cermets, using a variety of stainless steel binders, and could be explained by a significantly higher yield strength for the IC-50 Ni_3Al alloy (~470 MPa [55]) comparing to typical stainless steel values (i.e. ~190 MPa for 304L [56]); it should also be noted that the yield strength for the IC-50 alloy can be increased to >1,500 MPa through cold working [55], and some degree of similar strengthening can be anticipated through the constraint of the Ni_3Al in a cermet structure.

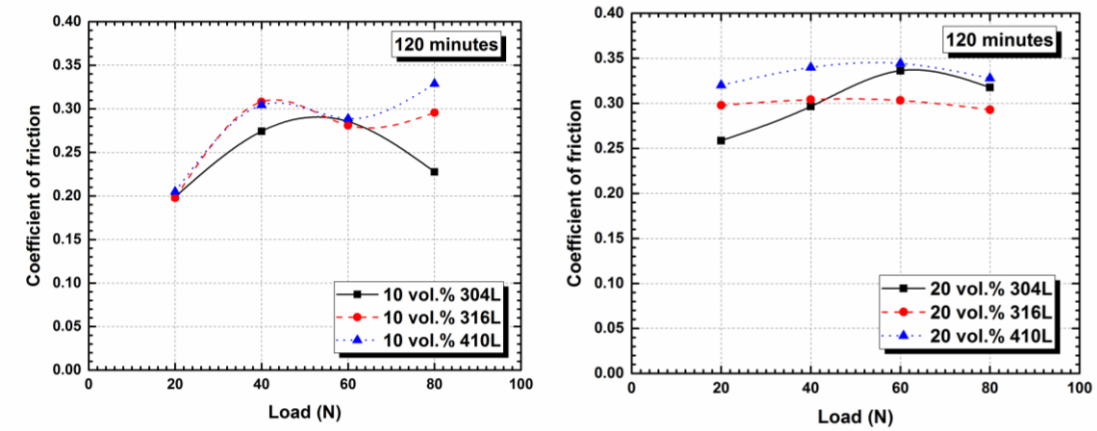

(a) (b)

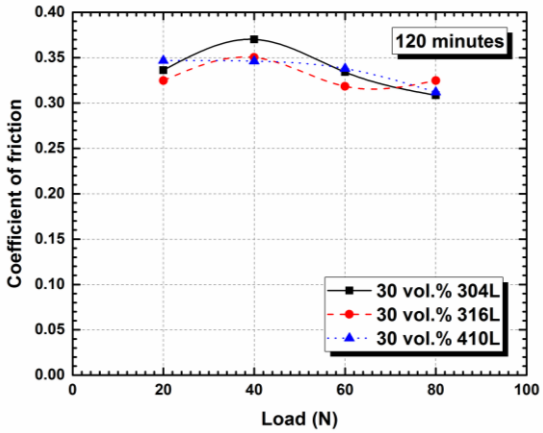

(c)

Figure 8.7: The effect of binder content on the average COF as a function of various applied load.

The specific wear rate, as a function of the applied load, for all cermets tested for 120 minutes, is presented in Figure 8.8. A consistent and essentially linear increase with applied load is noted for each of the cermets examined. A broadly similar linear trend has also been observed in WC-Co hardmetals, as the wear volume increases proportionally with increasing hardness [57]. In the present work, for each steel grade used, at a fixed load, the specific wear rate increases with increasing binder content. In this instance the volume fraction of the hard TiC phase is being reduced, which results in a decrease in hardness. As noted earlier, when the steel content increases, the binder MFP also increases, and the cermets deform with an increasingly ductile response. It can be seen that the specific wear rate increases more dramatically with higher binder contents, especially for 30 vol.% of each of the steels. For single-phase materials, the wear rate invariably increases when the hardness of the wearing material equals that of the counter face surface [58]. However, for equivalent hardness composites, the metallic binder phase has a lower hardness than the single-phase (ceramic) material, therefore the when the hardness of the abrasive particles exceeds the hardness of the hard reinforcing phase (i.e. TiC in this case), the wear rate can be much higher [58], even compared to a lower binder content material. In the current work, the specific wear rate values remain relatively close for all of the cermets at low loads, but the values deviate somewhat when subjected to higher loads (i.e. 80 N); previous work has demonstrated typical standard deviation errors

of ~25 % for these types of test, so this may be simply typical of the error. However, there is a general trend that materials with a 316L grade binder show higher specific wear rates at the highest loads, while 304L and 410L show a broadly consistent response.

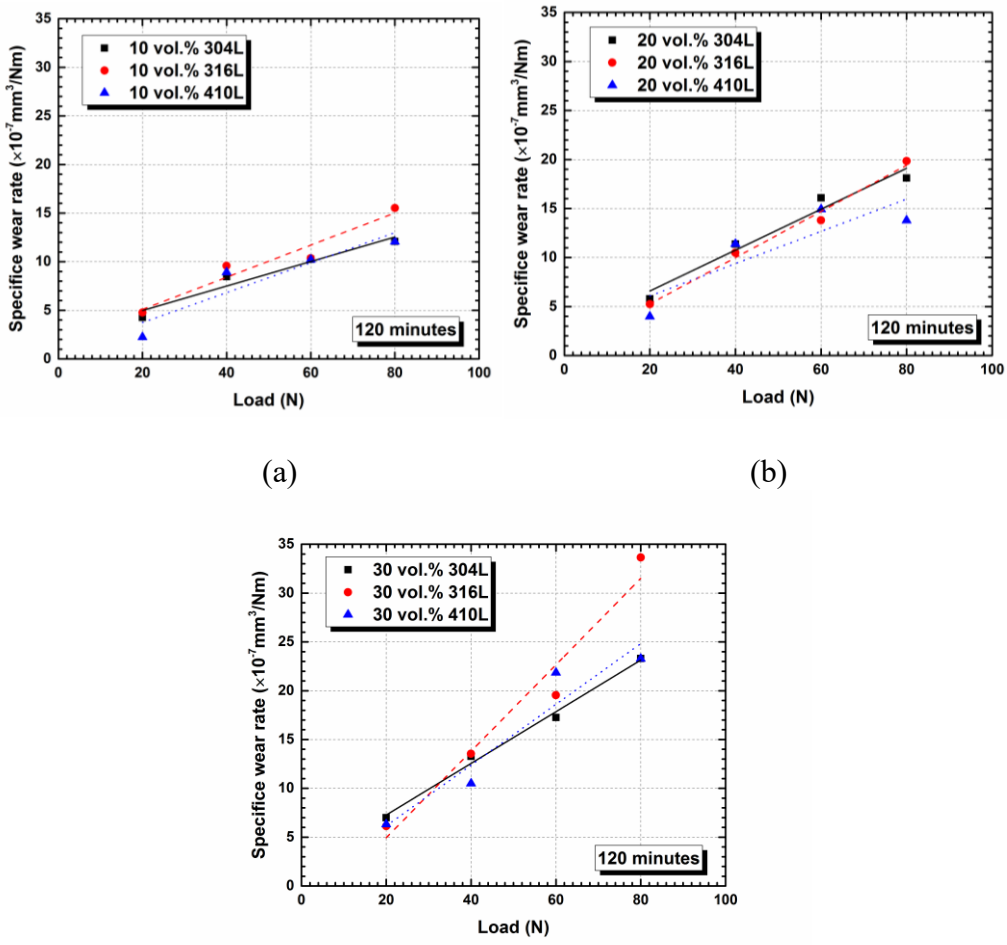

Figure 8.8: Effect of binder content on the specific wear rate as a function of load: (a) 10 vol.%, (b) 20 vol.%, and (c) 30 vol.% steel binder.

The volume wear loss is plotted as a function of the respective cermet hardness in Figure 8.9. To better understand the wear response of the tested material, microstructure parameters such as grain size and binder MFP are important. These parameters play an important role in controlling cermet mechanical properties, such as hardness and fracture toughness (in the current study, more precisely, the 'indentation fracture resistance', or

IFR). It can be seen that the wear loss against hardness follows a log fit relatively well. In prior work, the dependence of the hardness was also found to follow a log linear trend in cemented carbides, such that:

$$V = A\exp(-BH) \qquad \text{Equation 8.6}$$

or, alternately:

$$\log_{10}V = A - BH \qquad \text{Equation 8.7}$$

where A and B are constants [50,57,59]. The dependence of wear on fracture toughness has also been assessed in the study of the hardmetals [50,60], and a correlation was also found, indicating that both hardness and fracture toughness are important in the abrasion wear of hardmetal-type materials. Since the IFR values in the present work were determined using different equations (i.e. for either median/radial, or Palmqvist cracking), no such plots of the relationship between wear loss and indentation fracture resistance were conducted.

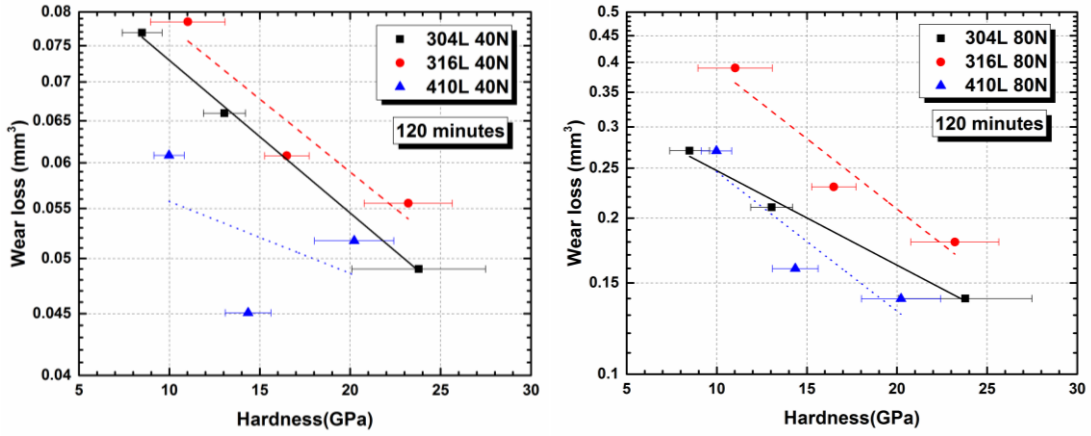

(a) (b)

Figure 8.9: The specific wear rates, as a function of hardness, for the three TiC-stainless steel cermets subjected to: (a) 40 N and (b) 80 N of load during reciprocating testing. Note that higher binder content samples will exhibit lower hardness values in these plots (i.e. increasing binder content from right to left). All samples were tested for 120 minutes.

Comparing the results from the current study it can be concluded that, by developing cermet structures, the wear resistance was dramatically increased compared to the steels alone. For example, 304L stainless steel itself exhibits a specific wear rate 2 to 3 orders of magnitude higher than the cermets, at 1.07×10^{-4} mm^3/Nm [61], when tested against a similar WC-Co counter face material. The specific wear rates for these cermets are, not surprisingly, similar to our recent research on TiC-316L stainless steel cermets with fine- and coarse-grained structures [29]. That study demonstrated specific wear rates for the coarse-grained cermets, with 30 vol.% of binder, of ~5×10^{-7} mm^3/Nm at low loads (i.e. 20 N), which increased considerably to up to ~65×10^{-7} mm^3/Nm at the highest loads (i.e. 80 N). Buchholz and colleagues studied related TiC cermets, using a Ni_3Al binder (alloy IC-50), with its content varied from 20 to 40 vol.% [52,62]. The reported specific wear rates were observed to vary between 1.5 and 10×10^{-7} mm^3/Nm, again increasing with applied load. A separate study reported slightly lower specific wear rates, ranging from 0.2 to 3.8 $\times10^{-7}$ mm^3/Nm, for a TiC-Ni_3Al cermet with 20 to 40 vol.%, using applied loads of 20 to 60 N of load [23]. This later material differed in both the manufacturing route, press-and-sinter rather than melt infiltration, and the Ni_3Al alloy composition; in the later work a stoichiometric Ni_3Al alloy was used. For other cermets systems, Pirso and colleagues have studied the dry abrasive wear of Cr_3C_2-Ni (with binder contents of 7.7 to 24.5 vol.%), TiC-NiMo (6.1 to 34.4 vol.% binder), and WC-Co (10 to 31.6 vol.% binder) cermets under 20 N of load [63]. They reported typical specific wear rates of 10 to 80×10^{-7} mm^3/Nm for the Cr_3C_2-Ni cermets, 12 to 75×10^{-7} mm^3/Nm for the TiC-NiMo cermets, and 5 to 85×10^{-7} mm^3/Nm for WC-Co. In each of these prior examples, as well as the present work it is apparent that there are increasing specific wear rates with increasing load. Given the nature of the Lancaster equation (Equation 8.1), where the volume loss of material is effectively normalised by dividing by the applied load [30], it might be expected that there would be no such dependency if the wear mechanism remained constant. As a consequence, this change in specific wear rate with load suggests a gradually evolving sequence of wear mechanism(s), as noted previously. This conclusion is supported by related microstructural studies, which are discussed in the companion paper [20].

8.3.3.2 Time Effects on the Wear Behaviour

In order to assess the cermet wear mechanism evolution in more detail, the effects of reciprocating sliding duration were assessed, with 40 and 80 N applied loads, for 15, 30 and 60 minutes testing time. Representative dynamic COF curves, for 10 and 30 vol.% stainless steel binder content, are shown in Figure 8.10 (for 15 minutes duration), highlighting the initial stages of wear. For the lower binder content there is a brief 'bedding-in' period, up to ~500s from the start of the tests, and then the COF shows a gradual and consistent increase with testing time. At the higher binder content, the 'bedding-in' period is significantly shorter, and there is far more fluctuation in the curves. Generally consistent with the specific wear rate data shown earlier, the 316L samples tend to show the highest COF values, while the 410L steel samples show the lowest COF values during these initial stages of testing (at 30 vol.% binder).

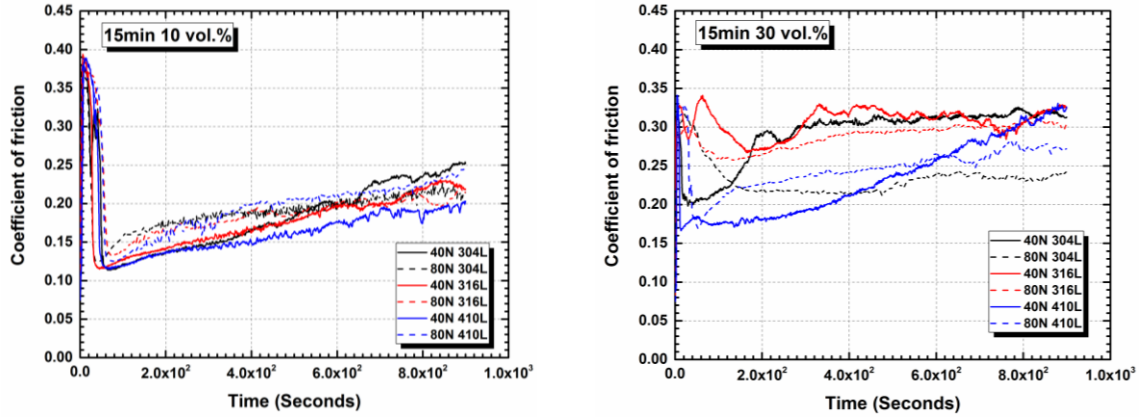

(a) (b)

Figure 8.10: The initial dynamic COF, as a function of time at 40 and 80 N applied load, for: (a) 10 vol.% steel binder, and (b) 30 vol.% steel binder.

Figure 8.11 presents the variation in the mean COF versus time for the TiC-stainless steel cermets, again for both 40 and 80 N applied load. It can be seen that COF for all the binder contents evaluated ranges from 0.16-0.38. This value of COF is at the lower end of the range of typical quoted values for the COF of ceramic-metal pairs, which is between 0.25 and 0.8 [64]. It can be seen that the COF values increase with both binder content and

testing duration, which again suggests a gradual change of the active wear mechanism with time.

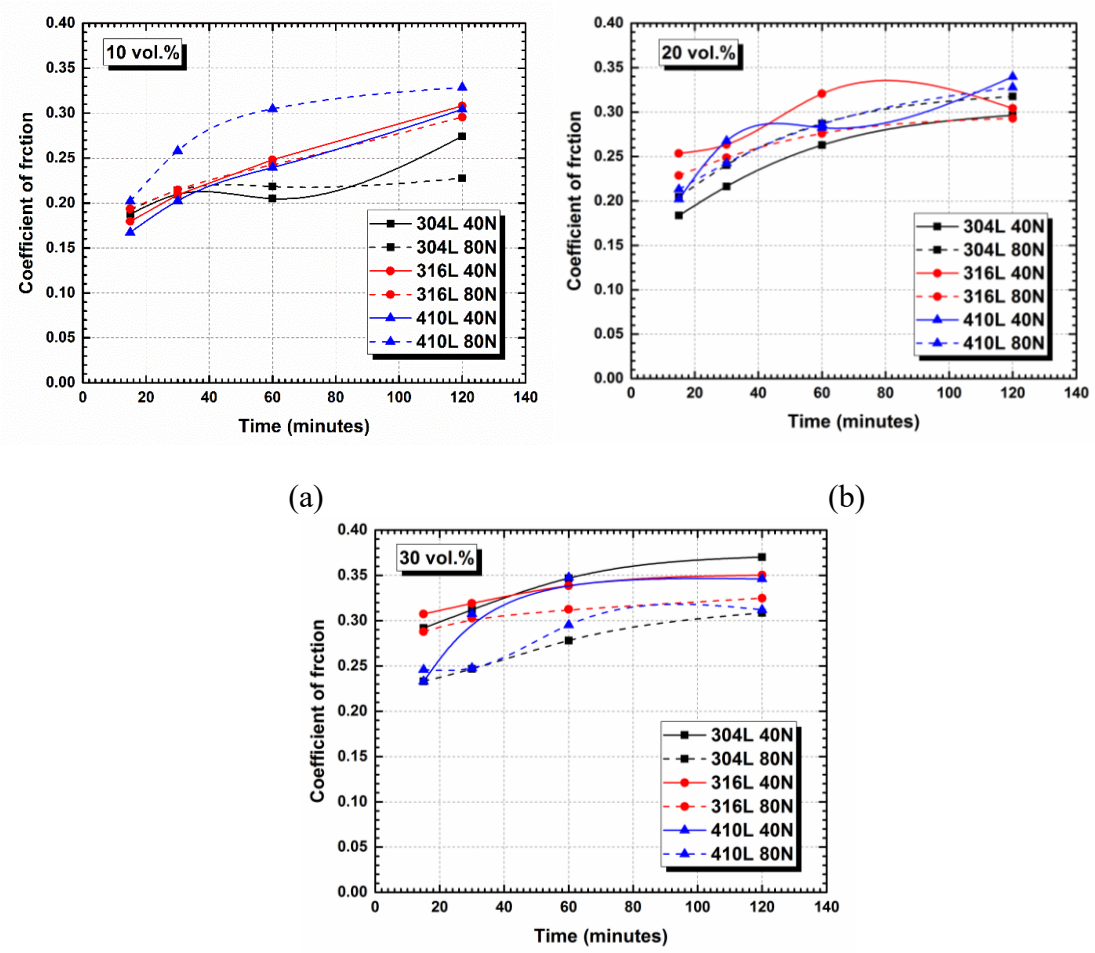

Figure 8.11: The effects of binder content and loads on the average COF as a function of testing time, for: (a) 10 vol.%, (b) 20 vol.%, and (c) 30 vol.% stainless steel binder.

During the continuing process of wear, the contact surface area increases and heat is generated through friction, leading to an increase in temperature in the region between the tribo-pair. As a consequence, it is invariably the case that the wear volume increases with time. The relationship of volumetric wear loss with time is shown in Figure 8.12; the samples were selected with 20 vol.% of binder for all three stainless steel, with applied

loads of 40 and 80 N. As can be seen, the volumetric wear loss increases with time, and nominally complies with the Lancaster model [30], where the volumetric wear loss has linear correlation with time, or distance covered. This behaviour can be attributed to a number of factors, including material loss during the initial two-body abrasive wear period, the loss of third-body material from the wear track, and the spalling off of segments of the tribolayer after attaining a critical thickness. This last scenario can potentially lead to high wear loss. These factors can be related to the work of Stachowiak, for wear testing at high sliding speed [65,66]. The mechanical attrition generates heat and incorporates oxygen into the newly exposed material surfaces, which leads to the generation of a layer of tribo-film within the wear track. Once the tribolayer reaches a critical thickness it can no longer support the frictional shear stress or applied load, and it spalls off, leading to high wear rate. This phenomenon is exacerbated by the high incorporation of oxygen into the tribolayer, such that it becomes far more brittle in nature. In the present case, it is noted that there is insufficient heat to lead to direct oxidation. However, as discussed in the companion paper [20], oxygen is incorporated through an attrition mechanism (during three-body wear), with the constant creation of new surfaces and their subsequent passivation (i.e. oxygen uptake).

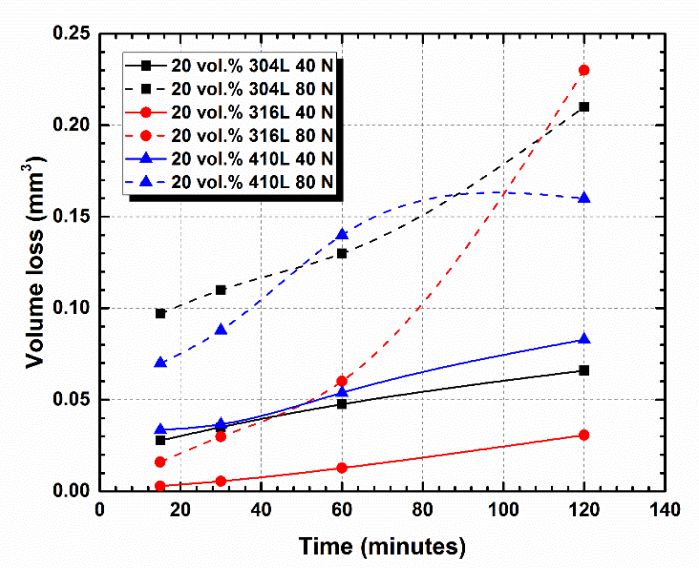

Figure 8.12: The effects of binder composition, sliding duration and load on the volumetric material loss for cermet samples with 20 vol.% of stainless steel binder.

It has been suggested for a composite material that parameters relating both directly and indirectly to the microstructure, such as the phase volume fractions, their size and shape, the distribution of the reinforcing phase, and the hardness, are important in predicting wear behaviour. The 'upper' and 'lower' wear resistance can be modelled in a number of modes, including 'equal wear rate (EW)' (or 'optimal load (OL)'), and 'equal pressure (EP)' (or 'minimal load (ML)'), modes [67,68]. The EW (or OL) mode follows a linear trend of the wear resistance as a function of the reinforcing phase content, as this mode assumes both of the phases wear at the same linear rate. Conversely, the EP (or ML) mode follows an inverse dependence, as it assumes both of the phases are subjected to the same load per unit area (i.e. the reinforcing particles make a smaller contribution to the wear resistance). These two modes set the 'upper' and 'lower' limiting bounds of wear resistance for a multiphase material. In the majority of actual practical scenarios multiphase materials usually follow an 'intermediate' response [69].

With large abrasive particles or high applied loads, the scale of the material being damaged may be larger than the dimensions of the microstructure, therefore the 'bulk' properties of the material are important [67]; improving the individual phase properties

would then be anticipated to increase the properties of the combined, composite material [68]. In the EW (or OL) mode, the more wear resistant phase takes a larger portion of the load, which usually occurs when the abrasive particles are smaller than the reinforcing phase. If the particles are small or, conversely, the reinforcing phases are larger, under low loads the material volume that is being worn is small; in this case, the reinforcing particles and the matrix would affect the wear resistance of the overall material. The matrix and particles in a multiphase composite may not wear under the same rate (e.g. matrix is worn at a higher rate), which would leave a rough surface. To compensate for this situation, and to maintain a 'steady wear rate', the reinforcing phase will have to break down in some manner, such as grain fragmentation and pull-out. This phenomenon would be likely to occur in a composite with a low volume fraction of a hard (reinforcing) phase [68]. However, for cermets and hardmetals with a low amount of metallic binder (and a small MFP), the softer binder component is removed more rapidly than the high hardness phase. This will leave the hard ceramic grains to be subjected to the load, therefore the wear resistance of the cermet or hardmetal is closer to the pure ceramic phase (e.g. WC, or TiC in the present case) [68]. However, as it can be seen in the present work, as well as prior studies, the wear rate does not remain constant and the situation is invariably more complex. It is proposed in the current study, together with previous investigations, that one or more transitions in the predominant wear mechanism arises. In order to more convincingly confirm this, detailed microstructural observation is required for various testing conditions, which is explained in greater detail in a companion paper to the current article [20].

8.4 Conclusions

High density TiC-based cermets, with stainless steel grades 304L, 316L and 410L as binder alloys, were produced by a simple melt-infiltration technique for binder contents from 5 to 30 vol.%. It was noted that the TiC-TiC contiguity decreases with increasing steel content, while the binder MFP concurrently increases; the responses were essentially independent of steel grade. The densified cermets have high hardness (~25 GPa with 5 vol.% of binder), which decreases with increasing binder content, while the

indentation fracture resistance increases. It was found that the cermets with 410L as the binder have a slightly lower hardness and indentation fracture resistance, in comparison to 3xx series steels.

Samples with binder contents ranging from 10 to 30 vol.% were subjected to reciprocating wear tests, sliding against a WC-Co counter face sphere, with loads of up to 80 N. The dynamic coefficient of friction demonstrated that the materials exhibit an initial 'run-in' period, which can exceed 30 minutes, but invariably maintain a steady state for longer durations. Cermets with lower binder content (i.e. higher TiC volume fractions) typically have shorter 'run-in' times, when compared to the high binder samples. When subjected to higher applied loads, the dynamic COF invariably decreases with increasing load, indicating a transition in the primary wear mechanism. The specific wear rates of the current materials were determined using optical profilometry to measure the wear track volume. For a fixed binder content and test duration, the specific wear rate was seen to increase with increasing applied load in a nominally linear manner. Overall, cermets prepared with the 316L grade binder typically exhibited the highest specific wear rate for any given set of test conditions, while 304L and 410L behaved in an essentially identical manner. The cermets developed in the current study have specific wear rate values within the range of $\sim 2\times10^{-7}$ to 35×10^{-7} mm^3/Nm, depending on binder content and applied load, showing comparable wear resistance to the more traditional WC-Co 'hardmetals' and related TiC based cermets.

Acknowledgements

The authors gratefully acknowledge financial support from the Natural Sciences and Engineering Research Council of Canada (NSERC), through both the Collaborative Research and Development programme (grant #CRDPJ381565-09) and the Discovery Grants programme (grant #283311-2011), and Petroleum Research Atlantic Canada (PRAC), under grant C09-10. The Canada Foundation for Innovation, the Atlantic Innovation Fund, and other partners who helped fund the Facilities for Materials Characterisation, managed by the Dalhousie University Institute for Materials Research, are also appreciated. The authors would also like to thank Dean Grijm and Patricia Scallion for their technical assistance.

8.5 References

1. S. Kang, Cermets, pp.139-181 in Comprehensive Hard Materials, Vol. 1 (Ed. V.K. Sarin), Elsevier Ltd., New York, 2014.
2. N. Durlu, Titanium carbide based composites for high temperature applications. J. Eur. Ceram. Soc. 19 (1999) 2415-2419.
3. H. Klaasen, L. Kollo, J. Kübarsepp, Mechanical properties and wear performance of compression sintered TiC based cermets. Powder Metall. 50 (2007) 132-136.
4. E.K. Storms. The refractory carbides. Academic Press, New York, 1967.
5. R. Edwards, R. Edwards. Institute of materials, London, 1993.
6. J.A. Picas, F. Forn, G. Mattaus, HVOF coatings as an alternative to hard chrome for pistons and valves, Wear 261 (2006) 477-484.
7. T. Sahraoui, S. Guessasma, M.A. Jeridane, M.Hadji, HVOF sprayed WC-Co coatings: Microstructure, mechanical properties and friction moment prediction, Mater. Des. 31 (2010) 1431-1437.
8. D. Miller. Liquid-phase sintering of TiC-Ni composites, J. Am. Ceram. Soc. 66 (1983) 841-846.
9. B. Lograsso, R. German. Liquid Phase sintered Titanium carbide-tool steel composites for high temperature service, Prog. Powder Metall. 43 (1987) 415-439.
10. N. Durlu. Titanium carbide based composites for high temperature applications, J. Euro, Ceram. Soc. 19 (1999) 2415-2419.
11. H. Klaasen. Strength and failure of TiC based cermets, Metals Soc. 52 (2009) 111-115.
12. D. Alman, O. Dogan. TiC-reinforced 304L-stainless steel-matrix composites via reactive sintering, Albany Research Centre (ARC), Albany, OR, 2000.
13. A. Farid, S. Guo, X. Yang, Y. Lian. Stainless steel binder for the development of novel TiC-reinforced steel cermets, J. Univ. Sci. Technol. B. 13 (2006) 546-550.
14. M. Komac, S. Novak. Mechanical and wear behaviour of TiC cemented carbides, Int. J. Refract. Hard. Met. 4 (1985) 21-26.
15. C. Degnan, P. Shipway. A comparision of the reciprocating sliding wear behaviour of steel based metal matrix composites processed from self-propagating high-temeprature synthesised Fe-TiC and Fe-TiB_2 masteralloys, Wear 252 (2002) 832-841.

16. J. R. Davis. Tool Materials, ASM International Handbook Committee, ASM International, Materials, Park, OH, 1995.
17. F. Akhtar, S.J. Guo, Microstructure, mechanical and fretting wear properties of TiC-stainless steel composites. Mater. Charact. 59 (2008) 84-90.
18. E. Pagounis, V. Lindroos. Processing and properties of particulate reinforces steel matrix composites. Mater. Sci, Eng A. 246 (1998) 221-234.
19. S. Tjong, K. Lau. Abrasion resistance of stainless-steel composites reinforced with hard TiB_2 particles. Compos. Sci. Technol. 60 (2000) 1141-1146.
20. C. Jin, C.C. Onuoha, Z.N. Farhat, G.J. Kipouros, K.P. Plucknett, Microstructure development and assessment on the reciprocating wear of TiC-steel based cermets, submitted to Tribol.Int.
21. T.L. Stewart, R.B. Collier, Z.N Farhat, G.J. Kipouros, K.P. Plucknett. Melt-infiltration processing of titanium carbide-stainless steel cermets, Ceram. Eng. Sci. Proc. 31 (2010) 97-104.
22. C.C. Onuoha, Z.N Farhat, G.J. Kipouros, K.P. Plucknett, The reciprocating wear behaviour of TiC-304L stainless steel composites prepared by melt infiltration, Wear 303 (2013) 321-333.
23. T.L. Stewart. The characterization of TiC and Ti(C,N) based cermets with and without Mo_2C. MSc Thesis, Dalhousie University, Canada, 2014.
24. R.B. Collier K.P. Plucknett, Spherical indentation damage in TiC-Ni_3Al composites. Int. J. Refract. Met. Hard Mater. 30 (2012) 188-195.
25. M.I. Mendelson, Average grain size in polycrystalline ceramics, J. Am. Ceram. Soc. 52 (1969) 443-446.
26. J. Gurland, The measurement of grain contiguity in two phase alloys, Trans. Metall. Soc. AIME, 212 (1958) 452-455.
27. G.R. Anstis, P. Chantikul, B.R. Lawn, D.B Marshall. A critical evaluation of indentation techniques for measuring fracture toughness: I, direct crack measurements, J. Am. Ceram. Soc. 64 (1981) 533-538.
28. C.B. Ponton, R.D. Rawlings. Vickers indentation fracture toughness test Part 1: Reviews of literature and formulation of standardized indentation toughness equations, Mater. Sci. Technol. 5 (1989) 865-872.

29. C.C. Onuoha, C. Jin, Z.N. Farhat, G.J. Kipouros, K.P. Plucknett. The effects of TiC grain size and steel binder content on the reciprocating wear behaviour of TiC-316L stainless steel cermets, Wear 350-351 (2016) 116-120.
30. J.K. Lancaster, The influence of substrate hardness on the formation and endurance of molybdenum disulphide films, Wear 10 (1967) 103-107.
31. I. Hussainova, J. Kübarsepp, J. Pirso. Mechanical properties and features of erosion of cermets, Wear 250 (2001) 818-825.
32. I. Hussainova, Effect of microstructure on the erosive wear of titanium carbide-based cermets, Wear 255 (2003) 121-128.
33. C. Jin, K.P. Plucknett, Microstructural Instability in TiC-316L Stainless Steel Cermets, Int. J. Refract. Met. Hard Mater. 58 (2015) 74-83.
34. K.W. Chae, D.I. Chun, D.Y. Kim, Y.J. Baik, K.Y. Eun, Microstructural evolution during the infiltration treatment of titanium carbide-iron composite. J. Am. Ceram. Soc. 73 (1990) 1979-1982.
35. D.I. Chun, D.Y. Kim, K.Y. Eun, Microstructural evolution during the sintering of TiC-Mo-Ni cermets. J. Am. Ceram. Soc 76 (1993) 2049-2052.
36. H.E. Exner, Qualitative and quantitative interpretation of microstructures in cemented carbides, in: R. Viswanadham, D.J. Rowcliffe and J. Gurland (Eds.), Science of Hard Materials, Springer-Verlag, Berlin, 1983, pp. 233-262.
37. K.P. Plucknett, P.F. Becher, Processing and microstructure development of titanium carbide-nickel aluminide composites J. Am. Ceram. Soc. 84 (2001) 55-61.
38. I.M. Hutchings. Tribology: Friction and wear of engineering materials. Butterworth-Heinemann Ltd, Oxford, 1992.
39. I.M. Hutchings. Tribological properties of metal matrix composites, Mater. Sci. Technol. 10 (1994) 513-517.
40. J. F. Archard. Contact and rubbing of flat surfaces, J. Appl. Phys. 24 (1953) 981-988.
41. Friction, lubrication, and wear technology. ASM International, Handbook Committee, Materials Park, OH, 1992.
42. A.G. Evans, D.B. Marshall. Wear mechanisms in ceramics, pp. 439-452 in: D.A. Rigney, ed., Fundamentals of friction and wear of materials, ASM Materials Science Seminar, American Society for Metals, Metals Park, OH, USA (1980).

43. A.G. Evans. Abrasive wear in ceramics: An assessment, Report # LBL-8608 National Bureau of Standards-Ceramic Meeting, Gaithersburg, Washington, November 12, 1978.
44. I.M. Hutchings. Mechanisms of wear in powder technology: A review, Powder Metall. 76 (1993) 3-13.
45. A.G. Evans, E.A. Charles, Fracture toughness determinations by indentation, J. Am. Ceram. Soc. 59 (1976) 371-372.
46. B.R. Lawn, A.G. Evans, D.B. Marshall, Elastic/plastic indentation damage in ceramics: the median/radial crack system, J. Am. Ceram. Soc. 63 (1980) 574-581.
47. K. Niihara, R. Morena, D.P.H. Hasselman, Evaluation of K_{IC} of brittle solids by the indentation method with low crack-to-indent ratios, J. Mat. Sci. Lett. 1 (1982) 13-16.
48. J. Lankford, Indentation microfracture in the Palmqvist crack regime: implications for fracture toughness evaluation by the indentation mehod, J. Mat. Sci. Lett. 1 (1982) 493-495.
49. C. Maerky, M.O. Guillou, J.L Henshall, R.M. Hooper, Indentation hardness and fracture toughness in single crystal $TiC_{0.96}$, Mater. Sci, Eng A.209 (1996) 329-336.
50. M. Gee, A. Gant, B. Roebuck, Wear mechanisms in abrasion and erosion of WC-Co and related hardmetals, Wear 263 (2007) 137-148.
51. F. Sergejev, H. Klassen, J. Kübarsepp. Effect of residual stresses on the surface fatigue of TiC-based carbide composites, Procedia Eng. 10 (2011) 3152-3161.
52. A.L. Yerokhin, A. Leyland, C. Tsotsos, A.D. Wilson, X. Nile, A. Matthews, Duplex surface treatments combining plasma electrolytic nitrocarburising and plasma-immersion ion-assisted deposition, Surf. Coat. Technol. 140-144 (2001) 1129-1136.
53. C.E. Foerster, F.C. Serbena, S.L. R. de Silva, C.M Lepienski, C.J. de M. Sequeira, M. Ueda, Mechanical and tribological properties of AISI stainless steel nitrided by glow discharge compared to ion implantation and plasma immersion ion implantation, Nucl. Instrum. Methods Phys. Res., Sect. B 257 (2007) 732-736.
54. S. Buchholz, Z.N. Farhat, G.J. Kipouros, K.P. Plucknett, The reciprocating wear behaviour of TiC-Ni_3Al cermets, Int. J. Refract. Met. Hard Mater. 33 (2012) 44-52.
55. J.R. Davis (Ed.), Nickel, cobalt and their alloys, pp 92-105 in Special-purpose Nickel alloys, ASM international, 2000.

56. S. Qu, C. Huang, Y. Gao, G. Yang, S. Wu, Q. Zang, Z. Zhang. Tensile and compressive properties and AISI 304L stainless steel subjected to equal channel angular pressing. Mater. Sci, Eng A. 475 (2008) 207-216.
57. A. J. Gant, M.G. Gee, B. Roebuck, Rotating wheel abrasion of WC/Co hardmetals, Wear 258 (2005) 178-188.
58. K. Zum Gahr. Wear by hard particles, Tribol. Int. 31 (1998) 587-596.
59. A.J. Gant, M.G. Gee. Abrasion of tungsten carbide hardmetals using hard counter faces. Int. J. Refract. Met. Hard Mater. 24 (2006) 189-198.
60. B. Roebuck, A.J. Gant, M.G. Gee. Abrasion and toughness property maps for WC/Co hardmetals, Powder Metall. 50 (2007) 111-114.
61. A.L. Yerokhin, A. Leyland, C. Tsotsos, A.D. Wilson, X. Nie, A. Matthews. Duplex surface treatments combining plasma electrolytic nitro-carburising and plasma-immersion ion-assisted deposition. Surf. Coat. Technol. 142-144 (2001) 1129-1136
62. S. Buchholz, Z.N. Farhat, G.J. Kipouros, K.P. Plucknett, Reciprocating wear response of Ti(C,N)-Ni_3Al cermets, Can. Metall. Q. 52 (2013) 69-80.
63. J. Pirso, M. Viljus, K. Juhani, S. Letunovits, Two-body dry abrasive wear of cermets, Wear 266 (2009) 21-29.
64. B. Buhshan, Introduction to tribology (2^{nd} Edition), John Wiley & Sons, New York, 2013.
65. L.J. O'Donnell, Tribology of 316L Austenitic Stainless steel carburized at low temperature, MSc Thesis, Case Western Reserve University, USA, 2010.
66. G. Stachowiak, A.W. Batchelor. Engineering tribology, Butterworth-Heinemann, 2013.
67. N. Axen, S. Jacobson. A model for abrasive wear resistance of multiphase materials, Wear 174 (1994) 187-199.
68. H. Engqvist, N. Axen. Abrasion of cemented carbides by small grits, Tribol. Int. 32 (1999) 527-534.
69. N. Axen, B. Lundberg. Abrasive wear in intermediate mode of multiphase materials, Tribol. Int. 28 (1995) 523-529.

Chapter 9 Microstructural Damage Following Reciprocating Wear of TiC-Stainless Steel Cermets

Chenxin Jin, Chukwuma C.Onuoha, Zoheir N. Farhat, Georges J. Kipouros, and K.P. Plucknett

Dalhousie University, 1360 Barrington Street, Materials Engineering Program, Department of Process Engineering and Applied Science, B3H 4R2, Nova Scotia, Canada

Status: *Submitted:* Tribology International

Abstract

High density TiC-based cermets were fabricated using a simple melt-infiltration/sintering method, with three different grades of stainless steel binder. Reciprocating wear tests were conducted using a ball-on-flat geometry, with the test material sliding against a WC-Co counter face. The morphology of the worn surface and wear debris were investigated using SEM and EDS chemical analysis. FIB microscopy was applied to study sub-surface damage within the wear tracks, to aid explanation of the operative wear mechanism(s). The wear behaviour is moderately complex, transitioning from two- to three-body abrasive wear, with both steel binder extrusion and TiC fragmentation observed to contribute towards third-body formation. A further transition to adhesive wear is also observed, with tribolayer generation on both tribo pair surfaces.

Keywords: Abrasive wear; tribolayer; scanning electron microscopy; focused ion beam microscopy

*Author for correspondence: kevin.plucknett@dal.ca

9.1 Introduction

Tungsten carbide-cobalt (WC-Co) 'hardmetals' are widely used in the mining and petrochemical industries to resist tribological damage [1-3]. As a consequence, the wear mechanisms of these more traditional hardmetals have been extensively studied. For the sliding wear of WC-Co (e.g. ball-on-flat geometry), several wear mechanisms have been suggested, including removal of the binder phase [4-8], plastic deformation and grooving of the binder phase [5,7,9], accumulation of plastic strain in WC grains, fracture and fragmentation of individual WC grains [4,7,9], cracking between WC grains and breakaway of unsupported WC grains [10]. However, in comparison, titanium carbide (TiC) based cermets invariably show better strength to weight ratio, with excellent mechanical properties including high hardness and fracture toughness, combined with relatively good wear and corrosion resistance. As a consequence, TiC based cermets have started to see applications in tooling, automotive, aerospace and tribology, etc. Several tribological studies have been conducted on TiC based cermets, with various binders [11-15], and the wear mechanisms for these materials were evaluated.

Recently, the sliding wear response of some new TiC-stainless steel based cermets has been evaluated [16,17], including assessing the effects of the mean TiC grain size. It was suggested that the wear was initially two-body. As binder extruded and removed from the surface, the debris falls between the counter-faces, leading to a three-body wear. Then the carbide grains begin to fragment under the high Hertzian compressive load. Under cyclic load the third body debris were rolled between the surfaces, slowly forming a thin 'tribolayer' film on the wear tracks, indicating transition to an adhesion wear mechanism.

For the present study, this recent work has been extended to assess the effects of the steel grade used upon the wear response, notably for the austenitic grades 304L and 316L, and the martensitic grade 410L. The effects of binder content and composition, applied load, and test duration have been evaluated, with a companion paper presenting the direct wear characterisation parameters, such as coefficient of friction and specific wear rate [18]. To highlight the microstructural evolution that arises during the wear process, a variety of microscopy techniques have been applied to characterise the worn materials. In the present paper, the damage evolution will be discussed for these new cermets. In addition,

simple ‘wear maps’ are developed, to give an indication of the severity of the wear process under specific wear test conditions.

9.2 Experimental Procedure

A detailed description of the cermet materials and the related melt-infiltration/sintering preparation method can be found in the companion paper to the present study [18]. The materials were prepared with stainless steel grades 304L, 316L and 410L, with the nominal binder content varied from 10 to 30 vol.% for each composition. The densified samples were diamond ground and polished down to a 0.25 μm surface finish for subsequent evaluation and wear testing. The polished samples were examined using optical microscopy (OM; Model BX-51, Olympus Canada, Richmond Hill, Ontario, Canada), with the option for Nomarksi differential interference contrast (DIC) imaging. The samples were also assessed at higher magnifications using scanning electron microscopy (SEM; Model S-4700, Hitachi High Technologies, Tokyo, Japan), operated in both conventional combined secondary electron/backscattered electron (SE/BSE) mode, and also in a dedicated backscattered electron (BSE) mode, were a detector bias of -50 V is applied. The SEM also allows in-situ chemical analysis of the materials, using energy dispersive X-ray spectroscopy (EDS; Model X-Max/Inca, Oxford Instruments, Concord, MA, USA).

Details relating to the reciprocating wear test procedures, conducted on the polished samples, can also be found in the companion study [18], along with data relating to the coefficient of friction and specific wear rates measured for these materials. Subsequent OM and SEM analyses were conducted to study the material removal/damage mechanism(s) during wear, with chemical analysis of the resultant wear tracks conducted using EDS. In order to study the sub-surface damage, a focused ion beam microscope (FIB; Model FB-2000A, Hitachi High Technologies, Tokyo, Japan) was used. The FIB allows site specific micro-machining of the samples, and specifically the wear tracks, using a gallium ion beam. Typically, this is performed through the use of a ‘staircase’ cut into to the sample, as shown schematically in Figure 1(a), with the sample then tilted in the SEM to image the newly cut surface. This procedure then allows a cross-section

through the wear track to be assessed. Normally three staircase cuts were conducted, as illustrated schematically in Figure 9.1(b), at the end of the wear track (i.e. region ‘a’), roughly in the centre of the wear track (‘b’), and at the edge of the wear track (‘c’). For the staircase cut location ‘c’, the cross-section has a worn surface area on one side of the cut and an unworn surface on the other. The relative reciprocating sliding directions are vertical for all of the wear track FIB sections presented in this paper. Initially, a tungsten (W) protective strip was deposited on top of the sections to be FIB machined. The staircase cuts were then ion milled adjacent to the W protective strip using a gallium liquid metal source, with a 30 kV accelerating voltage. Typical examples of the subsequent SEM analysis are also shown in the schematic representation in Figure 9.1(b), with the samples imaged at a tilt angle of 30°. The counter-face WC-Co spheres were also examined within the SEM, with chemical analyses of the counter-face material conducted using EDS.

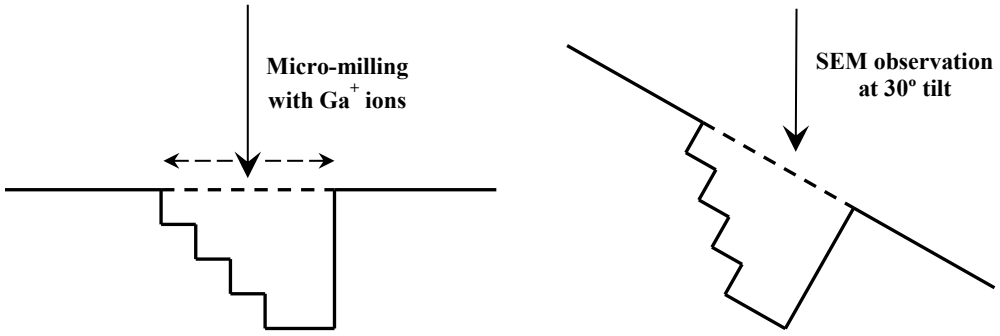

(a)

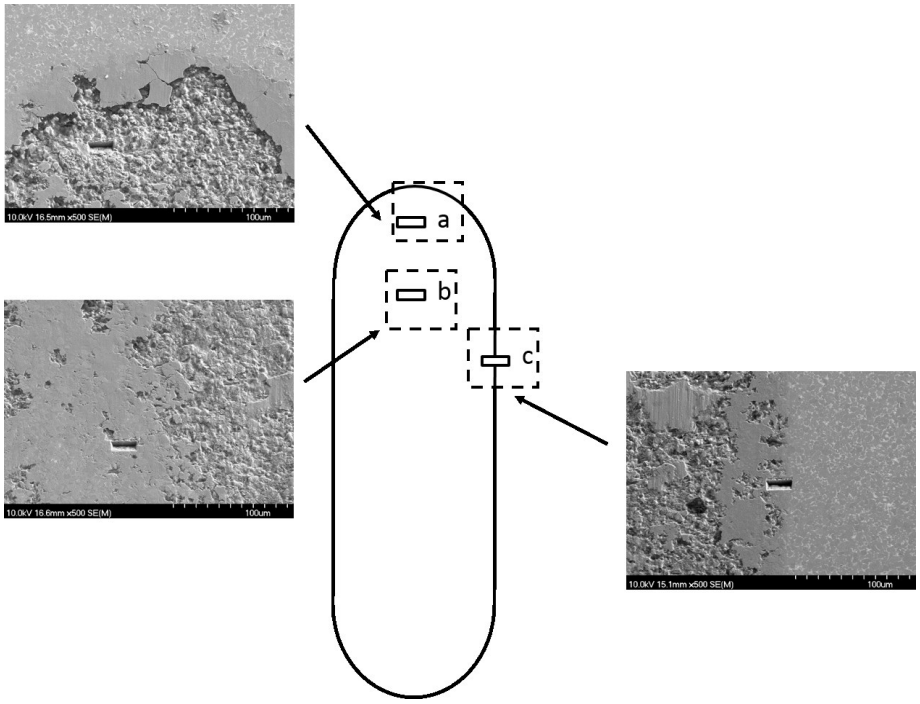

(b)

Figure 9.1: (a) Schematic figure of a series of FIB 'cuts' from side view (b) Schematic representation of the typical locations for FIB staircase cuts applied on a wear track. The sliding direction is vertical in this figure.

9.3 Results and Discussions

9.3.1 Wear Response of the Materials

Representative OM and SEM images of selected sintered and polished samples are shown in Figure 9.2. The OM images highlight the general level of homogeneity and densification that can be achieved through the use of the melt-infiltration/sintering process. It can be observed from the SEM image that a subtle 'core-rim' structure was generated (Figure 9.2(b)), which was discussed in more detail in an earlier study [19]. It has been proposed that the 'core-rim' structure may be beneficial to the wear resistance of cermet-type materials [20-22].

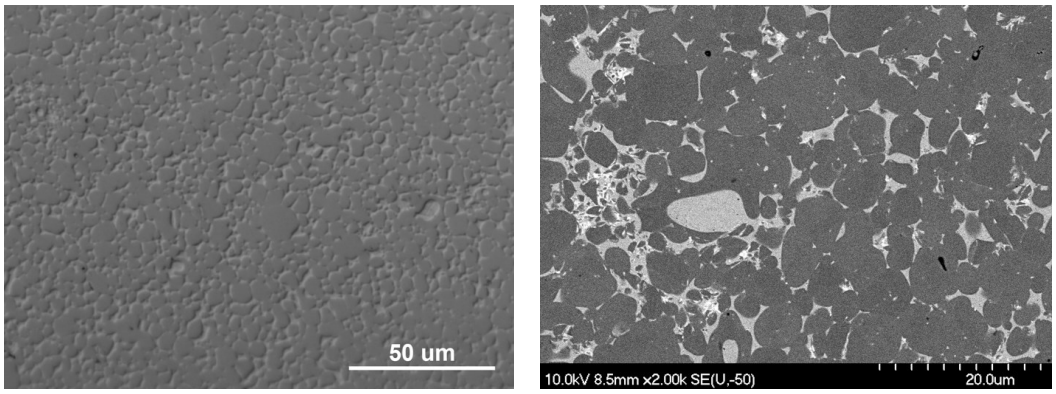

(a) (b)

Figure 9.2: (a) Representative OM image of the microstructure of a TiC-20 vol.% 316L cermet sample. (b) SEM image of a TiC-10 vol.% 410L sample, showing a W concentrated area to the left hand side.

In order to determine the volumetric wear loss during the wear tests, high-resolution optical profilometry is used. Figure 9.3 demonstrates a typical image that was generated using the profilometry method, in both a pseudo three dimensional and cross-sectional view. These examples are taken after wear for 15, 30 and 60 minutes, at both 40 and 80 N applied load. The difference in the extent of wear is clearly shown when comparing the depths of the wear tracks. Careful examination at the ends of the wear tracks reveals that third-body wear debris is pushed to these regions and gradually accumulates. An abrasive wear mechanism, in the form of ploughing along the centre of the track, is apparent as continuous grooving, which is indicative of two-body wear.

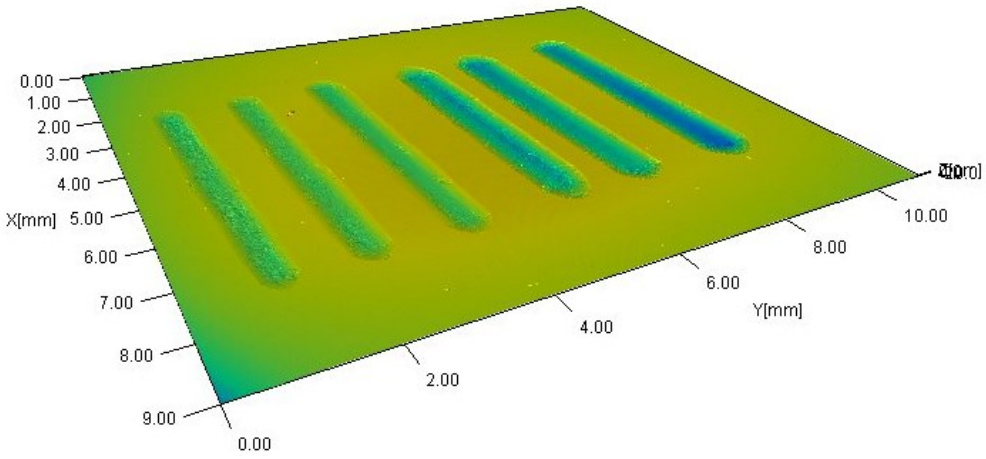

(a)

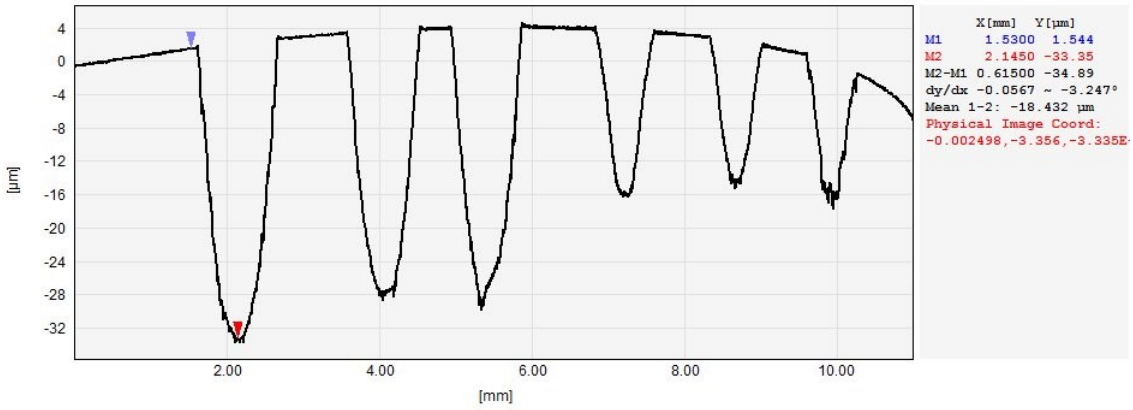

(b)

Figure 9.3: Optical profilometry images of a series of wear tracks for TiC-10% 410L steel based cermets, at different test durations and applied loads: (a) Pseudo three-dimensional plot, and (b) line-scan type plot. Note that the wear tracks in (a) are in order (left to right) of 40 N applied load after 15, 30, and 60 minutes, and 80 N applied load after 15, 30, and 60 minutes, while this order is reversed in (b).

When the materials have undergone elastic deformation through Hertzian contact, the maximum shear stress is located underneath the sliding surface, at a depth of ~0.5a, where a is the contact radius. The contact radius can be assessed following [23]:

$$a^3 = \frac{4kPr}{3E} \qquad \text{Equation 9.1}$$

where E is the Young's modulus, P is the applied load, and k can be determined following:

$$k = \frac{9}{16}\left[(1-\nu^2) + (1-\nu'^2)\frac{E}{E'}\right] \qquad \text{Equation 9.2}$$

where ν is the Poisson's ratio of the surface, and the prime notation indicates the indenter material.

In order to determine the Young's modulus and the Poisson's ratio of both the cermets and the WC-Co counter face material, the bulk modulus, K, and shear modulus, μ, should be first obtained [24]. According to Hashin and Shtrikman [25], the modulus can be obtained from the upper and lower boundary limits as follows:

$$K^{\text{upper}} = K_{\text{R}} + (1-f)\left[\frac{1}{K_{\text{M}} - K_{\text{R}}} + \frac{3f}{3K_{\text{R}} + 4\mu_{\text{R}}}\right]^{-1} \qquad \text{Equation 9.3}$$

$$K^{\text{lower}} = K_{\text{M}} + (1-f)\left[\frac{1}{K_{\text{R}} - K_{\text{M}}} + \frac{3(1-f)}{3K_{\text{M}} + 4\mu_{\text{M}}}\right]^{-1} \qquad \text{Equation 9.4}$$

$$\mu^{\text{upper}} = \mu_{\text{R}} + (1-f)\left[\frac{1}{\mu_{\text{M}} - \mu_{\text{R}}} + \frac{6f(K_{\text{R}} + 2\mu_{\text{R}})}{5\mu_{\text{R}}(3K_{\text{R}} + 4\mu_{\text{R}})}\right]^{-1} \qquad \text{Equation 9.5}$$

$$\mu^{\text{lower}} = \mu_{\text{M}} + f\left[\frac{1}{\mu_R - \mu_M} + \frac{6(1-f)(K_M + 2\mu_{\text{M}})}{5\mu_{\text{M}}(3K_{\text{M}} + 4\mu_{\text{M}})}\right]^{-1} \qquad \text{Equation 9.6}$$

where f is the volume fraction of the reinforcing particles, and the subscripts M and R identify the matrix and reinforcement, respectively.

Therefore, according to Budiansky [26], the Young's modulus and the Poisson's ratio of the final composites can be determined following:

$$E = \frac{9K}{1 + (\frac{3K}{\mu})}$$ Equation 9.7

$$\nu = \frac{3K - 2\mu}{2(\mu + 3K)}$$ Equation 9.8

As noted above, the maximum shear tress is located a distance ~0.5a below the contact surface, and has a value determined from:

$$\tau_m = 0.48 p_0$$ Equation 9.9

where p_0 is the mean contact pressure (or 'indentation stress'), which can be calculated following:

$$p_0 = \frac{P}{\pi a^2}$$ Equation 9.10

Therefore, using the TiC-316L stainless steel cermets as an example, with 30 vol.% of binder, under an applied load of 60 N, with a WC-Co counter face sphere [27-29], the maximum shear stress is projected to occur at approximately 98 μm below the surface, with a maximum shear stress of ~237 MPa. Comparing this with previous study of TiC, with a higher binder content of 40 vol.% of Ni_3Al, tested under the same load, the maximum shear stress was projected to occur at ~44 μm below the surface [30]. A further study [31], using quasi-static loading with a WC-Co sphere (1.98 mm diameter), revealed the depth of indentation damage through DIC optical microscopy. The sample used in that work, TiC with 40 vol.% Ni_3Al binder, loaded to 500 N, showed sub-surface damage to a depth of ~100 μm. However, some caution should be taken in making such comparisons, as the quasi-static loading and reciprocating wear tests will be effectively quite different. In particular, there is cyclic component to reciprocating wear, and there will also be shear involved in plane with the surface (i.e. perpendicular to the loading direction). As a consequence, work hardening of the metallic binder may be more prominent for the wear cyclic scenario.

9.3.2 Microstructural Observation of Samples Following Reciprocating Wear

In a preliminary study examining TiC-304L cermets [16,17], the damage evolution was investigated as a function of the applied load. A similar approach is followed in the present study, with the focus primarily on both the applied load and test duration effects, for a variety of steel grades. However, in particular this approach is followed for the cermets prepared with 410L stainless steel as the binder phase. Optical microscopy, with an associated DIC/Nomarski imaging capability, was used to initially assess the evolution of the wear tracks. Figure 9.4 shows DIC images of a TiC cermet with 30 vol.% 410L binder, after testing at both 40 and 80 N applied load, for 15 and 60 minutes. A clear contrast is present between the worn and unworn regions of the samples. The sliding directions are horizontal in each of the images, and the unworn material with intact TiC grains and binder can be clearly seen, without detectable plastic deformation, at the bottom of each image. The material in the wear tracks shows several interesting features, as differing reflectivity is highlighted under the halogen lamp illumination. The light contrast rounded regions are individual and aggregated TiC grains which have high reflectivity (cf. Figure 9.2); these are either originally polished grains. In comparison, the mid-grey contrast areas highlight the initial stages of tribolayer formation, while the dark contrast regions show where the tribolayer has cracked and spalled away, leaving a roughened surface with very low reflectivity. It is apparent that the highly reflective TiC grains are still intact, but it can also be seen that there are large areas between the grains were the TiC is apparently missing, and a tribolayer region has replaced the TiC (c.f. Figure 9.2(a)); in these regions the TiC grains at the original polished surface have been fragmented and removed during a two- to three-body wear transition. These observations have confirmed that the tribolayer formation process is actually relatively fast, since the sample tested after only 15 minutes is already showing this damage feature. With increasing testing time, the tribolayer continues to form, covering a larger percentage of the worn area. When subjected to an 80 N applied loads, the formation of the tribolayer occur much faster, and cracks occasionally appear within the wear track itself, perpendicular to the sliding direction.

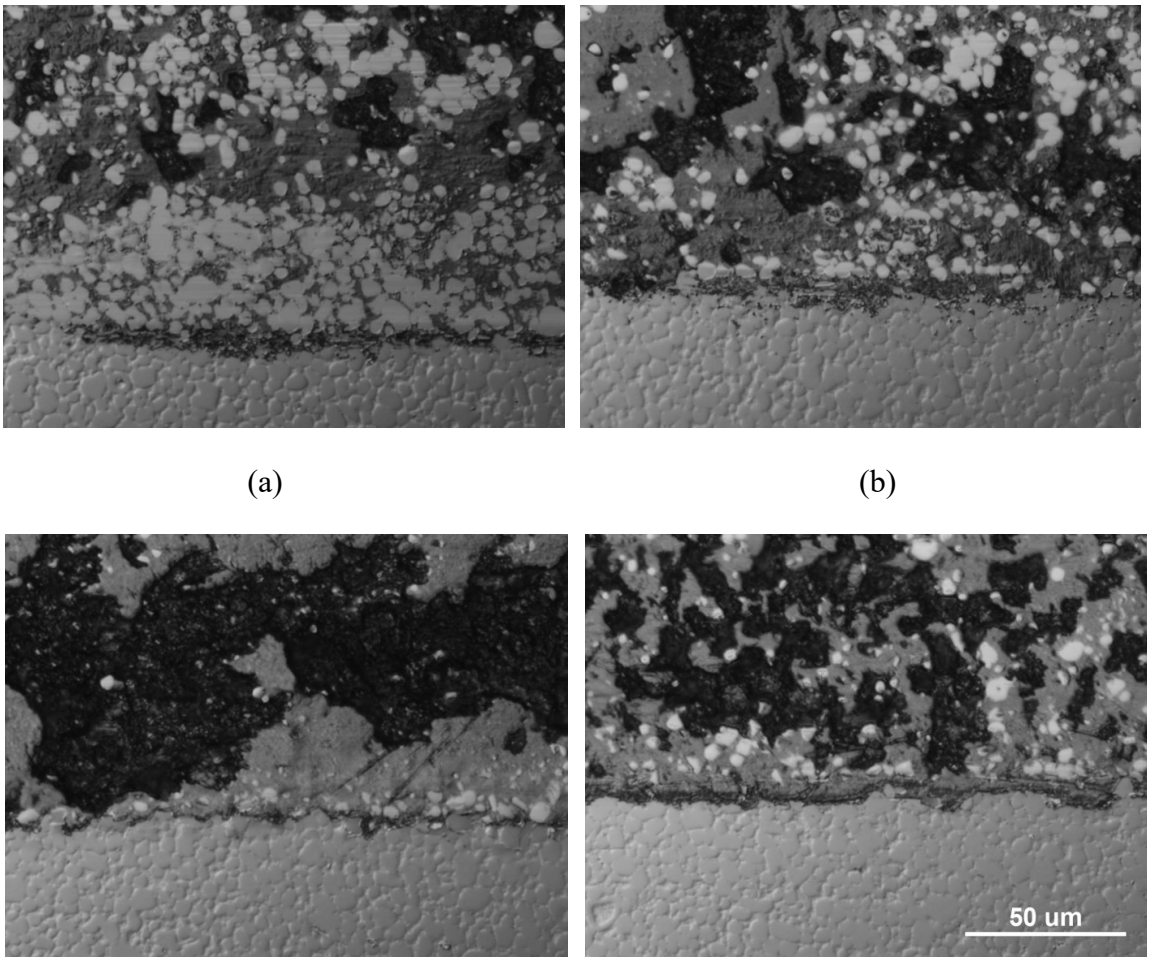

(a) (b)

(c) (d)

Figure 9.4: Representative DIC optical microscopy images, showing a TiC-30 vol.% 410L cermet sample after wear testing under the following conditions: (a) 40 N/15 minutes, (b) 40 N/60 minutes, (c) 80 N/15 minutes, and (d) 80 N/60 minutes.

Representative SEM images of cermets prepared with 10 vol.% 410L stainless steel binder, after wear testing under 40 N of applied load, for 15, 30 and 60 minutes, are presented in Figure 9.5. Figure 9.5(a) highlights the initial stage of wear for the low binder content cermets. It is apparent that, in the middle of the wear track or at the beginning of the wear process, the surface area is relatively smooth, indicating a mechanical polishing mechanism following initial diamond polishing [11]. Plastic deformation of surface asperities has also been suggested [11]. Under the Hertzian contact load, the binder is partially extruded from the surface, and then effectively 'smeared'

over the surface of the wear track. It can be observed from Figure 9.5(b) that, after 30 minutes of wear, the surface has undergone more severe elastic-plastic deformation, showing dark regions, indicating the binder is being removed; this third-body material has now started to be deposited at the ends of the wear track. It can also be noted that there is no grain cracking at the edge of the wear track, indicating an abrasive wears mechanism still predominates [16]. After 60 minutes of wear (Figure 5(c)), it can be seen that the wear surface is relatively smooth, while some parallel cracks can also be observed. This suggests that a uniform thin layer of tribofilm material has been deposited onto the surface. In fact, the initial tribolayer generation occurs very rapidly, as noted earlier, and clearly happens within the first 15 minutes of wear.

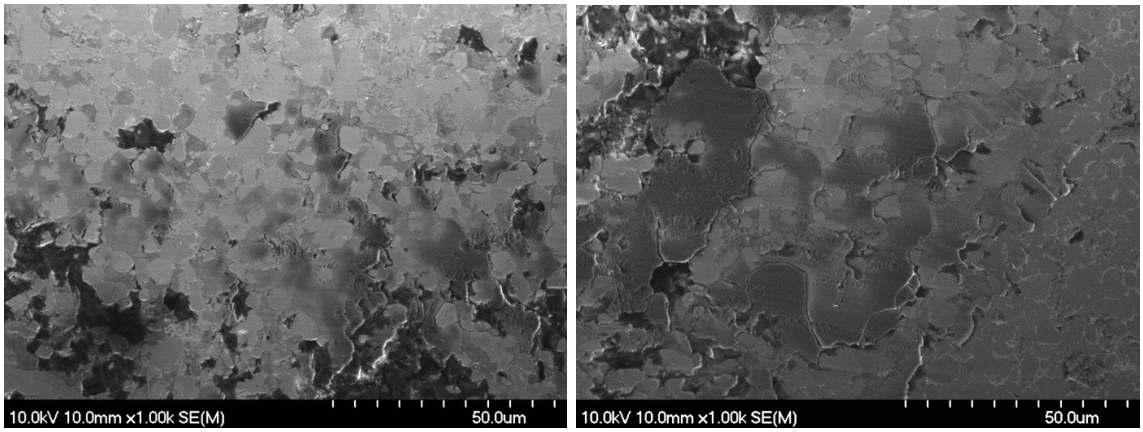

(a) (b)

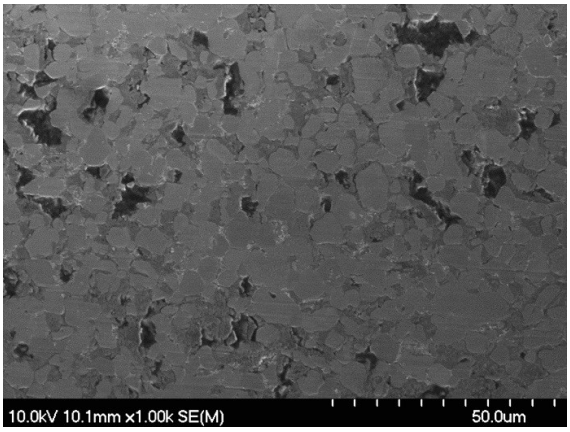

(c)

Figure 9.5: Representative SEM images of the TiC cermets with 10 vol.% 410-L stainless steel binder, following wear testing with and applied load of 40 N of load after testing for: (a) 15 minutes, (b) 30 minutes, and (c) 60 minutes. The sliding direction is horizontal in each of the images.

Typical SEM images of the edges of wear tracks on the TiC cermets with 30 vol.% of 410-L steel binder, subjected to a 40 N applied load, and after 15, 30 and 60 minutes of wear, are shown in Figure 6. There is clear evidence that while many of the TiC particles are retained *in-situ*, a significant portion of the binder has been removed at the surface when the steel content is increased (Figure 6(a)), since the high elastic moduli TiC particles take a smaller fraction of the applied load in the composites (due to their reduced volume/area fraction). It can be observed that at the side the wear track, the binder phase has been subjected to a compressive force (i.e. pushed out between the

harder TiC grains), while ‘rings’ of residual binder can also still be seen around some of the TiC particles away from the wear track edge; at the edges of the TiC grains the steel binder is protected somewhat from removal by the high modulus ceramic. Figure 6(b) shows the edge of the wear track after 30 minutes testing. It is apparent that there is now significant TiC damage/fragmentation and removal, although some grains from the original polished surface are still retained. The wear debris that is generated acts as a third-body, leading to an aggressive three-body wear mechanism. There is also evidence for a deposited triobolayer being accumulated, especially near the edge of the wear track, with subsequent spalling also being apparent. The tribolayer formed at the edge of the track shows occasional parallel cracks, indicating the brittle nature of this layer. A previous study on related cermets prepared with a 316L stainless steel binder (designed to have either fine- or coarse-grained TiC structures), demonstrated a tribolayer thickness of approximately 6 to 8 μm after 120 minutes of wear [17]. Similarly, Figure 6(c) shows the wear track after 60 minutes. The edge of the wear track now has moderate tribolayer build-up, while TiC grains remain intact within the tribolayer. Cracks are again visible perpendicular to the wear direction.

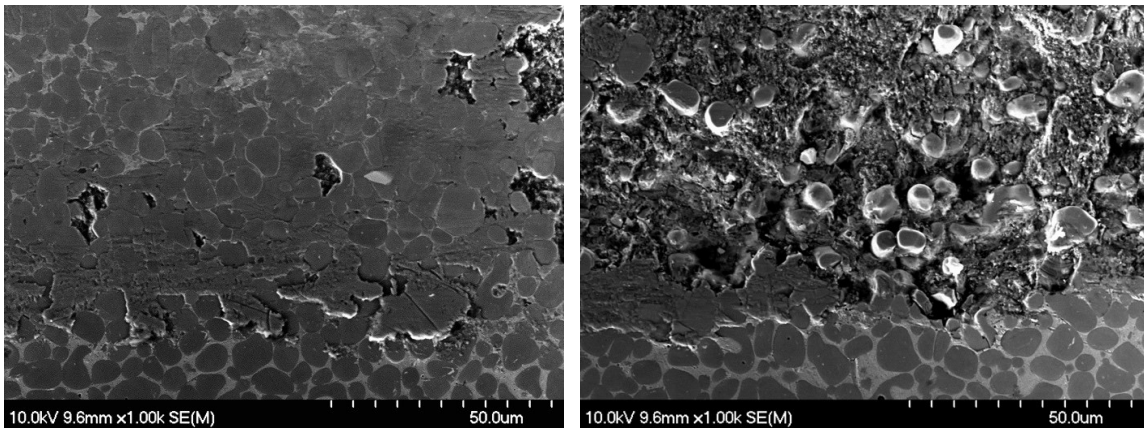

(a) (b)

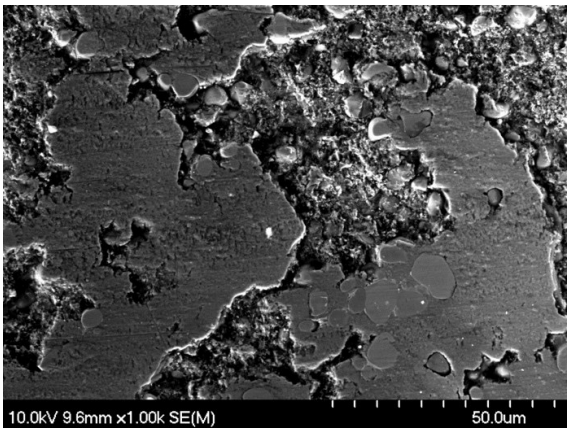

(c)

Figure 9.6: Representative SEM images of the TiC cermets with 30 vol.% 410L stainless steel binder, following wear testing at 40 N applied load for: (a) 15 minutes, (b) 30 minutes, and (c) 60 minutes. The sliding direction is horizontal in each of the images.

In order to further elucidate the wear mechanisms relating to the TiC-steel based cermets, SEM analysis was conducted on the wear debris generated for various conditions (Figure 9.7). The SEM micrographs presented in Figure 9.7(a,b) show the wear debris generated under a 40 N load from TiC cermets prepared with 30 vol.% binder, for 316L and 410L, respectively. The morphology of the wear debris in Figure 9.7(a) is essentially spherical, indicating a rolling action of the debris between two nominally parallel surfaces (on a micro-scale), and confirms the abrasive three-body wear mechanism. The fine-scale, micro-composite nature of these individual particles is clearly visible, with predominantly sub-micron grains (presumably TiC or WC) present within what appears to be a metallic binder phase. Spherical wear debris has been observed during fretting and rolling-contact fatigue studies by Samuel and colleagues [32], and during sliding by Rigney [33]. The particle in Figure 9.7(b) is more plate-like, indicating the probability of an adhesive wear mechanism [34], where there is successive adhesion and transfer which initially may result in relatively round debris composed of constituents from both sliding surfaces. As the wear process continues and the particle continues to grow, it would likely become flattened by plastic deformation as it is sandwiched [21,34]; alternatively, this may simply represent a segment of tribolayer that has spalled away, but which is effectively formed through a similar mechanism. Figure 9.7(c,d) show SEM micrographs

of typical wear debris generated from the same cermets, but at a higher load of 60 N. The spherical morphology apparent Figure 9.7(c) again suggests three-body wear, while Figure 9.7(d) shows both spherical and irregularly shaped particles, indicating both three-body abrasion and adhesive wear mechanisms. As with the earlier example, the micro-composite nature of each spherical particle is clearly apparent.

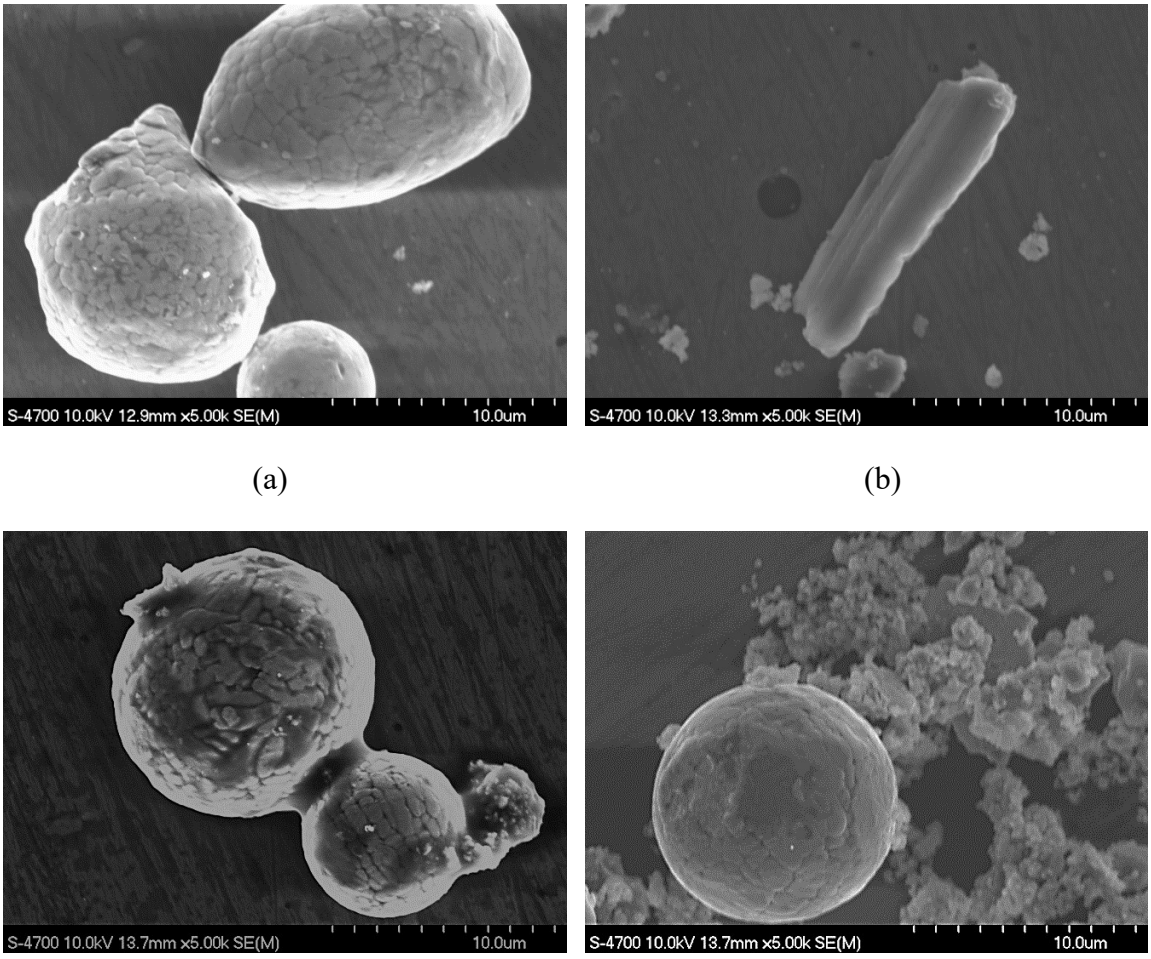

Figure 9.7: Representative SEM micrographs of wear debris formed from TiC cermets with 30 vol.% steel binder: (a) 316L at 40 N, (b) 410L at 40 N, (c) 316L at 60 N, and (d) 410L at 60 N.

9.3.3 Micro-chemical Analysis of the Wear Damage

The formation of a tribolayer can be potentially beneficial if the coefficient of friction is effectively reduced. In this instance, when a tribolayer of sufficient thickness forms, direct contact of the sliding surfaces is effectively reduced. Under dry sliding conditions the interfacial shear strength provided by the tribolayer limits sub-surface deformation and strain accumulation, consequently reducing wear [35]. This would then be confirmed through a decreasing wear rate. Quinn [36] reported that oxide films, either discontinuous or otherwise, on the surface of steel reach a critical thickness before breaking up to form wear debris. The potential spalling of the tribolayer, after reaching a certain thickness, can assist in explaining why the rate of volumetric wear loss often increases with time.

Figure 9.8 demonstrates representative EDS analysis data obtained on a TiC-20 vol.% 316L sample, following wear testing at 40 N for 60 minutes, with the associated mean chemical composition for this region provided in Table 9.1. It is apparent that the tribolayer is extremely homogeneous in composition, indicating very fine scale mixing of the various constituents. It is also apparent that there are components from the TiC and steel, as well as from the WC-Co counter face material, incorporated into the tribolayer. Finally, the tribolayer region itself also has a very high content of O, which is essentially absent from the starting cermet composition.

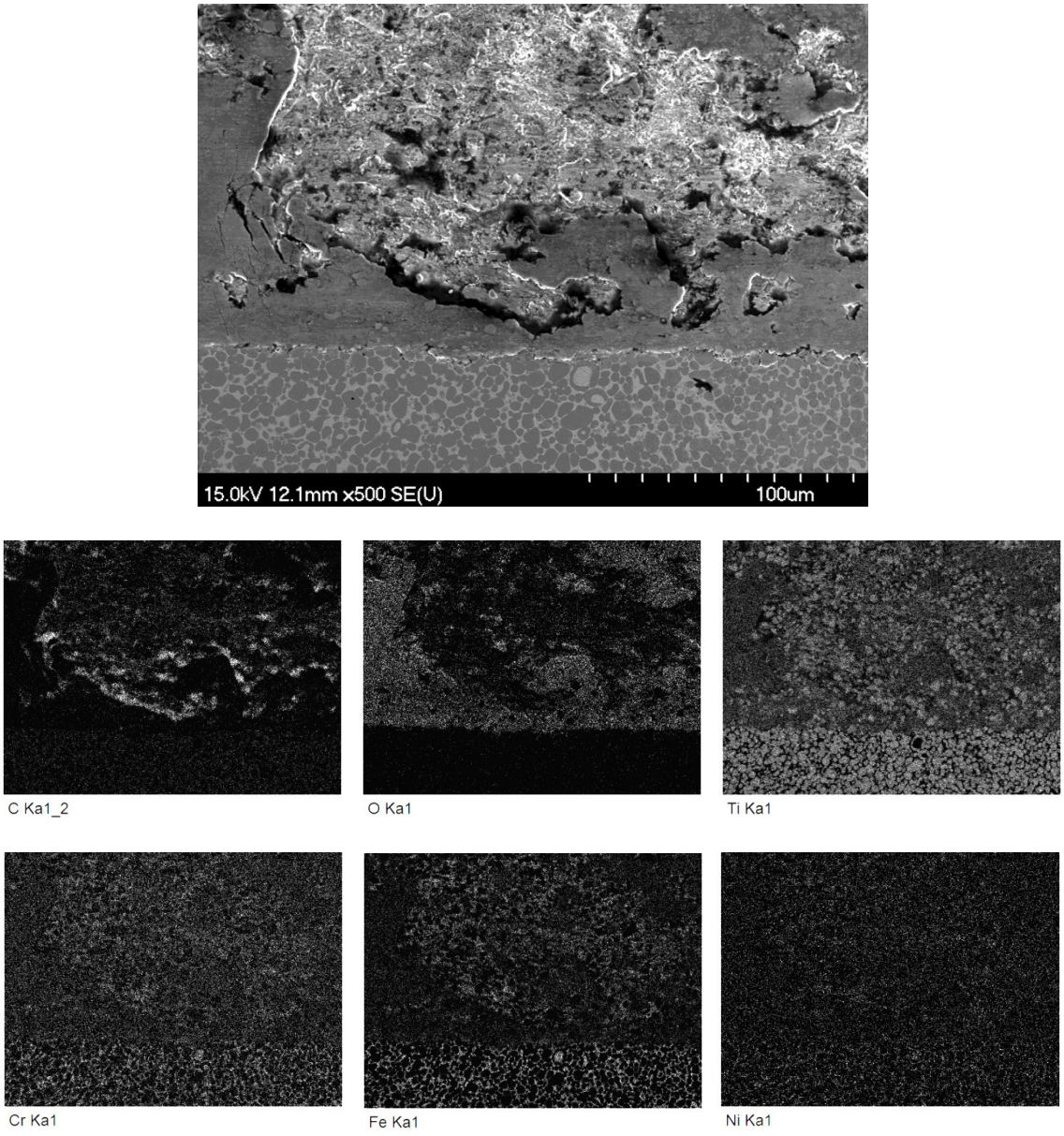

Figure 9.8: EDS elemental maps and associated SEM EDS electron image of the edge of a wear track a TiC-20 vol.% 316L sample testing at 40 N for 60 minutes.

Table 9.1: Average EDS mapping analysis of the region shown in Figure 9.8.

Element	Weight %	Atomic %
C K	15.16	35.10
O K	16.22	28.20
Ti K	31.79	18.46
Cr L	16.86	9.02
Fe K	14.36	7.15
Ni L	3.78	1.79
W M	1.83	0.28
Totals	100.00	

Figure 9.9 presents EDS analysis conducted on a WC-Co counter-face sphere following wear testing, with the associated mean chemical composition of this region presented in Table 9.2. From the SEM EDS electron image below, dark areas with vertical cracks can be observed (suggesting the horizontal sliding motion of the wear test), with the general appearance of a tribolayer, as on the cermet surfaces. The use of EDS mapping indicated these regions have a high concentration of O, not originally present in the WC-Co prior to testing, confirming the generation of a tribolayer during wear tests. Traces of Ti, Fe, Co were also found, indicating that the tribolayer on the couter face surface has also incorporated fine-scale fragments from both materials into the tribo-pair. It can therefore be seen that this tribolayer is transferred onto both the counter-face sphere and the cermet being evaluated, a typical feature of adhesive wear.

Stott [37] outlined the beneficial effects of the presence of oxides at low sliding speeds, when the applied force is sufficiently low. Under such conditions it was noted that the frictional heat is low, and only externally applied heat can lead to oxidation of the surfaces. The oxide and oxidized metal debris can be retained and compacted onto the contacting surfaces, giving wear protection. At a high speed, or at sufficiently high load, there would be higher frictional force and, as a result, a higher temperature leading to the formation of thicker oxides on the contacting surface. When the oxide has reached a critical thickness on the contacting surface, it would spall off leading to mild oxidation

wear. It was suggested that at very high speeds, surface temperatures may be high enough for the oxide to melt, leading to severe oxidation wear. A recent study on wear of Ti(C,N) cermets [20] also proposed that a 'thermal oxidation' mechanism may lead to a tribochemical reaction, and hence the high oxygen content incorporated into the tribolayer. However, through the use of a thermal imaging camera in our recent work on Ti(C,N)-Ni_3Al cermets [38,39], the maximum temperature rise only appeared to ~100°C, which is significantly lower than necessary for thermally induced oxidation. This indicates that the oxidation mechanism for the current cermets is one relating to passivation of fresh, exposed surfaces, rather than high temperature oxidation, which thus relates to an attrition process during three-body wear; the third-body particles are consistently being refined in size through micro-fracture, leading to the constant exposure and passivation of new surfaces; this is effectively a similar process to mechanical alloying, in this instance in an oxidising environment.

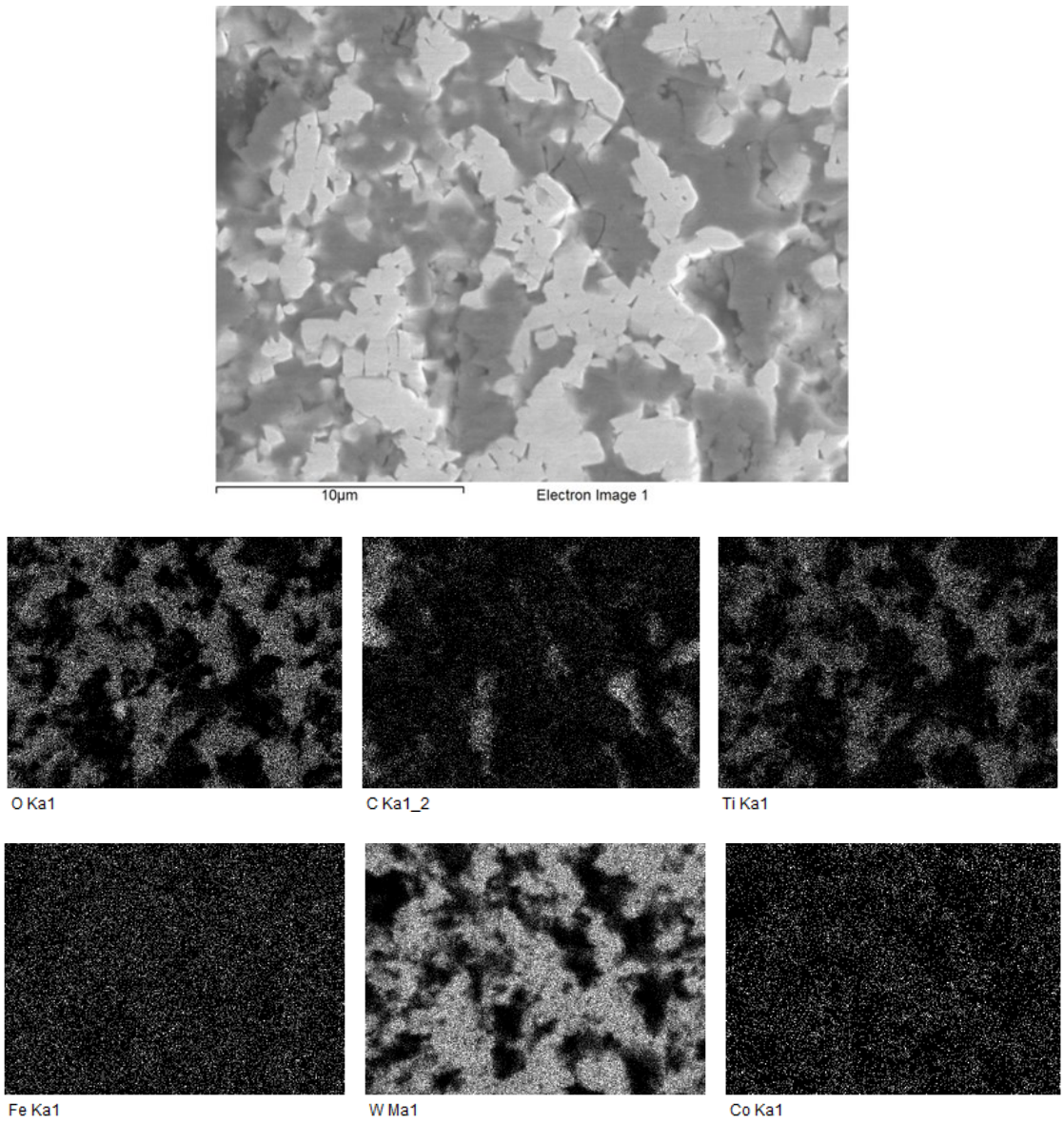

Figure 9.9: EDS mapping of a WC-Co counter-face ball.

Table 9.2: EDS mapping analysis.

Element	Weight %	Atomic %
C K	8.29	29.23
O K	15.95	42.20
Ti K	10.07	8.90
Fe L	7.24	5.49
Co L	1.50	1.08
W M	56.95	13.11
Totals	100.00	

Further evidence for this mechanism can be seen in two additional characteristics of the worn materials. Firstly, when examining EDS maps of the tribolayers for the current materials, as well as in prior related studies [16,17,30,39], there are very distinct boundaries between the worn and unworn materials, showing the unworn region immediately adjacent to the tribolayer has no O content at all. Secondly, when examining the initial stages of wear, such that many of the original TiC surface grains remain intact, and some initial tribolayer material is being built-up between the TiC grains, EDS analysis confirms that O is restricted entirely to the tribolayer material deposited between the TiC grains, and that there is no measurable oxide formed on the TiC grains that are immediately in contact with the tribolayer region (Figure 9.10). This is also apparent with the counter face material, as shown previously in Figure 9.9, where the presence of significant O is entirely constrained within the tribolayer region built-up between the WC grains; at the same time, there is no evidence of O incorporation on the WC themselves, even though they are in contact with the tribolayer film. These three pieces of evidence all point towards the incorporation of O into the tribolayer through mechanical attrition, and subsequent surface passivation, rather than through thermal oxidation.

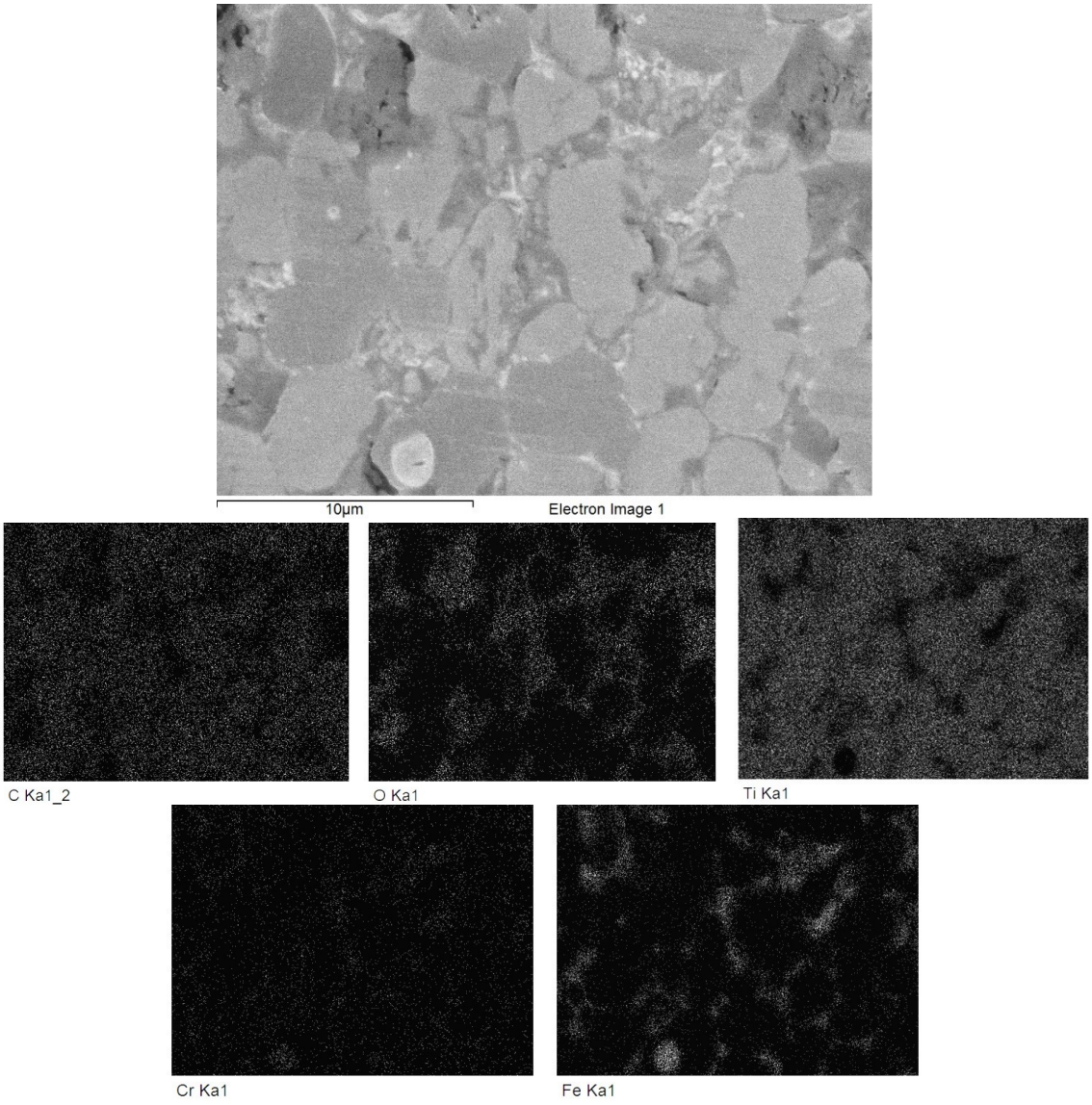

Figure 9.10: EDS elemental maps and associated SEM EDS electron image of a TiC-10 vol.% 410L sample following wear testing. Sample was tested at 80 N for 15 minutes.

9.3.4 Characterisation of Sub-surface Damage

Several previous studies have applied FIB-based techniques to assess the tribological and tribo-corrosion responses of WC-Co cemented carbides [40-43]. The wear mechanisms suggested plastic deformation of the Co-based binder, and fragmentation of the WC grains. The fractured WC grains can be re-embedded into the binder phase, forming a layer that might help to protect the surface. Recently, FIB has also been used to look into

the wear mechanism of TiC and Ti(C,N) based cermets, using a Ni_3Al alloy binder [30]. The sub-surface damage of fine- and coarse-grained TiC-316L stainless steel cermets has also been recently assessed, using essentially the same wear testing conditions as the current work [17]; note that the current cermets are effectively 'intermediate' grain size compared to our prior investigation. Similar FIB approaches were applied to the present study, especially on TiC-410L cermets, investigating the effects of time on the wear damage.

SEM images of the FIB cross-section of the generated tribolayer for TiC-30 vol.% 410L cermets are shown in Figure 9.11. There is evidence of extensive binder extrusion immediately outside of the tribolayer in wear track in Figure 9.11(a); a moderate amount of binder was 'pushed out' from the surface, showing severe plastic deformation, to a distance of ~10 μm from the edge of the tribolayer. Hertzian cracks forming perpendicular to the sliding direction can be observed at the bottom of the image (in these FIB/SEM micrographs the sliding directions are vertical), indicating the brittle nature of the tribolayer that is formed. In Figure 9.11(b,c), a closer examination of the FIB section is presented. It can be seen that a relatively uniform layer of tribo-film is 'smeared' on top of the wear track, while the near sub-surface grains remain relatively intact; the tribolayer itself is of the order of 5 to 7 μm thick. Previous research utilising the FIB excision method has revealed that the cracks are generated and then propagate through the metal binder where the ligaments are thin [17], this is because the stress is likely to exceed the yield stress of the binder, therefore effectively making the binder more brittle through the pile-up of dislocations.

In related work, micro-tribology scratch tests were conducted on a WC-Co hardmetal, with 250 mN or 400 mN loads and a diamond indenter of 20 or 30 μm tip radius (test speed of $100 \mu m \cdot s^{-1}$ were used, with a sliding length of 3 mm) [40]. Cracks were found in the binder phase, and the FIB cross sections indicated that the cracking in the WC grains does not extend to the surface even after 50 repeat tests. When the number of repeats was increased to 100, WC grains exhibited fracturing and material was then re-embedded into the Co binder phase. Cracks in the sub-surface region were also found to be relatively parallel to the surface. Cracks appeared to travel further down from the surface, but some of them only partially crack a WC large grain. After 200 repeats, the WC grains were

severely damaged, and this damage fully covered the surface. The study also suggested that the tribolayer formed did not have a uniform depth. A related publication assessed a slightly wider applied load range, between 20 and 250 mN, with a higher number of repeat tests, starting from 100 and increasing up to 1600 [43]. The damage response was similar, and the extent of damage was estimated for a 250 mN applied load after 1600 repeats; the damage was assessed to be to a depth of ~17 μm under the surface.

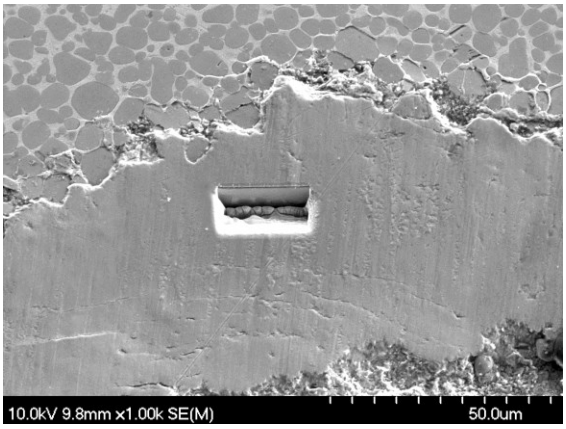

(a)

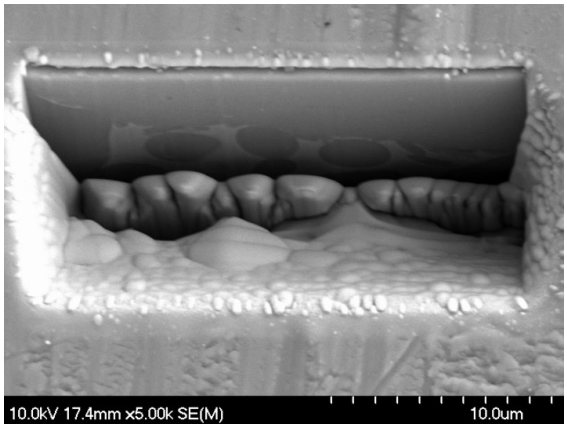

(b)

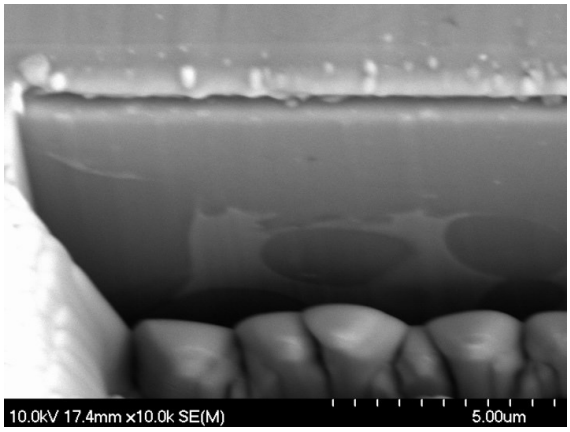

(c)

Figure 9.11: SEM images of a FIB excision cut through the tribolayer of a TiC-30 vol.% 410L cermet, tested with an applied load of 40 N for 15 minutes: (a) general overview of the FIB cut location, (b) higher magnification of the full FIB cut, and (c) a close-up view within the FIB cut area, showing the general absence of damage below the tribolayer after short term wear at a relatively low applied load.

Figure 9.12 presents another FIB section on the same sample, in a wear track area that does not exhibit significant tribolayer build-up; here there are still surface TiC grains remaining from the original sample polishing. From Figure 9.12(a,b) it can be seen that the surrounding binder material is partially extruded, and then effectively 'mashed up' with TiC fragments and deposited back onto the surface. Some regions show a related damage stage, where fragmented and removed grains can be seen. In Figure 9.12(b,c), the sequence of SEM images highlight the sub-surface damage within this region. Clear evidence of crack formation is apparent, with damage in the binder phase around the TiC grains, which indicates the local stresses have exceeded the yield stress of the binder phase; it is highly likely that the cyclic nature of the wear test results in some degree of work hardening of the binder, and a concurrent reduction in ductility. There is also some initial evidence of cracking within the TiC grains The cracks underneath the worn surface are somewhat 'lateral' in their character. Although this kind of crack pattern is related to wear, according to a similar study conducted in WC-Co [44], the cracks do not seem to propagate through multiple grains, which suggests that it is more likely a fatigue related mechanism, rather than one associated with indentation.

In a prior work, scratch testing of WC-Co was assessed using FIB/SEM analysis [41]. Here a spherical indenter of 200 μm tip radius was used, with an applied load of 30 N and a 'sliding' distance of 5 mm; various numbers of repeats were conducted (i.e. 1, 2, 5 and 10 tests), on both fine- (~1.5 μm) and coarse-grained (~6.4 μm) WC-Co samples. FIB sectioning after 10 passes showed that nano-sized fragmented WC grains were generated and embedded into the surface. Intergranular fracture was observed within the grains or tribolayer around the scratch. It was noted that crack growth usually follows a transgranular pattern in the WC-Co hardmetals, while in the current work both transgranular and intergranular cracks are observed in the TiC cermets. In comparing the two classes of material, the yield stress of the Co-based binder can be anticipated to be somewhat lower than the steels used, thereby allowing greater surface re-arrangement and binder extrusion. It is also likely that work hardening is more prevalent in the current study, due to the significantly greater number of cycles endured by the TiC-based materials (roughly 2 to 4 orders of magnitude higher).

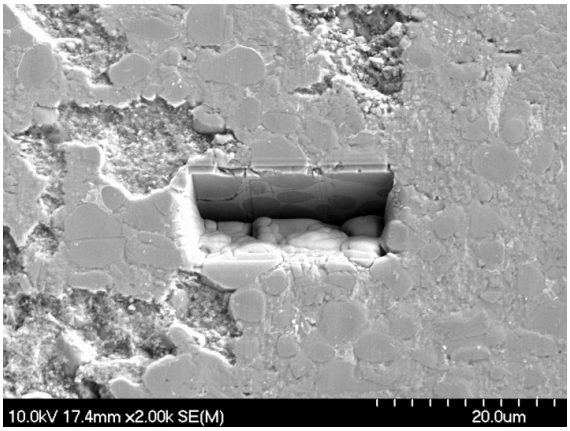

(a)

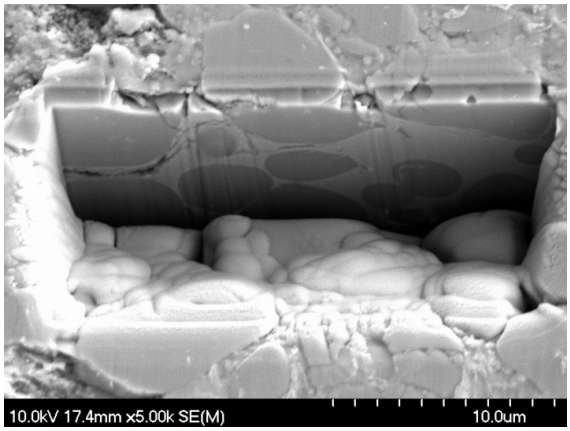

(b)

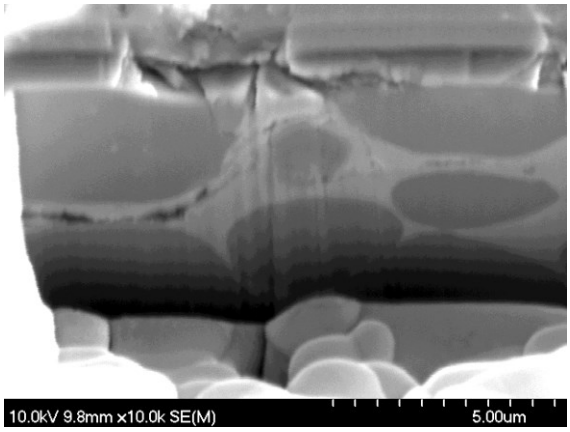

(c)

Figure 9.12: SEM images of a FIB excision cut through the worn region, prior to tribolayer formation, of a TiC-30 vol.% 410L cermet, tested with an applied load of 40 N for 15 minutes: (a) general overview of the FIB cut location in the wear track, (b) higher magnification of the full FIB cut, and (c) close-up view within the FIB cut area showing cracking within the binder.

Figure 9.13 shows the same TiC-30 vol.% 410L composition sample after wear testing with an applied load of 80 N, maintained for 60 minutes. The FIB excision region was selected in a moderately thick, well-developed tribolayer area. The TiC grains were covered by the tribolayer buildup, and cannot be seen in the initial plan view (Figure 13(a)). However, the SEM images show an interesting feature of the tribolayer in this region; voids can be seen to be present underneath the cracked tribolayer (Figure 13(b,c)). It appears that while the tribolayer is being smeared onto the surface of the worn materials, it has not been able to conform to all of the surface asperities, leaving some voids. Related scratch testing studies on WC-Co hardmetals have confirmed that a Co rich layer was built up on the surface of the material, along with fragments of the WC phase [44,45]. It was shown that, with a 0.1 mm tip, after applying a load of 150 mN, the WC grains have undergone increasing severity of cracking as the number of repeat scratches in increased. The mechanism determined in that work was the build-up of plastic deformation, resulting in fracture of the grains. As the number of repeat scratches increases, the damage also increases within the fractured layer of grains covering the top surface.

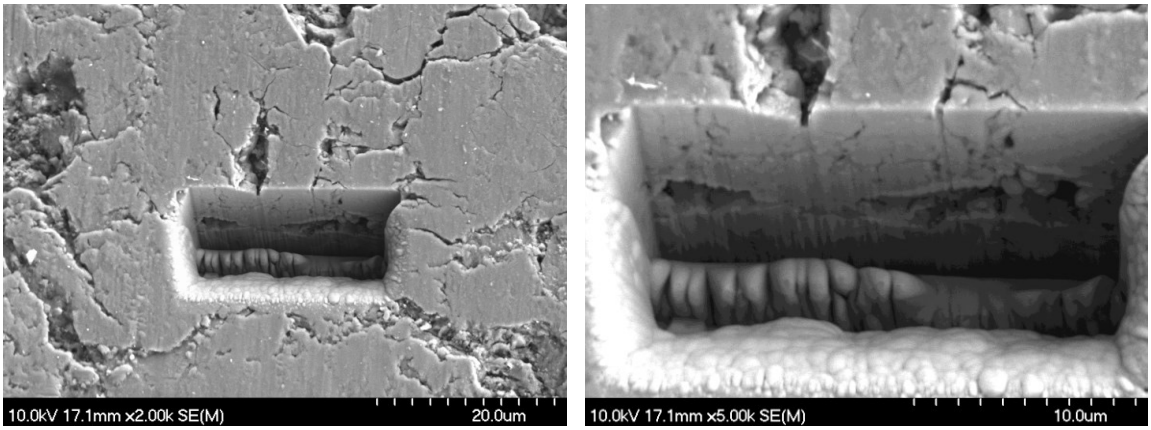

(a) (b)

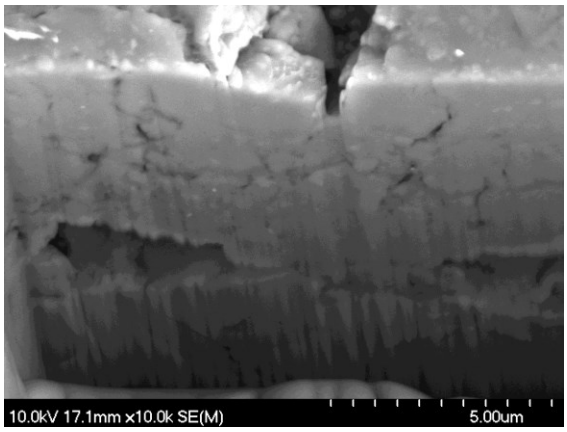

(c)

Figure 9.13: SEM images of a FIB step figure on the tribolayer of a TiC-30vol.% 410L cermet, tested with 80N of load after 60min.

Another extreme of the sub-surface wear response was observed for the TiC-10 vol.% 410L cermet samples (Figure 9.14). The FIB excision example is taken within the rough wear track, shown in Figure 9.14(a), and tested under 40 N applied load for 15 minutes. Here the tribolayer has spalled away, leaving the high roughness surface of the cermet; this is effectively a layer of material originally just below the initial polished surface, such that any polished (i.e. flattened) TiC grains are removed during wear. This example shows how the shear stresses below the tribo-surface have generated small voids at TiC-

TiC interfaces (Figure 9.14(c)), and also that the yield point of the steel has been exceeded in certain areas, leading to crack formation in the binder phase (Figure 9.14(d)).

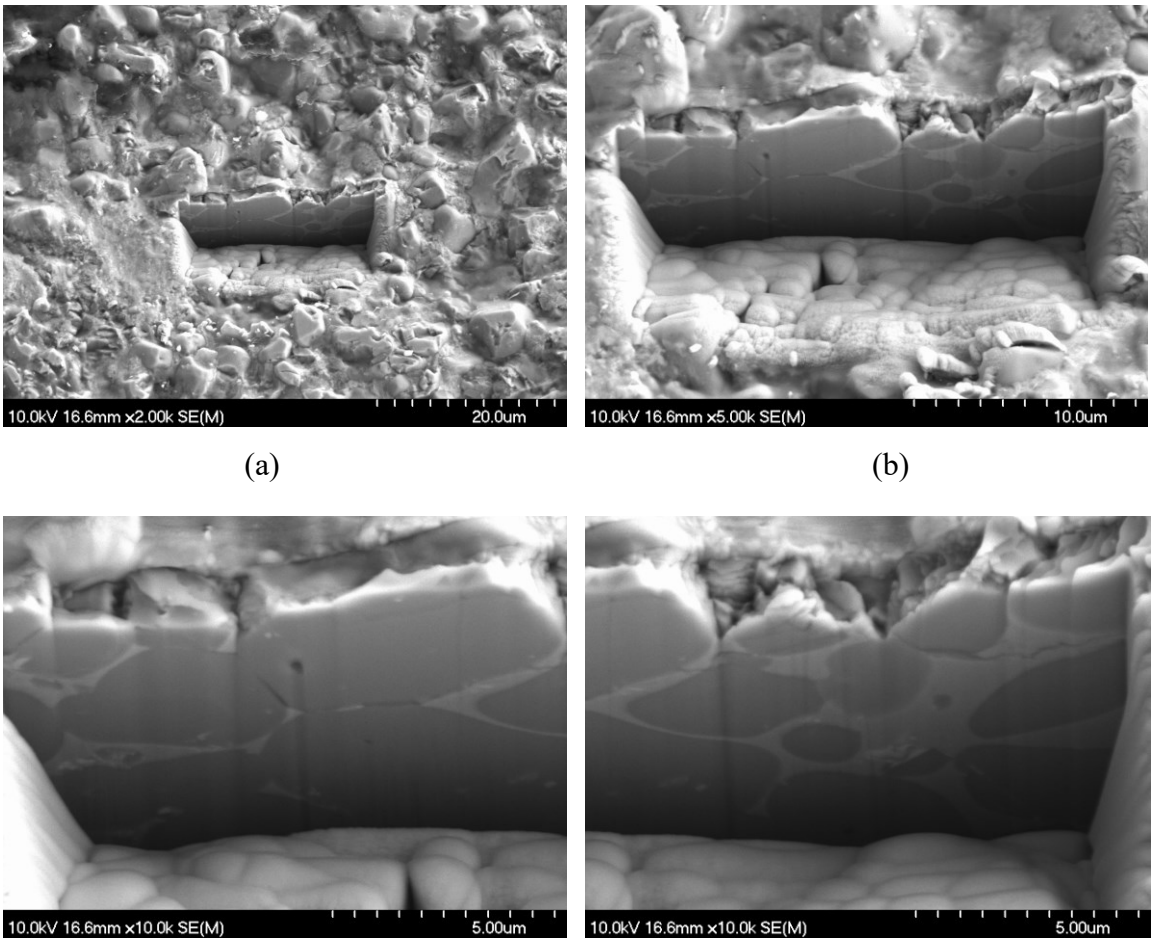

Figure 9.14: SEM images of a FIB excision cut through the worn region, after tribolayer spallation, for a TiC-10 vol.% 410L cermet, tested with an applied load of 40 N for 15 minutes: (a) general overview of the FIB cut location in the wear track, (b) higher magnification of the full FIB cut, (c) close-up view within the FIB cut area showing shear and void generation between the TiC grains, and (d) cracking occurring in the steel binder close to the worn surface.

9.3.5 Development of Cermet Wear Mechanism Maps

In prior work, the development of wear maps was studied by Kato and colleagues, including for both metallic alloy [46,47] and ceramic [48-50] representative systems. As an

example, for steel the wear map was plotted for the indentation depth/contact radius as a function of the contact interface/wear material shear strength, to show the well-known 'cutting', 'wedge forming' and 'ploughing' modes of wear [46]. Wear mechanism and mode maps were also studied for ceramics, and in particular for alumina, zirconia and silicon carbide [48,50,51]. The wear modes were divided into 'mild wear' and 'severe wear', based on the ratio of surface roughness (R_y) to the mean grain size (D_g). With $R_y/D_g <$ 0.2, the worn surfaces are relatively smooth, and the wear rate ranges from 10^{-9} to 10^{-6} mm^3/Nm. For $R_y/D_g > 0.5$, the worn surfaces are rough, with a much higher wear rate, between 10^{-6} and 10^{-2} mm^3/Nm. It was also determined that the transition from mild to severe wear could be ascertained by defining the 'mechanical severity of contact', $S_{c,m}$, and the 'thermal severity of contact', $S_{c,t}$. The critical value for these materials for the transition from mild to severe wear, if driven by the tensile stress which causes vertical cracking, is given by:

$$S_{c,m} = \frac{(1 + 10\mu)P_{max}\sqrt{d}}{K_{IC}} \geq 6 \qquad \text{Equation 9.11}$$

where μ is the coefficient of friction, P_{max} is the maximum Hertzian contact pressure, K_{IC} is fracture toughness, and d is the vertical crack length, which was taken as half of the grain size for the calculation.

Hsu and colleagues, based on considerable data obtained for 'structural ceramics' such as alumina, ytrria-doped zirconia, silicon carbide and silicon nitride, and have developed detailed wear maps [52-57] for these materials. They have classified them into three different categories [58,59], termed 'mild wear' (stress intensity < K_{IC}), 'severe wear' (stress intensity > K_{IC}), and 'ultra-severe wear' (stress intensity >> K_{IC}). The overlapping wear volume ranges for these were outlined as 10^{-7} to 10^{-4} mm^3, 10^{-5} to 10^{-2} mm^3 and 10^{-3} to 10^{1} mm^3, respectively. They were also able to determine the dominant wear mechanism for each of the modes, as 'asperity-scale failure mode', 'nominal scale failure mode', and 'nominal scale plus few large debris/thermal shock mode'. The models used include the traditional 'lateral crack' mode, the tensile crack mode, and thermal shock mode.

To study the effects of both material and test parameters on the present TiC-stainless steel cermets, simple wear 'maps' were plotted, specifically relating to wear rate changes as a function of conditions within the processing and testing envelope. In previous research, a qualitative wear rate 'map' for $Ti_{0.3}N_{0.7}$-Ni_3Al cermets, with varying Mo_2C additions was developed [39]. These 'maps' were plotted versus the applied load and Mo_2C content, for 20 and 40 vol.% of Ni_3Al binder. In terms of quantification, 'low wear' was defined as < 10×10^{-7} mm^3/Nm, and 'high wear' was > 30×10^{-7} mm^3/Nm, with 'intermediate wear' lying in between.

Figure 9.15 shows the effects of applied load and steel binder content on the specific wear rate, with the same wear rate definitions used previously [39], highlighted by different grey scale levels. For a 'low' wear rate the area is indicated in dark grey, while light grey indicates 'intermediate' wear, and white shows the 'high wear' conditions. This information is also presented in a three-dimensional image, giving a comparison between the three binder types. Overall, it can be concluded that TiC-316L stainless steel invariably has a higher specific wear rate over the range of examined loads, and this increases steadily as the load and/or binder content increases, as noted in our previous conclusions in the first section of the current study [18]. In terms of the severity of wear, for each material it can be seen that the worst case scenario occurs for a combination of high applied load and high binder content.

Kumar [20] *et al.* studied the sliding wear of Ti(C,N)-WC-Ni cermets, with various applied loads, and with a WC content ranging from 5-25 wt.%. It was shown that the friction response reaches a steady state after ~5,000 cycles, and the coefficient of friction decreases with an increasing load. The wear rates also decrease with an increasing load for a fixed binder content, but increase with the binder content at any particular given load. They have suggested that an iron-titanate layer (i.e. tribolayer) was formed, which decreases the contact friction, leading to a decrease in the specific wear rate when the applied load is increased.

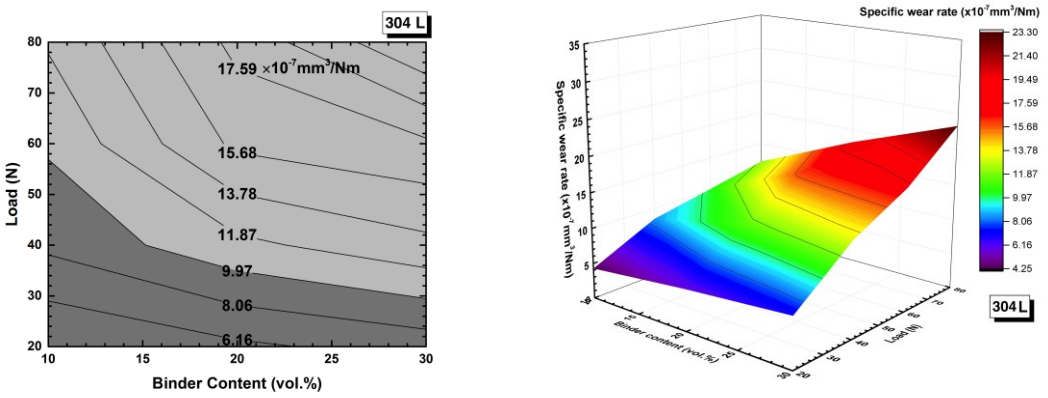

(a)

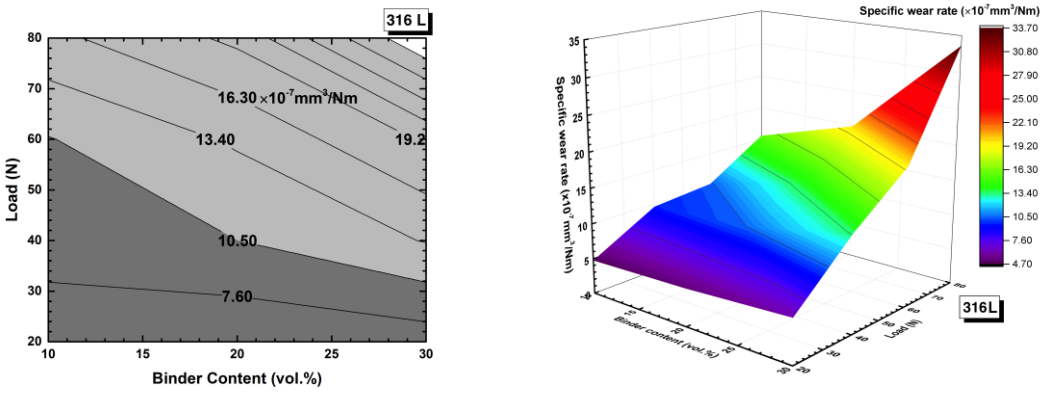

(b)

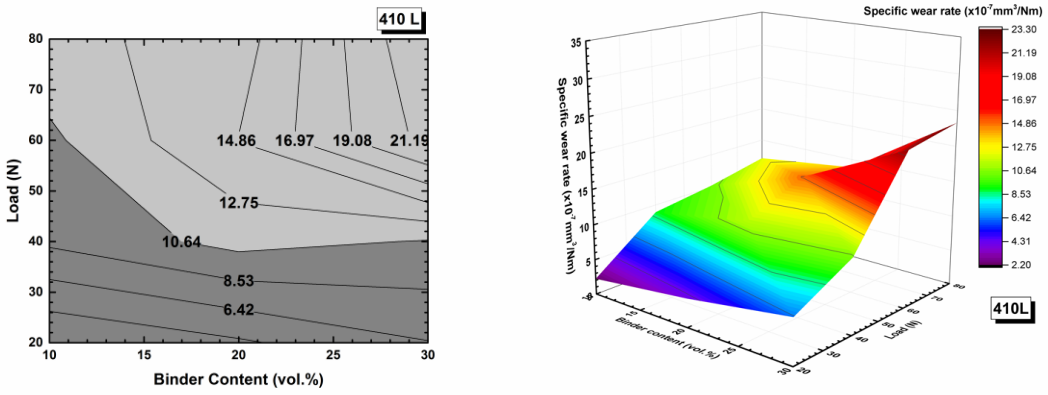

(c)

Figure 9.15: Wear mechanism ‘maps’ for the TiC-stainless steel cermets, with the effects of load and binder content shown for: (a) 304L, (b) 316L, and (c) 410L stainless steel binders.

9.3.6 Wear Mechanism(s)

Several studies of the wear mechanism(s) arising for WC-Co 'hardmetals' have been conducted [4-10,44,45,60-63]. The various suggested mechanisms were mainly focused on plastic deformation [5,7,9] or plastic grooving [5,9], binder phase extrusion and removal [4-6,8], fracture of WC grains [4,7,9], or Palmqvist cracking and subsequent material spalling [10]. Work by Gee and colleagues [44,45,60-63] has provided a large amount of useful data on both two-body and three-body abrasive wear for various hardmetals. This includes both low and high binder content materials, with either Co or Ni as the binder phase [45]; comparison was also made with selected ceramics materials. Tests were conducted using both low load (i.e. 4 N) scratch tests, for a single pass, and also multiple pass test using same load, but repeated for up to 100 scratches. It was found that with an increasing number of scratches, the width of the scratches increases, but with a decreasing rate. It was found that fracture damage was the dominant wear mechanism for the brittle ceramic materials, since ceramics with the same hardness values have a smaller scratch width for the initial tests, but the width then increases much more rapidly than for the hardmetals after the same number of subsequent repeats. It was suggested that fracture of WC grains and plastic deformation were the main wear mechanisms, but re-embedding of the fragments was also observed. They proposed that small fragments remain at the surfaces through two mechanisms [43,61]: (i) the fragments are re-embedded in the structure as further contacts occur, or (ii) the binder phase is pushed out or extruded through the network of cracks that is formed in the WC grains [6,8]. Since there was no binder extrusion observed, the re-embedding of fragments was proposed. A Co containing film (i.e. tribolayer) was also formed. In a related study, concentrating on three-body abrasive wear [60], the hardmetals were sliding against a high speed steel wheel for 20 minutes, using silica sand (200-312 μm) as an abrasive, under various applied loads (50 to 200 N). The low binder content hardmetal samples was observed to have damage within the hard phase (i.e. WC), while binder extrusion was also noted. Conversely, ploughing, fracture and re-embedding of WC fragments dominated the wear mechanisms for the high binder hardmetals. Debonding between the WC grains and the binder matrix was also apparent. The use of either dry or wet environments was also a point of interest for the rotating wheel abrasion (three-body) tests conducted on the hardmetals [61], for both fine- and

coarse-grained cemented carbides. Various types of abrasive tests [62], binder contents, and test geometries [44] have also been studied. It was shown that the extent of wear increases proportionally with increasing load; the wear volume also has a log linear relationship with the hardness. Similar mechanisms were found, with no observation of binder extrusion. This work also found cracks present in the grains on the wearing surface [44,61,62], but the cracks did not propagate through multiple grains, therefore an indentation generated Palmqvist crack was not proposed, but rather a fatigue-related mechanism.

It has been noted that abrasive wear is dominated by either plastic deformation or brittle fracture [64]. Several studies on wear through brittle fracture have indicated that the wear rate increases with the square root of the particle size [65-67]. It has also been suggested that the wear rate predicted by brittle fracture is higher than that arising through plastic deformation, has a stronger dependence on fracture toughness than hardness, and that fracture has to occur when a critical load is exceeded [68]. It can be seen that such transitions may not follow these basic predictions. These materials were assumed to be homogeneous, but cermets, cemented carbides or other composites are actually heterogeneous when wear occurs from hard particles [68].

The wear of ceramics depends on the tribological contact stress [69]. The dominating wear mechanism at low contact stress is plastic deformation (e.g. binder extrusion). At some critical point, cracks will be generated with an increasing contact stress. Then the various cracks would begin to interact with each other, transitioning into a crack-controlled type of wear, leading to a severe wear rate [69]. Finally, fracture-controlled wear would dominate the process if the contact stress keeps increasing, causing grain fragmentation. Tribochemical reactions can then occur when the fragments become trapped between the surfaces.

For the present case it can be seen that the response of the TiC-based cermets is complex, and evolves through the duration of the wear test. Initially, the contract stress promotes some limited extrusion of the binder material from between the TiC particles. This is driven by the much lower hardness and elastic modulus of the steel, potentially combined with a significantly higher Poisson ratio. The reciprocating contact action of the counter

face material also introduces a cyclic loading. Ultimately, sub-surface cracking of the binder arises (as evidenced through the FIB excision experiments). It is proposed that this occurs through work hardening of the steel, at least in part, and eventually the yield stress of the metal is exceeded and failure occurs. At the same time, there is some cracking/fragmentation of the hard TiC phase, although this only appears for extreme surface grains, such that damage is restricted to less than one grain diameter depth. These various features mark a transition from two- to three-body wear, with the third-body being a combination of the TiC particle fragments and the extruded steel binder (as evidenced by the micro-composite wear debris particles that are generated (Figure 9.7)). These observations mark a predominantly abrasive wear mechanism. The fragmented TiC and steel particles are then further refined in size; some of these fragments become embedded back into binder rich regions (as seen, for example, in Figure 9.12(a)). Further attrition results in the third-body debris being refined to such an extent that individual fragments are no longer recognisable when observed in the SEM, and this material is effectively deposited as a semi-continuous tribolayer within the wear track, especially towards the ends and edges of the track. The extent of attrition of the third-body material is further highlighted by the incorporation of relatively high O contents in the tribolayer material. Based on several observations, it is proposed that for the present TiC-based cermets the O content predominantly arises through passivation of freshly exposed surfaces during three-body wear and not, contrary to several other observations, from elevated temperature oxidation. The tribolayer itself is brittle, and exhibits multiple cracking during cyclic loading, eventually leading to spallation of small segments during testing.

9.4 Conclusions

Microstructure assessment by OM, SEM/EDS and FIB were conducted in in order to characterise the effects of dry sliding reciprocating wear tests on TiC-stainless steel cermets. Using optical microscopy, the difference between the retained, intact TiC grains, any tribolayer, and any spalled regions can be readily detected, due to the different reflectivity of these areas within the wear tracks. It was found that the wear response of

the current materials was not governed by a single mechanism. Binder extrusion was found under Hertzian contact loading, in combination with fracture/fragmentation and pull out of the harder TiC grains. Transitions from an initially two-body abrasive wear mode to three-body abrasive wear is apparent due to the formation of debris from these constituents. The wear debris itself can be spherical or 'plate-like', with the spherical particles typically exhibiting a fine-scale, micro-composite structure; this morphology forms from the third-body material being constrained between nominally rolling planar contacts (on a micro-scale).

A further transition to adhesive wear was also observed through the formation of a tribolayer within the wear tracks and on the contact surface of the counter face sphere. The structure and extent of this tribolayer evolves during wear. Initially, the third-body micro-composite material is compacted in regions between the harder TiC grains. With increasing wear time and/or load, this material is significantly refined is structural scale, such that individual TiC grain fragments are no longer resolvable, and is more uniformly distributed across both the wear track and counter face surfaces. The compositions of the tribolayers on both tribo pair surfaces were assessed by EDS analysis, which highlighted constituents from both components in combination with a high O content. It was confirmed that the mechanism of O incorporation into the tribolayer is through particle attrition, rather than thermal oxidation. Site specific FIB micro-sections, cut through the tribolayer/wear surface, highlighted the extent to which sub-surface damage occurs. This included crack formation within the steel binder ligaments, arising from the complex compression/shear loading during sliding wear which, it is proposed, leads to work hardening of the binder and a concurrent loss in ductility. A shear loading component contributed to isolated micro-void formation between contacting TiC grains. Limited cracking of TiC grains was also noted, although this only occurs very close to the wear contact surface (less than one grain diameter depth). Simple 'wear maps' were developed for each cermet family, using specific wear rate data to categorise the severity of the wear. It was noted that wear increased with a combination of high applied load and high binder content, with materials processed with 316L steel showing the highest wear rates.

Acknowledgements

The authors gratefully acknowledge financial support from the Natural Sciences and Engineering Research Council of Canada (NSERC), through both the Collaborative Research and Development programme (grant #CRDPJ381565-09) and the Discovery Grants programme (grant #283311-2011), and Petroleum Research Atlantic Canada (PRAC), under grant C09-10. The Canada Foundation for Innovation, the Atlantic Innovation Fund, and other partners who helped fund the Facilities for Materials Characterisation, managed by the Dalhousie University Institute for Materials Research, are also appreciated. The authors would also like to thank Dean Grijm and Patricia Scallion for technical assistance.

9.5 References

1. R. Llewellyn, Materials for controlling wear in surface mining, CIM bulletin 89 (1996) 76-82.
2. R. Llewellyn, Resisting wear attack in oil sands mining and processing, CIM bulletin 90 (1997) 75-82.
3. M. Anderson, S. Chiovelli, S. Hoskins, Improving reliability and productivity at Syncrude Canada Ltd. through materials research: Past, present, and future, CIM bulletin 97 (2004) 1-5.
4. J. Larsen-Basse, Wear of hard-metals in rock drilling: A survey of the literature, Powder Metall. 16 (1973) 1-32.
5. J. Larsen-Basse, C.M. Shishido, P. Tanouye, Some features of abraded WC/Co surfaces, J. Australian Inst. Metals 19 (1974) 270-275.
6. J. Larsen-Basse, C.M. Perrott, P.M Robinson, Abrasive wear of tungsten carbide-cobalt composites. I. Rotary drilling tests. Mater. Sci, Eng 13 (1974) 83-91.
7. J. Larsen-Basse, N. Devnani, Binder extrusions as a controlling mechanism in abrasion of WC-Co cemented carbides, Science of Hard Materials (1984) 883-895.
8. J. Larsen-Basse, Binder extrusion in sliding wear of WC-Co alloys, Wear 105 (1985) 247-256.

9. H. Feld, P, Walter, Contribution to the understanding of mineral hard metal abrasive wear, Powder Metall. Int. 7 (1975) 188-190.
10. S. F. Wayne, J.G. Baldoni, S.T. Buljan, Abrasions and erosion of WC-Co with controlled microstructures, Tribology transactions 33 (1990) 611-617.
11. J. Pirso, M. Viljus, S. Letunovits, Sliding wear of TiC-NiMo cermets, Tribol. Int. 37 (2004) 817-824.
12. J. Pirso, M. Viljus, S. Letunovits, Friction and dry sliding wear behaviour of cermets, Wear 260 (2006) 815-824.
13. J. Pirso, M. Viljus, K. Juhani, S. Letunovits, Two-body dry abrasive wear of cermets, Wear 266 (2009) 21-29.
14. J. Pirso, M. Viljus, K. Juhani, M. Kuningas, Three-body abrasive wear of TiC-NiMo cermets, Tribol. Int. 43 (2010) 340-346.
15. J. Pirso, M. Viljus, S. Letunovits, K. Juhani, R. Joost, Three-body abrasive wear of cermets, Wear 271 (2011) 2868-2878.
16. C. C. Onuoha, Z.N Farhat, G.J. Kipouros, K.P. Plucknett, The reciprocating wear behaviour of TiC-304L stainless steel composites prepared by melt infiltration, Wear 303 (2013) 321-333.
17. C.C. Onuoha, C. Jin, Z.N. Farhat, G.J. Kipouros, K.P. Plucknett. The effects of TiC grain size and steel binder content on the reciprocating wear behaviour of TiC-316L stainless steel cermets, Wear 350-351 (2016) 116-120.
18. C. Jin, C.C. Onuoha, Z.N. Farhat, G.J. Kipouros, K.P. Plucknett, Microstructural damage assessment following reciprocating wear testing of TiC stainless steel cermets, submitted to Tribol. Int.
19. C. Jin, K.P. Plucknett, Microstructure instability in TiC-316L stainless steel cermets, Int. J. Refract. Met. Hard Mater. 58 (2015) 74-83.
20. B.V. Manoj-Kumar, B.Basu, M. Kalin, J. Vizintin, Load-dependent transition in sliding wear properties of TiCN-WC-Ni cermets, J. Am. Ceram. Soc. 90 (2007) 1534-1540.
21. I. Hussainova, Effect of microstructure on the erosive wear of titanium carbide-based cermets, Wear 255 (2003) 121-128.

22. I. Hussainova, Microstructure and erosive wear in ceramic-based composites, Wear 258 (2005) 357-365.
23. B.R. Lawn, Indentation of ceramics with spheres: a century after Hertz, J. Am. Ceram. Soc. 81 (1998) 1977-1994.
24. N. Chawla, Y.L. Shen, Mechanical behavior of particle reinforced metal matrix composites, Adv. Eng. Mater. 3 (2001) 357-370.
25. Z. Hashin, S. Shtrikman, A variational approach to the theory of the elastic behaviour of multiphase materials. J. Mech. Phys. Solids 11 (1963) 127-140.
26. B. Budiansky, On the elastic moduli of some heterogeneous materials, J. Mech. Phys. Solids 13 (1965) 223-227.
27. I. A. Ibrahim, F.A. Mohamed, E.J. Lavemia, Particulate reinforced metal matrix composites- a review, J. Mater. Sci. 26 (1991) 1137-1156.
28. L.S. Sigl, S. Schmauder, A finite element study of crack growth in WC-Co, Int. J. Fract. 36 (1998) 305-317.
29. H. Doi, Y, Fujiwara, K. Miyake, Y. Oosawa. A systematic investigation of elastic moduli of WC-Co alloys. Metall. Mater. Trans. 1 (1970) 1417-1425.
30. T.L. Stewart, K.P. Plucknett, The sliding wear of TiC- and Ti(C,N) cermets prepared with a stoichiometric Ni_3Al binder, Wear 318 (2014) 153-167.
31. R.B. Collier, K.P. Plucknett, Spherical indentation damage in TiC-Ni_3Al composites, Int. J. Refract. Met. Hard Mater. 30 (2012) 188-195.
32. A.G. Evans, D.B. Marshall, D.A. Rigney. Fundamentals of friction and wear of materials. Am. Soc. Metals 439, ASM Intl., Materials Park, OH, USA (1981).
33. D.A. Rigney, Paper X (i) The role of characterization in understanding debris generation, Tribology Series 21 (1992) 405-412.
34. G. Stachowiak, A.W. Batchelor. Engineering tribology, Butterworth-Heinemann, 2013.
35. L.J. O'Donnell, Tribology of 316L Austenitic Stainless steel carburized at low temperature, MSc Thesis, Case Western Reserve University, USA, 2010.
36. T. Quinn, J. L. Sullivan, D. M. Rowson, Origins and development of oxidational wear at low ambient temperatures, Wear 94 (1984) 175-191.
37. F.H. Stott, The role of oxidation in the wear of alloys, Tribol. Int. 31 (1998) 61-71.

38. T. L. Stewart. The characterization of TiC and Ti(C,N) based cermets with and without Mo2C. MSc Thesis, Dalhousie University, Canada, 2014.
39. T.L. Stewart, K.P. Plucknett, The effects of Mo_2C additions on the microstructure and sliding wear of $TiC_{0.3}N_{0.7}$-Ni_3Al cermets, Int. J. Refract. Met. Hard Mater. 50 (2015) 227-239.
40. M.G. Gee, K.P. Mingard, A.J. Gant and H.G. Jones, FIB/SEM determination of sub-surface damage caused by micro-tribology scratching of WC/Co hardmetal samples, in 1 International conference on 3D materials science, (eds M. De Graef, H. F. Poulsen, A. Lewis, J. Simmons and G. Spanos), John Wiley & Sons, Inc., Hoboken, NJ, USA. (2012).
41. J.C.P. Zunega, M.G.Gee, R.J.K. Wood, J. Walker, Scratch testing of WC/Co hardmetals, Tribol.Int. 54 (2012) 77-86.
42. A.J. Gant, M.G. Gee, D.D. Gohil, H.G. Jones, L.P. Orkney, Use of FIB/SEM to assess the tribo-corrosion of WC/Co hardmetals in model single point abrasion experiments, Tribo.Int. 68 (2013) 56-66.
43. C. Pignie, M.G. Gee, J. W. Nunn, H. Jones, A.J. Gant, Simulation of abrasion to WC/Co hardmetals using a micro-tribology test system, Wear 302 (2013) 1050-1057.
44. M. Gee, A. Gant, B. Roebuck, Wear mechanisms in abrasion and erosion of WC-Co and related hardmetals, Wear 263 (2007) 137-148.
45. M.G. Gee, Low load multiple scratch tests of ceramics and hard metals, Wear 250 (2001) 264-281.
46. K. Kato, K. Hokkirigawa, Abrasive wear diagram, Proc. Eurotrib. 85 (1985) 1-5.
47. K. Hokkirigawa, K. Kato, An experimental and theoretical investigation of ploughing, cutting and wedge formation during abrasive wear, Tribol. Int. 21 (1988) 51-57.
48. K. Adachi, K. Kato, N. Chen, Wear map of ceramics, Wear 203-204 (1997) 291-301.
49. K. Kato. Classification of wear mechanisms/models, Proceedings of the institution of mechanical engineering, Part J: Journal of Engineering Tribology 216 (2002) 349-355.
50. K. Kato, K. Adachi, Wear of advanced ceramics, Wear 253 (2002) 1097-1104.
51. K. Kato, Tribology of ceramics, Wear 136 (1990) 117-133.

52. S.M. Hsu, Y.S. Wang, R.G. Munro, Quantitative wear maps as a visualization of wear mechanism transition in ceramic materials, Wear 134 (1989) 1-11.
53. S.M. Hsu, D.S. Lim, Y.S. Wang, R.G. Munro, Ceramics wear maps: concept and method development, Lubrication engineering, 47 (1991) 49-54.
54. S.M. Hsu, D.S. Lim, R.G. Munro, Ceramic wear maps, V.J. Tennery (Ed.), Proc. of the 3rd Int. Symp. Ceramic Materials and components of Engines, Am. Ceram. Soc., New York (1989), pp. 1236-1245.
55. S.W. Lee, S.M. Hsu, R.G. Munro, Ceramic wear maps: SiC whisker reinforced alumina, P.K. Rohatgi, P.J. Blau, C.S. Yust (Eds.), Tribology of Composite Materials, ASM International, Metals Park, OH (1990), p. 35.
56. S.W. Lee, S.M. Hsu, M.C. Shen, Ceramic wear maps: zirconia, J. Am. Ceram. Soc. 76 (1993) 1937-1947.
57. Y.S. Wang, S.M.Hsu, R.G. Munro, Ceramic wear maps: alumina, Lubricating Engineering 47 (1991) 63-69.
58. S.M. Hsu, M.C. Shen, Ceramic wear maps, Wear 200 (1996) 154-175.
59. S.M. Hsu, M.C. Shen, Wear prediction of ceramics, Wear 256 (2004) 867-878.
60. A.J. Gant, M.G. Gee, Wear of tungsten-carbide-cobalt hardmetals and hot isostatically pressed high speed steels under dry abrasive conditions, Wear 251 (2001) 908-915.
61. A.J. Gant, M.G. Gee, B. Roebuck, Rotating wheel abrasion of WC/Co hardmetals, Wear 258 (2005) 178-188.
62. A.J. Gant, M.G.Gee. Abrasion of tungsten carbide hardmetals using hard countefaces. Int. J. Refract. Met. Hard Mater. 24 (2006) 189-198.
63. M.G. Gee, L. Nimishakavi, Model single point abrasion experiments on WC/Co hardmetals, Int. J. Refract. Met. Hard Mater. 29 (2011) 1-9.
64. I.M. Hutchings. Tribology: Friction and wear of engineering materials. Butterworth-Heinemann Ltd, 1992.
65. B.J Hockey, R.W. Rice, The science of ceramic machining and surface finishing 2, NASA STI/Recon Technical report N 80 (1979) 20441.
66. D.A. Rigney, Fundamentals of friction and wear of materials, DTIC Document, 1980.

67. D.B. Marshall, B. R. Lawn, A.G. Evans, Elastic/plastic indentation damage in ceramics: the lateral crack system, J. Am. Ceram. Soc. 65 (1982) 561-566.
68. I.M. Hutchings, Mechanisms of wear in powder technology: A review, Powder Technol. 76 (1993) 3-13.
69. Y. Wang, S.M. Hsu, Wear and wear transition mechanisms of ceramics, Wear 195 (1996) 112-122.

Chapter 10 Conclusions and Future Work

10.1 Conclusions

Material loss through wear and/or erosion has resulted in significant costs in maintaining and repairing components in the mining, tooling, and oil/gas industries. To reduce the damage, the microstructure and topography of the worn material should be studied. The current research produced a new family of TiC stainless steel cermets with various binders, and studies relating to wear were conducted (i.e. sharp and blunt contact damage). To optimise the material's mechanical properties and performance, the microstructural evolution was first assessed. Indentation behaviour of the materials was evaluated. 'Sharp' Vickers indentation was conducted since different crack patterns may lead to the removal of the material, and it also simulated the erosion behaviour of the cermets with a fixed geometry 'sharp' indenter. 'Blunt' Hertz indentation was also studied, under quasi-static loading and following reciprocating wear, which provides information relating to the cermets in contact with a sphere under both static and dynamic loads (e.g. for a bearing scenario).

Stainless steel binders (austenitic 304-L and 316-L, and martensitic 410-L) were incorporated with the TiC ceramic phase, and varied from 5 to 30 vol.%. Samples were densified using a simple 'melt infiltration/sintering' method, with a variety of different sintering conditions: (i) 1475 °C for 15 minutes, (ii) 1550 °C for 60 minutes (1500 °C for reciprocating wear tests), and (iii) 1550 °C for 240 minutes. This allowed the fabrication of fine-, intermediate- and coarse-grained TiC cermets. The sintered cermets consistently achieved densities greater than 95% theoretical, even with only 5 vol.% steel binder. A slight decrease of the measured densities with the increasing binder content was found, which is believed to be the combination of microstructure/compositional modification during the sintering process and volatilisation of the steel binders.

For evaluation of the microstructural evolution of the cermets, scanning electron microscopy (SEM) analysis was conducted on the samples, and revealed a homogenous distribution of the TiC grains, and no evidence abnormal grain growth. It has found that the grain size distribution of the cermets followed a logarithmic Gaussian fit, with a

broader distribution when the sintering duration increased. The microstructural parameters (i.e. mean grain size, contiguity and binder mean free path) were measured, as they are important in predicting the mechanical properties of the materials. The mean grain size increases with increasing sintering temperature, and is relatively independent of the binder content. The contiguity of the cermet decreases with increasing binder content, as the contact between the TiC grains were decreased. Conversely, the binder mean free path of the cermets increased with increasing binder content. A complex, irregular 'C-shape' and 'O-shape' morphology of the TiC grains arose during the sintering process, especially for the samples sintered at 1475 °C for 15 minutes. This phenomenon can be explained by the 'instability of solid-liquid interface' theory, in which the dissolution of specific constituents produced a coherent strain at the surface of the TiC grain, causing the tensile stress to push the grain inwards. This is related to the competition between the minimisation of interfacial energy and the coherency strain energy. Focused ion beam microscopy (FIB) was conducted and showed that the 'O-shape' grains are, in fact, an artefact of the sectioning, and are actually 'cup-shaped'.

A multi-layer 'core-rim' structure was developed after sintering, which is believed to be a result of Oswald ripening during the 'dissolution/re-precipitation' process of the liquid phase sintering. Energy dispersive X-ray spectroscopy (EDS) analysis revealed the 'core' is pure TiC, while the rim consisted of a lighter contrast 'inner-rim' and a darker contrast 'outer-rim'. It was found that the Mo, which is originally in the 316-L stainless steel, was fully depleted from the binder and deposited onto the pure TiC cores; a maximum concentration of Mo was found in the 'inner-rim'. The other constituents, Cr, Ni are also detected in the rim phase, but mainly in the 'outer-rim'. A small amount of Fe was also detected within the TiC grains, but the majority remains in the binder.

Indentation with 'sharp' Vickers indenters, with various applied loads, was conducted on the TiC-316-L stainless steel samples, in part to study the indentation-induced cracks, but also to assess fundamental hardness and indentation fracture resistance characteristics. Differential interference contrast (DIC) optical microscopy revealed a slight 'uplift' phenomenon around indentation sites without spalling. The hardness of the cermets decreases with increasing binder content, as the binder mean free path of the materials increase. Hardness was evaluated with various loads (1, 5, 10 and 30 kgf), and an

apparent ‘indentation size effect’ (ISE) was found, as the hardness number increases with decreasing load at a fixed binder content. The ISE was analysed using both Meyer’s law and the proportional specimen resistance (PSR) model. Measurement of the indentation fracture resistance (IFR) was also conducted, again with various indentation loads. The IFR values were calculated using either ‘median/radial’ or ‘Palmqvist’ crack models, depending on the predicted crack pattern (assessed initially from the *c*:*a* ratio), and the values increases with increasing binder content, as anticipated. ‘*R*-curve’ behaviour was found, as the IFR increases with increasing crack length/load. This phenomenon is due to the ductile binder ligaments bridging the crack in its wake; the longer the crack, up to some maximum length, the greater the number of bridging ligaments. FIB micro-machining cuts were conducted within the crack paths, to view sub-surface damage, and these revealed a transgranular-type of cracking. Both ‘median’ and ‘Palmqvist’ cracks were found in the system. When applied with a fixed load, cermets with higher binder content are likely to produce ‘Palmqvist’ type of cracking; when the binder content is fixed and applied with high load, ‘median’ type of cracking are favoured.

‘Hertzian’ indentation, with blunt spherical indenters, was also assessed with the TiC-316L cermets. Various diameter WC-Co spheres were used as indenters, ranging from 1.19 mm to 3.96 mm, with the applied loads ranging from 250 N to 2000 N. Standard 4140/4142 steel samples were also indented to provide a baseline comparison. The indentation stress-strain curves were plotted to study the ‘quasi-plastic’ behaviour of the material. It was found that the cermets deviated from the calculated ‘elastic Hertz response’ and exhibited a ‘strain-hardening’ effect. The cermets demonstrated three nominal regions of ‘quasi-plasticity’: (i) pseudo-elastic, (ii) elastic-plastic, and (iii) pseudo-plastic. The residual indentation sites were observed using optical microscopy and SEM, while an optical profilometer was used to obtain the final indentation depth, which was compared with the maximum deflection values recorded during the spherical indentation tests.

Relating to the spherical indentation assessment, the reciprocating wear behaviour was also studied using a sphere-on-flat test geometry. Two main aspects of sliding wear were assessed: (i) the effect of the grain size, binder content and applied loads on the TiC-316-L cermets, and (ii) the effects of the steel grade (340L, 316L, and 410L), binder content,

applied load and the testing time. To assess the grain size effect for the TiC-316-L cermets, fine- and coarse-grained materials, with binders ranging from 10 to 30 vol.%, were tested with 20 to 80 N applied load for 120 minutes. The fine- and coarse-grained cermets both exhibited a decrease in hardness with increasing binder content, while the fine-grained cermets have overall higher hardness values; this is primarily attributed to the finer steel ligament dimensions (binder mean free path) generating a higher yield stress in the metal (following the Hall-Petch relationship). The fine-grained cermets also exhibited better wear resistance than the coarse-grained equivalents. The specific wear rates for the fine- and coarse-grained cermets are in the order of 10^{-7} mm^3/Nm, which is broadly consistent with WC-Co hardmetals. The specific wear rate for fine- and coarse-grained cermets increases with increasing binder content and applied load. SEM analysis was used to study the wear mechanism(s). Binder extrusion and TiC fragmentation were detected, indicating a transition from two-body to three-body abrasive wear. The formation of tribolayer confirmed the further transition to an adhesive wear mode. High concentrations of oxygen were found within the tribolayer through EDS analysis. The use of FIB micro sections, within and at the edge of the wear tracks, revealed shear induced sub-surface damage. This was manifest in form of: (i) brittle nature of the tribolayer, (ii) fragmentation of the TiC grains, (iii) void formation between TiC grains, and (iv) cracking of the steel binder ligaments.

A study of the effects of different grades of stainless steel binders was conducted using the same reciprocating wear test geometry; samples were all sintered for 1500°C for 60 minutes, to generate broadly identical microstructures. The binder contents were varied from 10 to 30 vol.%, and the cermets were tested with loads ranging from 20 to 80 N, for durations from 15 to 120 minutes. For the lowest binder content, the ‘run-in’ time to reach a steady state coefficient of friction is somewhat longer than for the highest content. It was found that the wear resistance of the TiC-410-L cermet is slightly higher than the austenitic binder cermets, particularly those prepared with 316L. Optical microscopy confirmed that the formation of a tribolayer is a fast process, as the samples examined after only 15 minutes of wear already exhibited initial stages of tribolayer formation. The wear mechanism(s) are again, initially two-body abrasive wear, transitioning to three-body abrasive wear. A further transition to adhesive wear then

occurs, with tribolayer formation; a tribolayer is also deposited on the WC-Co counter-face sphere, which is confirmed with EDS. Simple wear maps were developed, as a function of binder content and applied load, which categorised the 'mild' to 'severe' wear regions.

It can be concluded from above, a combination of good mechanical properties and steel grade would provide the ideal candidate material in terms of wear resistance. Fine-grained cermets with a medium binder content (i.e. ~ 15-20 vol.%) would provide both high hardness and indentation fracture resistance, which could enhance resistance to both wear by plastic deformation and brittle fracture mechanisms. Overall, cermets with martensitic 410L grade steel as a binder has the highest wear resistance within this family of materials in the current study.

10.2 Recommendations for future work

The current study has conducted indentation tests, with both sharp and blunt indenters, on a family of TiC-stainless steel cermets. It would be desirable to apply the bonded interface method to analyse the cermets, particularly to study the cracking behaviour and sub-surface damage within the cermets. For Vickers indenter-induced cracks, the current study has utilised FIB micro-machining of regions within the crack path to determine the sub-surface crack patterns. However, the cracks may not be as ideal in shape as is illustrated in the schematic figures. The sequential polishing method was conducted in the current work, but was not very successful, as the debris from polishing was pushed into the cracks and the residual indents, causing issues in the identification of the sub-surface crack patterns. For 'blunt' indentation, the bonded-interface-method is a very useful tool to study the sub-surface deformation, particularly the shape, magnitude and location of the deformation zone; information relating to the mechanism of 'quasi-plastic' deformation can also be identified by this method. Indentation fatigue, with multiple repeated loading cycles (effectively a form of contact fatigue), and high temperature indentation are also worth considering for assessing spherical indentation on these and related cermets. Nano-indentation with a diamond Berkovich tip is also suggested, to obtain the localized, 'in-situ' values of the Young's modulus of the phases (i.e. on a

micro-scale), as the current study uses a rule of mixtures to estimate the composites elastic modulus. This would nominally provide the true materials parameters for future analysis. By using nano-indentation method, the hardness of the ceramic and the metallic phase can be obtained respectively, and this would also allow some determination of the degree of work hardening that may occur during the 'cyclic' reciprocating wear tests. Similarly, the bulk elastic moduli should also evaluated, for example using a Grindosonic system.

Another important aspect of such a study is to utilise the finite element method to simulate the indentation process. Hertzian indentation models have been widely adapted in many commercial simulation packages, therefore extending the current study is suggested, starting with modelling of the spherical indentation on the cermets as a 'continuum' material initially. By comparing the modelling and experimental work, potential discrepancies between the two can be identified. The model could then be revised to apply to the composite cermets by incorporating interactions between the ceramic and the metallic phases. Further research utilising the FEM method in terms of the Vickers indentation response could then be applied.

Finally, for the reciprocating wear studies, to help better understand the operative wear mechanism(s), the use of electron back-scattered diffraction (EBSD) is suggested to examine the plastic deformation. EBSD would provide important information on the plastic deformation accumulated, and to determine the critical plastic strain and when the TiC grains would start to crack. EBSD analysis would also provide the initial orientation of the TiC grains, as well as the degree of plastic deformation through the reduction of the indexed patterns.

Appendix. A Microstructure Characterisation of the Cermets

Appendix A presents the sample characterisation results, which were not shown in the previous sections. All sintered samples were characterised with SEM with their microstructure parameters calculated. In Figure A. 1 and Figure A. 2, are the representative SEM images and corresponding grain size distribution histograms of the TiC-316L samples with 20 and 30 vol.% of steel binder, sintered at 1475ºC for 15 minutes (fine-grained), 1550ºC for 60 minutes (intermediate-grained) and 1550ºC for 240 minutes (coarse-grained). It can be seen that the sintered samples are homogeneous in microstructure and were fully densified. Again, the fine-grained cermets show a more complex microstructure than the other two. A multi-layer 'core-rim' structure of the sintered samples can be seen from the SEM images. The grain size distribution follows a log normal distribution, and becomes wider as the sintering temperature and duration increases.

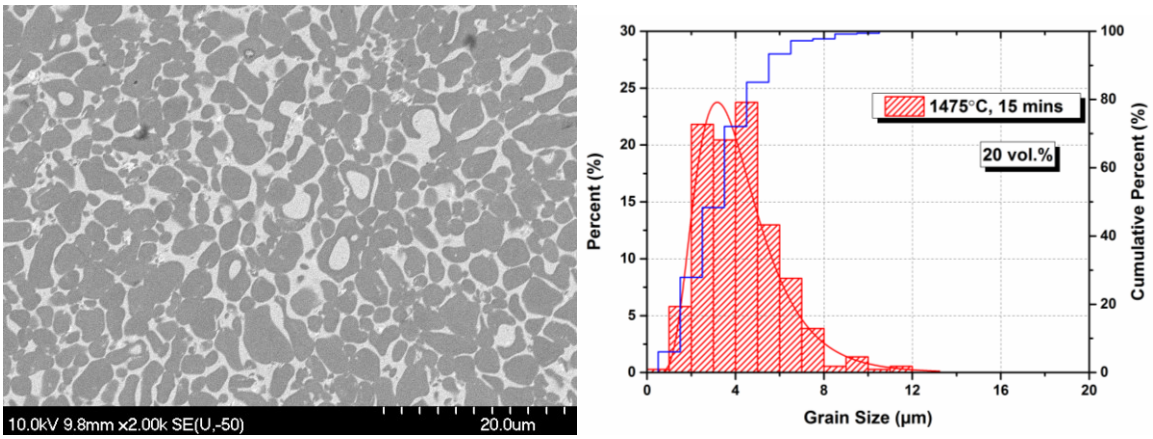

(a)

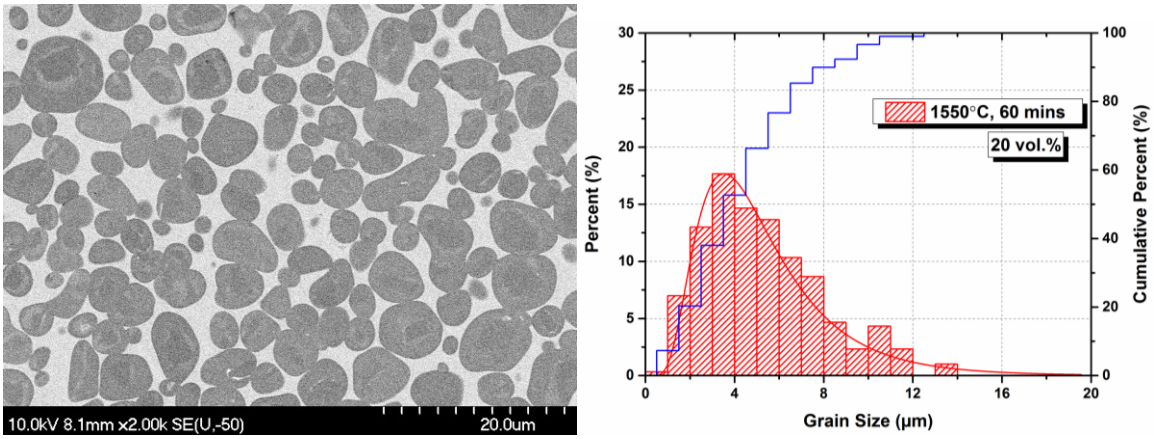

(b)

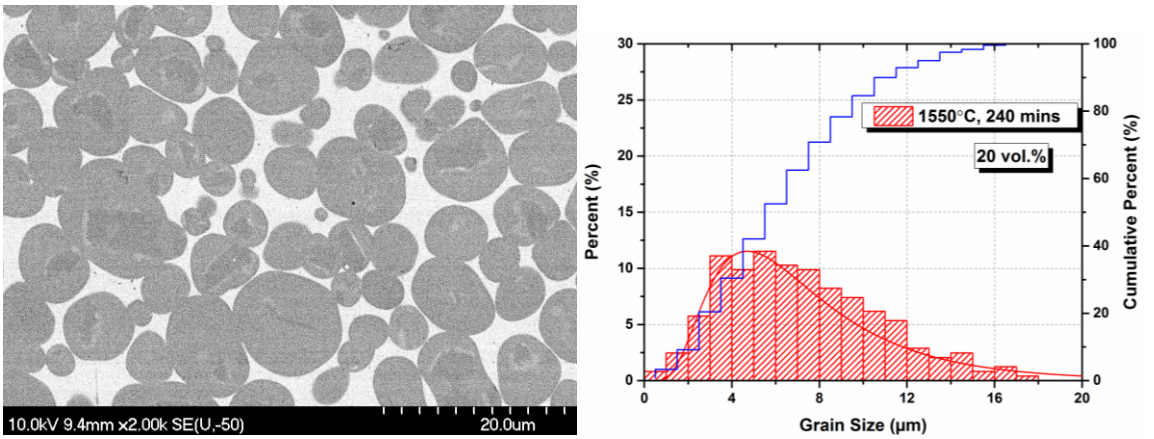

(c)

Figure A. 1: Representative SEM images of TiC cermets with 20 vol.% 316-L binder content and corresponding grain size distributions sintered at (a) 1475°C/15 min (fine), (b) 1550°C/60 min (intermediate) and (c) 1550°C /240 min (coarse).

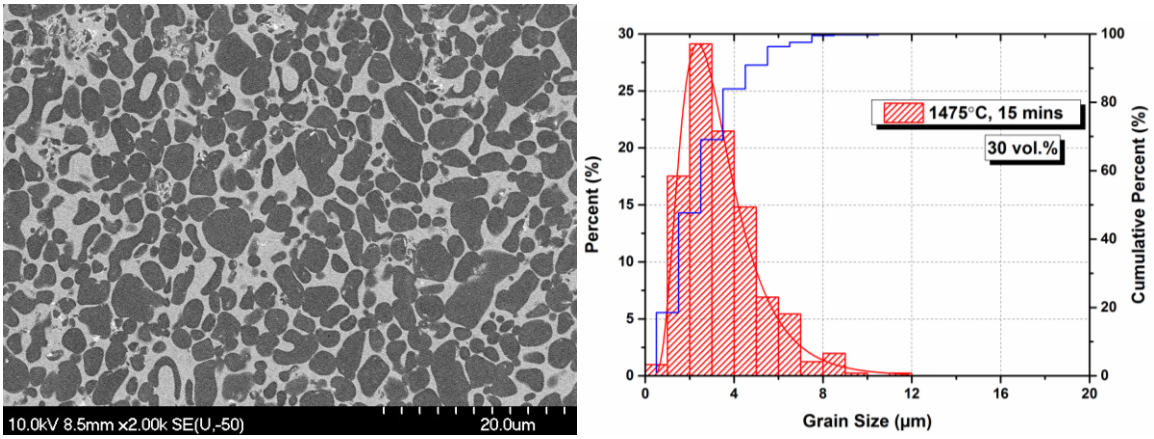
10.0kV 8.5mm x2.00k SE(U,-50)
20.0um
1475°C, 15 mins
30 vol.%
Percent (%)
Cumulative Percent (%)
Grain Size (μm)

(a)

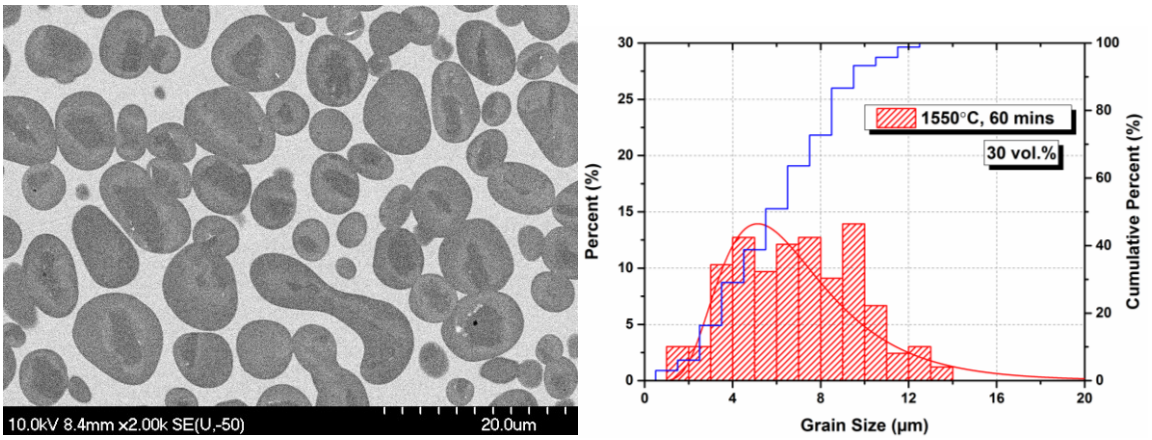
10.0kV 8.4mm x2.00k SE(U,-50)
20.0um
1550°C, 60 mins
30 vol.%
Percent (%)
Cumulative Percent (%)
Grain Size (μm)

(b)

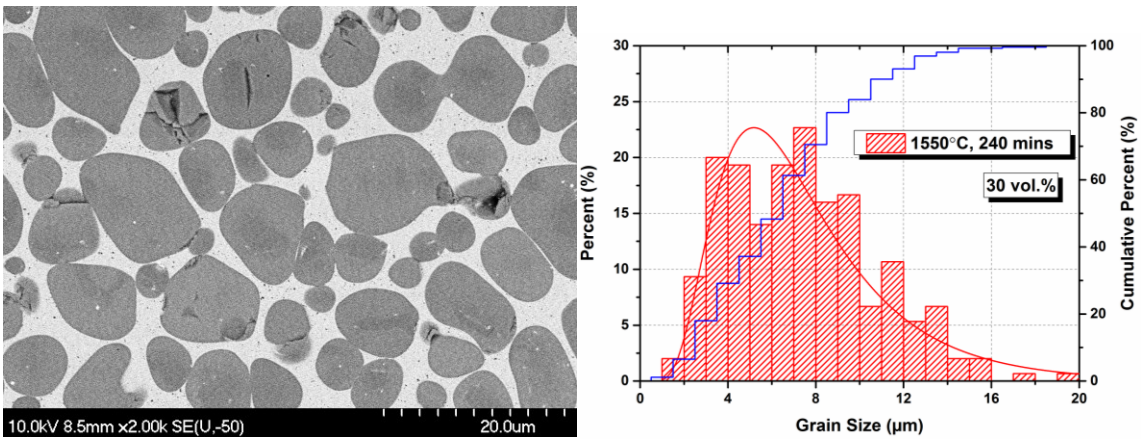

(c)

Figure A. 2: Representative SEM images of TiC cermets with 30 vol.% 316-L binder content and corresponding grain size distributions sintered at (a) 1475°C/15 min (fine), (b) 1550°C/60 min (intermediate) and (c) 1550°C /240 min (coarse).

The XRD trace of the intermediate- and coarse-grained TiC-316L cermets are shown in Figure A. 3. The spectra fit the TiC powder diffraction file (#03-065-8416) and austenitic stainless steel powder diffraction file (#00-033-0397), respectively.

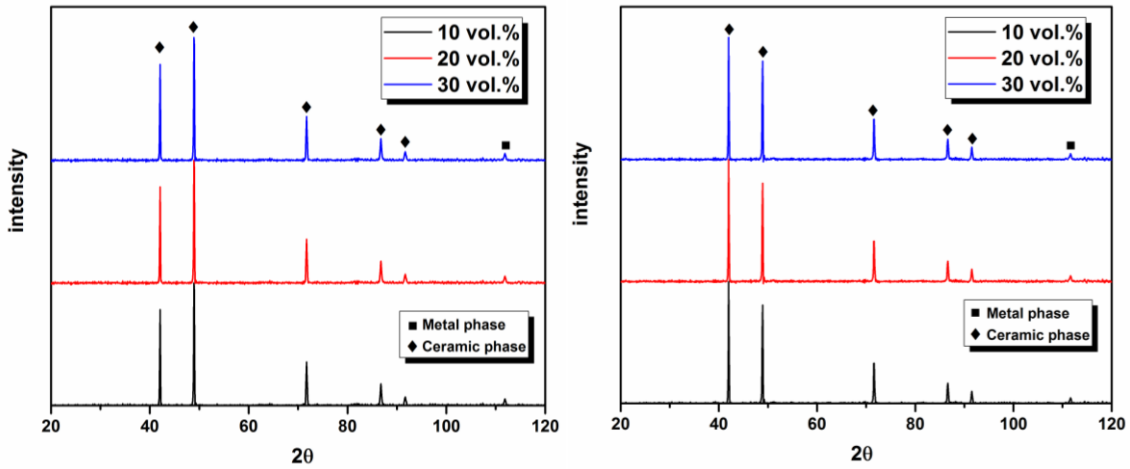

(a) (b)

Figure A. 3: XRD spectra obtained for (a) intermediate- and (b) coarse-grained cermets.

The multi-layer ‘core-rim’ structure of the sintered samples were categorized with four different regions as ‘binder’, ‘core’, ‘outer-rim’ and ‘inner-rim’, which was further

analysed by EDS. Figure A. 4 shows the weight percentage of the detected constituents as bar graphs, to give a comparison of an intermediate-grained cermet with 15 and 30 vol.% of binder. Values were listed in Table 4.4 and detailed discussion can be found in Chapter 4.

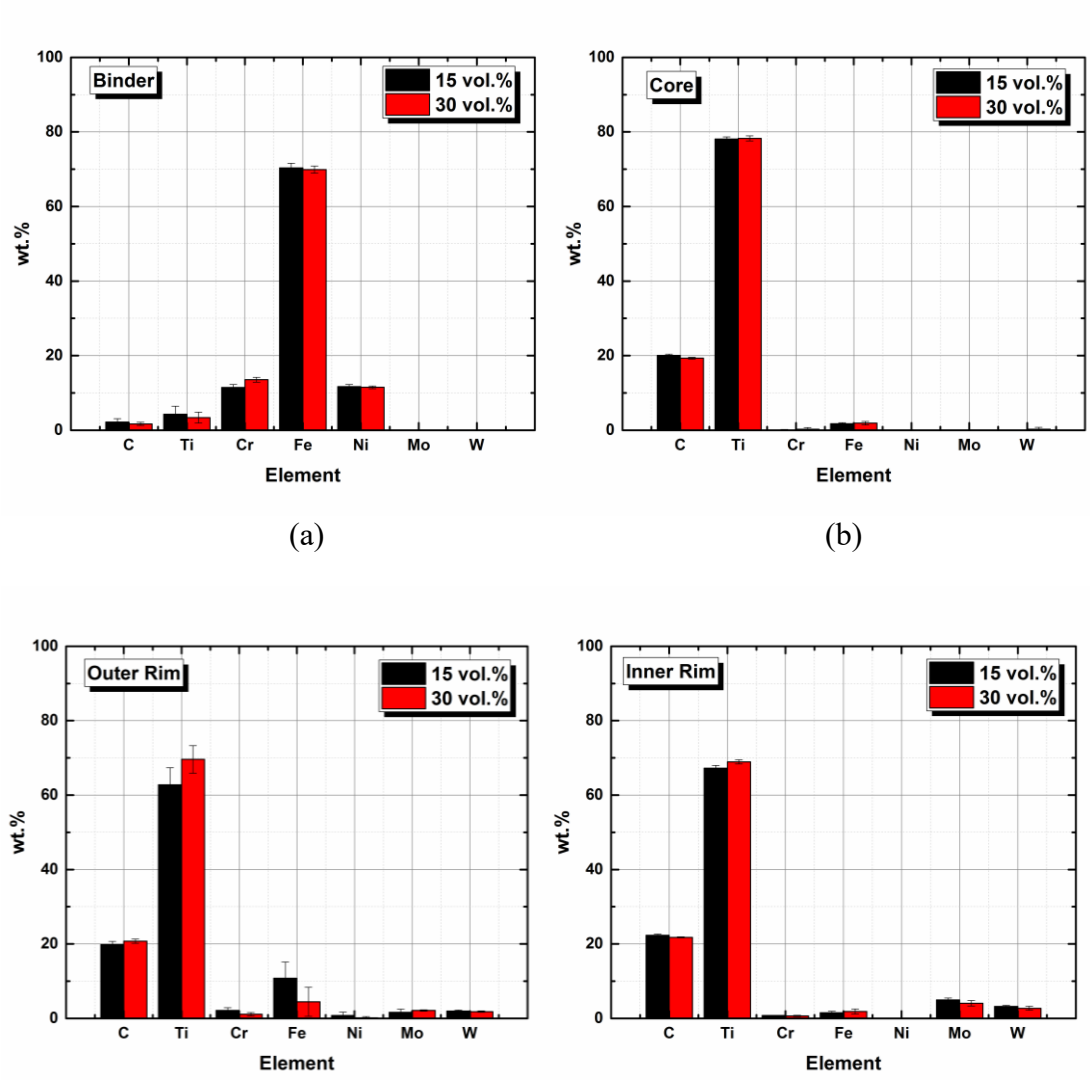

Figure A. 4: Representative EDS core-rim structure intensities of a TiC-316-L intermediated grained sample with 15 and 30 vol.% of binder, as (a) binder, (b) core, (c) outer-rim and (d) inner-rim.

The sintered samples prepared for the reciprocating wear tests were also examined with SEM. Figure A. 5 to Figure A. 7 are the intermediate-grained cermets, with 304L, 316L and 410L as binder. Binder contents are 10, 20 and 30 vol.%. Areas with high concentration of W can be seen.

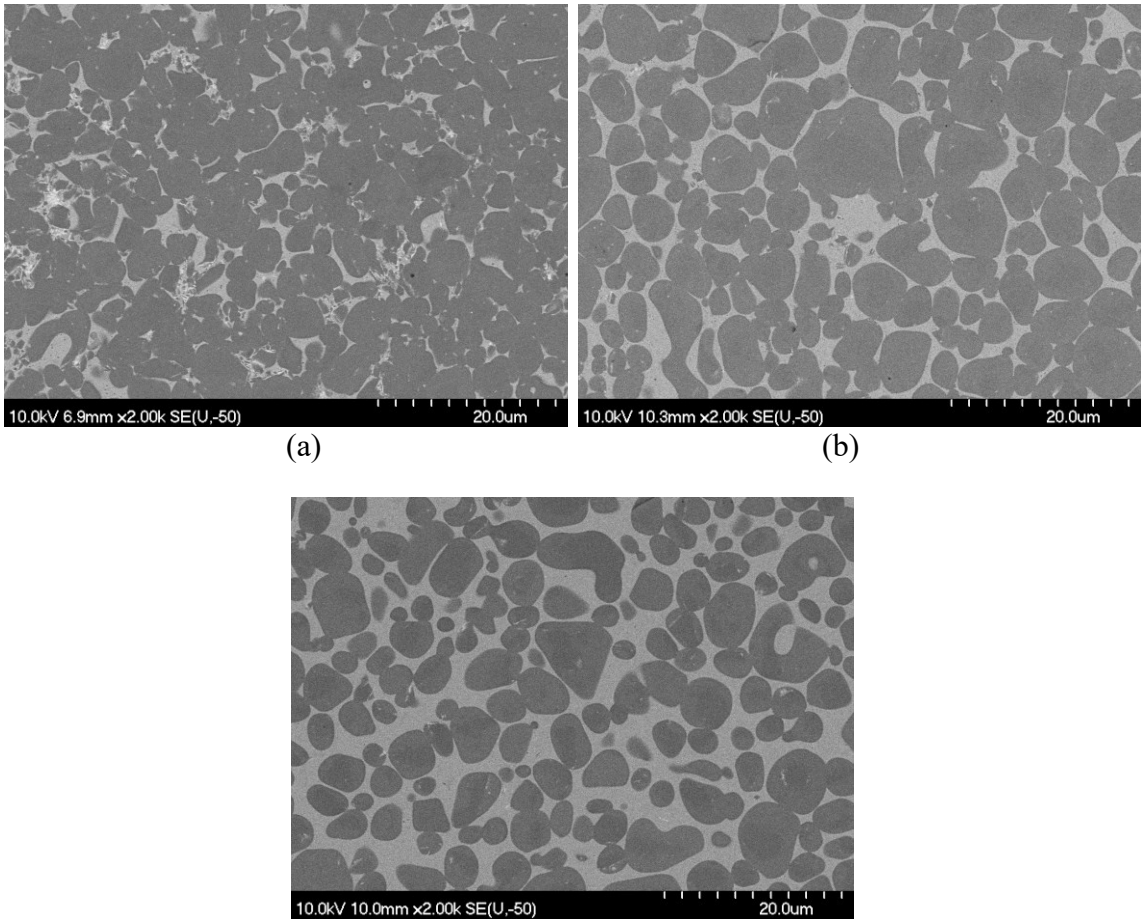

Figure A. 5: TiC- 304L cermet sintered for 1500°C for 60 minutes with (a) 10 (b) 20 and (c) 30 vol.% of binder.

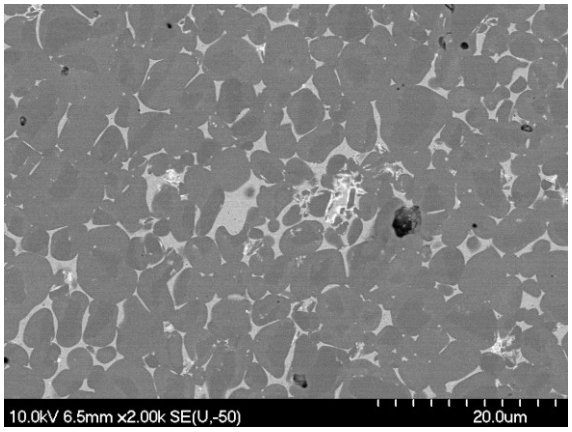

(a)

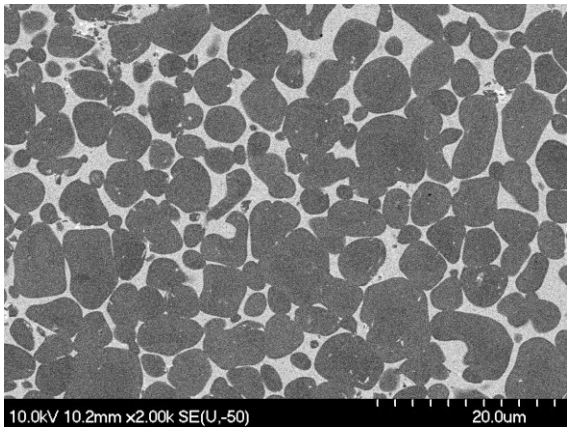

(b)

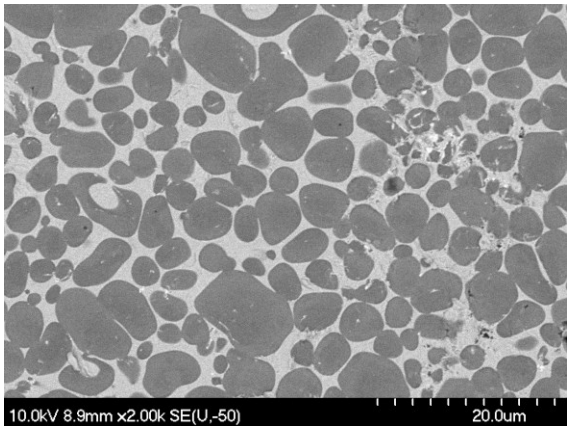

(c)

Figure A. 6: TiC-316L cermet sintered for 1500°C for 60 minutes with (a) 10 (b) 20 and (c) 30 vol.% of binder.

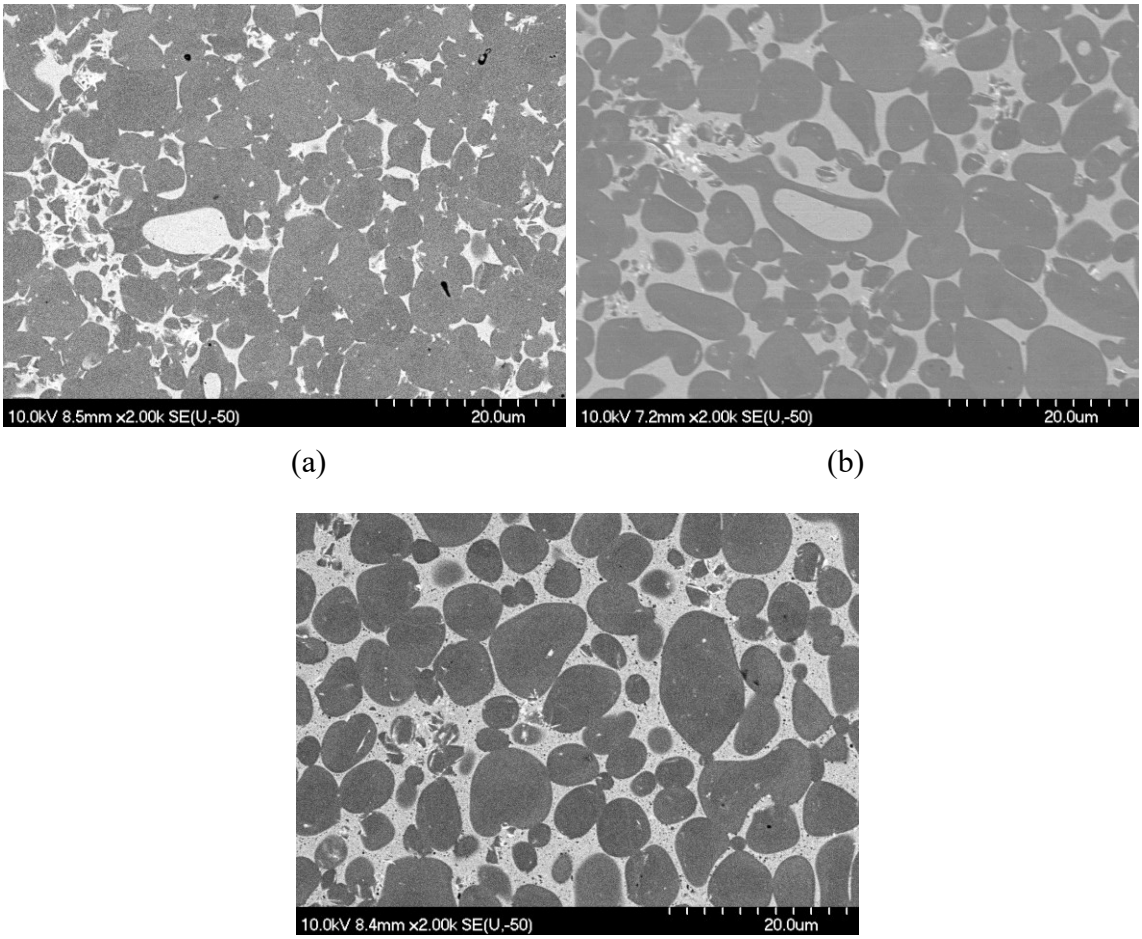

Figure A. 7: TiC-410L cermet sintered for 1500°C for 60 minutes with (a) 10 (b) 20 and (c) 30 vol.% of binder.

Appendix. B Vickers Indentation Data

Appendix B presents the 'sharp' Vickers indentation data and images, which were not shown in the previous sections. Figure B. 1 is the hardness data, and Figure B. 2 is the fitting plot using PSR model of TiC-316L coarse-grained samples.

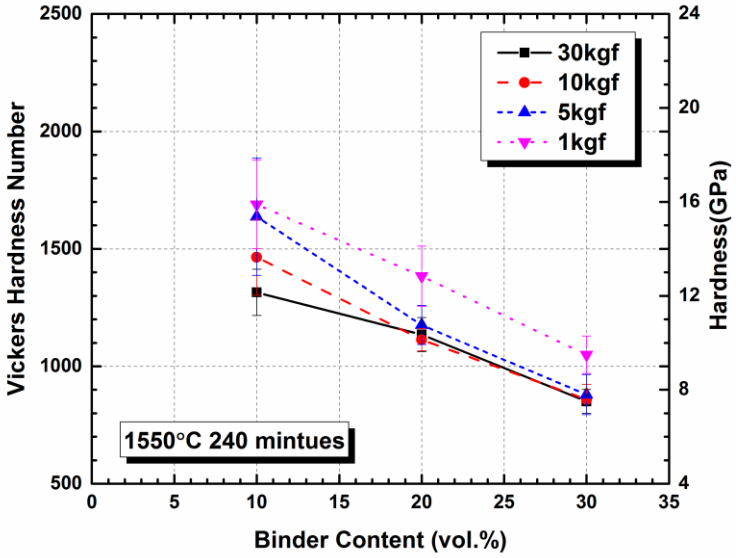

Figure B. 1: Hardness as a function of binder for a TiC- 316L coarse-grained cermet.

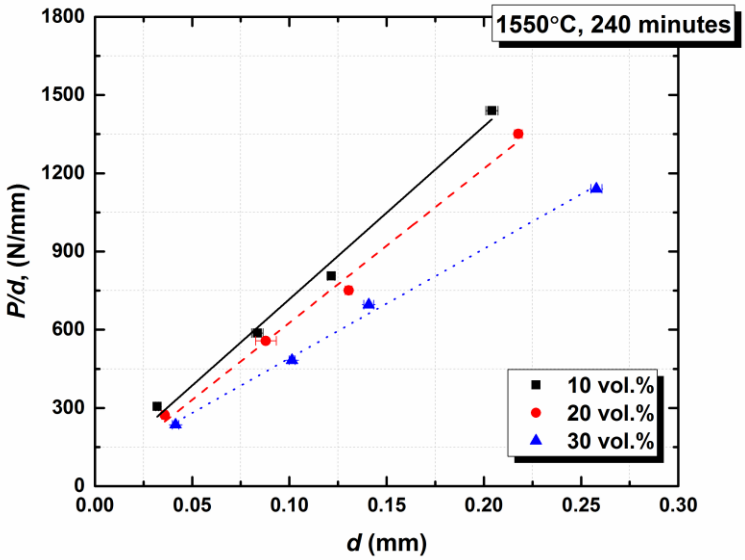

Figure B. 2: PSR model for P/d versus d, for a TiC-316L coarse-grained cermet.

DIC optical microscope images of TiC-316L cermets with various binder contents were shown in the following section, loaded with 1, 5, 10 and 30 kgf of force. Figure B. 3 is TiC-30 vol.% fine-grained. Figure B. 4 and Figure B. 5 intermediate-grained cermets with 10 and 30 vol.% of binder. Figure B. 6 and Figure B. 7 are coarse-grained cermets with 10 and 30 vol.% of binder, respectively. The samples all show a slight 'pileup' effect. Intermediate-grained cermets sample shows relatively well-defined radial cracks than the coarse-grained at 10 vol.% binder.

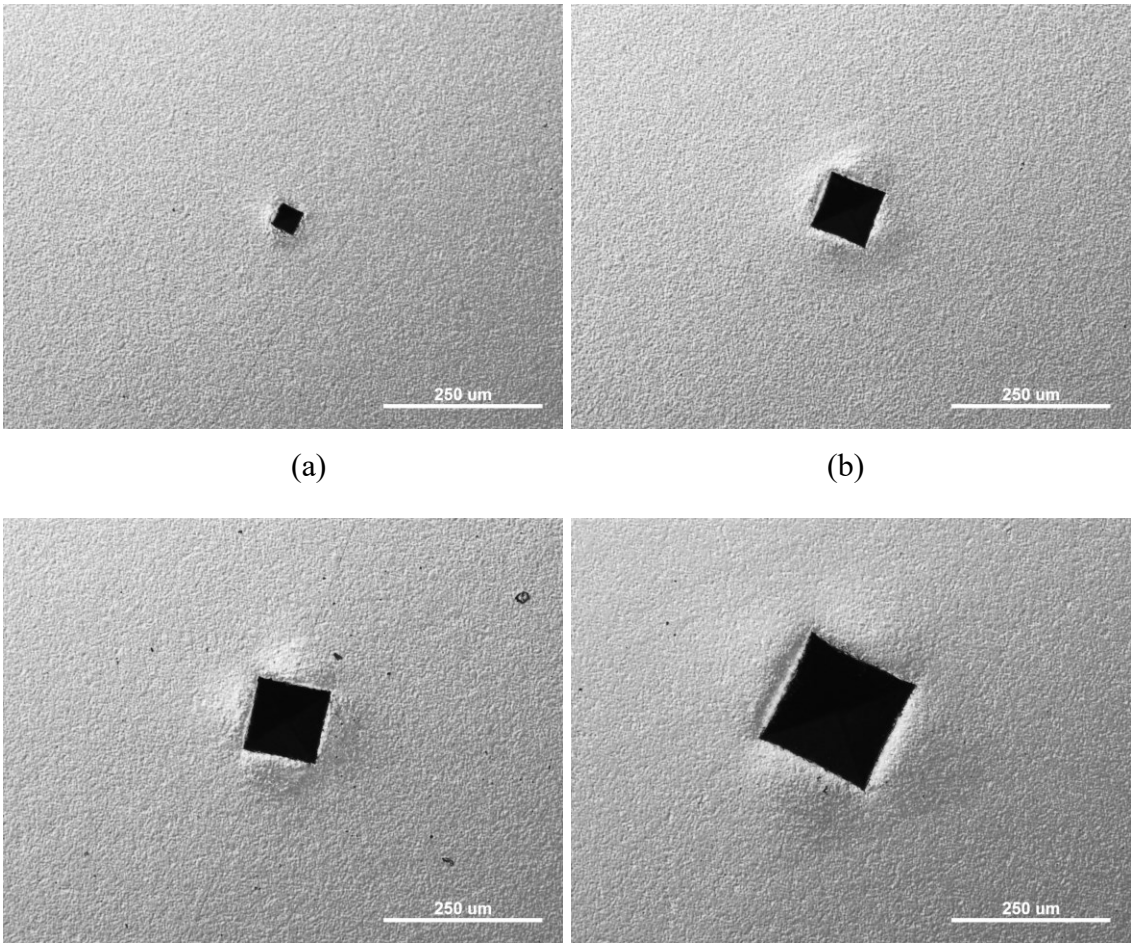

Figure B. 3: DIC optical microscopy images of a TiC- 316L 30 vol.% fine-grained cermet, indented with a Vickers indenter with (a) 1, (b) 5, (c) 10, and (d) 30 kgf of load.

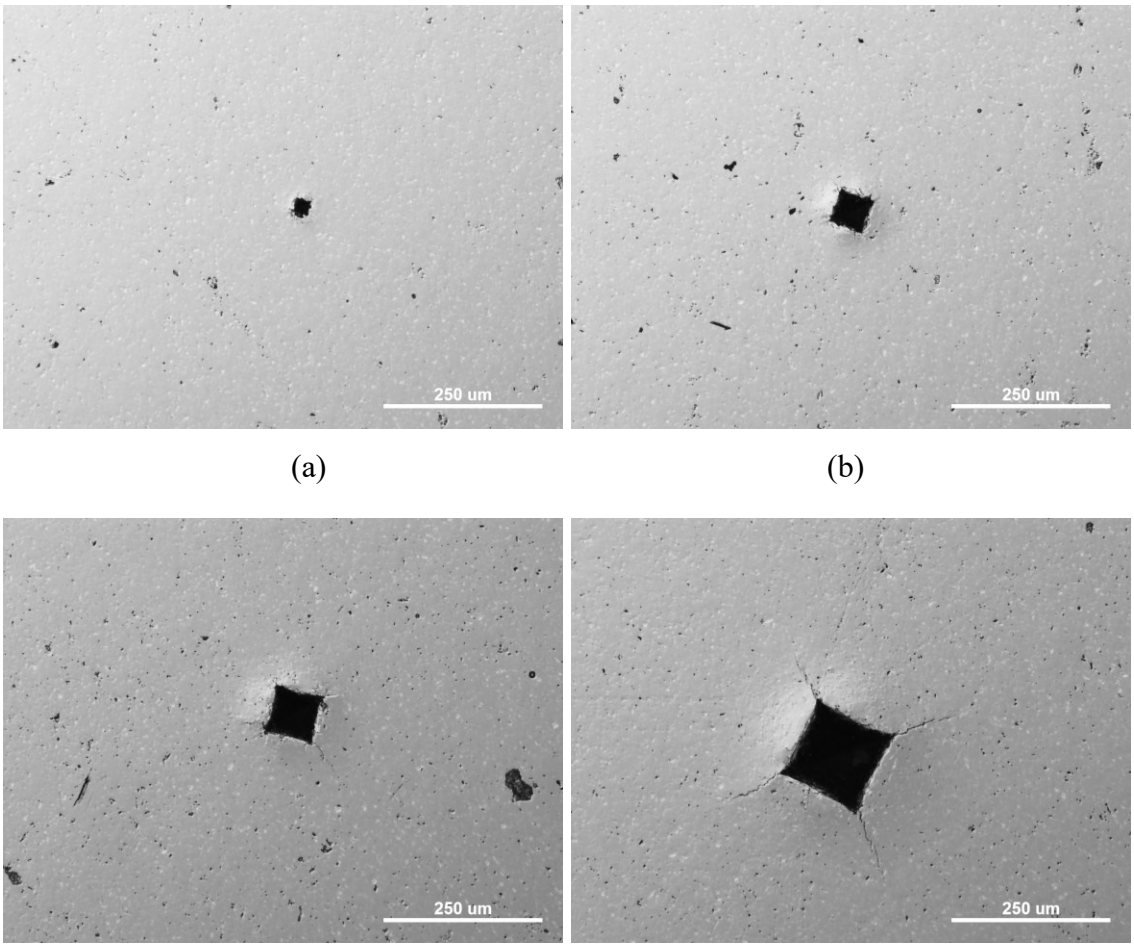

(a) (b)

(c) (d)

Figure B. 4: DIC optical microscopy images of a TiC- 316L 10 vol.% intermediate-grained cermet, indented with a Vickers indenter with (a) 1, (b) 5, (c) 10, and (d) 30 kgf of load.

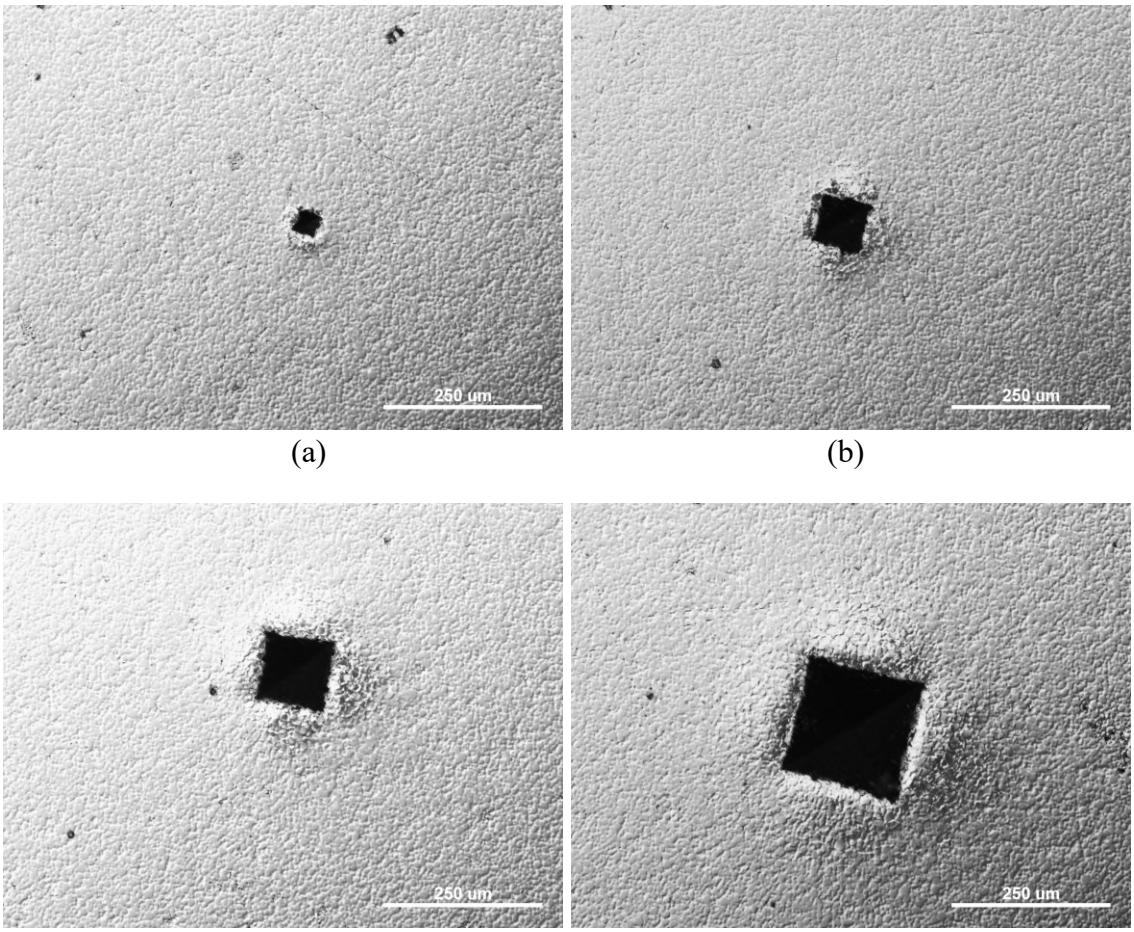

(a) (b)

(c) (d)

Figure B. 5: DIC optical microscopy images of a TiC- 316L 30 vol.% intermediate-grained cermet, indented with a Vickers indenter with (a) 1, (b) 5, (c) 10, and (d) 30 kgf of load.

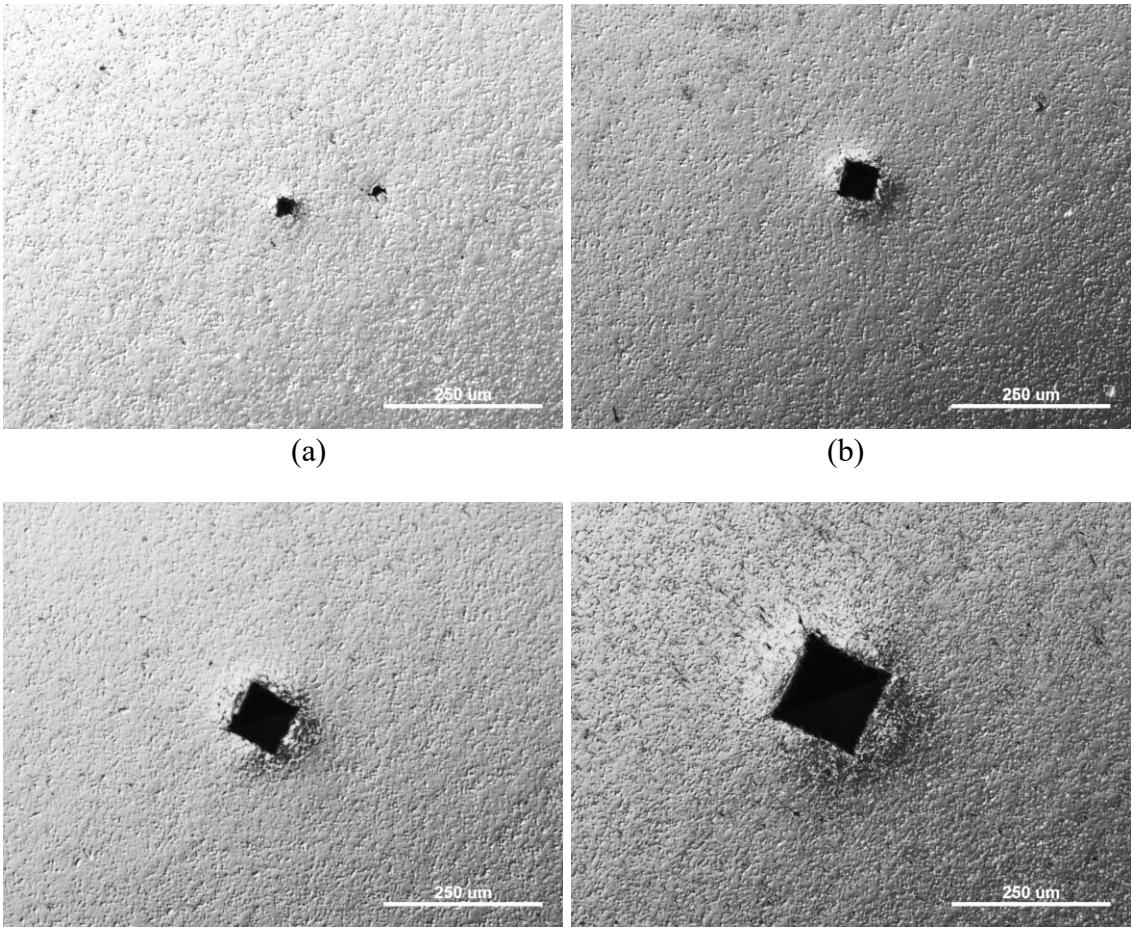

(a) (b)

(c) (d)

Figure B. 6: DIC optical microscopy images of a TiC- 316L 10 vol.% coarse-grained cermet, indented with a Vickers indenter with (a) 1, (b) 5, (c) 10, and (d) 30 kgf of load.

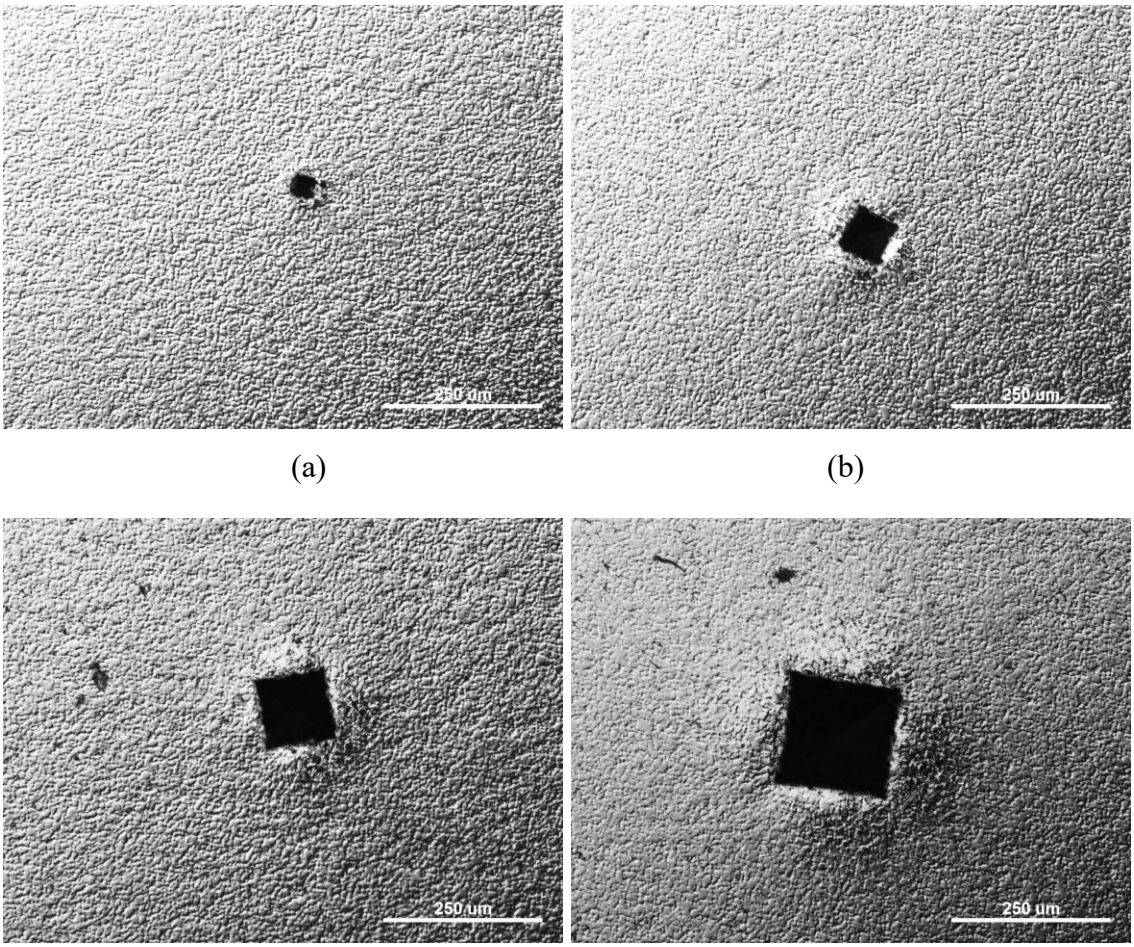

(a) (b)

(c) (d)

Figure B. 7: DIC optical microscopy images of a TiC- 316L 30 vol.% coarse-grained cermet, indented with a Vickers indenter with (a) 1, (b) 5, (c) 10, and (d) 30 kgf of load.

Appendix. C Hertz Indentation Data

Appendix C presents the representative images and figures of the 'blunt' Hertzian indentation test, which was not presented in Chapter 6. Figure C. 1 shows DIC optical microscope images of an intermediate-grained cermet with 30 vol.% binder after 2000N of load, the samples shows 'pileup' effect, the radius of the samples increases with increasing indenter sizes. Figure C. 2 shows a coarse-grained cermet with 10 and 30 vol.% of binder loaded with 250N of load, the contact radius increases with increasing binder content. Representative 3D images of the indentation depth obtained from the optical profilometry is shown in Figure C. 3, for an intermediate-grained cermet with 30 vol.% of binder, the residual impression depths decreases with increasing indenter spheres used. Another example of the optical profilometry is the load effect, which is shown in Figure C. 4, the cermets was also 30 vol.% intermediate-grained, loaded with both 250 N and 1000 N of force. The indentation depth increases with increasing load. In Figure C. 5 shows the residual indentation depth and peak deflection of coarse-grained cermet loaded with 250 N of force.

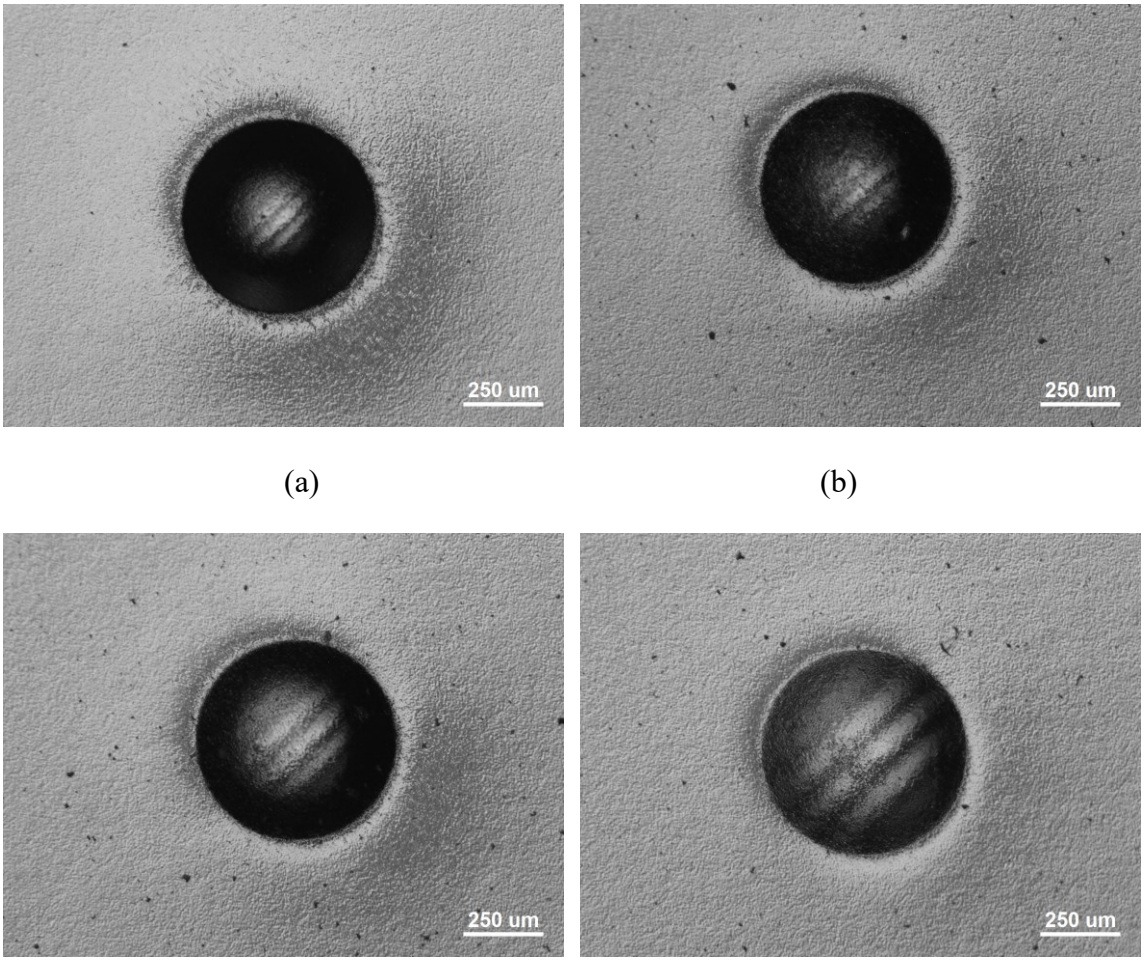

(a) (b)

(c) (d)

Figure C. 1: DIC optical microscope images of a TiC-316L 30 vol.% intermediate-grained cermet loaded with 2000 N of force, with WC-Co indenters, diameter shows (a) 1.58, (b) 1.98 (c) 2.38 and (d) 3.18 mm.

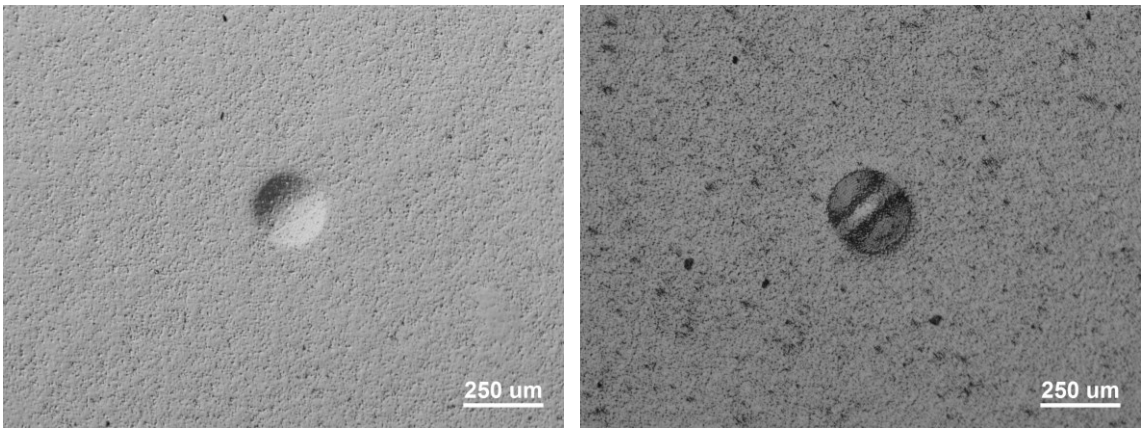

(a) (b)

Figure C. 2: DIC optical microscope images of TiC-316L coarse grained cermets, with (a) 10 and (b) 30 vol.% of binder, loaded with a 1.98mm indenter with 250 N of force.

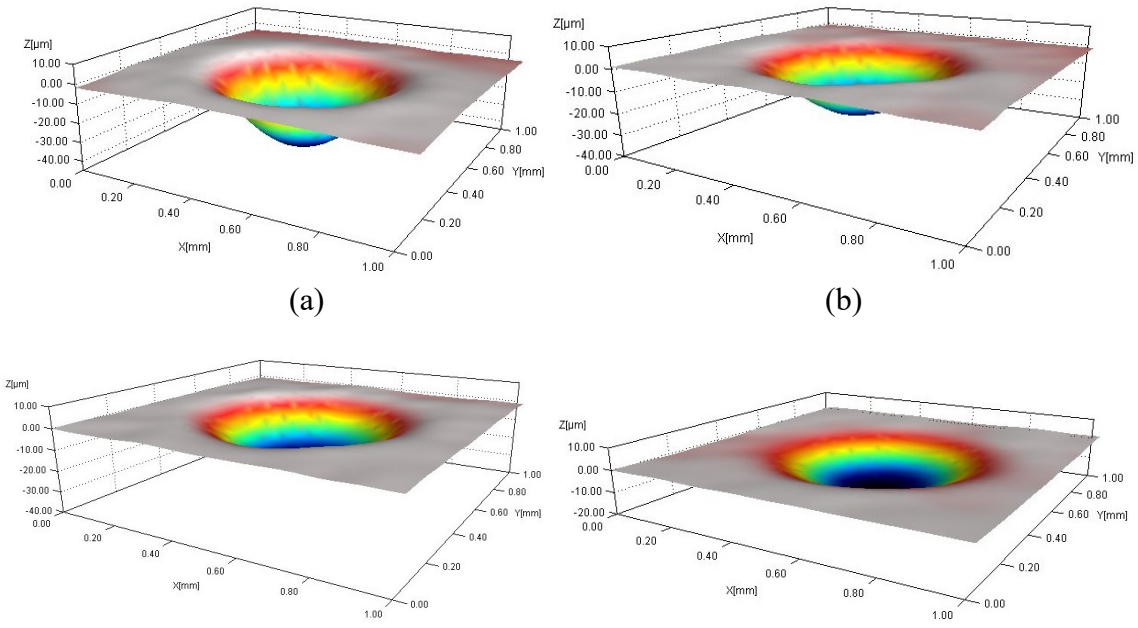

(a) (b)

(c) (d)

Figure C. 3: Pseudo colour 3D images obtained from optical profilometry. Load with 2000 N of force on TiC-30 vol.% intermediated grained cermet, with (a) 1.58, (b) 1.98 (c) 2.38 and (d) 3.18 mm indenter.

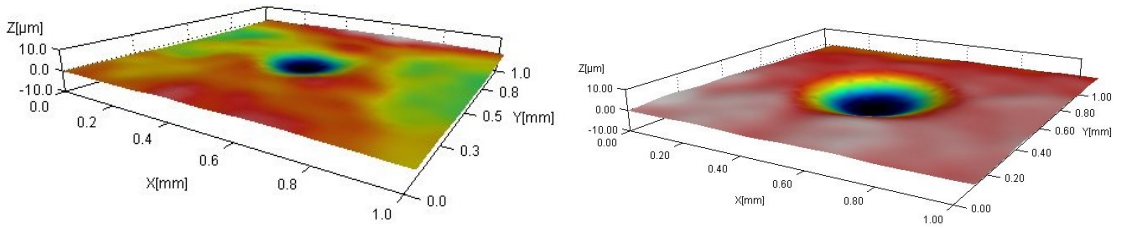

(a) (b)

Figure C. 4: Pseudo colour 3D images of TiC-30 vol.% intermediate grained cermets, loaded with 1.98 mm indenter, with (a) 250 N and (b) 1000 N of load.

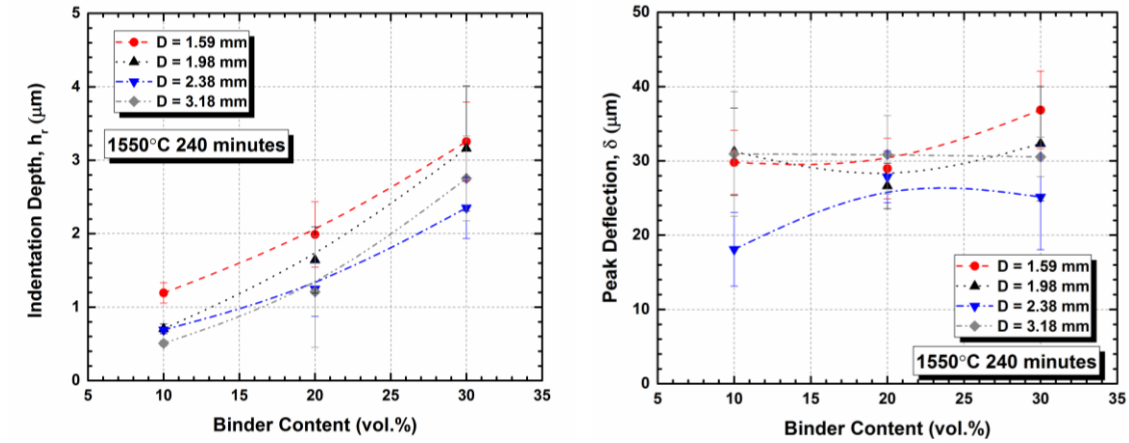

(a) (b)

Figure C. 5: Coarse-grained cermets loaded with 250 N of force showing (a) indentation depth and (b) peak deflection.

Appendix. D Reciprocating Wear Data

Appendix D shows the reciprocating wear data of the TiC-stainless steel cermets, which was not presented from Chapter 7 to 9. Figure D. 1 is the dynamic coefficient of friction data for TiC-410L intermediate-grained cermet with 20 and 30 vol.% of binder. The sample were subjected to load ranging from 20 to 80 N and tested for 120 minutes. Time effect on the reciprocating wear is also shown here. In Figure D. 2 shows the dynamic coefficient of friction for intermediate-grained cermets, with 10 and 30 vol.% of binder and for 30 and 60 minutes. All samples were subjected with both 40 and 80 N of load.

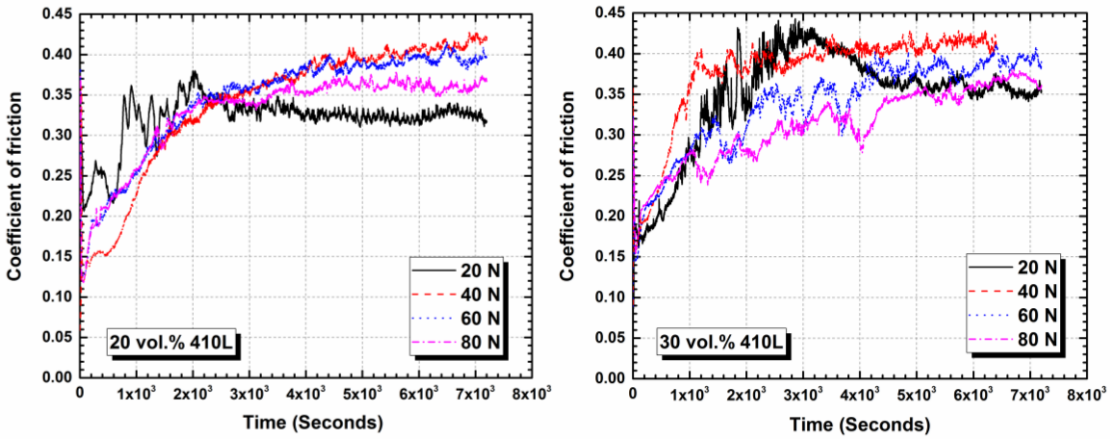

Figure D. 1: The effects of applied load on the dynamic COF curves of TiC with 20 and 30 vol.% 410-L stainless steel.

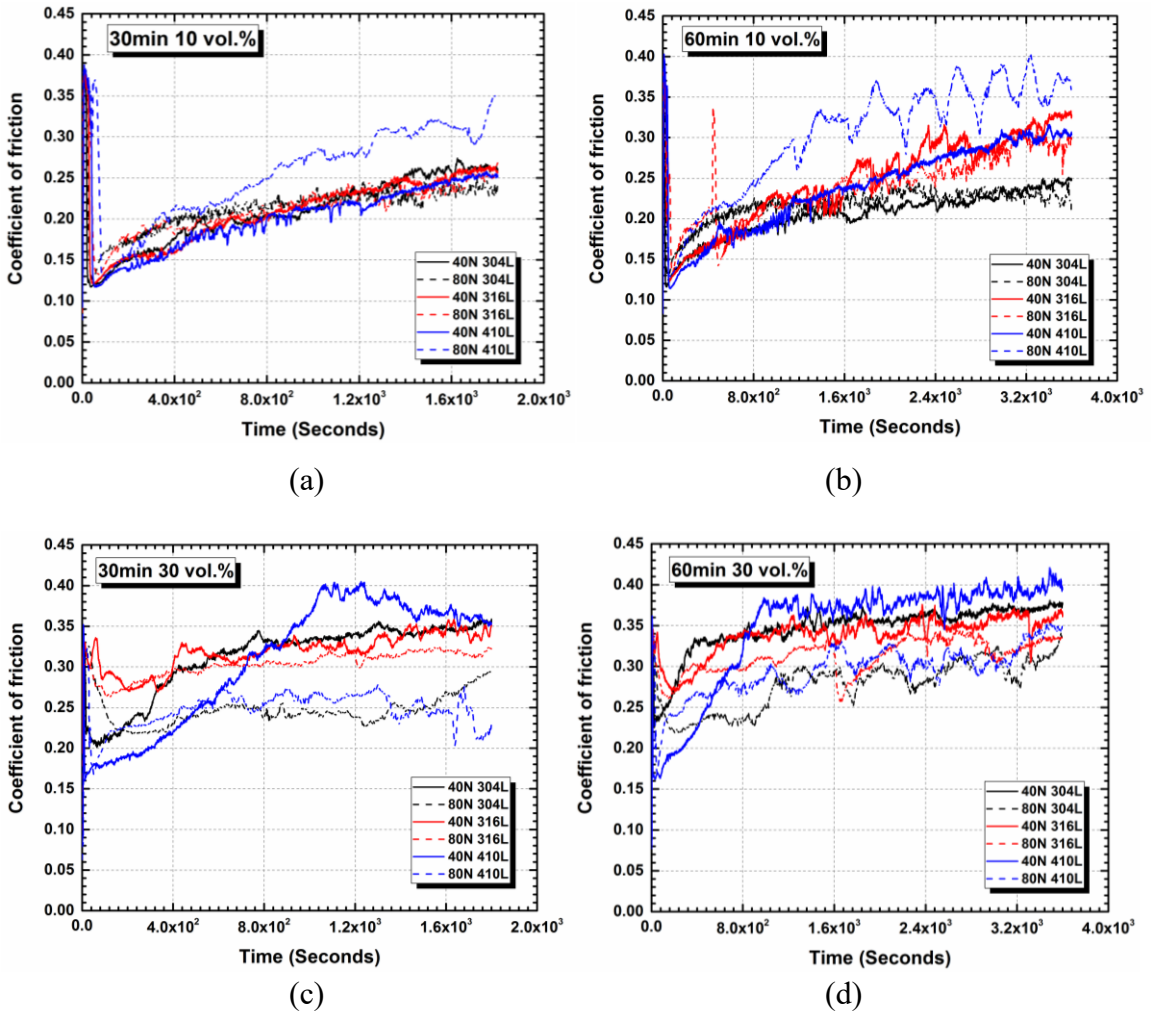

Figure D. 2: Dynamic COF of TiC cermets loaded with 40 and 80 N of force, tested for 30 and 60 min.

Appendix. E Copyright Permission Letters

ELSEVIER LICENSE
TERMS AND CONDITIONS

May 13, 2016

This is a License Agreement between Chenxin Jin ("You") and Elsevier ("Elsevier") provided by Copyright Clearance Center ("CCC"). The license consists of your order details, the terms and conditions provided by Elsevier, and the payment terms and conditions.

All payments must be made in full to CCC. For payment instructions, please see information listed at the bottom of this form.

Supplier	Elsevier Limited The Boulevard,Langford Lane Kidlington,Oxford,OX5 1GB,UK
Registered Company Number	1982084
Customer name	Chenxin Jin
Customer address	1360 Barrington Street Halifax, NS B3J 2K9
License number	3866561200185
License date	May 12, 2016
Licensed content publisher	Elsevier
Licensed content publication	International Journal of Refractory Metals and Hard Materials
Licensed content title	Microstructure instability in TiC-316L stainless steel cermets
Licensed content author	Chenxin Jin,Kevin P. Plucknett
Licensed content date	August 2016
Licensed content volume number	58
Licensed content issue number	n/a
Number of pages	10
Start Page	74
End Page	83
Type of Use	reuse in a thesis/dissertation
Portion	full article
Format	electronic
Are you the author of this Elsevier article?	Yes

Will you be translating?	No
Title of your thesis/dissertation	Indentation and wear damage of TiC-stainless steel cermet
Expected completion date	Aug 2016
Estimated size (number of pages)	250
Elsevier VAT number	GB 494 6272 12
Permissions price	0.00 CAD
VAT/Local Sales Tax	0.00 CAD / 0.00 GBP
Total	0.00 CAD

Terms and Conditions

INTRODUCTION

1. The publisher for this copyrighted material is Elsevier. By clicking "accept" in connection with completing this licensing transaction, you agree that the following terms and conditions apply to this transaction (along with the Billing and Payment terms and conditions established by Copyright Clearance Center, Inc. ("CCC"), at the time that you opened your Rightslink account and that are available at any time at http://myaccount.copyright.com).

GENERAL TERMS

2. Elsevier hereby grants you permission to reproduce the aforementioned material subject to the terms and conditions indicated.

3. Acknowledgement: If any part of the material to be used (for example, figures) has appeared in our publication with credit or acknowledgement to another source, permission must also be sought from that source. If such permission is not obtained then that material may not be included in your publication/copies. Suitable acknowledgement to the source must be made, either as a footnote or in a reference list at the end of your publication, as follows:

"Reprinted from Publication title, Vol /edition number, Author(s), Title of article / title of chapter, Pages No., Copyright (Year), with permission from Elsevier [OR APPLICABLE SOCIETY COPYRIGHT OWNER]." Also Lancet special credit - "Reprinted from The Lancet, Vol. number, Author(s), Title of article, Pages No., Copyright (Year), with permission from Elsevier."

4. Reproduction of this material is confined to the purpose and/or media for which permission is hereby given.

5. Altering/Modifying Material: Not Permitted. However figures and illustrations may be altered/adapted minimally to serve your work. Any other abbreviations, additions, deletions and/or any other alterations shall be made only with prior written authorization of Elsevier Ltd. (Please contact Elsevier at permissions@elsevier.com)

6. If the permission fee for the requested use of our material is waived in this instance, please be advised that your future requests for Elsevier materials may attract a fee.

7. Reservation of Rights: Publisher reserves all rights not specifically granted in the combination of (i) the license details provided by you and accepted in the course of this licensing transaction, (ii) these terms and conditions and (iii) CCC's Billing and Payment terms and conditions.

8. License Contingent Upon Payment: While you may exercise the rights licensed

immediately upon issuance of the license at the end of the licensing process for the transaction, provided that you have disclosed complete and accurate details of your proposed use, no license is finally effective unless and until full payment is received from you (either by publisher or by CCC) as provided in CCC's Billing and Payment terms and conditions. If full payment is not received on a timely basis, then any license preliminarily granted shall be deemed automatically revoked and shall be void as if never granted. Further, in the event that you breach any of these terms and conditions or any of CCC's Billing and Payment terms and conditions, the license is automatically revoked and shall be void as if never granted. Use of materials as described in a revoked license, as well as any use of the materials beyond the scope of an unrevoked license, may constitute copyright infringement and publisher reserves the right to take any and all action to protect its copyright in the materials.

9. Warranties: Publisher makes no representations or warranties with respect to the licensed material.

10. Indemnity: You hereby indemnify and agree to hold harmless publisher and CCC, and their respective officers, directors, employees and agents, from and against any and all claims arising out of your use of the licensed material other than as specifically authorized pursuant to this license.

11. No Transfer of License: This license is personal to you and may not be sublicensed, assigned, or transferred by you to any other person without publisher's written permission.

12. No Amendment Except in Writing: This license may not be amended except in a writing signed by both parties (or, in the case of publisher, by CCC on publisher's behalf).

13. Objection to Contrary Terms: Publisher hereby objects to any terms contained in any purchase order, acknowledgment, check endorsement or other writing prepared by you, which terms are inconsistent with these terms and conditions or CCC's Billing and Payment terms and conditions. These terms and conditions, together with CCC's Billing and Payment terms and conditions (which are incorporated herein), comprise the entire agreement between you and publisher (and CCC) concerning this licensing transaction. In the event of any conflict between your obligations established by these terms and conditions and those established by CCC's Billing and Payment terms and conditions, these terms and conditions shall control.

14. Revocation: Elsevier or Copyright Clearance Center may deny the permissions described in this License at their sole discretion, for any reason or no reason, with a full refund payable to you. Notice of such denial will be made using the contact information provided by you. Failure to receive such notice will not alter or invalidate the denial. In no event will Elsevier or Copyright Clearance Center be responsible or liable for any costs, expenses or damage incurred by you as a result of a denial of your permission request, other than a refund of the amount(s) paid by you to Elsevier and/or Copyright Clearance Center for denied permissions.

LIMITED LICENSE

The following terms and conditions apply only to specific license types:

15. **Translation**: This permission is granted for non-exclusive world **English** rights only unless your license was granted for translation rights. If you licensed translation rights you may only translate this content into the languages you requested. A professional translator must perform all translations and reproduce the content word for word preserving the integrity of the article.

16. **Posting licensed content on any Website**: The following terms and conditions apply as follows: Licensing material from an Elsevier journal: All content posted to the web site must maintain the copyright information line on the bottom of each image; A hyper-text must be included to the Homepage of the journal from which you are licensing athttp://www.sciencedirect.com/science/journal/xxxxx or the Elsevier homepage for books athttp://www.elsevier.com; Central Storage: This license does not include permission for a scanned version of the material to be stored in a central repository such as that provided by Heron/XanEdu.
Licensing material from an Elsevier book: A hyper-text link must be included to the Elsevier homepage at http://www.elsevier.com . All content posted to the web site must maintain the copyright information line on the bottom of each image.

Posting licensed content on Electronic reserve: In addition to the above the following clauses are applicable: The web site must be password-protected and made available only to bona fide students registered on a relevant course. This permission is granted for 1 year only. You may obtain a new license for future website posting.
17. **For journal authors:** the following clauses are applicable in addition to the above:
Preprints:
A preprint is an author's own write-up of research results and analysis, it has not been peer-reviewed, nor has it had any other value added to it by a publisher (such as formatting, copyright, technical enhancement etc.).
Authors can share their preprints anywhere at any time. Preprints should not be added to or enhanced in any way in order to appear more like, or to substitute for, the final versions of articles however authors can update their preprints on arXiv or RePEc with their Accepted Author Manuscript (see below).
If accepted for publication, we encourage authors to link from the preprint to their formal publication via its DOI. Millions of researchers have access to the formal publications on ScienceDirect, and so links will help users to find, access, cite and use the best available version. Please note that Cell Press, The Lancet and some society-owned have different preprint policies. Information on these policies is available on the journal homepage.
Accepted Author Manuscripts: An accepted author manuscript is the manuscript of an article that has been accepted for publication and which typically includes author-incorporated changes suggested during submission, peer review and editor-author communications.
Authors can share their accepted author manuscript:

- – immediately
    - via their non-commercial person homepage or blog
    - by updating a preprint in arXiv or RePEc with the accepted manuscript
    - via their research institute or institutional repository for internal institutional uses or as part of an invitation-only research collaboration work-group
    - directly by providing copies to their students or to research collaborators for their personal use
    - for private scholarly sharing as part of an invitation-only work group on commercial sites with which Elsevier has an agreement

- – after the embargo period
    - via non-commercial hosting platforms such as their institutional repository
    - via commercial sites with which Elsevier has an agreement

In all cases accepted manuscripts should:

- – link to the formal publication via its DOI
- – bear a CC-BY-NC-ND license - this is easy to do
- – if aggregated with other manuscripts, for example in a repository or other site, be shared in alignment with our hosting policy not be added to or enhanced in any way to appear more like, or to substitute for, the published journal article.

Published journal article (JPA): A published journal article (PJA) is the definitive final record of published research that appears or will appear in the journal and embodies all value-adding publishing activities including peer review co-ordination, copy-editing, formatting, (if relevant) pagination and online enrichment.

Policies for sharing publishing journal articles differ for subscription and gold open access articles:

Subscription Articles: If you are an author, please share a link to your article rather than the full-text. Millions of researchers have access to the formal publications on ScienceDirect, and so links will help your users to find, access, cite, and use the best available version.

Theses and dissertations which contain embedded PJAs as part of the formal submission can be posted publicly by the awarding institution with DOI links back to the formal publications on ScienceDirect.

If you are affiliated with a library that subscribes to ScienceDirect you have additional private sharing rights for others' research accessed under that agreement. This includes use for classroom teaching and internal training at the institution (including use in course packs and courseware programs), and inclusion of the article for grant funding purposes.

Gold Open Access Articles: May be shared according to the author-selected end-user license and should contain a CrossMark logo, the end user license, and a DOI link to the formal publication on ScienceDirect.

Please refer to Elsevier's posting policy for further information.

18. **For book authors** the following clauses are applicable in addition to the above: Authors are permitted to place a brief summary of their work online only. You are not allowed to download and post the published electronic version of your chapter, nor may you scan the printed edition to create an electronic version. **Posting to a repository:** Authors are permitted to post a summary of their chapter only in their institution's repository.

19. **Thesis/Dissertation**: If your license is for use in a thesis/dissertation your thesis may be submitted to your institution in either print or electronic form. Should your thesis be published commercially, please reapply for permission. These requirements include permission for the Library and Archives of Canada to supply single copies, on demand, of the complete thesis and include permission for Proquest/UMI to supply single copies, on demand, of the complete thesis. Should your thesis be published commercially, please reapply for permission. Theses and dissertations which contain embedded PJAs as part of the formal submission can be posted publicly by the awarding institution with DOI links back to the formal publications on ScienceDirect.

- – Systematic distribution via e-mail lists or share buttons

Posting or linking by commercial companies for use by customers of those companies.

20. **Other Conditions**:

v1.8

Questions? customercare@copyright.com or +1-855-239-3415 (toll free in the US) or +1-978-646-2777.

ELSEVIER LICENSE
TERMS AND CONDITIONS

May 13, 2016

This is a License Agreement between Chenxin Jin ("You") and Elsevier ("Elsevier") provided by Copyright Clearance Center ("CCC"). The license consists of your order details, the terms and conditions provided by Elsevier, and the payment terms and conditions.

All payments must be made in full to CCC. For payment instructions, please see information listed at the bottom of this form.

Supplier	Elsevier Limited The Boulevard,Langford Lane Kidlington,Oxford,OX5 1GB,UK
Registered Company Number	1982084
Customer name	Chenxin Jin
Customer address	1360 Barrington Street Halifax, NS B3J 2K9
License number	3866570102929
License date	May 12, 2016
Licensed content publisher	Elsevier
Licensed content publication	Wear
Licensed content title	The effects of TiC grain size and steel binder content on the reciprocating wear behaviour of TiC-316L stainless steel cermets
Licensed content author	Chukwuma C. Onuoha,Chenxin Jin,Zoheir N. Farhat,Georges J. Kipouros,Kevin P. Plucknett
Licensed content date	15 March 2016
Licensed content volume number	350
Licensed content issue number	n/a
Number of pages	14
Start Page	116
End Page	129
Type of Use	reuse in a thesis/dissertation
Intended publisher of new work	other
Portion	full article
Format	electronic
Are you the author of this Elsevier article?	Yes

Will you be translating?	No
Title of your thesis/dissertation	Indentation and wear damage of TiC-stainless steel cermet
Expected completion date	Aug 2016
Estimated size (number of pages)	250
Elsevier VAT number	GB 494 6272 12
Permissions price	0.00 CAD
VAT/Local Sales Tax	0.00 CAD / 0.00 GBP
Total	0.00 CAD
Terms and Conditions	

INTRODUCTION

1. The publisher for this copyrighted material is Elsevier. By clicking "accept" in connection with completing this licensing transaction, you agree that the following terms and conditions apply to this transaction (along with the Billing and Payment terms and conditions established by Copyright Clearance Center, Inc. ("CCC"), at the time that you opened your Rightslink account and that are available at any time at http://myaccount.copyright.com).

GENERAL TERMS

2. Elsevier hereby grants you permission to reproduce the aforementioned material subject to the terms and conditions indicated.

3. Acknowledgement: If any part of the material to be used (for example, figures) has appeared in our publication with credit or acknowledgement to another source, permission must also be sought from that source. If such permission is not obtained then that material may not be included in your publication/copies. Suitable acknowledgement to the source must be made, either as a footnote or in a reference list at the end of your publication, as follows:

"Reprinted from Publication title, Vol /edition number, Author(s), Title of article / title of chapter, Pages No., Copyright (Year), with permission from Elsevier [OR APPLICABLE SOCIETY COPYRIGHT OWNER]." Also Lancet special credit - "Reprinted from The Lancet, Vol. number, Author(s), Title of article, Pages No., Copyright (Year), with permission from Elsevier."

4. Reproduction of this material is confined to the purpose and/or media for which permission is hereby given.

5. Altering/Modifying Material: Not Permitted. However figures and illustrations may be altered/adapted minimally to serve your work. Any other abbreviations, additions, deletions and/or any other alterations shall be made only with prior written authorization of Elsevier Ltd. (Please contact Elsevier at permissions@elsevier.com)

6. If the permission fee for the requested use of our material is waived in this instance, please be advised that your future requests for Elsevier materials may attract a fee.

7. Reservation of Rights: Publisher reserves all rights not specifically granted in the combination of (i) the license details provided by you and accepted in the course of this licensing transaction, (ii) these terms and conditions and (iii) CCC's Billing and Payment terms and conditions.

8. License Contingent Upon Payment: While you may exercise the rights licensed

immediately upon issuance of the license at the end of the licensing process for the transaction, provided that you have disclosed complete and accurate details of your proposed use, no license is finally effective unless and until full payment is received from you (either by publisher or by CCC) as provided in CCC's Billing and Payment terms and conditions. If full payment is not received on a timely basis, then any license preliminarily granted shall be deemed automatically revoked and shall be void as if never granted. Further, in the event that you breach any of these terms and conditions or any of CCC's Billing and Payment terms and conditions, the license is automatically revoked and shall be void as if never granted. Use of materials as described in a revoked license, as well as any use of the materials beyond the scope of an unrevoked license, may constitute copyright infringement and publisher reserves the right to take any and all action to protect its copyright in the materials.

9. Warranties: Publisher makes no representations or warranties with respect to the licensed material.

10. Indemnity: You hereby indemnify and agree to hold harmless publisher and CCC, and their respective officers, directors, employees and agents, from and against any and all claims arising out of your use of the licensed material other than as specifically authorized pursuant to this license.

11. No Transfer of License: This license is personal to you and may not be sublicensed, assigned, or transferred by you to any other person without publisher's written permission.

12. No Amendment Except in Writing: This license may not be amended except in a writing signed by both parties (or, in the case of publisher, by CCC on publisher's behalf).

13. Objection to Contrary Terms: Publisher hereby objects to any terms contained in any purchase order, acknowledgment, check endorsement or other writing prepared by you, which terms are inconsistent with these terms and conditions or CCC's Billing and Payment terms and conditions. These terms and conditions, together with CCC's Billing and Payment terms and conditions (which are incorporated herein), comprise the entire agreement between you and publisher (and CCC) concerning this licensing transaction. In the event of any conflict between your obligations established by these terms and conditions and those established by CCC's Billing and Payment terms and conditions, these terms and conditions shall control.

14. Revocation: Elsevier or Copyright Clearance Center may deny the permissions described in this License at their sole discretion, for any reason or no reason, with a full refund payable to you. Notice of such denial will be made using the contact information provided by you. Failure to receive such notice will not alter or invalidate the denial. In no event will Elsevier or Copyright Clearance Center be responsible or liable for any costs, expenses or damage incurred by you as a result of a denial of your permission request, other than a refund of the amount(s) paid by you to Elsevier and/or Copyright Clearance Center for denied permissions.

LIMITED LICENSE

The following terms and conditions apply only to specific license types:

15. **Translation**: This permission is granted for non-exclusive world **English** rights only unless your license was granted for translation rights. If you licensed translation rights you may only translate this content into the languages you requested. A professional translator must perform all translations and reproduce the content word for word preserving the integrity of the article.

16. **Posting licensed content on any Website**: The following terms and conditions apply as follows: Licensing material from an Elsevier journal: All content posted to the web site must maintain the copyright information line on the bottom of each image; A hyper-text must be included to the Homepage of the journal from which you are licensing athttp://www.sciencedirect.com/science/journal/xxxxx or the Elsevier homepage for books athttp://www.elsevier.com; Central Storage: This license does not include permission for a scanned version of the material to be stored in a central repository such as that provided by Heron/XanEdu.
Licensing material from an Elsevier book: A hyper-text link must be included to the Elsevier homepage at http://www.elsevier.com . All content posted to the web site must maintain the copyright information line on the bottom of each image.

Posting licensed content on Electronic reserve: In addition to the above the following clauses are applicable: The web site must be password-protected and made available only to bona fide students registered on a relevant course. This permission is granted for 1 year only. You may obtain a new license for future website posting.
17. **For journal authors:** the following clauses are applicable in addition to the above:
Preprints:
A preprint is an author's own write-up of research results and analysis, it has not been peer-reviewed, nor has it had any other value added to it by a publisher (such as formatting, copyright, technical enhancement etc.).
Authors can share their preprints anywhere at any time. Preprints should not be added to or enhanced in any way in order to appear more like, or to substitute for, the final versions of articles however authors can update their preprints on arXiv or RePEc with their Accepted Author Manuscript (see below).
If accepted for publication, we encourage authors to link from the preprint to their formal publication via its DOI. Millions of researchers have access to the formal publications on ScienceDirect, and so links will help users to find, access, cite and use the best available version. Please note that Cell Press, The Lancet and some society-owned have different preprint policies. Information on these policies is available on the journal homepage.
Accepted Author Manuscripts: An accepted author manuscript is the manuscript of an article that has been accepted for publication and which typically includes author-incorporated changes suggested during submission, peer review and editor-author communications.
Authors can share their accepted author manuscript:

- – immediately
    - via their non-commercial person homepage or blog
    - by updating a preprint in arXiv or RePEc with the accepted manuscript
    - via their research institute or institutional repository for internal institutional uses or as part of an invitation-only research collaboration work-group
    - directly by providing copies to their students or to research collaborators for their personal use
    - for private scholarly sharing as part of an invitation-only work group on commercial sites with which Elsevier has an agreement

- – after the embargo period
    - via non-commercial hosting platforms such as their institutional repository
    - via commercial sites with which Elsevier has an agreement

In all cases accepted manuscripts should:

- – link to the formal publication via its DOI
- – bear a CC-BY-NC-ND license - this is easy to do
- – if aggregated with other manuscripts, for example in a repository or other site, be shared in alignment with our hosting policy not be added to or enhanced in any way to appear more like, or to substitute for, the published journal article.

Published journal article (JPA): A published journal article (PJA) is the definitive final record of published research that appears or will appear in the journal and embodies all value-adding publishing activities including peer review co-ordination, copy-editing, formatting, (if relevant) pagination and online enrichment.

Policies for sharing publishing journal articles differ for subscription and gold open access articles:

Subscription Articles: If you are an author, please share a link to your article rather than the full-text. Millions of researchers have access to the formal publications on ScienceDirect, and so links will help your users to find, access, cite, and use the best available version.

Theses and dissertations which contain embedded PJAs as part of the formal submission can be posted publicly by the awarding institution with DOI links back to the formal publications on ScienceDirect.

If you are affiliated with a library that subscribes to ScienceDirect you have additional private sharing rights for others' research accessed under that agreement. This includes use for classroom teaching and internal training at the institution (including use in course packs and courseware programs), and inclusion of the article for grant funding purposes.

Gold Open Access Articles: May be shared according to the author-selected end-user license and should contain a CrossMark logo, the end user license, and a DOI link to the formal publication on ScienceDirect.

Please refer to Elsevier's posting policy for further information.

18. **For book authors** the following clauses are applicable in addition to the above: Authors are permitted to place a brief summary of their work online only. You are not allowed to download and post the published electronic version of your chapter, nor may you scan the printed edition to create an electronic version. **Posting to a repository:** Authors are permitted to post a summary of their chapter only in their institution's repository.

19. **Thesis/Dissertation**: If your license is for use in a thesis/dissertation your thesis may be submitted to your institution in either print or electronic form. Should your thesis be published commercially, please reapply for permission. These requirements include permission for the Library and Archives of Canada to supply single copies, on demand, of the complete thesis and include permission for Proquest/UMI to supply single copies, on demand, of the complete thesis. Should your thesis be published commercially, please reapply for permission. Theses and dissertations which contain embedded PJAs as part of the formal submission can be posted publicly by the awarding institution with DOI links back to the formal publications on ScienceDirect.

- – Systematic distribution via e-mail lists or share buttons

Posting or linking by commercial companies for use by customers of those companies.

20. **Other Conditions**:

v1.8

Questions? customercare@copyright.com or +1-855-239-3415 (toll free in the US) or +1-978-646-2777.